On the inversion of potential field data: Physical property estimations and model geometry changes

Dissertation
zur Erlangung des Doktorgrades
der Mathematisch-Naturwissenschaftlichen Fakultät
der Christian-Albrechts-Universität zu Kiel

vorgelegt von

Claudia Haase

Kiel 2014

Institut für Geowissenschaften
Abteilung Geophysik

Referent:	Prof. Dr. Hans-Jürgen Götze
Korreferent:	Prof. Dr. Jörg Ebbing
Tag der mündlichen Prüfung:	12.06.2014
Zum Druck genehmigt:	12.06.2014

gez. Prof. Dr. Wolfgang J. Duschl / Dekan

"Don't tell me the sky's the limit
- there's footprints on the moon."
(Paul Brandt)

Abstract

Inversion tools for potential field data are especially important for multi-method or integrated modeling approaches. Computational developments and the increasing amount of, e.g. gravity gradient data from satellite missions, also lead to increasingly complex models. Furthermore, forward modeling of gradient data is rather non-intuitive and inverse methods are preferable. This thesis focuses on the development of inversion tools for potential field data, aiming at the inversion of physical properties and the optimization of model geometries, that are applicable to models of varying geometric representations.
The first part regards the estimation of physical properties of subsurface models that are built of voxels or have a fixed geometry based on polyhedral model bodies. This inversion task allows the application of a linear method: The Minimum Mean Square Error (MMSE) method utilizes the mean square approach and Gaussian random variables within a statistical framework. A previous implementation of the method is extended and new features include inversion of all gravity tensor components, combined inversion of all available data sets, correlations between voxels and exact calculation of the potential fields in contrast to mass point approximation. The application of the tool in different case studies is shown: The tests involve a conceptional salt structure in voxel representation and two polyhedron-based models from the North German Basin for synthetic applications. A fourth model, describing the Capel and Faust Basins offshore Queensland, Australia, is given in both geometric representations and allows a comparative method assessment. Results show that the voxel tool performs well when the inversion is constrained by additional information, guiding the estimations and reducing ambiguity. The polyhedron tool is quite fast and provides improvements for the model densities. To evaluate the results, anomaly sensitivities towards model bodies are calculated and discussed.
In some cases the property estimation alone is not sufficient to achieve a satisfying interpretation of the subsurface. Therefore, the second part of the thesis deals with automated geometry modifications and anomaly fitting. When addressing model geometries, the inverse problem becomes non-linear and can no longer be solved with the previous method. An optimization tool was designed which modifies vertex-based model geometries by applying spatial operators to the model that use an adaptive, on-the-fly model discretization. These operators deform the existing model via vertex-dragging and their defining parameters are subject to the optimization process. This parametrization causes a strong reduction of unknowns (dimensionality of the search space), allows a variety of possible modifications and ensures that geometries are not destroyed by crossing polygon lines or punctured planes. A Particle Swarm Optimization (PSO) is implemented as a global searcher with restart option for the task of finding optimal operator parameters. The tool estimates an ensemble of model solutions which allows a selection and geologically reasonable interpretations. Although designed for 3D applications, the novel approach is implemented here in 2D and two case studies are shown: One model is a synthetic salt structure in a horizontally layered background model. Expected geometry modifications are considerably small and localized and the initial models contain rather little structural information. The Capel and Faust Basins model from the first part of the thesis provides the large scale example for the second study. With the aim to evaluate the seismically derived model, large scale operators are applied that mainly cause depth adjustments to the model horizons. In these case studies, that are used to test the parametrization and the performance of the optimization with varying set-ups, the developed tool performs well which is promising for future applications. Both presented tools and examples show the usefulness of potential field inversion and should be implemented in a multi-method workflow.

Zusammenfassung

Inversionsprogramme für Potentialfelddaten sind wichtig, insbesondere für Multi-Methoden- oder integrierte Modellierungsansätze. Computerorientierte Enwicklungen und die zunehmende Menge von beispielsweise Schweregradientendaten von Satellitenmissionen, führen darüberhinaus zu zunehmend komplexeren Modellen. Hinzu kommt, dass die Vorwärtsmodellierung von Gradientendaten eher nicht-intuitiv ist und Inversionsmethoden zu bevorzugen sind. Diese Arbeit beschäftigt sich mit der Entwicklung von Inversionsprogrammen für Potentialfelddaten und zielt auf die Inversion der physikalischen Eigenschaften und die Optimierung von Modellgeometrien ab, wobei die Programme auf Modelle mit verschiedenen geometrischen Darstellungen anwendbar sein sollen.
Der erste Teil der Arbeit beschäftigt sich mit der Bestimmung der physikalischen Eigenschaften von Untergrundmodellen. Diese können aus Voxeln aufgebaut sein oder eine starre Geometrie aus Polyedern haben. Diese Aufgabe erlaubt die Anwendung einer linearen Inversionsmethodik. Die sogenannte Minimum Mean-Square Error (MMSE) Methode benutzt den Ansatz der kleinsten Quadrate und Gauß'sche Zufallsvariablen innerhalb einer statistischen Betrachtung. Eine vorherigen Implementierung dieser Methode wurde erweitert und die neuen Bestandteile umfassen die Inversion aller Schweretensorkomponenten, kombinierte Inversion aller verfügbaren Datensätze, Korrelationen zwischen Voxeln und die exakte Berechnung der Potentialfelder im Gegensatz zu vorheriger Massenpunktapproximation. Die Anwendung des Programms auf verschiedene Fallbeispiele wird gezeigt: Die Tests beinhalten eine konzeptionelle Salzstruktur in Voxeldarstellung und zwei Polyeder-basierte Modelle aus dem Norddeutschen Becken. Ein viertes Modell, das die Capel und Faust Becken vor der Küste von Queensland, Australien, beschreibt, liegt in beiden geometrischen Darstellungen vor und erlaubt somit eine vergleichende Methodenbewertung. Die Voxelanwendung arbeitet gut, wenn die Inversion durch Zusatzinformationen eingegrenzt wird, welche die Berechnungen leiten und Mehrdeutigkeiten einschränken. Die Polyedervariante ist recht schnell und liefert Verbesserungen der Modelldichten. Um die Ergebnisse zu beurteilen, wird die Sensitivität der Anomalien bezüglich der einzelnen Modellkörper bestimmt und diskutiert.
In einige Fällem ist die Bestimmung der physikalischen Eigenschaften allein nicht ausreichend, um eine zufriedenstellende Interpretation des Untergrundes zu erlangen. Daher beschäftigt sich der zweite Teil der Arbeit mit automatisierten Geometriemodifikationen und Anpassung der Potentialfeldanomalien. Betrachtet man die Modellgeometrie, so wird das Inversionsproblem nichtlinear und kann nicht länger mit der vorherigen Methode gelöst werden. Ein Optimierungsprogramm wurde entwickelt, das Eckpunkt-basierte Modellgeometrien mithilfe von räumlichen Operatoren modifizieren kann, welche eine adaptive, "on-the-fly" Modelldiskretisierung durchführen. Die Operatoren deformieren eine bestehende Modellgeometrie mittels Eckpunktmitführung und die sie definierenden Parameter sind Gegenstand des Optimierungsprozesses. Diese Art der Parametrisierung bietet ein Mittel zur Reduzierung der Unbekannten (der Dimension des Suchraums), erlaubt eine Vielfalt an möglichen Modifikationen und stellt sicher, dass Geometrien nicht durch sich kreuzende Polygone oder sich durchstechende Ebenen zerstört werden. Als globaler Suche für die Bestimmung optimaler Operatorparameter wurde eine Partikelschwarm Optimierung (PSO) mit der Option zum Neustart implementiert. Das Programm bestimmt ein Ensemble von Modelllösungen, was eine Selektion und geologisch sinnvolle Interpretationen ermöglicht. Obwohl für eine 3D-Anwendung konzipiert, ist der neue Ansatz hier in 2D implementiert und zwei Fallbeispiele werden gezeigt: Das eine Modell ist eine synthetische Salzstruktur in einem söhlig gelagerten Hintergrundmodell. Die erwarteten Geometrieänderungen sind verhältnismäßig klein und örtlich begrenzt und die Startmodelle enthalten eher wenig Information bezüglich der zu erwartenden Struktur. Das

Modell der Capel und Faust Becken aus dem ersten Teil der Arbeit bietet ein großskaliges Beispiel für die zweite Fallstudie. Mit dem Ziel, dass aus seismischen Interpretationen generierte Modell zu beurteilen, werden großskalige Operatoren angewendet, die hauptsächlich Tiefenanpassungen der Horizonte vornehmen. Diese Fallbeispiele dienen dem Test der Parametrisierung und Leistung der Optimierung mit unterschiedlichen Konfigurationen. Das ent-wickelte Programm arbeitet gut und ist vielversprechend für zukünftige Anwendungen. Beide vorgestellten Programme und die Besipiele zeigen die Zweckmäßigkeit der Potentialfeldinversion und sollten in multi-disziplinäre Arbeitsabläufe implementiert werden.

Table of Contents

Abstract I

Zusammenfassung III

Table of Contents V

1. Introduction 1

2. Potential field modeling 5
2.1. Potential fields . . . 5
2.1.1. Gravity field . . . 5
2.1.2. Geomagnetic field . . . 6
2.1.3. Gradients of the potential fields . . . 7
2.2. Interpretation and modeling . . . 8
2.2.1. Methodology and dimensions . . . 9
2.2.2. A closer look at 3D models . . . 11
2.2.3. Limitations of potential field interpretation . . . 14

3. Linear property inversion 17
3.1. The inversion method . . . 17
3.1.1. The inverse problem . . . 17
3.1.2. Implementation of method for voxel models . . . 19
3.2. New features of the inversion tool . . . 20
3.2.1. Combined inversion . . . 20
3.2.2. Correlations between related regions . . . 22
3.2.3. Exact forward calculation and polyhedral model bodies . . . 23
3.2.4. Background density/susceptibility . . . 24
3.2.5. Anomaly shift . . . 25
3.3. Evaluation of results by sensitivity analysis . . . 26

4. Applications with inversion tool 31
4.1. Synthetic salt diapir . . . 31
4.1.1. Inversion modes and correlations . . . 32
4.1.2. Data with noise . . . 36
4.2. North German Basin . . . 37
4.2.1. Bramsche Anomaly . . . 38
4.2.2. Pritzwalk Anomaly . . . 46
4.3. Capel and Faust Basins . . . 50
4.3.1. Voxel-based approach . . . 54
4.3.2. Polyhedra-based approach . . . 58

4.4. Discussion . . . 63

5. Model geometry optimization **65**
5.1. Optimization . . . 65
5.1.1. The main components . . . 65
5.1.2. Major stochastic optimization methods . . . 66
5.2. Parametrization . . . 69
5.2.1. Variant 1: Direct movement of vertex positions . . . 70
5.2.2. Variant 2: Spatial distortion . . . 71
5.2.3. Variant 3: Spatial operator . . . 71
5.3. Implementation of spatial operator . . . 72
5.3.1. Adaptive discretization . . . 75
5.4. Particle Swarm Optimization (PSO) . . . 80
5.4.1. PSO using the GWO parametrization . . . 84
5.5. Implementing constraints . . . 84
5.5.1. Property constraints . . . 85
5.5.2. Geometry constraints . . . 86
5.6. Optimization result assessment . . . 87
5.7. Implementation and application in three dimensions . . . 87

6. Applications with optimization tool **89**
6.1. Synthetic salt model . . . 89
6.1.1. Parameter set-up . . . 90
6.1.2. Optimization . . . 93
6.2. Capel and Faust Basins . . . 100
6.2.1. Optimization . . . 101
6.3. Discussion . . . 105

7. Conclusions and Outlook **109**

8. References **113**

A. Supplementary maps **121**

B. Supplementary tables **129**

List of Figures **135**

List of Tables **137**

List of Symbols and Abbreviations **139**

Acknowledgments **141**

1. Introduction

Gravity and magnetic methods represent the oldest disciplines in geophysics. They have been used for geological mapping and in exploration for minerals and hydrocarbons over decades. However, they were overtaken by and made way mainly to seismic methods which provide better resolution for the imaging of the subsurface (especially when surveyed in 3D like in the exploration business). But development continued and progress in gravity gradiometry was e.g. forced by developments in rocket science, as high accuracy is required for ballistic missile launching (Nabighian et al., 2005a). The advancements in moving platform systems together with increasing location accuracy due to GPS increased data resolution and helped to maneuver potential field methods to better appreciation again. Then, at the turn of the millennium, a whole new era of gravity field determination from space was introduced, with three dedicated Earth observation satellite missions that now provide global data coverage and high accuracy. The advances in gravity gradiometry and the start of the satellite missions CHAMP[1], GRACE[2] and GOCE[3] caused a reanimated interest in potential field methods. And this initiated in turn new developments and upgrade of existing software to deal with the data. Potential field data is assistant because it complements other geophysical methods in areas where they have, e.g. assessment or resolution weaknesses. This can be due to restricted access to the survey area (due to rough terrain or political borders) or sparse data sampling. The methods took up the role for preliminary assessment of potential survey areas, as airborne surveying of large areas is faster and more cost-efficient than seismic surveying. And potential field data assist in model development and subsurface imaging in domains where other methods suffer from signal loss (e.g. sub-salt and sub-basalt domains). Gravity and magnetic methods are no longer just convenient additions to seismic imaging but have gained a more accepted status as important complementary methods. This acceptance is especially given in hydrocarbon and mineral exploration (e.g. Kimbell et al., 2004; DiFrancesco et al., 2009).

Technical and computational developments led to multi-method or integrated interpretations that now become more and more common in geophysics. These approaches use data from several different geophysical methods for the construction of models and the understanding of the subsurface. Prominent methods to combine in exploration geophysics are e.g. seismics, gravity, magnetics, controlled-source electromagnetics and magnetotellurics. Such approaches can be realized because an increased diversity of data becomes available and also due to the increases in computational power. When taking into account different data sets, the resulting models should at best satisfy all involved data. For this reason it is beneficial to bring different data sets together in a way that they can consider each other during the modeling process - instead of being compared to one another only afterwards. In order to integrate a method in a multi-method modeling and interpretation process, automated model updates are required. Additionally, such an integrated approach requires that all involved disciplines can be modeled and updated in a similar time frame. While forward modeling is a common approach in the interpretation of potential field data, it can

[1] *http://op.gfz-potsdam.de/champ/*
[2] *http://www.csr.utexas.edu/grace/*
[3] *http://www.esa.int/Our_Activities/Observing_the_Earth/GOCE*

get very wearisome and time-consuming, especially in 3D. To have a competitive interpretation tool, potential field modeling must be accelerated and also automated, which is why inversion is required. It has the potential to speed up construction, update and improvement of models. It is also required for gradient data because forward modeling is a process where the interpreter takes advantage of basic relations (e.g. density deficit causes a gravity low) and it relies on the interpreters geological knowledge, experience and a bit of intuition. Gradient data modeling on the other hand is rather not intuitive. The most understandable of the spatial derivatives is the gradient of the vertical gravity component. In order to make use of the increasingly available gradient data, inversion is demanded. When using inversion methods, model parameters are inferred directly from the measurements. The process is automated and besides providing an initial model, the interpreter can influence the solution by defining constraints that are based on additional data and information.

This work focuses only on inversion of potential field data. The developments are oriented towards the compilation of a tool that provides estimates and updates of potential field models in a reasonable time frame and which can be combined with a forward modeling software, e.g. as a plug-in solution. The latter is desired because potential field modeling is confronted with the non-uniqueness of its model solutions. The combination of forward and automated modeling would permit the integration with other methods but comes also along with the advantage that the interpreter does not "lose control" and can still interact in the model buildup. The different components of the toolkit aim to provide applicability for models of varying geometrical representations, aiming at the most commonly used and most flexible ones. They shall allow for the estimation of physical properties but also for structural changes, i.e. model geometry deformations. Although aimed at an integration in existing software, the implementations of the here developed tools will be stand-alone programs.

Overview over the chapters

Chapter 2 is an introduction and addresses potential fields, data and modeling, giving a short overview over theory, concepts and techniques.
In **Chapter 3** a method for linear inversion of physical model properties in 3D is described. This implementation is a voxel-based approach that applies minimum mean-square error estimation. Within this work the program was further developed and improved. It now performs exact 3D calculations and its applicability is extended to non-voxel models. Furthermore, it now also allows for combined inversion of several potential field data sets. A method for result evaluation is proposed and some resolution tests are shown.
In **Chapter 4** the updated property inversion is applied to four models, testing different features of the tool. The first model is a synthetic salt structure. It is used to test the main features of the inversion available for voxel models. The following two examples are polyhedron models from the North German Basin. They serve as synthetic models for tests of the tool on this kind of model representation. The fourth example is from an area located offshore eastern Australia. The model is given as voxel model and also as polyhedron model. This allows for a comparison of the inversion tool on both model representations. This final example identifies some points where the property inversion reaches its limits. One particular issue is the inability to automatically modify model geometries. As a consequence an approach was required that changes model geometry in

order to optimize the model fit. The choice fell to a global optimization algorithm based on swarm intelligence in combination with a novel model parametrization which uses a spatial operator to perform model deformations. The development of this tool is described in **Chapter 5**. It is suitable for 3D gravity and magnetic models, i.e. vertex-based geometries in general, but the initial implementation presented here is in 2D and only for gravity interpretation.
The optimization tool is then applied to two examples in **Chapter 6**. A synthetic salt structure with small overhangs is used first, to show the behavior of the optimization, depending on varying parameters of the spatial operator and of the swarm. For the second example, the last data set from Chapter 4 is used. A 2D vertical section is extracted from the 3D model. Compared to the salt structure this second example has a larger extent and focus is more on geometry modifications that cause long wavelength effects on the anomaly.
In the final **Chapter 7** the results and outcome of this work will be concluded and an outlook on possible continuative work will be given.
Appendices A and **B** contain additional maps and tables for reasons of completeness, that are only referenced in the chapters. These maps and tables mainly belong to the applications in Chapters 4 and 6.

2. Potential field modeling

In geophysics, potential field modeling describes modeling of the subsurface by applying potential field methods. Those methods comprise approaches that involve Earth's own physical properties like the gravitational field and the magnetic field. This chapter gives an introduction to the physical background of potential fields, their properties and interpretation. Different model representations and modeling approaches will be discussed.

2.1. Potential fields

The gravitational attraction of an object or the magnetic field induced by electrical currents are described as vector force field that act at each point of space at a given time. A vector force field is characterized by its field lines that are tangent to the field at every point. If work is independent on the path a particle takes through a vector field then the field is *conservative*. A conservative force field $\boldsymbol{F}$ can be described by a scalar potential Φ in a way that $\boldsymbol{F} = \boldsymbol{\nabla}\Phi$. $\boldsymbol{F}$ is then called *potential field*.
At points that are not occupied by sources of field $\boldsymbol{F}$ the potential Φ satisfies *Laplace's equation* $\nabla^2\Phi = 0$. If, in addition, the potential has continuous, single-valued first derivatives and also second derivatives, the potential is harmonic. It allows for a mathematical description using spherical harmonics. A full description of the theory can e.g. be found in Blakely (1996) or Jacoby and Smilde (2009). The here used notation follows mainly the one used in Blakely (1996).

2.1.1. Gravity field

The gravitational attraction produced by a mass m is an irrotational, conservative force field. At the observation point P, located at a distance r from the mass, the attraction reads

$$\boldsymbol{g}(P) = -\gamma\frac{m}{r^2}\hat{\boldsymbol{r}}$$

where γ is the gravitational constant and $\hat{\boldsymbol{r}}$ a unit vector pointing from mass to observation point. The attraction can also be described by the scalar potential

$$\boldsymbol{g}(P) = \boldsymbol{\nabla}U(P) \tag{2.1}$$

$U = \gamma\frac{m}{r}$ is also referred to as the gravitational or *Newtonian potential* (Blakely, 1996). The potential obeys the principle of superposition and the continuous mass distribution m within a volume R can be given as a superposition of a great number of small masses dm:

$$U(P) = \gamma\int_R \frac{dm}{r} \tag{2.2}$$

When expressing the distribution of masses by a density distribution ($dm = \rho(x, y, z)\, dv$), equation 2.2 becomes

$$U(P) = \gamma \int_R \frac{\rho(Q)}{r}\, dv \tag{2.3}$$

and Q is the location of dv. Going back to equation 2.1 the gravitational attraction, i.e the gravity field, at point P is given by

$$\boldsymbol{g}(P) = -\gamma \int_R \rho(Q) \frac{\hat{\boldsymbol{r}}}{r^2}\, dv \tag{2.4}$$

The gravity field of the Earth is a combination of the attractive force caused by the mass of the Earth and the centrifugal force caused by the rotation of the Earth. When measuring the Earth's field, both components are registered. In order to investigate the density structure of the crust and upper mantle, measurements need to be *corrected* by the effects that interfere with the gravity signal from these domains. The procedure of gravity reductions accounts for the mass, shape and spin of the so-called normal Earth (reference ellipsoid), for tidal effects and instrumental drift, for station elevation, and the effect of terrain in the near surroundings of the station. What remains after the reductions is a gravity anomaly caused by density variations in the subsurface. Only this corrected measurements will be used for the modeling procedures described in this work and referred to only as measurements or gravity anomaly.

2.1.2. Geomagnetic field

The main part of the Earth's magnetic field is believed to originate from convection in the outer core (Campbell, 1997). The field is dipolar and its strength lies between approximately 30,000 - 60,000 nT, plus additional spherical harmonic components. Measurements are effected by the interaction between the global field and magnetic fields associated with solar wind (Campbell, 1997). Daily variations at mid-latitudes of about 60 nT are caused by the compression of the Earth's field on the sunward side of the globe. Electrically charged particles generated by the interaction maintain the equatorial electrojet which produces magnetic field fluctuations of tens of nT due to instabilities. The strongest effect, which can reach amplitudes over 200 nT for the duration of several hours during solar magnetic storm, is caused near the poles by the entrainment of charged particles along field lines. With time the field slowly changes. On a time scale of approximately 100,000 years it undergoes collapse, followed by reversal (Nabighian et al., 2005b).

The magnetic induction field $\boldsymbol{B}$ is irrotational and has a scalar potential V if electric currents in the region of investigation are absent. This approximation is often suitable outside of magnetic materials and in geophysical application, electrical currents are often negligible in regions where the magnetic field is measured. Therefore, the magnetic field is considered as a potential field:

$$\boldsymbol{B} = -\boldsymbol{\nabla} V \tag{2.5}$$

For the derivation of the gravity field mass points are used as the fundamental elements of continuous density distributions. In analogy to that the description of the magnetic field considers magnetic dipoles as the elemental building block of magnetic sources. In fact, many magnetic bodies in nature are dipolar to first approximation. It usually is a matter of scale. Therefore, also the entire field of the Earth appears nearly dipolar from the perspective of the other planets (Blakely, 1996).

The potential of an elemental dipole at a point P reads

$$V(P) = -C_m \boldsymbol{m} \cdot \nabla_P \frac{1}{r}$$

where $\boldsymbol{m}$ is the dipole moment, C_m is used to balance units and has a value that depends on the system in use (in SI: $C_m = \mu_0/4\pi$, with μ_0 being permeability of free space) and r is the distance between observation point and dipole. A small element of magnetic material with magnetization $\boldsymbol{M}$ can be considered to act like a single dipole $\boldsymbol{M}\, dv = \boldsymbol{m}$. Magnetization is a function of position, therefore $\boldsymbol{M} = \boldsymbol{M}(Q)$ and Q is the position of the source element dv. Applying again the principle of superposition the magnetic potential of a source distribution is given by

$$V(P) = C_m \int_R \boldsymbol{M}(Q) \cdot \nabla_Q \frac{1}{r}\, dv$$

The magnetic induction, i.e. magnetic field at P, is then gained by going back to equation 2.5:

$$\boldsymbol{B}(P) = -C_m \nabla_P \int_R \boldsymbol{M}(Q) \cdot \nabla_Q \frac{1}{r}\, dv \tag{2.6}$$

Similar to the gravity field also the magnetic field requires reductions of the measurements in order to interpret them in terms of subsurface structures. The International Geomagnetic Reference Field (IGRF) is a mathematical representation of the low-degree parts of the geomagnetic field which are believed to represent in large parts the field of the Earth's core (Blakely, 1996). As the geomagnetic field changes with time the IGRF is updated in 5-year intervals by the International Association of Geomagnetism and Aeronomy (IAGA). This field is used to calculate magnetic field anomalies from the measurements which then in turn allow for inference of magnetization in the source rock which is a combination of remanent and induced magnetization. The latter is caused by an external magnetic field, the Earth's magnetic field in this case. Magnetic susceptibility (χ), which is commonly used for geophysical modeling, is the proportionality constant between magnetization and inducing field ($\boldsymbol{M} = \chi\ vecH$) and a measure of how rocks respond to an external magnetic field.

2.1.3. Gradients of the potential fields

Gradients are the spatial derivatives of the potential fields, i.e. the second derivatives of the gravitational or magnetic potential. The gradients in Cartesian coordinates (x, y, z) are arranged in the gradient tensor. For the gravity gradients, it is also called the Eötvös Tensor:

$$\begin{pmatrix} \frac{\partial^2 U}{\partial x^2} & \frac{\partial^2 U}{\partial x \partial y} & \frac{\partial^2 U}{\partial x \partial z} \\ \frac{\partial^2 U}{\partial y \partial x} & \frac{\partial^2 U}{\partial y^2} & \frac{\partial^2 U}{\partial y \partial z} \\ \frac{\partial^2 U}{\partial z \partial x} & \frac{\partial^2 U}{\partial z \partial y} & \frac{\partial^2 U}{\partial z^2} \end{pmatrix} = \begin{pmatrix} U_{xx} & U_{xy} & U_{xz} \\ U_{yx} & U_{yy} & U_{yz} \\ U_{zx} & U_{zy} & U_{zz} \end{pmatrix}$$

The tensor is symmetric as the sequence of differentiation is interchangeable. Its trace equals zero in source free regions (Laplace's equation). The unit for gravity gradients is Eötvös, with $1\mathrm{E} = 10^{-9}\, 1/\mathrm{s}^2$.
First measurements were taken with a torsion balance in 1896 by Roland von Eötvös. Because of its high sensitivity, compared to common gravity measurements, the gravity gradient method

is utilized in exploration geophysics and geodesy. However, because measurement procedures are slow and also highly sensitive to external influences, the gravity meters prevailed. Triggered by the need for precise knowledge of the gravity gradients for missile launching in the 1970s, a new generation of gravity gradiometers emerged (Jacoby and Smilde, 2009). With the approach of airborne systems in 1999 and the first installation on satellite systems in 2000, and in combination with ever improving global positioning systems (GPS), gravity gradients returned to the focus of exploration geophysics. In the most recent satellite mission GOCE (ESA, 1999), three pairs of accelerometers are installed on bars ca. 0.5 m apart. One bar has radial orientation, one is in flight direction and one is across flight direction. So the orientation of the measured gradients is the Gradiometer Reference Frame (GRF), here denoted by $\hat{U}$. The constellation of the accelerometers enables the measurement of the full tensor with high spatial resolution, whereby the gradients $\hat{U}_{xx}, \hat{U}_{yy}, \hat{U}_{zz}$ and $\hat{U}_{xz}$ have a higher accuracy than $\hat{U}_{xy}, \hat{U}_{yz}$ (Bouman et al., 2011). To utilize the gradients however, a coordinate transformation is required because geophysical modeling is done in a Model Reference Frame (MRF), e.g., in UTM coordinates.
Mathematically gravity gradients do not contain any more information than gravity itself because they are all explained by the same potential U and caused by the same source(s). However, measurement instrumentation for gradients provides a better signal-to-noise ratio. Due to the arrangement of the accelerometers it is possible to eliminate data noise that is caused by the motion of the measuring platform. Furthermore, gravity gradients have higher sensitivity to near-surface sources than conventional vertical gravity and can provide information about variations in both the vertical and horizontal plane of the gravity field (Ebbing et al., 2013).

With the just recently launched satellite mission SWARM[1], also gradients of the magnetic field are coming into focus. The mission uses a system of three satellite, two of them orbiting the Earth side-by-side and the third one in higher altitude, with high-precision vector field magnetometers. Their constellation will allow to estimate gradients of the magnetic field. Similar to the gravity gradient tensor, the full magnetic gradient tensor is given as the second derivatives of the magnetic potential:

$$\begin{pmatrix} \frac{\partial^2 V}{\partial x^2} & \frac{\partial^2 V}{\partial x \partial y} & \frac{\partial^2 V}{\partial x \partial z} \\ \frac{\partial^2 V}{\partial y \partial x} & \frac{\partial^2 V}{\partial y^2} & \frac{\partial^2 V}{\partial y \partial z} \\ \frac{\partial^2 V}{\partial z \partial x} & \frac{\partial^2 V}{\partial z \partial y} & \frac{\partial^2 V}{\partial z^2} \end{pmatrix} = \begin{pmatrix} V_{xx} & V_{xy} & V_{xz} \\ V_{yx} & V_{yy} & V_{yz} \\ V_{zx} & V_{zy} & V_{zz} \end{pmatrix}$$

2.2. Interpretation and modeling

Potential field models reflect subsurface structures and their properties, i.e. they are characterized by geometries and assigned property values like densities and susceptibilities. Representations of potential field models depend on their mathematical description because the effect of the model on the gravity/magnetic fields needs to be calculated. A variety of options on how to define a model geometry are available. Dimensionality of modeling came along and increased with the development of algorithms to calculate the potential field effect of varying geometric representations and the computational power that is necessary to actually perform these calculations.

[1] *http://www.esa.int/Our_Activities/Observing_the_Earth/Swarm*

2.2.1. Methodology and dimensions

Modeling the subsurface can be done in several different ways, depending on the dimensions that are modeled and the methods that are used. The modeling dimensions range from 1D (vertical profile, e.g. seismic velocity profiles, electric resistivity profiles) to 2D (vertical planes, e.g. seismic sections, density model) over 2.5D and 3D (pseudo and real 3-dimensional, e.g. density model, seismic velocity tomography) to even 4D (3-dimensional and time dependent, e.g. monitoring of density changes in a hydrocarbon reservoir under exploration).
The approaches on how to establish a subsurface model offer different possibilities, each with its own advantages and drawbacks. The classical and well developed method in potential field modeling is forward modeling (Blakely, 1996). Inversion methods became more relevant during the last decades as computation power increased and now allows for calculations of massive and complex models. And with this also optimization methods as solvers for the non-linear inverse problems experienced increased attention (Nabighian et al., 2005a).

Forward modeling

Blakely (1996) describes the basic difference between forward and inverse modeling with the help of the potential field integral. So the vertical attraction of gravity and the total magnetic field anomaly can both be written in the same general form. When a volume R is occupied by a causative source, the potential field at point P is given as

$$f(P) = \int_R S(Q)\Psi(P,Q)\,dv \tag{2.7}$$

$S(Q)$ describes a physical property (density/magnetization) at the point of integration Q. $\Psi(P,Q)$ is a function depending on the geometric placement of observation point P and source point Q. Relating to this equation the *forward method* represents a repeated adjustment of $S(Q)$ and R followed by the calculation of $f(P) = f_{calc}(P)$ in order to compare it to measured values of the potential field $f_{meas}(P)$. Adjustment is carried out until the fit of measured and calculated field is satisfying.
Together with geological and geophysical intuition model parameters are inferred from existing subsurface information in the survey area. The first guess is referred to as the initial model. The anomaly is calculated and compared to the measured anomaly. See Figure 2.1 (left) for the iterative process of parameter adjustment, anomaly calculation and comparison, in which the misfit between the two anomalies is reduced until a maximal defined discrepancy is reached. As the forward method is a process of trial and error, it usually is relatively time consuming and a certain degree of experience if certainly beneficial.

Inversion modeling

Considering Equation 2.7 again, the *inverse method* takes measurements for $f(P) = f_{meas}(P)$ and solves for some aspect of $S(Q)$ or R. In case of solving for $S(Q)$ the inverse problem is linear, solving for R constitutes a non-linear inverse problem.
The development of inversion methods followed two directions: One approach solves for the source geometry and the other for the distribution of physical properties. In gravity modeling the inversion methods are used, e.g., to estimate the depth to or location of certain horizons like basin

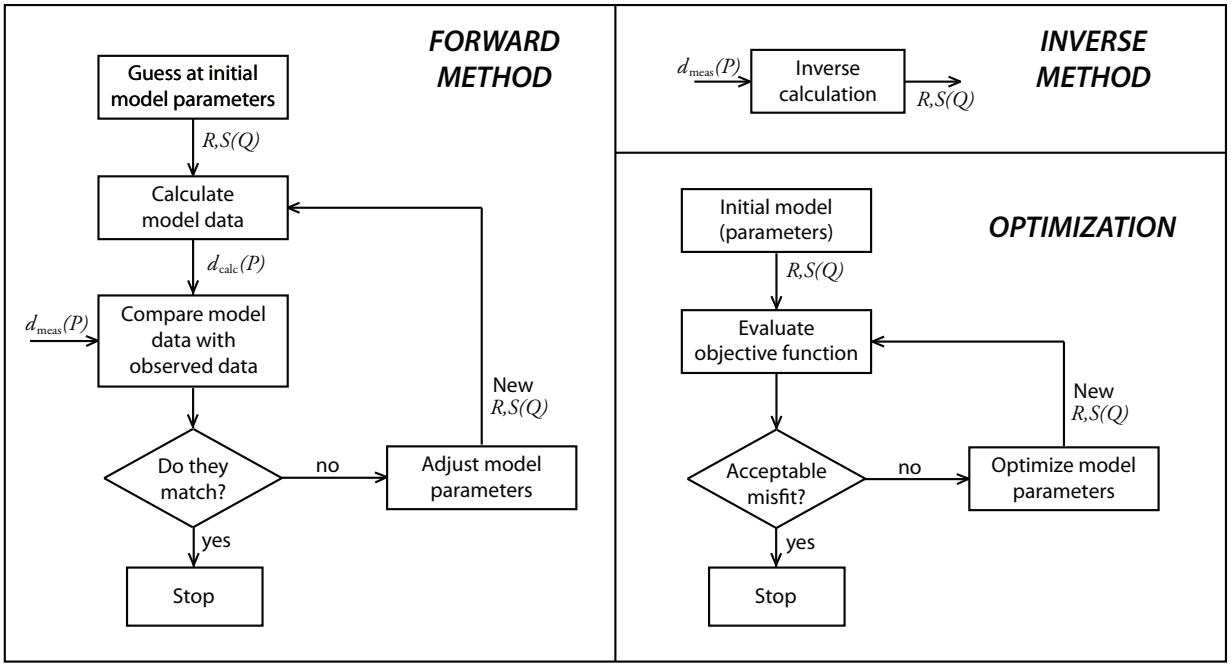

Figure 2.1.: *Flowcharts illustrating forward and inverse methods for modeling and the optimization process. $f_{meas}(P)$ is measured data, $f_{calc}(P)$ is modeled data. Model parameters are given by R (e.g. geometries) and $S(Q)$ (e.g. density, seismic velocity, resistivity, magnetization, etc.) (modified after Blakely (1996)).*

depth, top or base of salt, and recently also base of basalt flows. Other targets are density-depth functions or density contrasts as function of position. Also the geometry of isolated, causative bodies defined by their vertices are estimated.
Model parameters are inferred and calculated directly from the observations in an automated approach, see flowchart in Figure 2.1 (top right). Because of the infinite number of measurements an inverse problem does not necessarily have an unique solution. Depending on the physical relationships between model parameters and measurements the inverse problems can be linear or non-linear. Simplifying assumption are often inevitable. For example, density inversion in potential field modeling is linear if model bodies have constant density distributions. If the density distribution is inhomogeneous or the inversion aims at the geometry of subsurface structures, the inverse problem becomes non-linear.

Optimization methods

These methods are global or local search algorithms that explore the model parameter space in order to find an optimal set of parameters. This does not necessarily imply inverse routines but optimization methods are usually used as means of solvers for the non-linear inverse problem. The decision, whether a parameter set is optimal or not, is made through the evaluation of an objective function (also: cost function). See the flowchart in Figure 2.1 (bottom right) for illustration. Examples for objective functions are the misfit between calculated and measured anomaly in potential field modeling or the misfit between slowness-frequency spectra of Scholte-wave dispersion in seismics (Wilken and Rabbel, 2012). A variety of search algorithms exist, e.g.

gradient methods, secant methods, sequential quadratic programming methods and stochastic methods and the interested reader is referred to e.g. Sen and Stoffa (2013). Global and local stochastic optimization methods will be addressed later in Chapter 5.

Dimensions and development

Potential field modeling is usually done in two or three dimensions. However, first steps in the interpretation of gravity and magnetic anomalies were done using characteristic curves that were calculated for simple models (Nettleton, 1942) or, in case of magnetics, also by comparison with anomalies calculated over tabular bodies (Vacquier et al., 1951). This was before the use of computers. The first use of computers for gravity modeling followed after Talwani et al. (1959) presented equations for computing gravity anomalies produced by 2D bodies of polygonal cross section. For magnetic modeling the equations followed a bit later and were presented by Talwani and Heirtzler (1964). The location of the model section is usually chosen to lie perpendicular to an elongated potential field anomaly which is generally the striking direction of the expected geological structure. The structure is then assumed to extend infinitely in both directions of the vertical section which is a valid assumption for anomalies with a length that is 4 to 5 times their width. And even today, when 3D models become more regular, 2D modeling can still be regarded as a sufficient means if the above mentioned assumption can be justified. Seismic profiles are often oriented in the same direction as the potential field model section and when available they are used to guide the modeling. It is also possible to describe the subsurface by prisms or rectangles. When approximating the prisms by mass points computation time is improved significantly.
Initial equations for 3D forward modeling of density distributions were introduced by Talwani and Ewing (1960). For magnetic modeling the first formula for 3D bodies applied right rectangular prisms (Bott, 1963; Bhattacharyya, 1964; Nagy, 1966). 3D modeling allows far more realistic replications of the subsurface. It is therefore more complex in terms of visualization and model editing. It is also computationally much more demanding. Several software exist that are based on different model geometries, like e.g. prisms or voxels, girds, surfaces or polyhedra. A closer look on the geometric representations will be given in the following section. For a full historical review of the developments see e.g. Nabighian et al. (2005a,b)

2.2.2. A closer look at 3D models

Model representations play a major role in this work as the developed tools can be applied to different representations. This section explains a few basic 3D model representations in more detail, focusing on the geometric aspects.

Voxel models are 3D discrete regular grids of volume elements (Kaufmann et al., 1993). Voxels are rectangular cuboids that can be understood as the 3D equivalents of 2D pixels, with an assigned value or property (i.e. density/susceptibility). For their geometric description it is sufficient to define one corner of the 3D grid, the number of voxels in each direction and their size. They fill the entire modeling area without empty spaces in between. The assignment of properties to the voxels leads indirectly to the definition of structures in the 3D grid. Depending on the voxel size this model representation allows for very detailed modeling including the replication of overhangs or well-defined, distinctive source domains. On the other hand, detailed modeling goes along with small voxel sizes which in turn increases the number of voxels in a model. The number of voxels

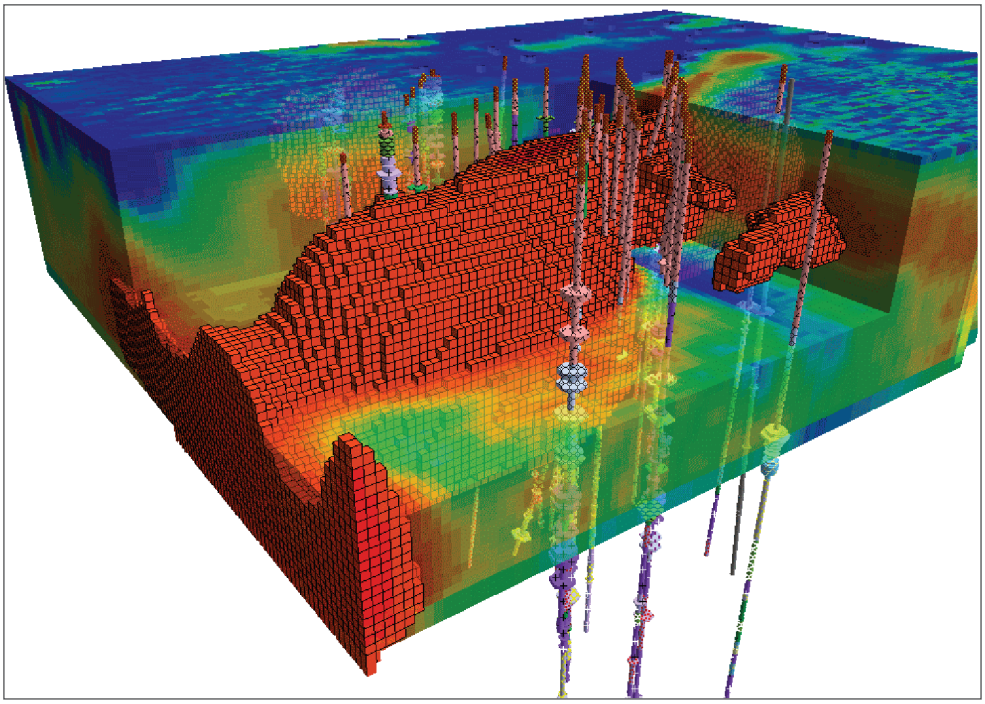

Figure 2.2.: *Example of a voxel model where colors indicate the various geological domains (www.encom.com.au (modified)).*

is essential for calculation time and memory requirements, especially when matrix operations are involved.
To save computation time the potential field effect of voxels is often calculated by applying a mass point approximation. A software that uses voxel models is e.g. GeoModeller[2] which is also applying the inversion algorithms from UBC-GIF[3] that are based on Li and Oldenburg (1996, 1998). GMSYS-3D[4] and IGMAS+[5] are utilizing voxels as well, even though the main geometry is usually defined by grids or polyhedrons (see below).

Right rectangular prism models constitute a generalized representation of voxel models. The model elements are also rectangular cuboids, the difference is that these models can have cuboids of varying sizes. Each is defined by its x,y,z-coordinates and dimensions (dx, dy, dz). The option to use varying prism sizes throughout the same model provides the opportunity to use different resolutions. Because of the inverse-square law of gravitation this comes in handy as it allows to decrease resolution with depth and therein save memory requirements and computation time. Further features are the same as for voxel model. But caution is advised when applying the mass point approximation to large prisms. Despite the differences the notation voxel and right rectangular prism is used interchangeably in this thesis.

[2] *http://www.geomodeller.com*
[3] *http://www.eos.ubc.ca/ubcgif*
[4] *http://www.geosoft.com*
[5] *http://www.ifg.uni-kiel.de/1275.html, http://www.potentialgs.com*

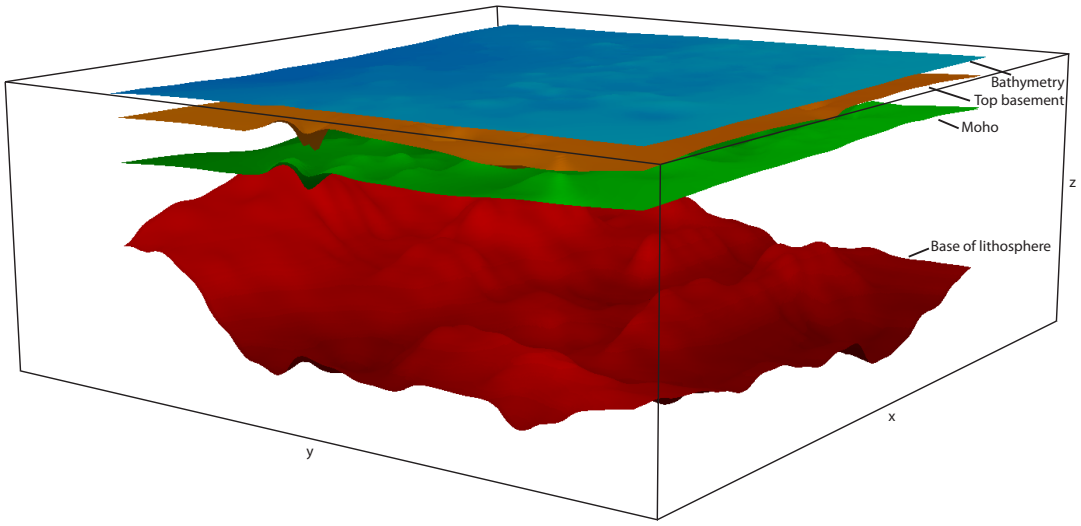

Figure 2.3.: *Example of a grid-based model in GMSYS-3D.*

Grid-based models can be created when depth information to characteristic horizons, where a property contrast can be defined, is available on regular 2D grids. The physical properties are then assigned to the space between the grids (or horizons). Figure 2.3 shows a GMSYS-3D model as an example of such a model representation. Properties are usually defined for the space underneath the grid downwards until the next grid is reached. The properties can be constant between two grids or given as lateral or vertical distributions (e.g. a vertical density gradient in a sedimentary layer that accounts for compaction). Grid-based models provide fast model response calculations that are done in the Fourier domain. Their manipulation however is not as straight forward as for voxel models. And they are limited in their capability to simulate certain subsurface structures and geometries. Because a grid point can only have one depth-value, the modeling of overhangs or twisted structures becomes very complicated. Software that use grid-based model representation are e.g. GMSYS-3D and Petrel[6].

Polyhedral model bodies allow almost unlimited options of simulating 3D structures. The surface of a polyhedron can be defined as a triangulated hull, with triangles being the most flexible geometry elements for interactive graphics (Schmidt et al., 2011). It therein allows the construction of arbitrarily complex shapes. The difficulty with this representation is how to edit, manipulate and visualize polyhedral model bodies in a geophysical modeling environment. A software that offers interactive editing and modeling of polyhedral bodies is IGMAS+. In this software model bodies are defined as polygons on parallel vertical 2D section. A triangulation between the sections then constructs the actual 3D polyhedral bodies. Figure 2.4 shows an example of the concept and possibility. The lateral spacing of the sections is linked to the model resolution and geometry changes are achieved by moving the polygon vertices within the sections. Ongoing developments head away from the 2D-section-concept and will soon offer more freedom for vertex positioning in all three dimensions (Götze, pers. comm.).
Polyhedral model bodies not only allow the definition of geometrically complicated structures (e.g. overhangs, discrete bodies, folds), the representation also benefits from fast calculation of

[6] *http://www.software.slb.com/products/platform/Pages/petrel.aspx*

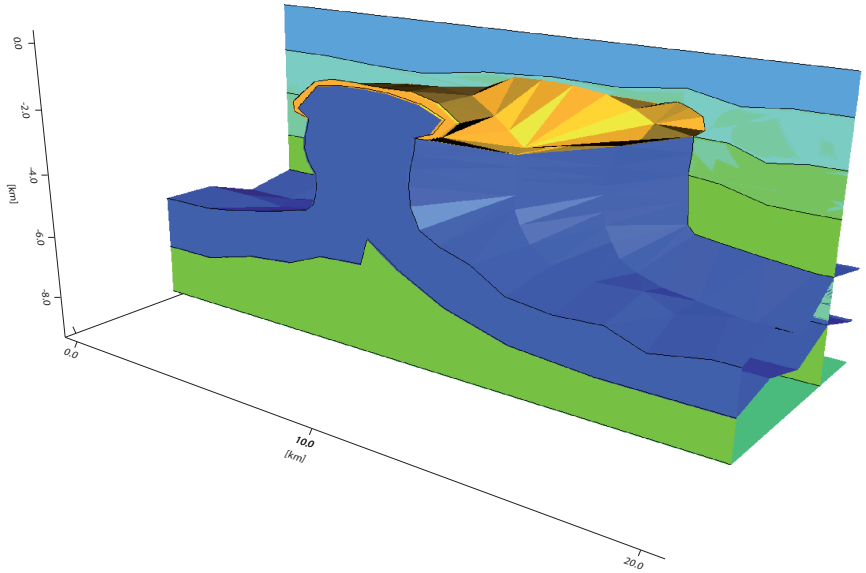

Figure 2.4.: *Example of a polyhedron model from the software IGMAS+. This software uses a triangulation for the polyhedron representation.*

the potential fields. The calculation of the volume integral over a homogeneous polyhedron is reduced to the calculation of a sum of line integrals (Götze, 1984; Götze and Lahmeyer, 1988) which speeds up calculation time significantly.

Triangulated surface models are based on the definition of characteristic horizons or interfaces. Similar to for grid-based models, physical properties are assigned to the space between surfaces that lie upon each other. But that is all both representations have in common. Where a grid can only define the depth to a horizon, a triangulated surface defines the complete geometry of the horizon. This enables construction of similar complexity as those possible with polyhedral model bodies. In fact, the visualization of both representations is nearly the same, except that polyhedral model bodies are closed structures and their vertices usually belong to at least two polyhedrons. Triangulated surfaces are e.g. used by GOCAD[7] and IGMAS+ provides export of these geometries.

These were some basic principles for 3D models that are mainly used today. Depending on the interpretation and modeling software, plenty of different constraints can be used in addition to guide the modeling. Some of the mentioned software offer the conversion into or even parallel use of different model representations. This work is focusing only on voxels, right rectangular prisms and polyhedral model bodies, although applicability of the developed tools is not restricted to these.

2.2.3. Limitations of potential field interpretation

The interpretation of potential fields is confronted with the problem of inherent ambiguity. The non-uniqueness was constituted in the 18th century by Green's theorems. They state that an

[7] *http://www.pdgm.com/products/GOCAD*

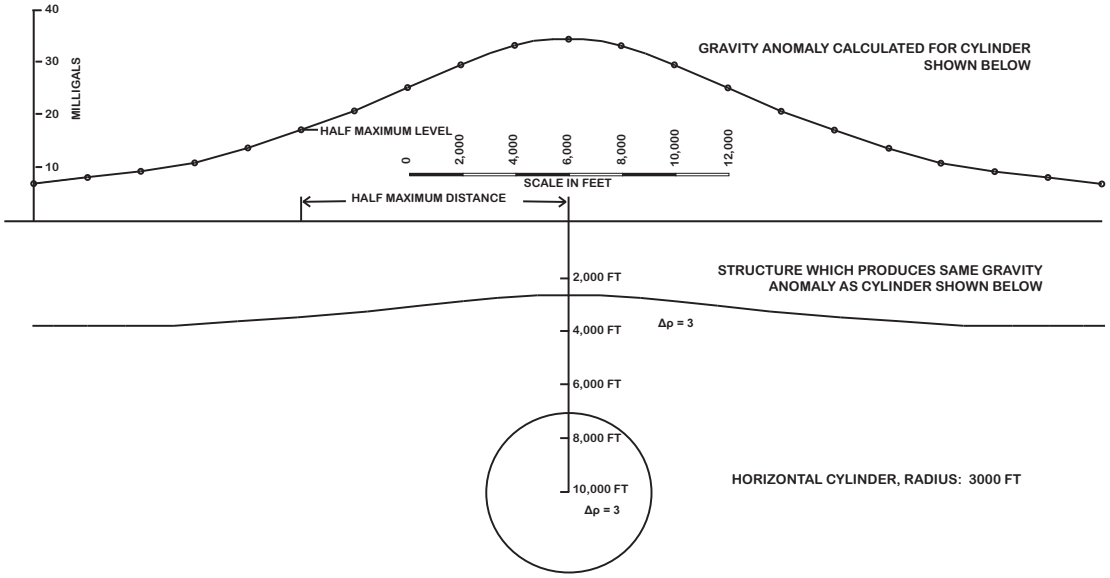

Figure 2.5.: *Gravity effect of a horizontal cylinder and a broad anticline at much shallower depth which will produce an identical effect (Skeels, 1947), with 1 milligal = $10^{-5}\,m/s^2$ and 1000 FT = 304.8 m.*

infinite number of equivalent source distributions within a boundary can produce the same field response at the bounding surface (Blakely, 1996). Consequently, this applies for gravity and magnetic anomalies. Figure 2.5 gives a 2D example of two sources that cause the same potential field although their shape and depth location varies. In general, modeling can never define or prove a "true" model but can definitely prove an assumed model wrong (Jacoby and Smilde, 2009).
Ambiguity can be reduced by including constraints in the modeling that keep the solution in a reasonable geophysical and geological model space. Constraints can originate from various sources like other geophysical methods or geological modeling. For example, seismic methods can provide structural information and indicate ranges for density values that match the estimated seismic velocities. Bore hole data provides density and depth information. And incorporation of geological modeling results helps to constrain the geometries of geological structures. In the forward modeling process the interpreter would consider available constraints during the modeling as best as possible, taking care of the geological reasonability. However, when applying inversion not all information can be considered in the same way. A lot of constraints are usually integrated during the construction of the initial model that enters the inversion. Further options are then to regard the confidence of a priori information, to correlate parameters or to add definite restrictions to model parameters. Nonetheless, the resulting model from an inversion may not be reasonable, e.g. in terms of physical properties, geometry of subsurface structures or geological interpretation. Therefore it is inevitable to have a qualitative selection process of reasonable model solutions following the inverse modeling. Furthermore , it is very useful to have a tool that provides the combination of forward and inverse modeling and the developments carried out in this thesis were aiming at this possibility. Because the combination of both allows the interpreter to interactively add information or eliminate unreasonable trends that begin to evolve during the modeling process.

3. Linear property inversion

This chapter addresses the inversion of physical properties in potential field modeling, i.e. estimation of densities and susceptibilities for subsurface models. The inverse problem is solved by using a minimum mean-square error (MMSE) method. A short introduction to method and previous implementations for voxel models will be described. The following sections then deal with extensions and new developments that were carried out in this work. These include amongst others exact calculations of potential fields, joint inversion using several potential field anomalies and applicability to polyhedron model. The method description is followed by some tests with simple synthetic block model. Application of the method to structural models is given in Chapter 4.

3.1. The inversion method

3.1.1. The inverse problem

In potential field modeling, the inversion for physical properties is usually defined as a linear inverse problem which can be done without the deficit of excessive simplifications. It is common practice to define constant properties within model bodies or model layers. And when the inversion does not aim at the change or estimation of geometry parameters the problem can then be described by the linear equation:

$$\boldsymbol{y} = \boldsymbol{A}\boldsymbol{x} + \boldsymbol{v} \tag{3.1}$$

where $\boldsymbol{y} \in \mathbb{R}^m$ is the measurement vector with entries for m station locations, $\boldsymbol{x} \in \mathbb{R}^n$ is the vector of model parameters to be estimated for n model bodies, and matrix $\boldsymbol{A} \in \mathbb{R}^{m \times n}$ relates the model parameters to the measurements. $\boldsymbol{v} \in \mathbb{R}^m$ is a vector of measurement noise.
With this approach the potential field expressions from the previous chapter (Equations 2.4 and 2.6) can be simplified to linear expressions. The formula for the gravity field becomes

$$\boldsymbol{g}(P) = -\gamma \int_R \frac{\hat{\boldsymbol{r}}}{r^2}\, dv \cdot \rho$$

and ρ is now constant for the model volume R. With $\boldsymbol{M}$ being constant throughout the source region, the magnetic induction is calculated by

$$\boldsymbol{B}(P) = -C_m \nabla_P \int_R \nabla_Q \frac{1}{r}\, dv \cdot \boldsymbol{M}$$

This leads to the anomaly matrices

$$\boldsymbol{A}_g = -\gamma \int_R \frac{\hat{\boldsymbol{r}}}{r^2}\, dv \qquad\qquad \boldsymbol{A}_m = -C_m \nabla_P \int_R \nabla_Q \frac{1}{r}\, dv$$

for gravity ($\boldsymbol{A}_g$) and magnetic ($\boldsymbol{A}_m$) inversion, respectively.
The implementation of a linear approach can be utilized for all models that use a volume-based

geometry representation (voxels, prisms, polyhedrons, etc.) and where the principle of superposition is applied to summarize the effect of the individual volumes.

To solve the linear problem (Equation 3.1), the minimum mean-square error (MMSE) method is applied. The method was successfully used for the improvement of 2D susceptibility models built of rectangular cells (Sæther, 1997) and for a 3D voxel application to gravity and magnetic data in Haase (2008). The theory is based on Mendel (1995) and Boyd (1996) and was explained in the two above mentioned studies. Therefore, only an outline from the descriptions in Sæther (1997) will be given in the following.

In equation 3.1 vector $\boldsymbol{x}$ contains variables that are not known. With the given measurements $\boldsymbol{y}$ an estimate $\hat{\boldsymbol{x}}$ for the unknowns $\boldsymbol{x}$ is sought, in other words, a function f such that

$$\hat{\boldsymbol{x}} = f(\boldsymbol{y})$$

The idea of the MMSE method is to minimize the mean-square prediction error $\boldsymbol{E}\|f(\boldsymbol{y}) = \boldsymbol{x}\|^2$ by defining a suitable function f. The measurements $\boldsymbol{y}$ are known and in the general case, the optimal function for f is the conditional expectation of $\boldsymbol{x}$ given $\boldsymbol{y}$ (Mendel, 1995):

$$f(\boldsymbol{y}) = \boldsymbol{E}(\boldsymbol{x}|\boldsymbol{y})$$

MMSE uses a statistical framework which makes it a special case of, e.g. Maximum-Likelihood Estimation, Maximum a Posteriori Estimation and Regularization methods. Referring to equation 3.1 a statistical framework means that all parameters are random variables which are Gaussian distributed, i.e. $\boldsymbol{x} \sim N(\bar{\boldsymbol{x}}, \boldsymbol{C_x})$, $\boldsymbol{y} \sim N(\bar{\boldsymbol{y}}, \boldsymbol{C_y})$ and $\boldsymbol{v} \sim N(\bar{\boldsymbol{v}}, \boldsymbol{C_v})$. Here, $\bar{\boldsymbol{x}} \in \mathbb{R}^n$, $\bar{\boldsymbol{y}} \in \mathbb{R}^m$ and $\bar{\boldsymbol{v}} \in \mathbb{R}^m$ are vectors of mean or expected value and $\boldsymbol{C_x}$, $\boldsymbol{C_y}$ and $\boldsymbol{C_v}$ are their related covariance matrices. The matrix $\boldsymbol{A}$ is deterministic.

In connection with Gaussian random variables the multivariate (n-variate) **Gaussian density function** p for a random variable $\boldsymbol{x} \in \mathbb{R}^n$ is reflected (e.g. Tarantola, 2005):

$$p(\boldsymbol{x}) = \frac{1}{\sqrt{(2\pi)^n (\det \boldsymbol{C_x})}} \exp\left(-\frac{1}{2}(\boldsymbol{x} - \bar{\boldsymbol{x}})^T \boldsymbol{C_x}^{-1} (\boldsymbol{x} - \bar{\boldsymbol{x}})\right)$$

This implies that $\det(\boldsymbol{C_x}) > 0$. A similar density function applies for the random variable $\boldsymbol{y} \in \mathbb{R}^m$. Considering now the **conditional density function** for variable $\boldsymbol{x}$ with a given variable $\boldsymbol{y}$ reads (Kolmogorov, 1933)

$$p(\boldsymbol{x}|\boldsymbol{y}) = \frac{p(\boldsymbol{x}, \boldsymbol{y})}{p(\boldsymbol{y})}$$

And if $\boldsymbol{x}$ and $\boldsymbol{y}$ are jointly Gaussian this equation leads to (Mendel, 1995)

$$p(\boldsymbol{x}|\boldsymbol{y}) = \frac{1}{\sqrt{(2\pi)^n (\det \boldsymbol{C_{x|y}})}} \exp\left(-\frac{1}{2}(\boldsymbol{x} - \hat{\boldsymbol{x}})^T \boldsymbol{C_{x|y}}^{-1} (\boldsymbol{x} - \hat{\boldsymbol{x}})\right)$$

with

$$\boldsymbol{C_{x|y}} = \boldsymbol{C_x} - \boldsymbol{C_{xy}} \boldsymbol{C_y}^{-1} \boldsymbol{C_{xy}}^T$$

$$\hat{\boldsymbol{x}} = \bar{\boldsymbol{x}} + C_{\boldsymbol{xy}} C_{\boldsymbol{y}}^{-1} (\boldsymbol{y} - \bar{\boldsymbol{y}})$$

where $\hat{\boldsymbol{x}}$ is the mean of $\boldsymbol{x}|\boldsymbol{y}$, which represents the sought estimate, and $C_{\boldsymbol{x}|\boldsymbol{y}}$ is its covariance.

For Gaussian variables the optimal function f has the following form:

$$f(\boldsymbol{y}) = \boldsymbol{E}(\boldsymbol{x}|\boldsymbol{y}) = \hat{\boldsymbol{x}} = \bar{\boldsymbol{x}} + \boldsymbol{B}(\boldsymbol{y} - \bar{\boldsymbol{y}})$$

$\hat{\boldsymbol{x}}$ is called the MMSE estimate, $\bar{\boldsymbol{x}}$ is the expectation (or first guess) of the unknown variables and $(\boldsymbol{y} - \bar{\boldsymbol{y}})$ is the difference between the actual and the hypothetical measurement if we assume that $\bar{\boldsymbol{x}}$ is correct, with $\bar{\boldsymbol{y}} = \boldsymbol{A}\bar{\boldsymbol{x}}$. With $\boldsymbol{x}$ and $\boldsymbol{v}$ being mutually uncorrelated $\boldsymbol{B}$ is given by

$$\boldsymbol{B} = \boldsymbol{C_{xy}} \boldsymbol{C_y}^{-1} = \boldsymbol{C_x} \boldsymbol{A}^T (\boldsymbol{A} \boldsymbol{C_x} \boldsymbol{A}^T + \boldsymbol{C_v})^{-1}$$

The derivation is given in detail in Sæther (1997). The final estimator expression of the method reads

$$\hat{\boldsymbol{x}} = \bar{\boldsymbol{x}} + \boldsymbol{C_x} \boldsymbol{A}^T (\boldsymbol{A} \boldsymbol{C_x} \boldsymbol{A}^T + \boldsymbol{C_v})^{-1} (\boldsymbol{y} - \boldsymbol{A}\bar{\boldsymbol{x}})$$

To apply this formula it is required that $\boldsymbol{x}$ and $\boldsymbol{v}$ are independent and that $\bar{\boldsymbol{x}}$, $\boldsymbol{C_x}$, $\bar{\boldsymbol{v}}$ and $\boldsymbol{C_v}$ are known. In practice, these assumptions are reasonable: $\bar{\boldsymbol{x}}$ is interpreted as an initial guess of what $\boldsymbol{x}$ really is, i.e. the start model. The covariance matrix $\boldsymbol{C_x}$ indicates how reliable this guess is, i.e. how big is the allowed variability of the start values. The mean measurement noise $\bar{\boldsymbol{v}}$ is interpreted as a constant offset or a systematic error in the measurements, which can be corrected. This yields $\bar{\boldsymbol{v}} = \boldsymbol{0}$ for the estimation. Its covariance matrix $\boldsymbol{C_v}$ is taken as a measurement noise level. As there is always some measurement noise, even after pre-processing, $\boldsymbol{C_v} > \boldsymbol{0}$ holds (Sæther, 1997).

The user defines the statistical parameters when setting up the inversion run. To create the covariance matrices $\boldsymbol{C_v}$ and $\boldsymbol{C_x}$, error and variability are given as standard deviations (σ) of the measurements and initial parameters, respectively. The measurement error is the same for the entire data set, the variability can be defined individually. The initial parameters and variabilities are used as mean values and standard deviations by the inversion. This means the variability is no hard limit and initial parameters can still experience changes that are larger than might be anticipated. The standard deviation of a normal distribution is always > 0. Therefore, measurement errors and property variabilities of 0 are not allowed. However, in order to fix a property during inversion, a variability of 0 seems necessary. This can be circumvented by setting the variability to a very low value instead. A value according to 3σ, which means that about 99.73% of the estimated property values will lie within the allowed variability, is usually sufficient to work as a hard limit. If a variability of 0 is found in the data, this special case is intercepted and the parameter will be completely excluded from the calculations.

3.1.2. Implementation of method for voxel models

Sæther (1997) used the method for a 2D application to models built of rectangular cells. This model representation allows for the incorporation of structural or geometric a priori information. Figure 3.1 schematically illustrates the concept: Cells of the same material or with the same property value can be clustered into *regions*. The inversion then estimates only one property value for the entire region and not values for each individual cell. In case no a priori information is available each cell is defined as its own region and the inversion is structurally unconstrained. This model representation even allows for a correlation of estimates. Regions that are supposed to be

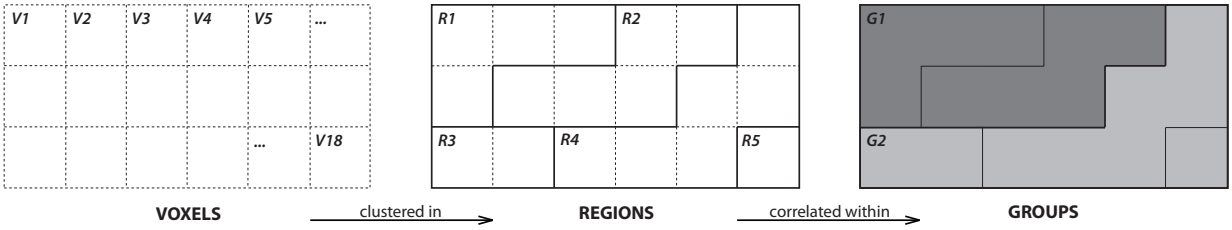

Figure 3.1.: *Illustration of a model used for voxel-based inversion (cross section through a 3D model). Within regions, the density/susceptibility is the same for all voxels. Within groups, several related regions are correlated by distance. For calculations of the potential field responses of a model only the bounding polyhedra of regions are used.*

geologically related can be correlated within so-called *groups of related regions*. A more detailed description will be given in section 3.2.2.

The concept of incorporating structural information and a priori information by defining groups and regions of cells is directly transferable to a 3D application using voxels instead of cells. An upgrading of the formulas to three dimensions and with the additional application to gravity data was given by Boyd and Noll (1999, 2000). Their code was translated and implemented in Java by myself previously, with a further upgrading that also allows the application of the inversion to vertical gravity gradient data, resulting in the tool named CHAIN[1] (Haase, 2008). All of these previous implementations use a mass point approximation for the voxels in the process of calculating the potential fields caused by the model. The tool was named

3.2. New features of the inversion tool

The previous Java implementation of the method, as given by Haase (2008), is expanded in this work to provide more features. These upgrades include the use of all (independent) elements of the full gravity tensor, option for different inversion modes (single and joint) and the correlation of structures. Exact calculations of model responses and the application of the method to non-voxel models is also implemented. The following sections describe these new features in detail.

3.2.1. Combined inversion

In the case that several potential fields have been measured, they all should be incorporated in the modeling and interpretation process. For example, the inversions of gravity and gravity gradient data both provide subsurface density distributions. Those distributions should match because they represent the same property. Instead of running single inversions on both fields the data sets should be combined and the inversion would then estimates only one density distribution which satisfies both data sets.

Gravity and gravity gradients

Gravity gradients and their additional benefit to modeling were discussed earlier (section 2.1.3) and the combination of both fields for the inversion suggests itself. The single inverse problems

[1] CHAIN = Claudia HAase's INversion

are given by

$$\boldsymbol{y}_{gz} = \boldsymbol{A}_{gz}\boldsymbol{\rho} + \boldsymbol{v}_{gz} \qquad \text{and} \qquad \boldsymbol{y}_{gzz} = \boldsymbol{A}_{gzz}\boldsymbol{\rho} + \boldsymbol{v}_{gzz} \tag{3.2}$$

the subscript gz stands for the vertical gravity component, gzz is used for the vertical gravity gradient component. However, here and in the following, gzz can be replaced by any other component of the full gravity tensor. Parameter vector $\boldsymbol{x}$ from Equation 3.1 is replaced by $\boldsymbol{\rho}$ for density. The combined inversion is realized by joining the equations 3.2. The density vector $\boldsymbol{\rho}$ is identical for all data sets because only one density distribution will be estimated. The measurement and noise vectors are enlarged by adding the supplementary data. In the same way also the matrix can be enlarged:

$$\begin{pmatrix} \boldsymbol{y}_{gz} \\ \boldsymbol{y}_{gzz} \end{pmatrix} = \begin{pmatrix} \boldsymbol{A}_{gz} \\ \boldsymbol{A}_{gzz} \end{pmatrix} \cdot \boldsymbol{\rho} + \begin{pmatrix} \boldsymbol{v}_{gz} \\ \boldsymbol{v}_{gzz} \end{pmatrix} \tag{3.3}$$

It is not required that measurements of different data sets are taken at the same locations. This freedom allows the combination of gridded gradient data (e.g. from airborne or satellite surveys) with single station terrestrial gravity data, after leveling the data to the same height. To enable the above given combination of data sets it is necessary to scale the components of Equation 3.3. This is done by using the measurement error as scaling factor. Equations 3.2 are divided by the respective measurement error and become therewith dimensionless expressions and therewith also to anomalies are scaled to a similar numerical range.

Gravity and magnetics

The direct combination of gravity and magnetic data sets, equal to the above given combination of gravity and gravity gradient data, is problematic. Because of the linear approach used here, the method can only provide the estimate for a vector containing *either* densities *or* susceptibilities, but not both. Also, both properties do not have a physical relationship which could be used for expressing one through the other. Therefore, the parameter vector is required to contain both properties. Equation 3.3 could be transformed to the expression:

$$\begin{pmatrix} \boldsymbol{y}_{gz} \\ \boldsymbol{y}_{gzz} \\ \boldsymbol{y}_{m} \end{pmatrix} = \begin{pmatrix} \boldsymbol{A}_{gz} & 0 \\ \boldsymbol{A}_{gzz} & 0 \\ 0 & \boldsymbol{A}_{m} \end{pmatrix} \cdot \begin{pmatrix} \boldsymbol{\rho} \\ \boldsymbol{\chi} \end{pmatrix} + \begin{pmatrix} \boldsymbol{v}_{gz} \\ \boldsymbol{v}_{gzz} \\ \boldsymbol{v}_{m} \end{pmatrix}$$

where subscript m indicated the magnetic data set and $\boldsymbol{\chi}$ is susceptibility. However, the zeros in the anomaly matrix prevent a combined inversion because they effectively split the equation system into two and gravity and magnetics are dealt with as if separately inverted.

An option to combine gravity and magnetic data sets is given by the expression of so-called pseudo-anomalies. Consider that a point mass with a magnetic moment generates a gravity field and a magnetic field. The nature of the potential that describes the gravimetric and the magnetic fields makes it possible that one field can be expressed by the other by utilizing Poisson's relation. This relation can only be used under the crucial assumptions that the ratio between density (ρ) and magnetization (M) within the causative body is constant and the source boundaries are the same.

The equation describing the magnetic potential was given in the Chapter 2.1.2. It can be written

as:

$$V(P) = C_m \boldsymbol{M} \cdot \nabla_P \int_R \frac{1}{r}\, dv \tag{3.4}$$

Assuming a constant density distribution $\rho(Q) = \rho$, the gravity potential (Equation 2.3) can be written as:

$$U(P) = \gamma\rho \int_R \frac{1}{r}\, dv$$

Dividing this equation by $\gamma\rho$ and substituting the volume integral into Equation 3.4 yields

$$V(P) = \frac{C_m}{\gamma\rho}\, \boldsymbol{M} \cdot \nabla_P U \tag{3.5}$$

And here, $\nabla_P U = \boldsymbol{y}_{gm}$ gives the component of the gravity field in direction of the magnetization. In the following, the special case of only pole-reduced magnetic data and therein vertical gravity data is used. By taking the partial vertical derivative of Equation 3.5 and substituting C_m with $\mu_o/4\pi$, the formulation suggested by Militzer and Weber (1984) reads in the here used notation:

$$\boldsymbol{y}_{pm} = \frac{\mu_0}{4\pi\gamma\rho} \cdot M \cdot \boldsymbol{y}_{gzz} \tag{3.6}$$

where $\boldsymbol{y}_{pm}$ is the pseudo-magnetic anomaly and M is the vertical magnetization. The magnetic total field intensity can be expressed as $B = \mu_0 H$ and with the magnetization given by $M = \chi H$. Equation 3.6 can be reversed to calculate a pseudo-gravity gradient anomaly ($\boldsymbol{y}_{pgzz}$) from magnetic measurements ($\boldsymbol{y}_m$):

$$\boldsymbol{y}_{pgzz} = \boldsymbol{y}_m \cdot \frac{4\pi\gamma}{B} \cdot \frac{\rho}{\chi}$$

For the inversion, the ratio ρ/χ must be defined by the interpreter. The pseudo gravity gradient anomaly is then added to the combined inversion in the same manner as the other gravimetric anomalies - by enlarging the system of equations from Equation 3.3 to:

$$\begin{pmatrix} \boldsymbol{y}_{gz} \\ \boldsymbol{y}_{gzz} \\ \boldsymbol{y}_{pgzz} \end{pmatrix} = \begin{pmatrix} \boldsymbol{A}_{gz} \\ \boldsymbol{A}_{gzz} \\ \boldsymbol{A}_{pgzz} \end{pmatrix} \cdot \boldsymbol{\rho} + \begin{pmatrix} \boldsymbol{v}_{gz} \\ \boldsymbol{v}_{gzz} \\ \boldsymbol{v}_{pgzz} \end{pmatrix}$$

The inversion provides a density distribution for the model. Afterward the susceptibility distribution can be gained by transforming the estimated densities into susceptibilities using the predefined ratio.

3.2.2. Correlations between related regions

Earlier in this chapter the concept of defining regions and groups of geologically related regions to simulate and link subsurface structures was already shortly addressed (Section 3.1.2, Figure 3.1). So far, only the definition of regions was utilized. The definition of groups of related regions allows for parameter correlations within the specific groups. Boyd and Noll (1999) suggested a correlation via distance which is now implemented in the method. When defining correlations between voxels, the entries of the covariance matrix $\boldsymbol{C_x}$ change. They are calculated as follows

(after Boyd and Noll, 2000):

$$\mathrm{cov}(r_1, r_2) = \begin{cases} \sigma_{r_1}\sigma_{r_2} \cdot \exp\left(\frac{-\mathrm{dist}(r_1,r_2)^2}{D^2}\right) & \text{if } r_1 \text{ and } r_2 \text{ are related,} \\ \sigma_{r_1}^2 & \text{if } r_1 = r_2, \\ 0 & \text{else.} \end{cases}$$

where r_1 and r_2 are the related regions within a group, σ_{r_1} and σ_{r_2} are standard deviations assigned to the parameters of the specific regions, $\mathrm{dist}(r_1, r_2)$ is the Euclidean distance between centers of gravity of the regions and D is the correlation distance within the group of related regions to which r_1 and r_2 belong.

3.2.3. Exact forward calculation and polyhedral model bodies

The initial implementation (Sæther, 1997; Haase, 2008) uses mass point approximation for the calculation of the potential fields. This can cause bumps in the calculated anomaly if the station distribution is finer than the voxel size. An example of a spiky anomaly is given in Figure 3.2. This anomaly is calculated on a regular grid with 100 m station spacing. The voxel model contains an anomalous cubic density anomaly in the center at 500 m depth. Voxel edge length are of a constant 500 m. The bumps could be avoided by re-gridding the stations onto a coarser grid or by using smaller or deeper located voxels. But neither of these options is practical and an exact calculation is preferred instead. The resulting anomaly is given in Figure 3.2 (right). For the exact calculation a formula for right rectangular prisms would be suitable (e.g. Nagy, 1966). However, with the definition of regions and groups of related regions (Section 3.1), not the effect of every single voxel needs to be calculated but only the effect of the polyhedra which are enfolding the regions of voxels with same properties. Therefore, a formulation for the calculation of the potential field caused by a polyhedral body is more appropriate. The one used here is based on Götze (1976). The implementation uses triangulated polyhedra and follows Götze (1984) and Götze and Lahmeyer (1988). The essential part, that also makes the method quite fast, is the reduction of the calculation of the volume integral over a homogeneous polyhedron to the calculation of a sum of line integrals.
The implementation requires triangulated polyhedra but the inversion tool does not yet have an advanced triangulation routine. The triangulation of a voxel however is trivial. So all voxels

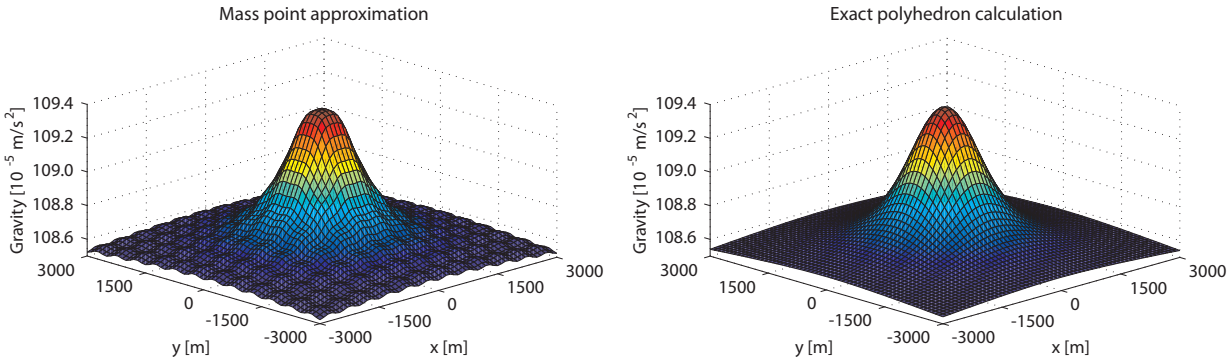

Figure 3.2.: *Comparison of gravity anomalies using mass point approximation and exact formula for the calculation of the potential field response of a voxel model. The mass point approximation shows bumps (Haase, 2008) that are avoided when using exact calculation.*

are triangulated but only those forming the hull of the polyhedra are used. A subroutine checks for region belonging of each voxel and its neighbors and decides which triangles belong to the surrounding polyhedron of a region and which are not needed for the calculation. This creates polyhedra that consist of more triangles than actually necessary. This will be accepted for now but should be kept in mind as it provides potential for a speed up of the calculations. The application of the new calculation results in modified anomaly matrices ($\boldsymbol{A}$ in Equation 3.2).

Having implemented the algorithm for exact calculation the inversion tool could now be applied to any model geometry of arbitrarily triangulated polyhedral model bodies. The model bodies are the analogy to the regions of a voxel model. However, the read routines for such models (triangulated polyhedral model bodies) are missing and also geometry files themselves of such models. Instead of implementing them, it proved to be more convenient to use an export function from the IGMAS software. It uses polyhedral model bodies and the above mentioned algorithms and provides the export of the anomaly matrix $\boldsymbol{A}$ that is needed in the inversion tool. So all triangulations and main calculations are done within IGMAS. After reading and allocating the matrix entries, the inversion tool starts directly with the MMSE calculation itself. This option is only applicable because once calculated, the anomaly matrix is not changed anymore by the inversion algorithm.

A few deficits come along with the use of polyhedron model geometries that were not approached in this work. The application of groups of related regions for constraining the property estimation requires a model geometry for the calculation of the correlations. With the missing geometry information within the inversion tool in the case of polyhedra (because of the imported $\boldsymbol{A}$-matrix), this option is not available. Also the refinement of the model, which is offered through the definition of smaller regions and gives the inversion more freedom in its estimations, can only be applied to polyhedral bodies by an external software (e.g. IGMAS offers the option for model body splitting).

3.2.4. Background density/susceptibility

Some software apply a *background* or *reference* density (ρ_{bg}) and susceptibility (χ_{bg}), respectively. If so, all modeling happens relative to this density/susceptibility value which is generally the one used for data processing. For example, when using Bouguer corrected data the background density is usually set to $2.67\,\mathrm{t/m^3}$, as this is the standard terrain density used for the correction. The background susceptibility is 0.0 SI in most cases.
The inversion toolkit presented here also works with a background density/susceptibility. In the voxel implementation this is only done indirectly. Inversion is done with relative property values and the background density/susceptibility is added to the estimated values afterward. The implementation for polyhedrons includes the background property in the calculations and all given and estimated densities are absolute values. The anomaly matrix $\boldsymbol{A}$ includes a column for the reference body which surrounds the entire model and produces a model response in opposition to all other model bodies. The background density/susceptibility is set by the user and never subject to inversion, it remains unchanged.

3.2.5. Anomaly shift

The anomalies calculated from subsurface models are generally shifted against the measured data because the models are limited in their extent and do not account for all the source effects that are actually contained in the measurements. It is therefore necessary to apply a shift which brings the anomalies to the same level and makes them comparable. The following description is limited to the case of gravity modeling but the same also applies to magnetic modeling.
In the forward modeling approach the shift is usually added to the calculated anomaly prior to misfit calculation. The shift-value g_s is often defined as the mean difference between measured and calculated anomaly:

$$g_s = \frac{1}{n}\sum_{i=1}^{n}(g_{meas,i} - g_{calc,i})$$

where n is the number of measurements. It can also be defined by the interpreter according to ones personal preference.
When using the inversion tool, measured and calculated anomalies also need to be adjusted. Otherwise the estimated densities have to compensate for the shift, i.e. they will be increased/decreased by a constant compensation density value ρ_c. Anomaly adjustment are usually done before the inversion, by subtracting the shift from the measured anomaly prior to inversion. For the inversion of polyhedron models the tool also offers the option to include the shift in the inversion. An additional model body, one that causes a long wavelength effect, is added to model in a congruent manner and the estimated density for this model body defines the actual shift. In the polyhedron variant of the code the geometry information of model bodies is contained in the anomaly matrix and adding a new model body means adding a column to the matrix. In case of gravity this new column is defined to cause the effect of a Bouguer slab:

$$g_s = 2\pi\gamma d \cdot \rho_s \tag{3.7}$$

with the gravitational constant γ, thickness of the overall model d and ρ_s as the *shift density* of the slab that will be estimated by the inversion. The option of an extra model body allows to get hold of the shift numerically. For models in the range of kilometers, the Bouguer slab variant allows shift estimations in the order of $1 \cdot 10^{-5}\,\mathrm{m/s^2}$ caused by the density estimation accuracy of $0.001\,\mathrm{t/m^3}$. However, when all model densities and the shift density are free to vary, there is no way to distinguish between what are the actual model densities and what is the shift density. One model body density needs to be set by the interpreter after inversion. To illustrate this, a small example is given here.

Example: The measured anomaly $\boldsymbol{g}_{meas}$ is given. A model is built to reproduced this anomaly, it consists of three model bodies with the densities ρ_1, ρ_2 and ρ_3. The anomaly matrix is $\boldsymbol{A}$, the gravity effect of the model is $\boldsymbol{g} = \boldsymbol{A} \cdot (\rho_1, \rho_2, \rho_3)^T$. Measured and calculated anomaly are shifted towards each other by the value g_s. The shift is the same for all gravity values and can also be written as a vector:

$$\boldsymbol{g}_{meas} = \boldsymbol{g} + \boldsymbol{g}_s$$

Assume a Bouguer slab with density ρ_s causes this shift (Equation 3.7) and the above expression can be written as:

$$\boldsymbol{g}_{meas} = \boldsymbol{A} \begin{pmatrix} \rho_1 \\ \rho_2 \\ \rho_3 \end{pmatrix} + \boldsymbol{A}_{BS}\rho_s = \boldsymbol{A}_s \begin{pmatrix} \rho_1 \\ \rho_2 \\ \rho_3 \\ \rho_s \end{pmatrix}$$

$\boldsymbol{A}_{BS}$ is a 1-column anomaly matrix that causes the Bouguer slab effect. $\boldsymbol{A}_s = (\boldsymbol{A}\boldsymbol{A}_{BS})$ is the anomaly matrix for all model bodies plus the additional one column for the Bouguer slab.

When inverting for the four densities without constraints, the result will most probably not be the expected values as written on the right side in the equation above. Instead, the result will look like this:

$$\boldsymbol{g}_{meas} = \boldsymbol{A}_s \begin{pmatrix} \rho_1 - \Delta\rho \\ \rho_2 - \Delta\rho \\ \rho_3 - \Delta\rho \\ \rho_s + \Delta\rho \end{pmatrix}$$

The interpreter has to decide on one of the density values and therewith defines $\Delta\rho$. Now all remaining densities can be corrected to the final results. In case one ore more body densities are fixed during inversion (using the 3σ convention mentioned in Section 3.1), a subsequent correction is not necessary because the $\Delta\rho$ would be 0.0 for this model body and it is the same $\Delta\rho$ for all model bodies. When inverting for the shift density it is not allowed to exclude model bodies entirely from the inversion (setting their variability to 0.0) because the subsequent correction of estimated densities cannot be applied. See also one of the applications in the next chapter for further discussion.

In case of magnetics the same principle is used. The additional model body that produces the shift is not the Bouguer slab but a body that comprises the entire model.

3.3. Evaluation of results by sensitivity analysis

The MMSE inversion only provides one solution and not a set of solutions. In the estimation of the model properties no stochastic components are involved and the same initial model always results in the same property estimates. The inversion result should be evaluated jointly with a sensitivity analysis. This analysis indicates how sensitive a potential field anomaly is to the individual bodies of a model. In other words, the sensitivity indicates how prominent or important a specific model body is for an anomaly. This measure, it will be called *prominence*, depends on the size (or volume) of model bodies and on their locations in the model, i.e. the distance between a model body and survey stations. An anomaly is less sensitive to small or very deep bodies, their effect is less visible in the anomaly. With increasing volume and/or decreasing depth they become more significant, the anomaly is more sensitive to them.

The prominence is a relative measure and given in %. All model bodies together have a prominence of $pmc = 100\%$. To estimate the pmc of the model bodies, a density or susceptibility (x_p) is specified, the x_p-dependency of the anomalies is linear. As a measure of prominence the absolute maximum of an anomaly is taken, which is then set into relation to the superposition of all

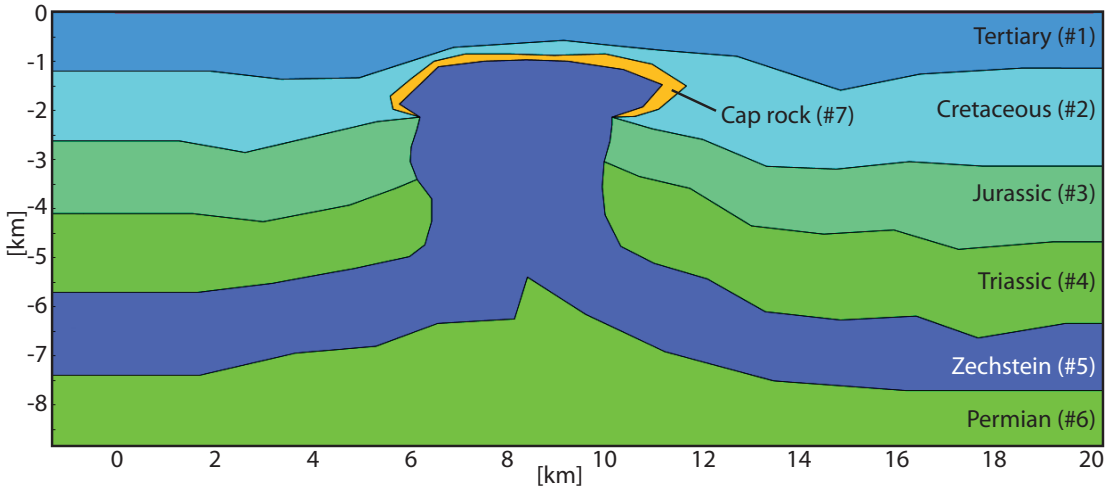

Figure 3.3.: *Cross section through the salt dome with labeling of the model bodies (3D view in Figure 2.4).*

anomalies. The prominence (in %) for a model body j is calculated as

$$pmc_j = \max(|A_{ij}x_p|) \cdot 100 \cdot \left(\sum_{j=1}^{n} A_{ij}x_p \right)^{-1}$$

with $j = 1 \ldots n$ model bodies, $i = 1 \ldots m$ stations and anomaly matrix A_{ij}. The potential field of the model body at all stations is calculated, using the density/susceptibility x_p, and the maximum value is estimated. Notice that the anomaly responses are different for different potential fields, i.e. model bodies are differently prominent depending on which potential field anomaly is regarded. Instead of taking the maximum of the anomalies also other measures can be used, e.g. the arithmetic mean of the anomaly or the RMS value.

The estimation of model body prominences (*pmc*) is here illustrated using the model example of a synthetic salt structure (from Schmidt, pers. comm.) built of seven polyhedral bodies. A 3D view was already given in Figure 2.4. A cross section of the model with labeled model bodies is given in Figure 3.3. For comparison, all three measures are plotted in Figure 3.5 as bar diagrams (maximum, mean and RMS). The diagrams show the prominences for the gravity and gravity gradient anomalies, the accurate numbers are given in the Appendix (Table B.1).
Figure 3.4 shows the gravity and gravity gradient anomalies caused by the individual model bodies of the salt structure. The magnetic anomalies are omitted here because the shape of the model response is the same as for the gravity gradients. The deeper bodies cause the long wavelength anomalies. Shallower bodies cause more detailed anomalies. In the gravity gradient/magnetic anomalies this effect is even enhanced due to the higher depth-dependency of the potential fields.

For the gravity anomaly the differences between the measures are rather small, as the individual anomalies are relatively smooth or have longer wavelengths, i.e. the extrema of an anomaly are close to the mean anomaly value. In case of the gravity gradient (or magnetic) anomalies there are some significant differences between the prominence measures because some of the anomalies are more inhomogeneous, with shorter wavelengths and localized bumps. Here, the RMS-measure

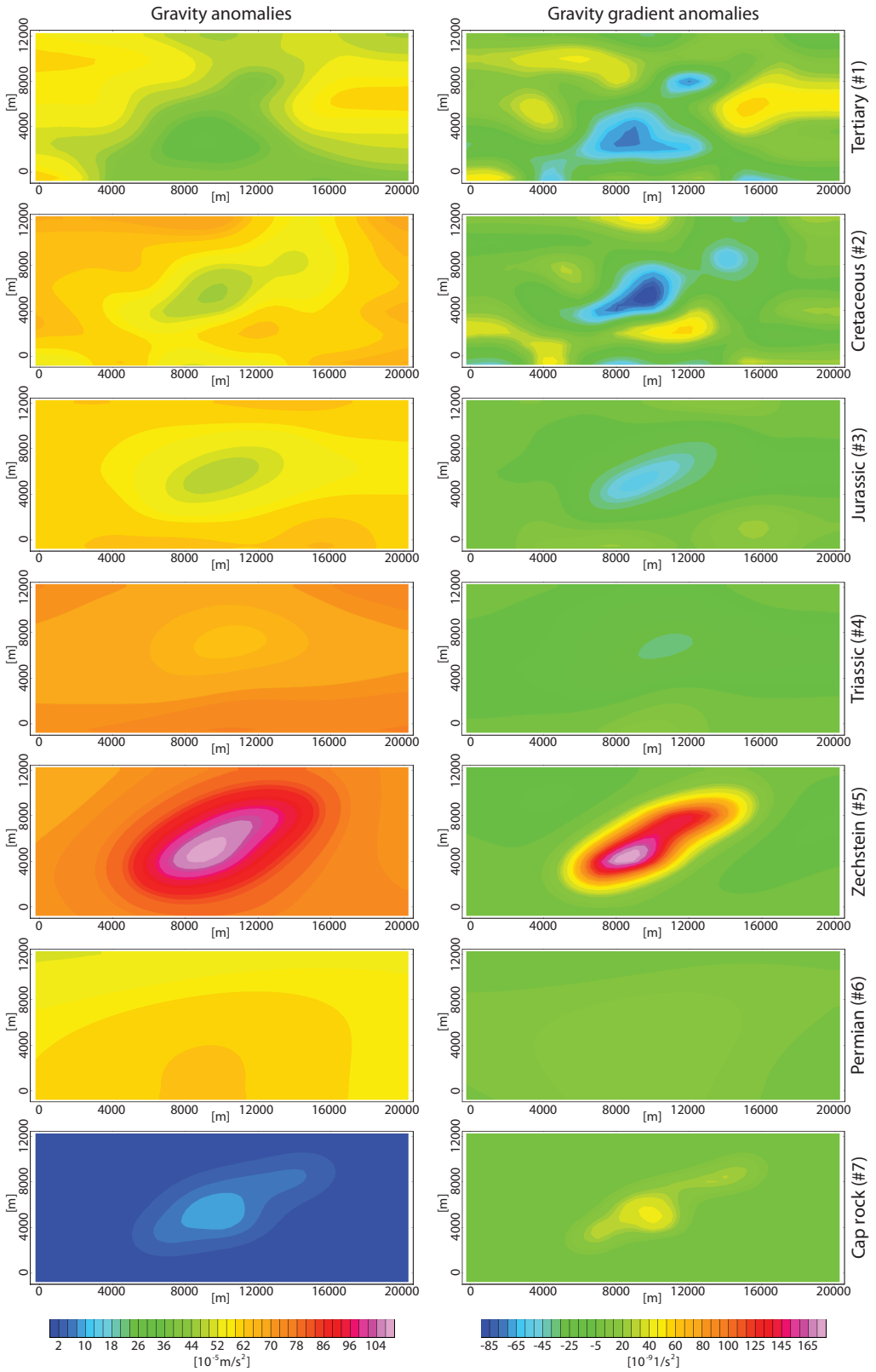

Figure 3.4.: *The prominence of model bodies illustrated on the example of the IGMAS salt dome. Shown are the gravity and gravity gradient anomalies caused when the density of the respective model body is set to* $1.0\,t/m^3$.

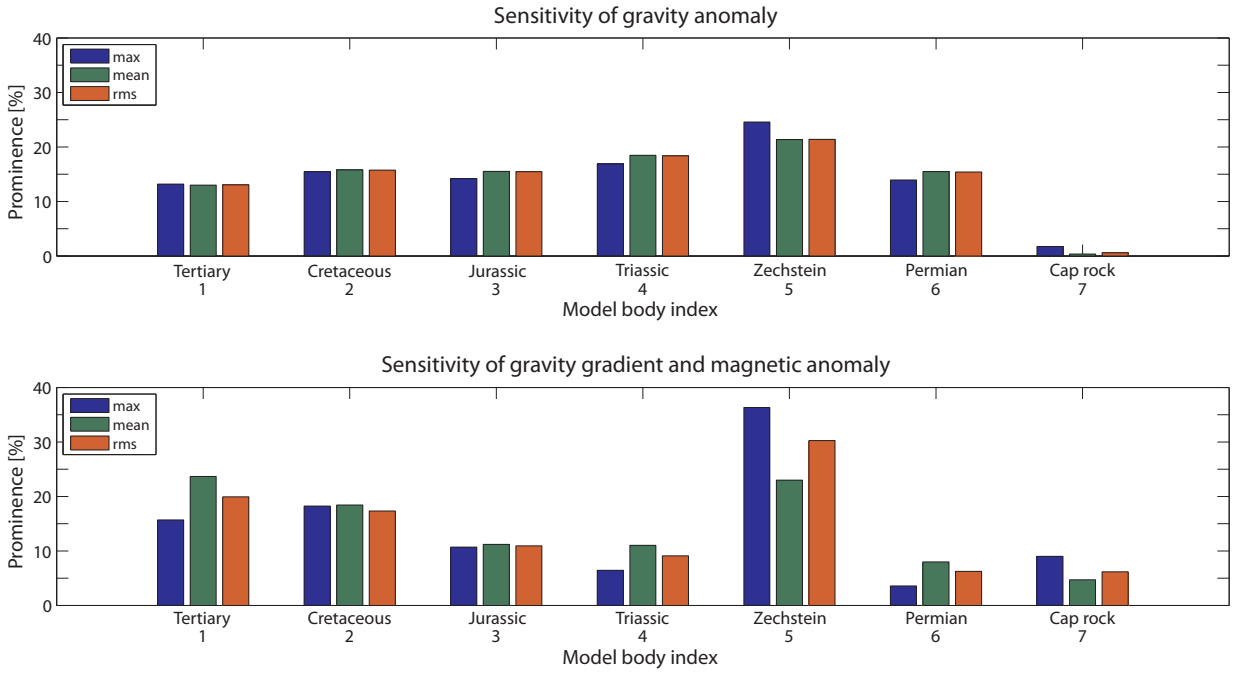

Figure 3.5.: *Prominence of model bodies from the IGMAS salt dome. Gravity and gravity gradient anomaly are differently sensitive for the model bodies. Top: Sensitivity of the gravity anomaly. Bottom: Sensitivity of the gravity gradient anomaly. Plotted is the prominence of each model body given in %.*

follows the max-measure as it better considers outliers (which is the absolute maximum in this case). Whereas the mean-measure averages over the entire anomaly and comes to significantly different *pmc* results (e.g. body #5, Zechstein).
Also evident in the max- and RMS-measures, less in the mean-measure, for the gradient/magnetic anomaly is the depth-dependency of the potential fields. The prominence of model bodies becomes stronger the shallower they are located. Especially the Cap rock body, which has a very low impact on the gravity anomaly, is more prominent in the gradient/magnetic anomaly.

The maps shown in Figure 3.4 provide a more clear assessment of the prominence than the bar diagrams in Figure 3.5. But with increasing number of model bodies it becomes impractical to show all maps (e.g. in the next chapter are models with up to 81 model bodies). Therefore, the general consideration of prominence uses the single values from the max-measure. In specific cases it can then be helpful to also plot the calculated anomaly of selected bodies.
The anomaly sensitivity consideration will be used for the evaluation results. It can help to explain probable outliers in the estimated property estimations. In the optimal case, outliers will only occur for those model bodies for which the anomaly has small sensitivity. In that case, their property estimation is not feasible from the given anomaly.

4. Applications with inversion tool

In the previous chapter the inversion toolkit CHAIN was further developed and now it allows for several different applications. These applications include single and joint inversions of potential field anomalies (magnetic, gravity and gravity gradient) as well as the usage of voxel- and polyhedra-based model geometries. In this chapter the tool is applied to four different models. The first is a synthetic voxel model of a salt diapir, used to test the different options of the tool available for voxel models. The following two models are quasi-synthetic polyhedron models of different complexity taken from the North German Basin. A fourth modeling area, with a much larger horizontal and vertical extent, is located offshore eastern Australia. This last model is available in both representations, voxels and polyhedral model bodies, and allows for a comparative application of the inversion tool.

The main focus of this chapter is on the application of the inversion method to different model geometries. The models vary in complexity, dimensions and representation and the applications are regarded as further tests of the method. The focus is less on new insights in or improved interpretations of the surveyed areas.

4.1. Synthetic salt diapir

In the beginning of the work the focus lay on the imaging of salt structures. Therefore, a synthetic salt model with a lateral extent of 4,000 m × 4,000 m and a depth extent of 3,500 m was created for this first application (Figure 4.1). It is located 500 m below the surface, with salt in the uppermost voxel layer, assuming the first 500 m are already reliably resolved. It is build of 2,560 voxels, each with an edge length of 250 m. Typically, the density contrast between salt and sediments increases with depth (roughly from 0.2 t/m^3 to 0.5 t/m^3 due to the compaction of sediments) but for reasons of simplicity only one constant property contrast is assigned to the model. So there are two domains: *salt structure* and *sediments*. Their properties are given in Table 4.1. The potential field anomalies of this model were calculated on a 20,000 m × 20,000 m irregular grid. The overall size of this grid was chosen to allow the anomalies to reach zero values at the borders in order to have the full spectrum of the anomaly available for inversion. The grid contains 2,588 stations that are densely distributed above the actual model. The station density decreases with increasing distance from the model. The computed anomalies are shown in Figure 4.2.

Property	Salt structure	Sediments	Initial value	Variability
Density [t/m^3]	-0.2	0.0	0.0	5.0
Susceptibility [SI]	-0.0004	0.0	0.0	0.01

Table 4.1.: *Physical properties of the original synthetic salt model and initial values and variabilities used for the tests.*

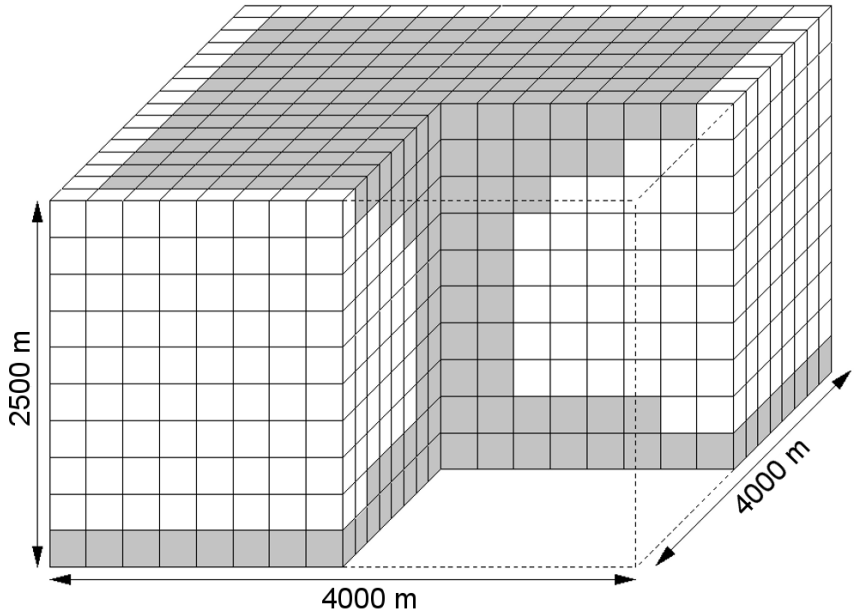

Figure 4.1.: *The synthetic model is built of 2,560 equally sized voxels. Grey voxels indicate salt structure, white voxels indicate sediments. The model surface is located at a depth of 500 m.*

A series of tests was performed with varying initial models (increasing model geometry restrictions) and varying start parameters (correlations between regions). All inversions were run with unconstrained properties, giving all regions initial values of 0.0 t/m^3 and 0.0 SI with standard deviations (variabilities) of 5.0 t/m^3 and 0.01 SI, respectively. These big variabilities allow the inversion to reach any reasonable density/susceptibility value without limitation. They are the default values of the tool.
The tests comprise inversion runs with different modes and varying geometry constraints. The influence of noise on the property estimation is investigated and remarks on its resolution are given.

4.1.1. Inversion modes and correlations

Several inversion modes were used and results are given as RMS error plots (Figure 4.3) and model snapshots (Figure 4.4). The RMS errors refer to the errors between expected and estimated density/susceptibility values. The different inversion modes were given abbreviations that are listed in Table 4.2. The values of the residual anomalies (synthetic anomaly minus model response anomaly after inversion) for all inversion modes are two orders of magnitude smaller than the assumed measurement errors. Because these residuals are almost negligible, their plots are omitted here.

Single inversions with unconstrained geometry

Single inversions were applied to the gravity anomaly, magnetic anomaly and the vertical gravity gradient anomaly. This first initial model is completely unconstrained. As described previously, property values are inverted for the regions of the model. When assigning a separate region to each

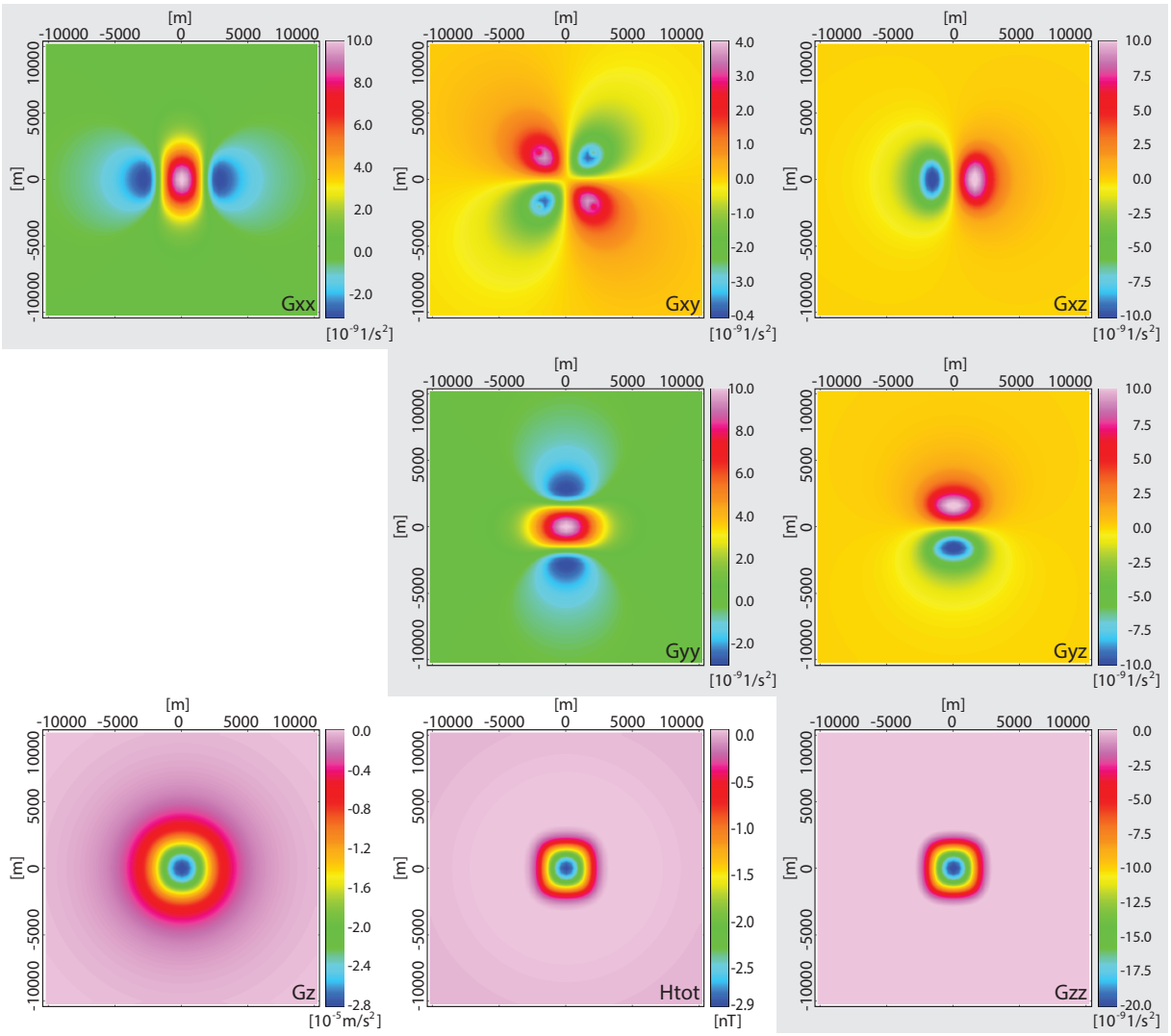

Figure 4.2.: *Computed potential field anomalies of the synthetic salt structure for gravity (Gz), gravity gradients (Gxx, Gxy, Gxz, Gyy, Gyz, Gzz), and magnetics (Htot).*

voxel the density/susceptibility of each voxel is allowed to vary and the inversion is unconstrained. In this first run, also no groups of related regions were defined. This led to the maximum number of 2,560 unknowns. Unfortunately, the estimated property distributions (Figure 4.4, top row) only give a very rough indication of the expected structure. An explicit geometry cannot be resolved. The RMS error values are accordingly large, with about $0.060\,\mathrm{t/m^3}$ and $1.187 \cdot 10^{-4}$ SI (Figure 4.3a (G1, GG1); Figure 4.3b (H1)).

Combined inversion with unconstrained geometry

The next runs were performed as combined inversions. Four different data set combinations are tested: (1) gravity and vertical gravity gradient; (2) gravity and all gravity gradients; (3) gravity, vertical gravity gradient, and magnetics and (4) gravity, all gravity gradients, and magnetics. No changes are made in terms of geometric definitions and the number of unknowns stays the

Abbreviation	Anomaly	Voxels	Regions	Groups
G1	Vertical gravity	2560	2560	2560
G3	Vertical gravity	813	813	813
G4	Vertical gravity	813	813	2
GG1	Vertical gravity gradient	2560	2560	2560
GG3	Vertical gravity gradient	813	813	813
GG4	Vertical gravity gradient	813	813	2
H1	Total magnetic field	2560	2560	2560
GGG1	Vertical gravity and gravity gradient	2560	2560	2560
GA1	Vertical gravity and all gradients	2560	2560	2560
HGGG1	Total magnetic field, vertical gravity, and gravity gradient	2560	2560	2560
A1	Total magnetic field, vertical gravity, and all gravity gradients	2560	2560	2560
A2	Total magnetic field, vertical gravity, and all gravity gradients	2560	2560	2560
A3	Total magnetic field, vertical gravity, and all gravity gradients	2560	813	813
A4	Total magnetic field, vertical gravity, and all gravity gradients	2560	813	2

Table 4.2.: *Abbreviations for the different inversion modes used in text and figures. The numbers 1-4 correspond to the definition and usage of regions and groups of related regions.*

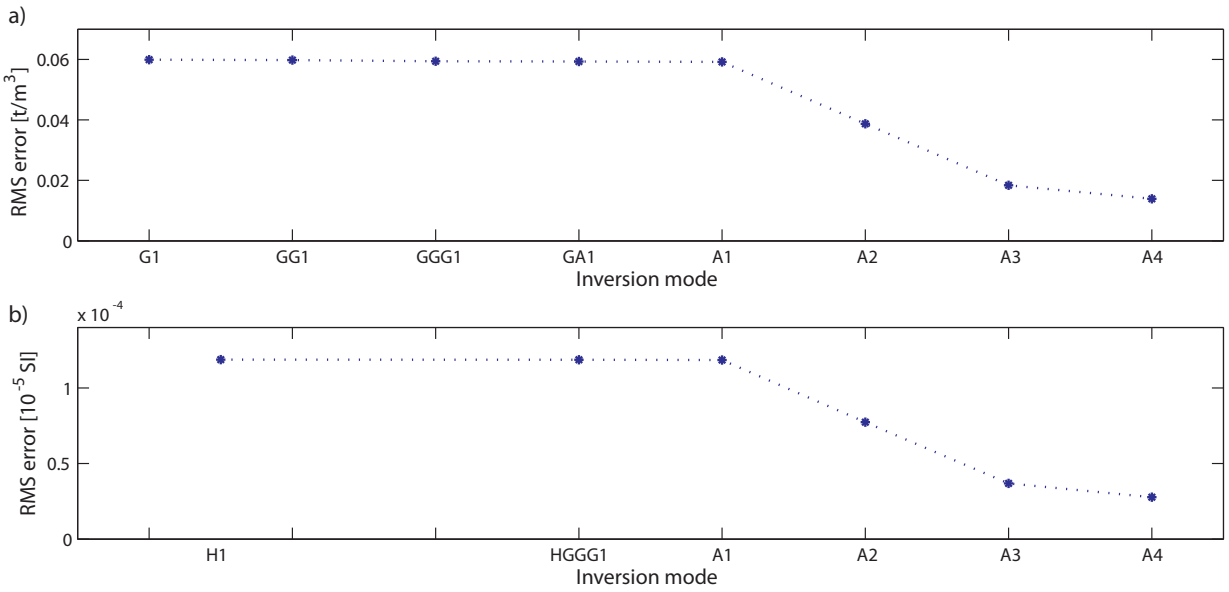

Figure 4.3.: *Results of inversions represented as RMS errors. Plotted are RMS errors between expected and estimated (a) densities and (b) susceptibilities. Given on the x-axes are the different inversion modes used: Characters indicate the used fields, numbers indicate the definition of regions and groups (see Table 2). The dashed line is no function but only connects the RMS values to better point out the trend.*

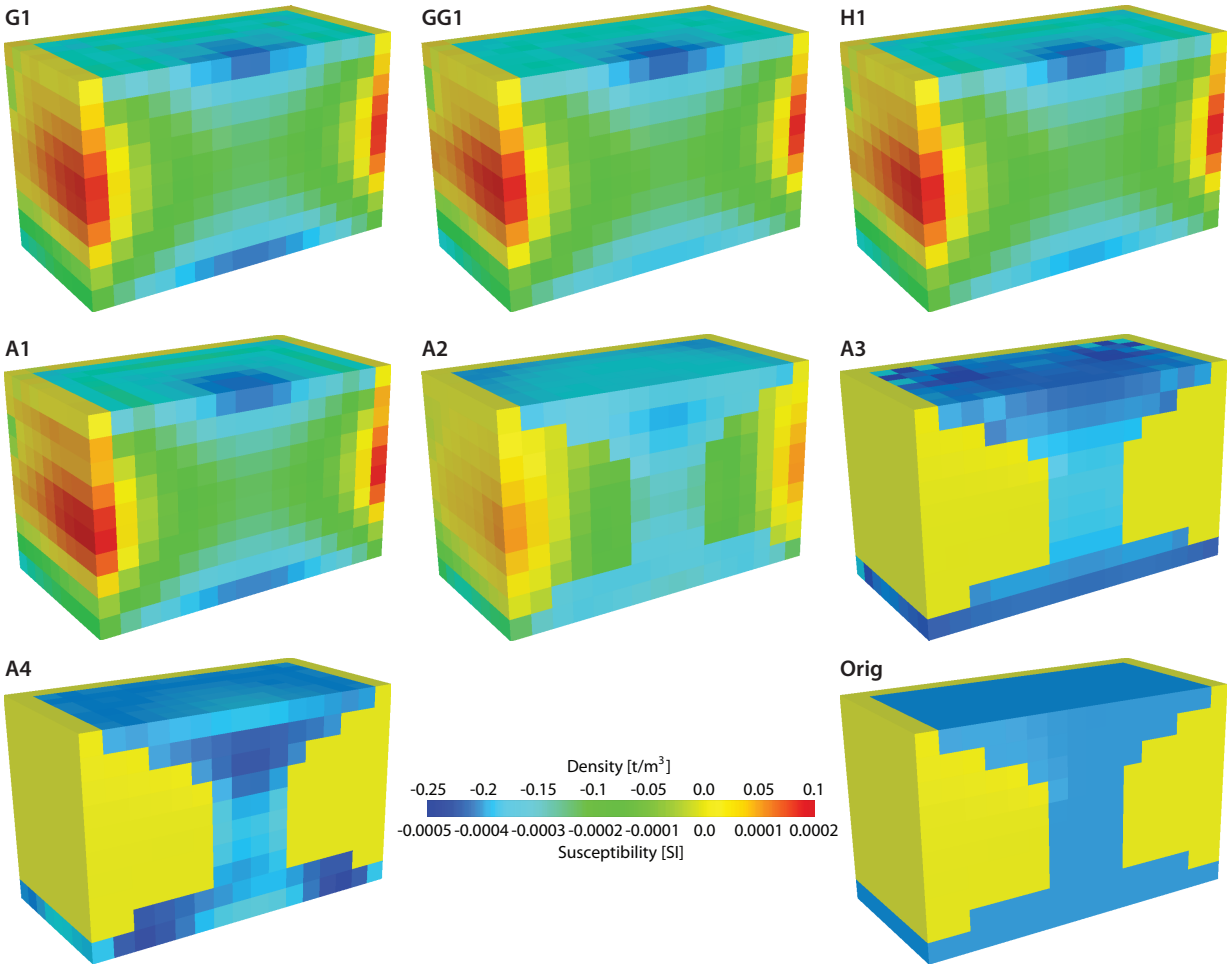

Figure 4.4.: *Density and susceptibility distributions after different inversion modes. The distributions are symmetric and the 3D views show only half of the model. Top row: Single inversions. Middle row and bottom right: Combined inversions. Bottom, right: Original property distribution. The color bar is representative for both quantities, as the ratio between densities and susceptibilities is constant. Labeling of the runs is described in Table 4.2.*

same as for the single inversions. The combined inversion however cannot improve the property estimations (Figure 4.4, A1). The improvement of the RMS errors is with an order of $10^{-4}\,\mathrm{t/m^3}$ negligible small (Figure 4.3a (GGG1, GA1, A1); Figure 4.3b (HGGG1, A1)).

Combined inversion with slightly constrained geometry - correlations within two groups

When some information of the subsurface is available but without any great detail, it is recommended to define groups of related regions. This introduces some first restrictions to the estimation, as the property inversion within these groups is correlated via distance. Of course in this example, it is exactly known what model geometry is expected. Two groups are defined, one encompasses the salt structure and the other the sediment structure. This means that the inversion is still applied to 2,560 unknowns (2,560 regions) but now 812 of them are correlated within the group "supposedly salt" and the remaining 1,748 are correlated within the group "supposedly sediments". The chosen correlation distance for both regions is 750 m which reaches as far as 3

voxels in a row. This and all following tests take all available data sets and a combined inversion is performed. The improvement in the density/susceptibility distribution is evident in Figure 4.4 (A2). The stem of the salt structure, which was previously completely missing in the estimations now comes into appearance. The improved estimation is also seen in the RMS error values which are now at $0.039\,\mathrm{t/m^3}$ and $0.774 \cdot 10^{-4}\,\mathrm{SI}$ (Figure 4.3 (A2)).

Combined inversion with constrained salt geometry and constrained sediment properties

The definition of groups of related regions clearly helped to improve the inversion results. The next test is now to tighten the constraints on the model geometry. Therefore, the group "supposedly sediments" is defined as just one region, explicitly outlining the salt structure. This definition reduces the number of unknowns to 813. As the outline of the structure is now regarded as known and with it the property distribution of the sediments, the goal of this inversion is now to reproduce the homogeneous property distribution of the salt. Correlation of voxels within the supposed salt was not applied here. Figure 4.4 (A3) shows a clear improvement in the results. The density/susceptibility distributions are slightly inhomogeneous but $0.018\,\mathrm{t/m^3}$ and $0.369 \cdot 10^{-4}\,\mathrm{SI}$ are small and acceptable RMS differences between expected and estimated values (Figure 4.3 (A3)).

Combined inversion with constrained salt geometry and correlation within the area

Previously the definition of groups of related regions was quite successful. Therefore, the final change in the initial model is to group the remaining regions within the specified contour of the salt structure into one group "supposedly salt". The results are displayed in Figure 4.4 (A4) and Figure 4.3 (A4). The smallest obtained RMS error values are $0.014\,\mathrm{t/m^3}$ and $0.277 \cdot 10^{-4}\,\mathrm{SI}$. Those are rather small improvements compared to the uncorrelated regions from the previous test. Compared to the previous test the homogeneous property distribution of the salt is better resolved only in the uppermost part of the model. The pattern at the edges disappears. However, the distribution within the stem becomes more inhomogeneous.

4.1.2. Data with noise

The tests of the method were done with noise-free data. In real applications however, data would contain a certain level of noise or uncertainty which could not be corrected or eliminated by data processing. Noise on data usually hampers inversion because it leaves more room for possible model solutions.

Figure 4.5 shows the performance of the method in density estimation with an increasing noise level. Single inversions were run on the gravity and the vertical gravity gradients, and then on a combination of data sets. One set of runs was unconstrained, the second set uses the correlation of related regions within two groups. In Figure 4.5 the mean density differences between estimated and expected densities are plotted against the increasing noise level. For the uncorrelated voxels the density estimation shows increasing discrepancies from the expected values. The method proves to be relatively robust against noise when joint inversion is applied and particularly when correlations within model domains are known and defined.

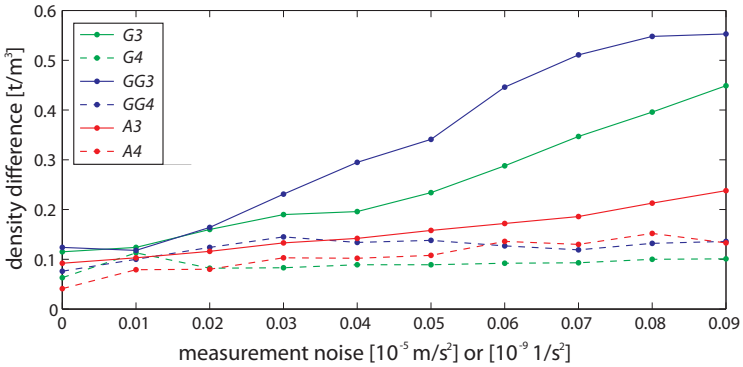

Figure 4.5.: *Effect of noise on density estimation. Different noise levels were applied to different anomalies (gravity, gravity gradient and all) using constrained and unconstrained geometries. The inversion modes are listed in Table 4.2.*

4.2. North German Basin

Two models from the North German Basin (NGB) are used in the following for mainly synthetic application. This means that real models from the NGB basin are used but, except for one case, no real data is used. The complex geological setting of the NGB has been subject to numerous investigations, modeling and various interpretations. The two models are from different parts of the basin, they are both using polyhedral model bodies. Their development involved different methods and data types, as described below. They represent realistic settings that are used here for testing the inversion tool.

The structure and evolution of the NGB is of major importance for the petroleum industry and still controversially discussed. The basin is intra-continental and part of the Central European Basin System (CEBS) (Figure 4.6). To the south it is limited by the Lower Saxony Basin and to the north it borders on the North Sea Basin (Brink, 2003). Its formation started in the early Carboniferous and late Permian on pre-Mesozoic consolidated, continental lithosphere (Bachmann and Grosse, 1989; Ziegler, 1990; Scheck, 1997). Rifting processes and extension of the crust was accompanied by magmatic and volcanic activity (Brink, 2003).
The basin has been intensively investigated by petroleum industry to assess occurrence and possible exploration of hydrocarbons. This led to a large amount of geoscientific data. The eastern part of the basin was surveyed within the DEKORP programme (Meissner and Bortfeld, 1990) which conducted reflection seismic profiles (DEKORPBasinResearchGroup, 1999) and wide-angle seismic profiles (Beilecke et al., 1998). Seismic investigations in the western part of the basin date back further (Brockamp, 1967). Furthermore, gravity field measurements (Bachmann and Grosse, 1989) and magnetotelluric data (Hoffmann et al., 1998, 2005) were gathered and laboratory measurements on rock samples were carried out (e.g. Inselmann, 1985).
Evident in the gravity data are two similar anomaly features, the Bramsche Anomaly (e.g. Giebeler-Degro, 1986; Bilgili et al., 2009) located in the Northwest German Basin (NWGB) and the Pritzwalk Anomaly (e.g. Kuder, 2002) in the Northeast German Basin (NEGB). These are two prominent positive anomalies and similarities are found in the interpretation and explanation of these gravity highs. Over the years two major model concepts were developed, improved, compared, disputed and discussed again. One explains the gravity anomalies by intrusive rocks in the

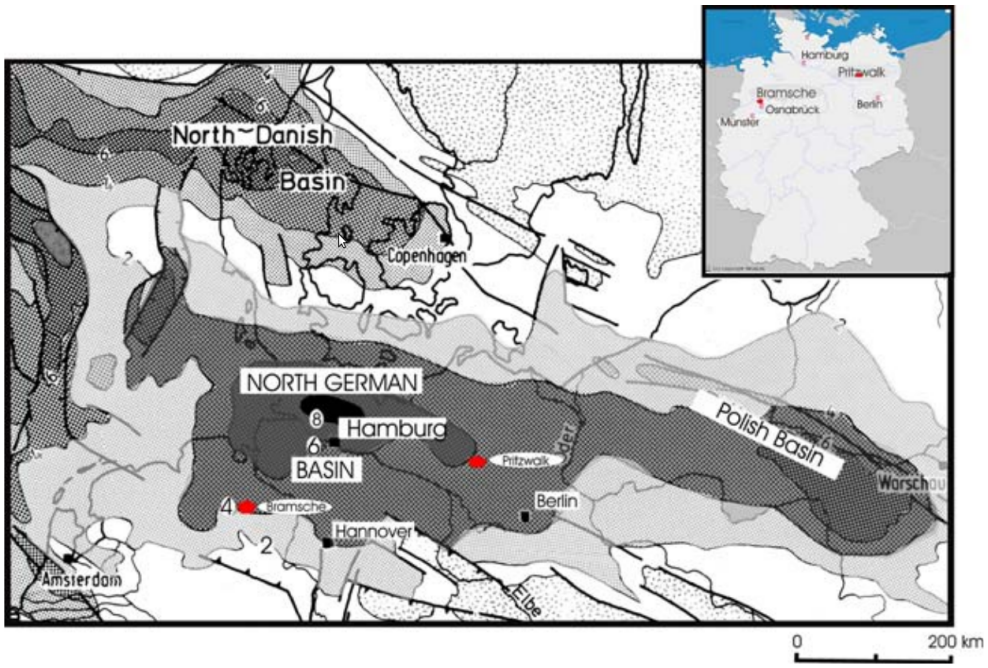

Figure 4.6.: *The geological map shows the North German Basin as part of the Central European Basin System (from Bilgili et al., 2009). Data for case studies is taken from investigations near the towns Bramsche and Pritzwalk (red dots).*

upper crust, the other by tectonic inversion, mantle uplift and/or a high density body (e.g. Brink, 2002; Kuder, 2002; Bilgili et al., 2009; Brink, 2013). For the following applications two of these models were provided, one from the NWGB and one for the NEGB.

4.2.1. Bramsche Anomaly

The modeling area is located at the southern rim of the NWGB (Figure 4.6). The strong, positive Bouguer anomaly (Bramsche Anomaly), that is characteristic for this area and of regional importance, is shown in Figure 4.7. It reaches up to $34{\cdot}10^{-5}\,\mathrm{m/s^2}$. A similarly prominent anomaly is also recognized in the magnetic data (140 nT). One interpretation for the high could be an intrusion between 6 and 10 km depth, the Bramsche Massif, which has e.g. been modeled by Giebeler-Degro (1986). The intrusion of rocks into the upper crust is believed to have happened during the Upper Cretaceous (Bachmann and Grosse, 1989). Their existence is supported by high thermal maturity in the southern part of the NWGB (Petmecky et al., 1999) and lack of reservoir rocks.
In a more recent interpretation, the Bramsche Anomaly is believed to be caused by subsequent tectonic inversion (Brink, 2002). This is in better agreement with the most recent interpretation of the Pritzwalk high (see 4.2.2) and supported by the level of hydrocarbon maturity measured in boreholes. This interpretation would allow the existence of gas-bearing, Mesozoic and Paleozoic sediments in the neighboring area.

Bilgili et al. (2009) tested the "intrusion model" (based on Giebeler-Degro, 1986) against the newly proposed "inversion model" (based on Brink, 2002) under the viewpoint of gravity modeling. The gravity data was provided by the GGA-Institute (Leibniz Institute for Applied Geosciences) in Hanover. From overall 57,000 available anomaly values a set of 4,900 stations was used which cov-

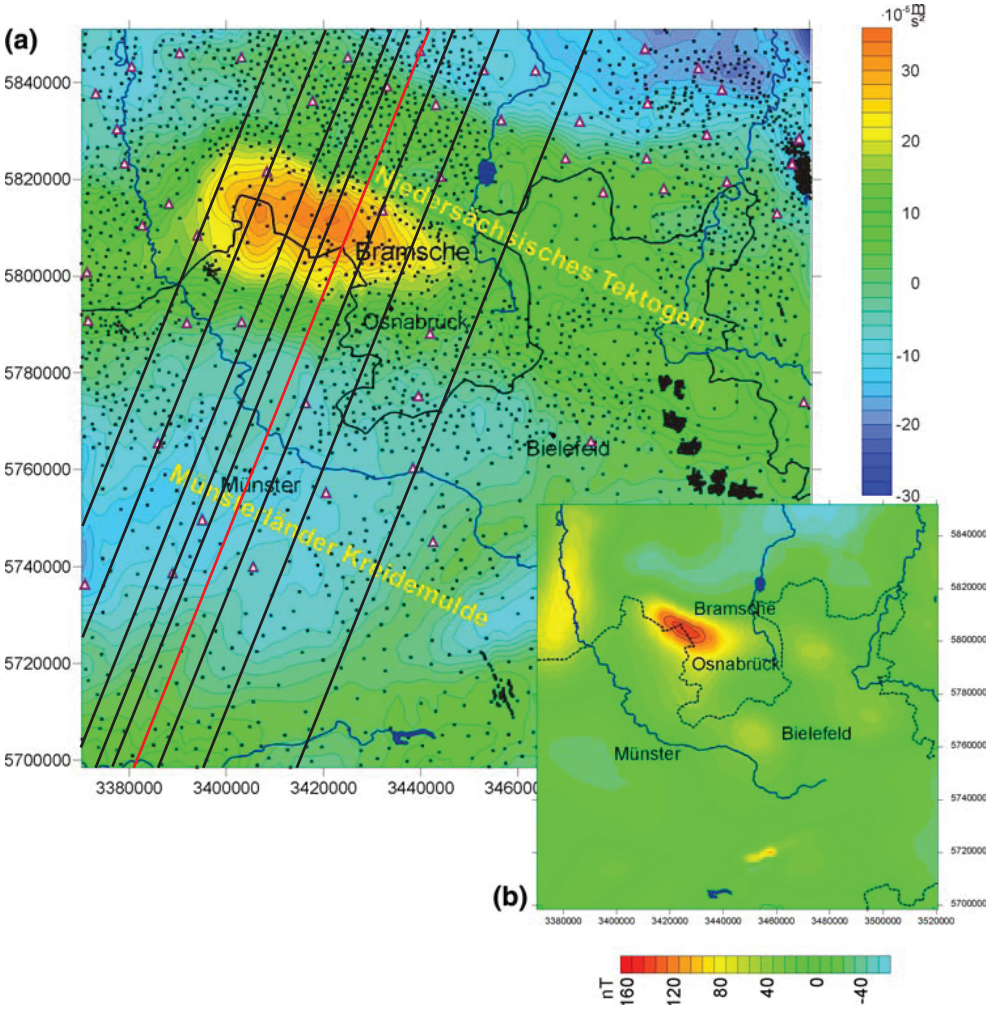

Figure 4.7.: *Bouguer gravity map (a) and magnetic map (b) of the NWGB (black points: measured points, black polygon lines: federal state boundary, blue polygon lines: rivers, triangles: boreholes, black lines: location of vertical model sections, red line: model section shown in Figure 4.8) (modified after Bilgili et al., 2009).*

ers an area of 150 km × 150 km. The stations are irregularly distributed with distances ranging from 25 m to 6.5 km (Figure 4.7). The following information were used to constrain the modeling: Boundaries of Zechstein and Post-Zechstein-formations from the Geotectonic Atlas (Baldschuhn et al., 2001), density values from Inselmann (1985, Table 1), seismic velocity structure (Brockamp, 1967), shape and depth of the "intrusion" or "high-density body" inferred from Euler source points. Due to the lack of sufficient information the interpretation of the magnetic anomaly was not addressed in Bilgili et al. (2009).

The model

For the following application, which is a test application of inversion on realistic model settings, one of the models from the study of Bilgili et al. (2009) was provided. Their most preferred density

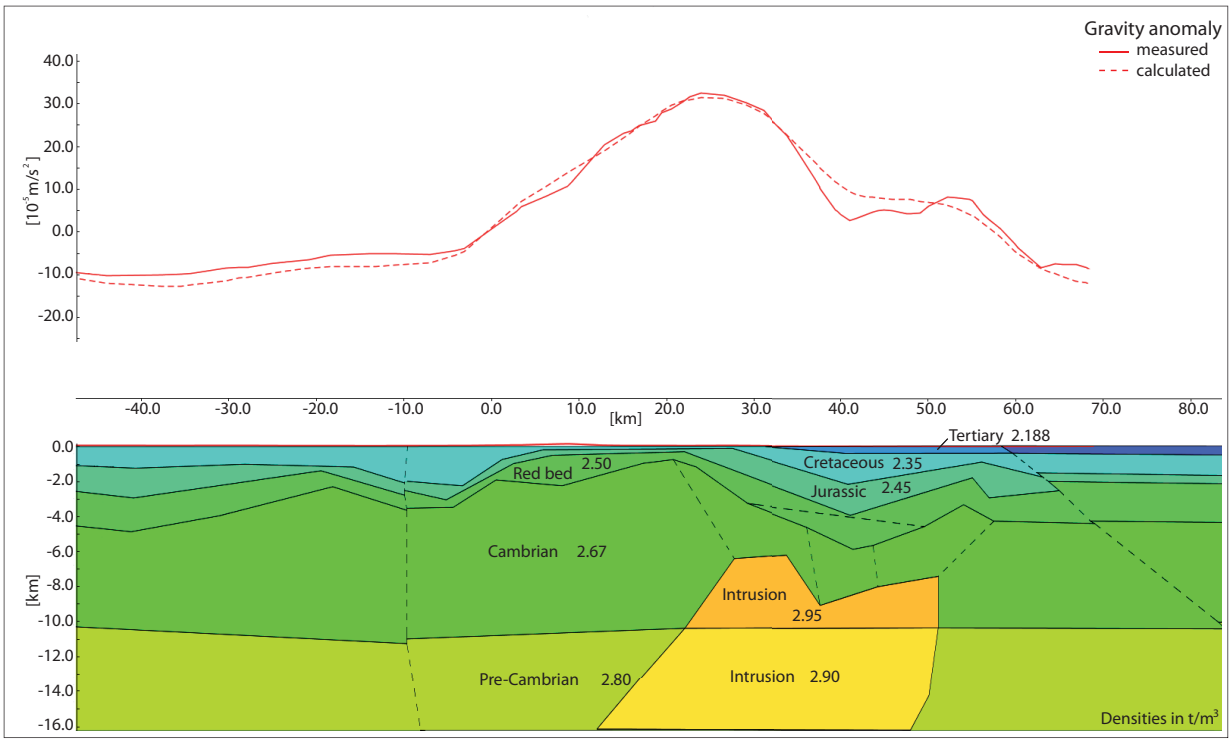

Figure 4.8.: *Bramsche model in the NWGB, a cross section from the model provided by Bilgili et al. (2009).*

model consists of 7 geological units, incorporating an intrusive body. The modeling was done with IGMAS and the model is defined on nine vertical sections (Figure 4.7). One of the sections is shown in Figure 4.8. The main intrusion is placed in the Cambrian crust, between 6 - 10 km, with a density contrast of 0.28 t/m^3. In greater depths the density contrast to the surrounding Pre-Cambrian is reduced to 0.1 t/m^3. The calculated model response fits the measured anomaly well (Figures 4.8 and 4.11) with a correlation of 85 % and a standard deviation of $4.86 \cdot 10^{-5}$ m/s^2 (Bilgili et al., 2009). The main differences in the anomalies are to the northwest and southeast of the Bramsche Anomaly. This is mainly caused by the model set-up and where the focus of modeling was set. The distance between the model sections is small in the area of the anomaly high (Figure 4.7) and allows more precise modeling. Away from the anomaly the space between sections increases and modeling becomes more rough, resulting in a less good fit of the anomalies. Although consisting of only 7 geological units, the model is constructed using 24 model bodies to account for fault offsets or variable model interpretation. This is indicated in Figure 4.8 by the dashed lines in the model cross section.

Inversion application 1

The first application is synthetic, using a realistic model but not real data. The model from Bilgili et al. (2009) is used as original model and its gravity response (gz) is used as original, "measured" anomaly. Also the vertical gravity gradient response of the model (gzz) is calculated and used as original, "measured" anomaly (Figure 4.9). With this example, single gravity inversion (gz-inversion) and gravity gradient inversion (gzz-inversion) are tested, and also the combined inversion of both ($joint$-inversion). The initial model for the following inversion runs uses the

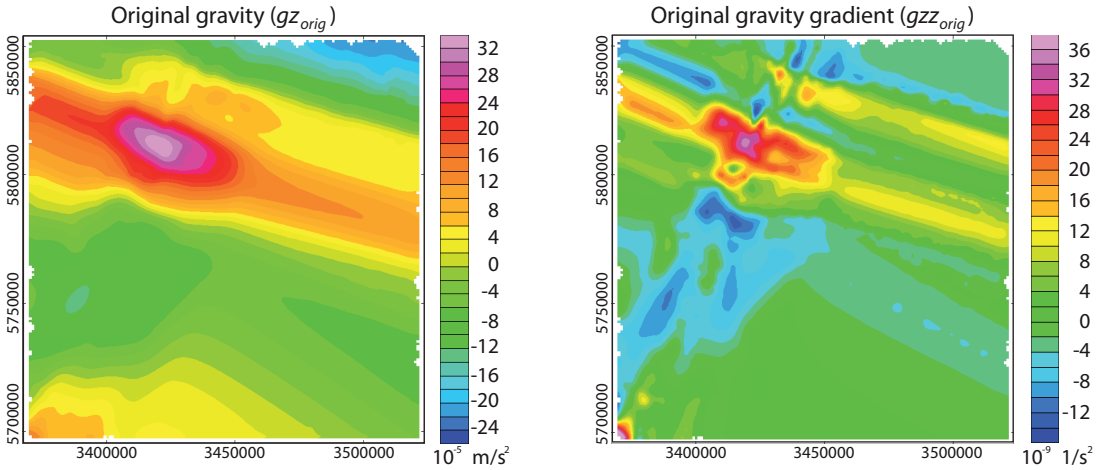

Figure 4.9.: *Gravity and gravity gradient map of Bramsche Anomaly, the original calculated anomalies from the model by Bilgili et al. (2009).*

original model geometry but without any density information (all densities are set to 0.0 t/m^3).

Run	Noise σ_{gz} [10^{-5} m/s^2]	Noise σ_{gzz} [10^{-9} 1/s^2]	$\Delta\rho_{RMS}$ [10^{-3} t/m^3] gz	gzz	*joint*
1	0.1	5.0	0.4	16.5	0.4
2	0.1	0.1	0.4	0.0	0.0
3	0.5	0.5	1.4	2.1	0.8
4	1.0	5.0	8.8	16.4	3.5

Table 4.3.: *Bramsche Anomaly inversion parameters and estimated densities. σ_{gz} and σ_{gzz} are the measurement errors in accordance to the added noise level. Density results are given as RMS errors between estimated and expected densities.*

Three different levels of normal distributed noise were added to the data, resulting in 10 applications: 3 single inversions of gz and gzz, and four combinations of joint inversions (Table 4.3). For *Run1* noise in the range of $\pm 0.1 \cdot 10^{-5}$ m/s^2 is added to the original gz-anomaly, this is consistent with the actual data accuracy (Bilgili et al., 2009). The noise level on the gravity gradient data is with $5.0 \cdot 10^{-9}$ 1/s^2 as to be expected from the AGG Falcon system (Dransfield, 2010) or the FTG error (Barnes et al., 2010). Relatively speaking, the gravity gradient noise is one order of magnitude higher than the gravity noise. Therefore, the gzz-noise level is adjusted to the same relative amount in *Run2*. The noise is then simultaneously increased on both anomalies in *Run3* and even further in *Run4*. The noise-manipulated original anomalies can be found in the appendix, Figures A.1 and A.2. Throughout this application the densities enter the inversion with the default variability of $\sigma_\rho = 5.0$ t/m^3.

Next to the noise levels, Table 4.3 also lists the inversion results for the densities which are given as RMS errors between the estimated and expected values. For a detailed look at the results see Figure 4.10 where the differences between expected and estimated densities for all 24 model bodies are shown as bar diagrams. The bottom panel of the figure shows the prominence of the model

bodies related to the gravity and gravity gradient anomalies. Resulting anomalies are calculated from the densities after single and joint inversions, respectively. The anomaly fit after inversion is given for the gravity anomaly (Table 4.4) and the gravity gradient anomaly (Table 4.5) in terms of anomaly correlation and standard deviation. The maps of calculated and residual anomalies can be found in the appendix, Figures A.1, A.2 and A.3.

	single		*joint*	
Run	gz_{corr} [%]	gz_{std} [10^{-5} m/s^2]	gz_{corr} [%]	gz_{std} [10^{-5} m/s^2]
1	100	0.058	100	0.073
2	100	0.058	100	0.058
3	99.9	0.294	100	0.291
4	99.8	0.572	99.8	0.572

Table 4.4.: *Gravity anomaly fit between original and model response after inversion. Given are the correlations between anomalies and the standard deviation. Listed are the fits after single and joint inversions for the four runs.*

	single		*joint*	
Run	gzz_{corr} [%]	gzz_{std} [10^{-9} 1/s^2]	gzz_{corr} [%]	gzz_{std} [10^{-9} 1/s^2]
1	90.5	2.871	90.5	2.882
2	100	0.058	100	0.058
3	99.9	0.295	99.9	0.291
4	90.5	2.871	90.5	2.878

Table 4.5.: *Gravity gradient anomaly fit between original and model response after inversion. Given are the correlations between anomalies and the standard deviation. Listed are the fits after single and joint inversions for the four runs.*

All runs provide satisfying results, considering that the RMS errors are in the order of 10^{-3} t/m^3 and the anomaly correlations are close too 100% for almost all results. *Run1* provides a very good result for the gz-inversion. Not as good but still satisfying is the gzz-inversion result. The *joint*-inversion resembles the result from the single gz-inversion, being not much negatively influenced by gzz-component. Interesting is the consideration of the model body prominences, especially with respect to the gzz results. Largest differences occur for the least prominent model bodies. Although the density estimation from the *joint*-inversion is improved, it does not improve the anomaly fit which remains at 90.5 %. This reflects the added noise on the data.
When adjusting the noise levels of the data by increasing the gravity gradient data quality in *Run2*, the results improve clearly. The gz-inversion remains the same but the gzz-inversion now has a RMS error much smaller than 10^{-3} t/m^3 and no longer visible in the difference plot in Figure 4.10. The *joint*-inversion maintains this good estimation.
With increased noise in *Run3* and *4* the results are still in an acceptable range. The noise is random which explains why the single inversions in some cases provide opposing density differences. Both runs however show the improvement gained by the joint inversion which provides better density estimates than each of the single inversions (Table 4.3). The joint inversion is at least as good as the single inversions but can even provide better results. As mentioned above,

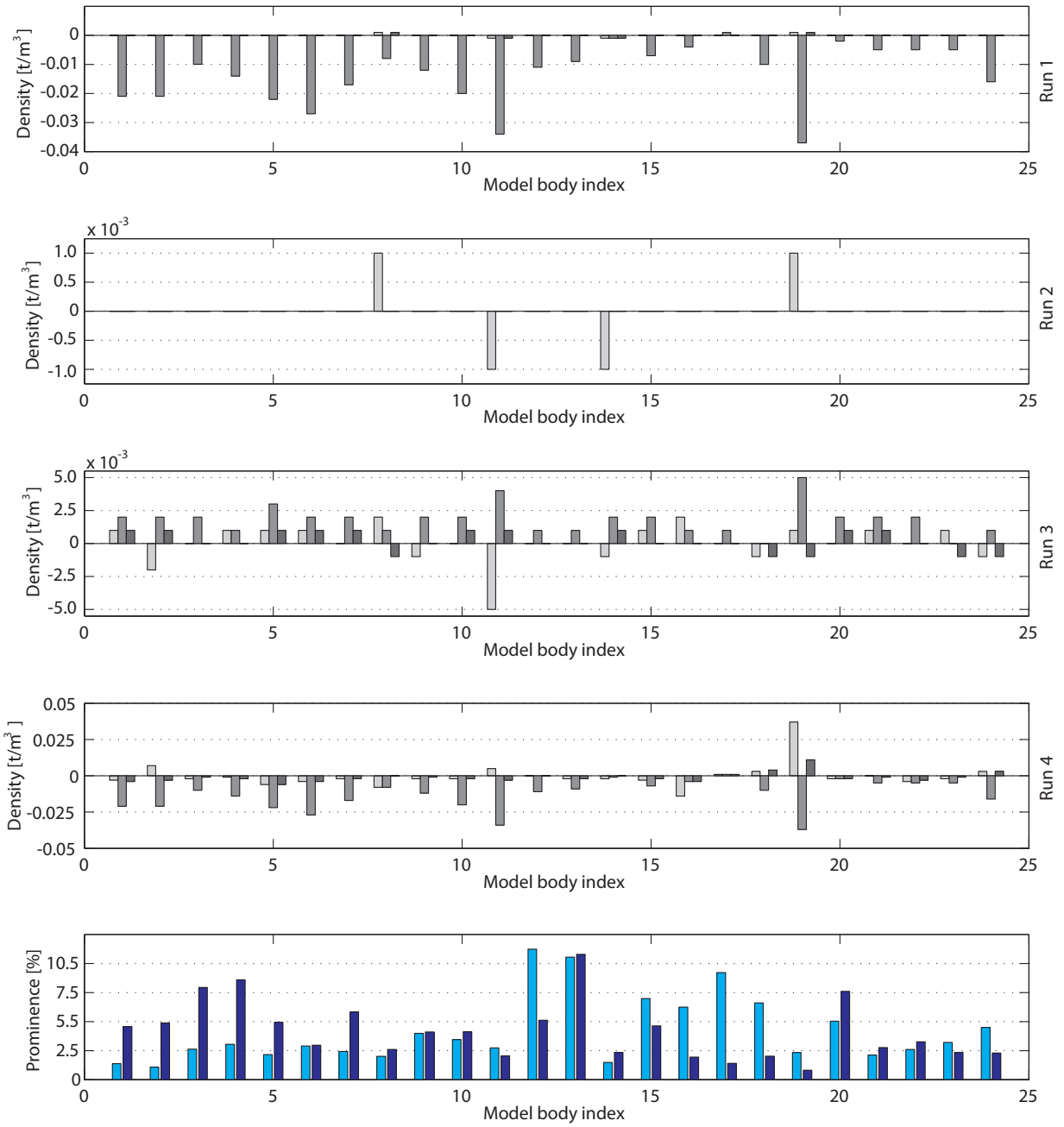

Figure 4.10.: *Results from inversion of the Bramsche Anomaly, Application 1. Panels 1-4 show the differences between expected and estimated densities from the single gravity inversion (light gray), single gravity gradient inversion (medium gray) and joint inversion (dark gray) for all four runs. Bottom: Prominence of the model bodies related to the gravity (light blue) and gravity gradient (blue) anomaly. Specification for the individual runs are given in the text.*

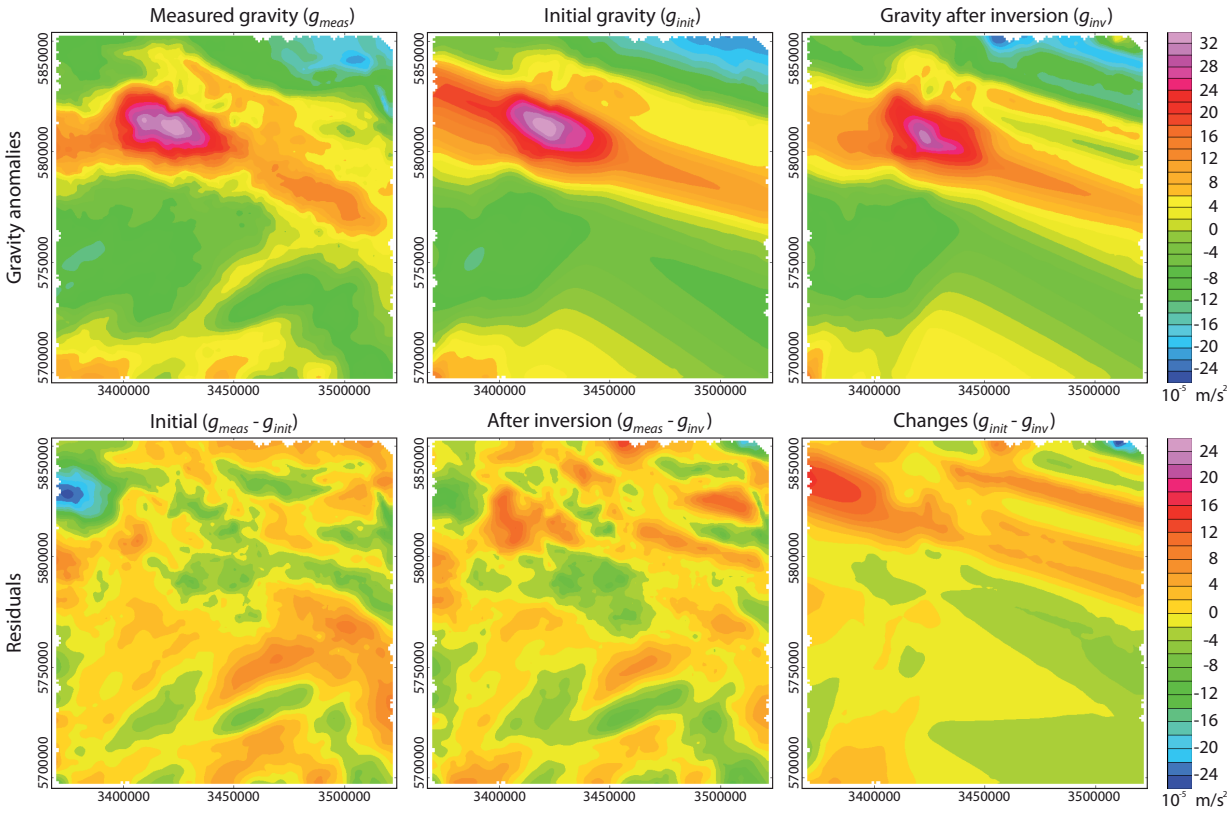

Figure 4.11.: *Gravity maps of Bramsche Anomaly showing the inversion results. Top: Measured and initial gravity and the anomaly after inversion. Bottom: Residual anomalies showing the initial misfit and the misfit after inversion, as well as the changes proposed by the gravity inversion.*

the remaining misfit between the anomalies is due to the added noise. This can be seen in the residual maps of the associated anomalies that only show the noise pattern (Figures A.1 and A.2 in Appendix A). Compared to the size of the model bodies the wavelength of the noise seems to be of too small to cause reasonable effects.

Inversion application 2

This is a real application, where the complete model by Bilgili et al. (2009) is used, including densities, and the inversion is applied to the measured anomaly to see what modifications are suggested in order to improve the misfit. The model was created with IGMAS and the software provides an automatic shift that adjusts the calculated to the measured anomaly ($2.344 \cdot 10^{-5}\,\mathrm{m/s^2}$ in this case). For the inversion, this shift is applied to the measured anomaly. The measurement error is given with $\sigma_{gz} = 0.1 \cdot 10^{-3}\,\mathrm{t/m^3}$ (Bilgili et al., 2009).

Measured, initial and calculated anomaly after inversion are shown in Figure 4.11, together with residual anomalies. The residuals show the differences between measured and initial anomaly, the differences after inversion and the changes between initial and final anomaly. The latter is given to show where improvement in the anomaly fit is gained. After the inversion the anomalies have an improved correlation of 93 % and a standard deviation of $3.32 \cdot 10^{-5}\,\mathrm{m/s^2}$ (the initial fit was

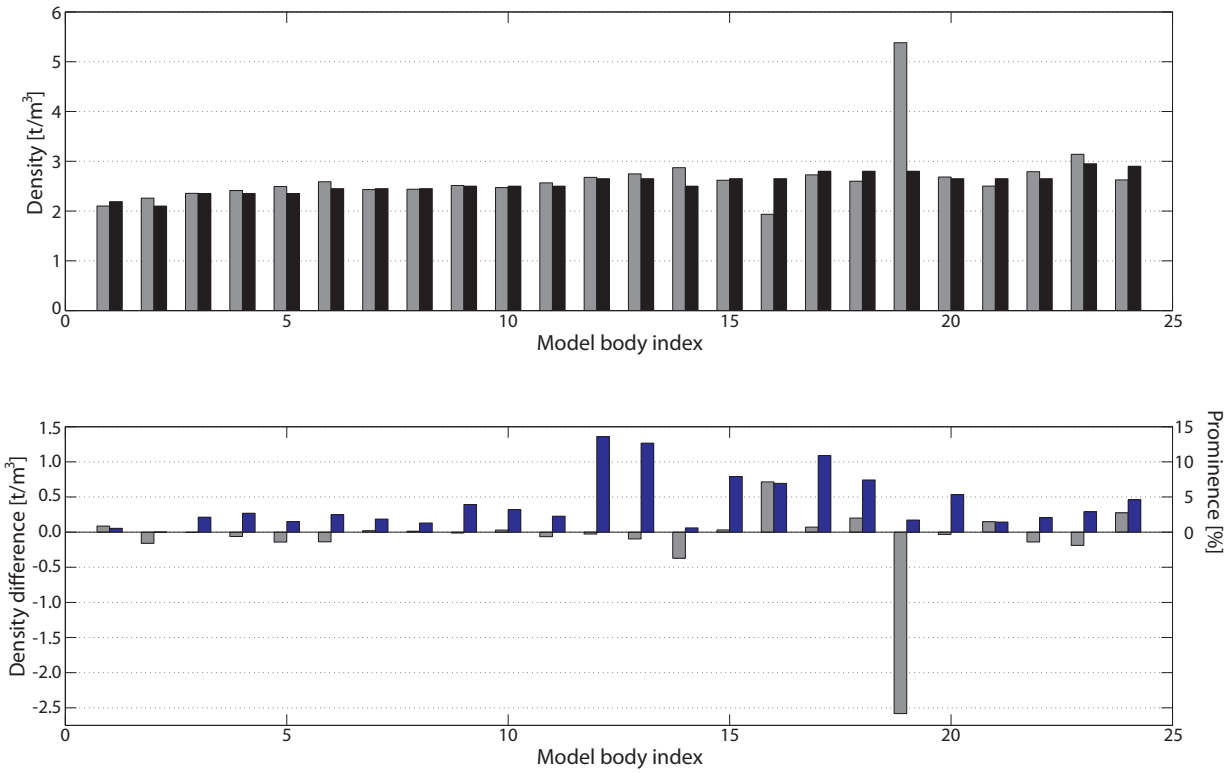

Figure 4.12.: *Results from inversion of the Bramsche Anomaly using measured data. Top: Estimated (gray) and initial (black) densities. Bottom: Differences between initial and estimated densities (gray) and prominence of the model bodies (blue).*

85 % $\pm 4.86 \cdot 10^{-5}\,\mathrm{m/s^2}$).
Results are given again as density bar diagrams (Figure 4.12). For most of the bodies only small density adjustments are proposed. They should be considered together with geological information in case of further development of the Bramsche Anomaly model. However, for two model bodies larger density changes are estimated: The resulting density of $5.382\,\mathrm{t/m^3}$ for the body with index 19 (a Pre-Cambrian unit) is obviously much too high and unreasonable. Its respective prominence related to the gravity anomaly on the other hand is rather small. Therefore, the confidence in this result should not be too strong. But rather than neglecting the inversion result completely, the density should be reconsidered from a geological point of view. The second conspicuity lies with the body with index 16 which is a unit of Cambrian. The change in density is relatively high (from 2.640 to $1.935\,\mathrm{t/m^3}$) and the prominence of the body is not negligible, it therefore demands a closer look.
Both above mentioned model bodies lie in the northeastern-most part of the survey area (north of 5,840,000 m and east of 3,450,000 m). The Pre-Cambrian unit (index 19) was not constrained during modeling. It is not covered by measurement stations and the model section spacing is already really wide. The Cambrian unit (index 16) lies to a large degree also in that area of the model where the section spacing is wide because no detailed modeling was desired. However, the area is covered by several stations which causes the relative prominence of this model body. Although the anomaly fit is improved due to the inversion, the result must be regarded with caution, in particular body 16. Changes in the model geometry might serve better than large

density changes. If the anomaly fit is wished to be improved, revising the structural modeling is recommended. Overall, this result does not change the interpretation of the Bramsche Anomaly and its explanation by an intrusion.

4.2.2. Pritzwalk Anomaly

This prominent Bouguer anomaly is located in the NEGB near the town of Pritzwalk (Figure 4.6). The horizontal extent of this basin is 230 km × 330 km. To the north lies the Caledonian Deformation Front (CDF) and to the south the Elbe Line, in the east the Polish Trough and to the west the NWGB. A frequently discussed question in context with the basin is whether or not it contains evidence for the Trans-European Fault Zone (TEF) (Kuder, 2002).
It was already mentioned that, because of the similarities of the gravity anomalies, interpretations of the Bramsche and Pritzwalk anomalies are compared, transferred and also adjusted when new insights in one area have led to an updated interpretation. The general modeling of those two anomalies should in the end be consistent as it has consequences for the understanding of the structural and thermal development and therein interpretation of the southern fringe of the Lower Saxony Basin which in turn is essential for exploration interests (Brink, 2013).

For the construction and improvement of structural models of the NEGB, Kuder (2002) modeled the area under the viewpoint of gravity interpretation and with focus on the explanation of the Pritzwalk high. The study basically resulted in two alternative models, including some minor variations. One model explains the gravity high by a high density body in depths of 6-12 km and the other by a mantle derived basic intrusion in about the same depth range. A gravity map showing the anomaly, which reaches values up to $30 \cdot 10^{-3}$ t/m^3 in the region of Pritzwalk, is given in Figure 4.13. Gravity data is available at 5,258 stations. The 3D modeling was constrained by geological and geophysical information, mainly reflection- and wide-angle seismic data from the DEKORP program which provides profiles of more than 1,700 km length (Meissner and Bortfeld, 1990; Beilecke et al., 1998). Additionally, interpretations from magnetotelluric data were used (Hoffmann et al., 1998) as well as a geological model of the basin and well data.
The two density models both fit the measured gravity well, with correlations of 84 % (model with high density body) and 94 % (model with intrusion). The existence of the TEF however could neither be confirmed nor disproved by gravity modeling as the measured field can be equally matched by both interpretations (Kuder, 2002).

The model

Again, only one model from the study of Kuder (2002) is used. This model is an "intrusion model with a low density body". The map in Figure 4.13 shows the locations of the vertical sections that build the IGMAS model (black lines). An exemplary cross section is given in the same figure. This section runs along the BASIN 9601 seismic line and line-drawing from the profile are included.
The model is built of 81 model bodies that define 17 geological units. The sedimentary fill of the basin has a fine subdivision into several layers to simulate an increasing density gradient with depth. This modeling is much more detailed than for the Bramsche Anomaly and the layered sequences encourage ambiguity in the property estimations. The intrusion in the Upper Crust is modeled with densities of 2.88 - 3.1 t/m^3. A low density body with a density of 2.44 t/m^3, constrained by wide-angle reflection seismics, is placed to the east of the intrusion.

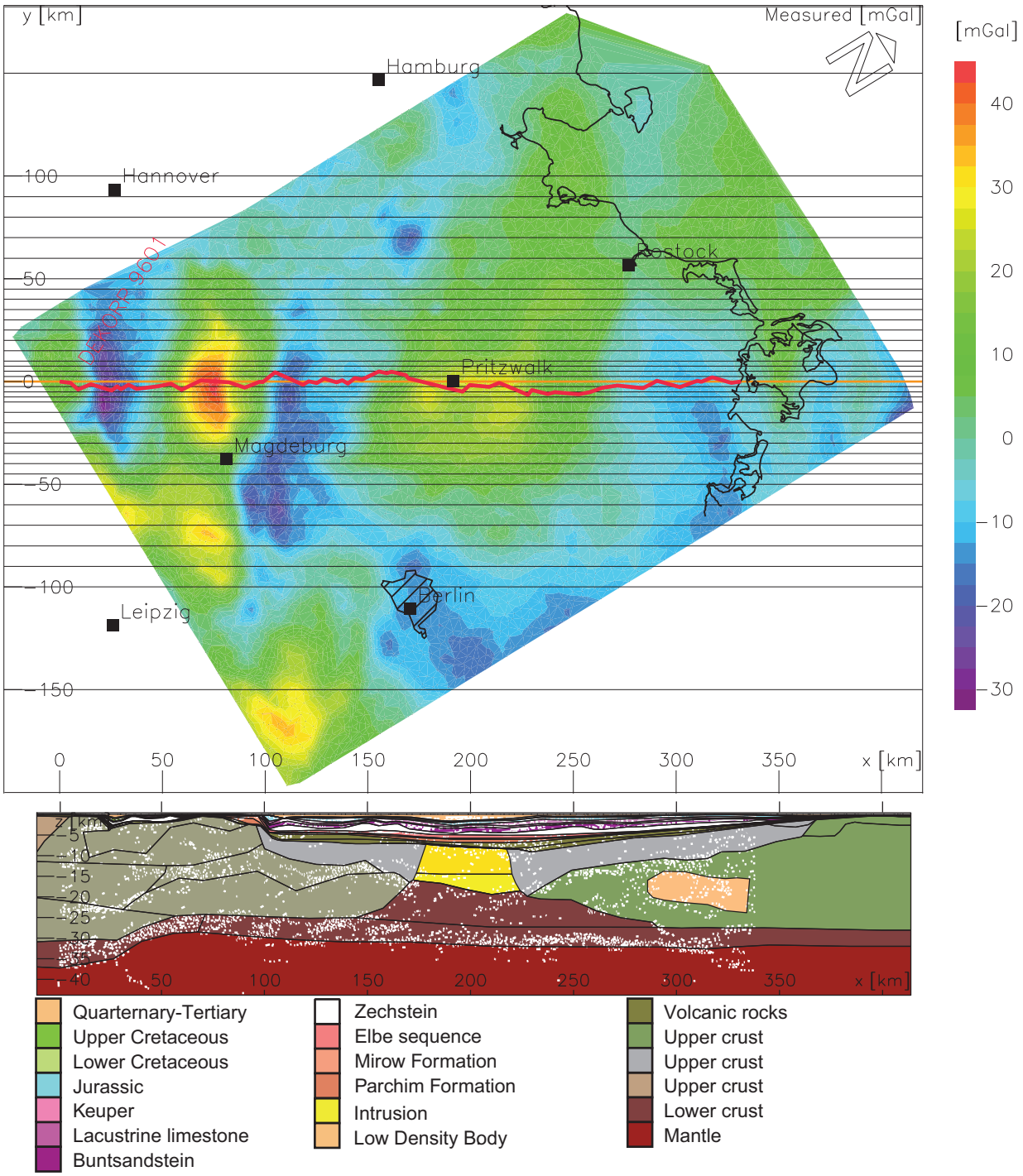

Figure 4.13.: *Gravity anomaly of the NEGB with a gravity high in the vicinity of the town Pritzwalk. The red line indicates the location of the seismic profile BASIN 9601, black lines indicate the vertical modeling sections of the IGMAS model and the orange line marks the cross section underneath the map (modified after Kuder, 2002).*

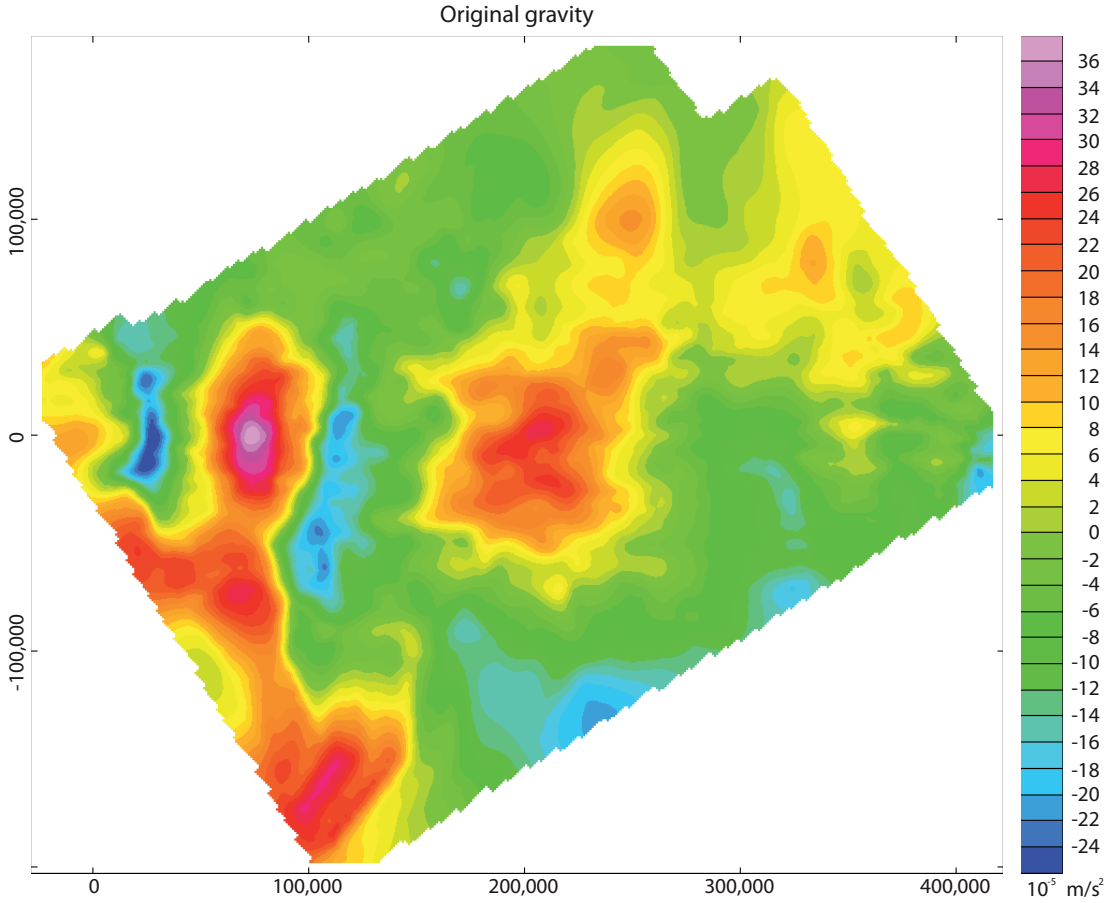

Figure 4.14.: *Pritzwalk Anomaly calculated anomaly from the model by Kuder (2002) model.*

Inversion

The application is quasi-synthetic again. The approach is similar to the one with the Bramsche Anomaly. The model from Kuder (2002) is used as original model and the gravity response is used as original, "measured" anomaly (Figure 4.14). The initial model for the inversion uses the model geometry from Kuder (2002), comprising 81 model bodies but no density information (all densities are set to $0.0\,\mathrm{t/m^3}$).
Two inversion runs are made for single inversions, differing in the level of noise that is added to the data. *Run1* uses a noise level that corresponds to the measurement error given in Kuder (2002) ($0.1 \cdot 10^{-5}\,\mathrm{m/s^2}$). *Run2* uses an increased noise level of $\pm 0.5 \cdot 10^{-5}\,\mathrm{m/s^2}$. The measurement error assigned for the inversion matches the noise level. All inversion parameters are summarized in Table 4.6, together with the inversion results which are given as RMS errors of the estimated densities and the correlation of the gravity anomalies after inversion.

Run1 provides good results, with an RMS error in the density estimation $<0.1\,\mathrm{t/m^3}$. The anomaly fit has a correlation of 100 % and a small standard deviations. In addition to Table 4.6 the results are also displayed in Figure 4.15 in the form of the density bar diagrams already used in the Bramsche example. Those diagrams show the difference between expected and estimated densities for all 81 model bodies. Also the prominence of the bodies is shown in that figure to

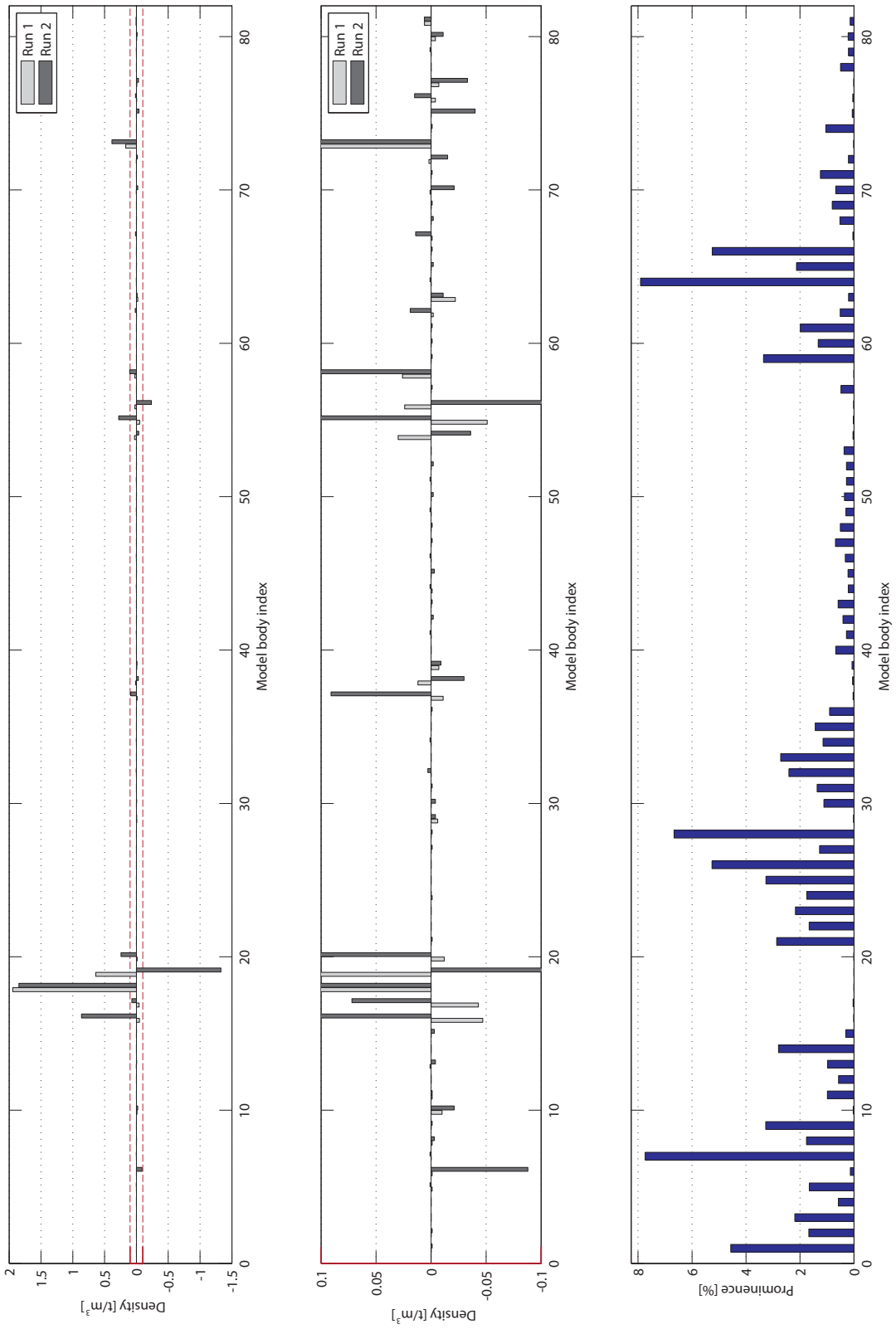

Figure 4.15.: *Results of gravity inversion for the Pritzwalk Anomaly.* Run1 *has a noise level of* $0.1 \cdot 10^{-5}\, m/s^2$, Run2 *has a noise level of* $0.5 \cdot 10^{-5}\, m/s^2$ *(see text). Top: Differences between expected and estimated densities. Middle: Same as above but zoomed in. Bottom: Prominence of the 81 model bodies related to the gravity anomaly.*

Run	σ_{gz} [10^{-5} m/s^2]	$\Delta\rho_{RMS}$ [t/m^3]	gz_{corr} [%]	gz_{std} [10^{-5} m/s^2]
1	0.1	0.179	100	0.0544
2	0.5	0.392	100	0.1390

Table 4.6.: *Inversion set-up and results for the Pritzwalk Anomaly: Noise level (σ_{gz}), RMS error of density estimation ($\Delta\rho_{RMS}$), anomaly correlation (gz_{corr}) and standard deviation (gz_{std}) after inversion.*

allow an evaluation of the estimated density values in terms of anomaly sensitivity. Both runs are successful as most of the estimates fit the expected values with a difference $< 0.1\,\mathrm{t/m^3}$. For the major part of the model bodies the difference is even much smaller. However, there are also some outliers. For a few model bodies the difference reach values almost up to $\pm 2.0\,\mathrm{t/m^3}$. The differences increase with increasing noise level. Without further consideration those estimates are not acceptable. The prominence of model bodies, shown in the top panel of Figure 4.15, is now of interest. Because there is a clear correlation between poorest density estimates and bodies with the smallest prominence. Regarding this information it is advisable to only accept estimates for the high-prominence bodies. The remaining values should be reconsidered and adjusted manually.

4.3. Capel and Faust Basins

The last model for application of the CHAIN tool is from the Capel and Faust Basins in the northern Tasman Sea, offshore eastern Australia (Figure 4.16). The basins are considered as remote frontier basins in terms of geological investigations and petroleum exploration. Assessment of the region with regard to petroleum productivity was carried out by Geoscience Australia (GA) (e.g. Petkovic, 2007; Hashimoto et al., 2008; Norvick et al., 2008; Hashimoto et al., 2009; Hackney et al., 2009) who provided to me potential field data and a density model, one of several described in Petkovic (2011).
Compared to the previous examples, this model has a much larger lateral and vertical extent. Its definition as a voxel model provides the first realistic application of the voxel-version of CHAIN. In addition to that it is also given as a polyhedron model which allows a comparative application of the inversion tool.

The area is located in a remote part of deep water 800 km east of Brisbane, near the former eastern Gondwana plate margin. The basins are Cretaceous rifts within the Lord Howe Rise which is formed by continental crust that became detached from Australia during fragmentation of the eastern Gondwana plate margin and the opening of the Tasman Basin. The Lord Howe Rise extends approximately 1,600 km from southwest of New Caledonia to the Bellona Trough (Hashimoto et al., 2008). The current structural configuration of the region is complex, driven by multiple extension events. It features a mosaic of continental fragments, rifts, and small oceanic basins (Gaina et al., 1998; Sdrolias et al., 2001; Norvick et al., 2001, 2008). The Lord Howe Rise itself is the largest of the continental fragments with an estimated crustal thickness of 14-34 km (Shor et al., 1971; Zhu and Symonds, 1994). It shows a north-south to northwest-southeast trend and is subdivided into three major structural zones: the Lord Howe Platform (eastern zone of high-standing basement), the Central Rift Province (includes Faust Basin in the northern Lord Howe Rise and the Moore Basin to the south), and Western Rift Province (includes Capel Basin

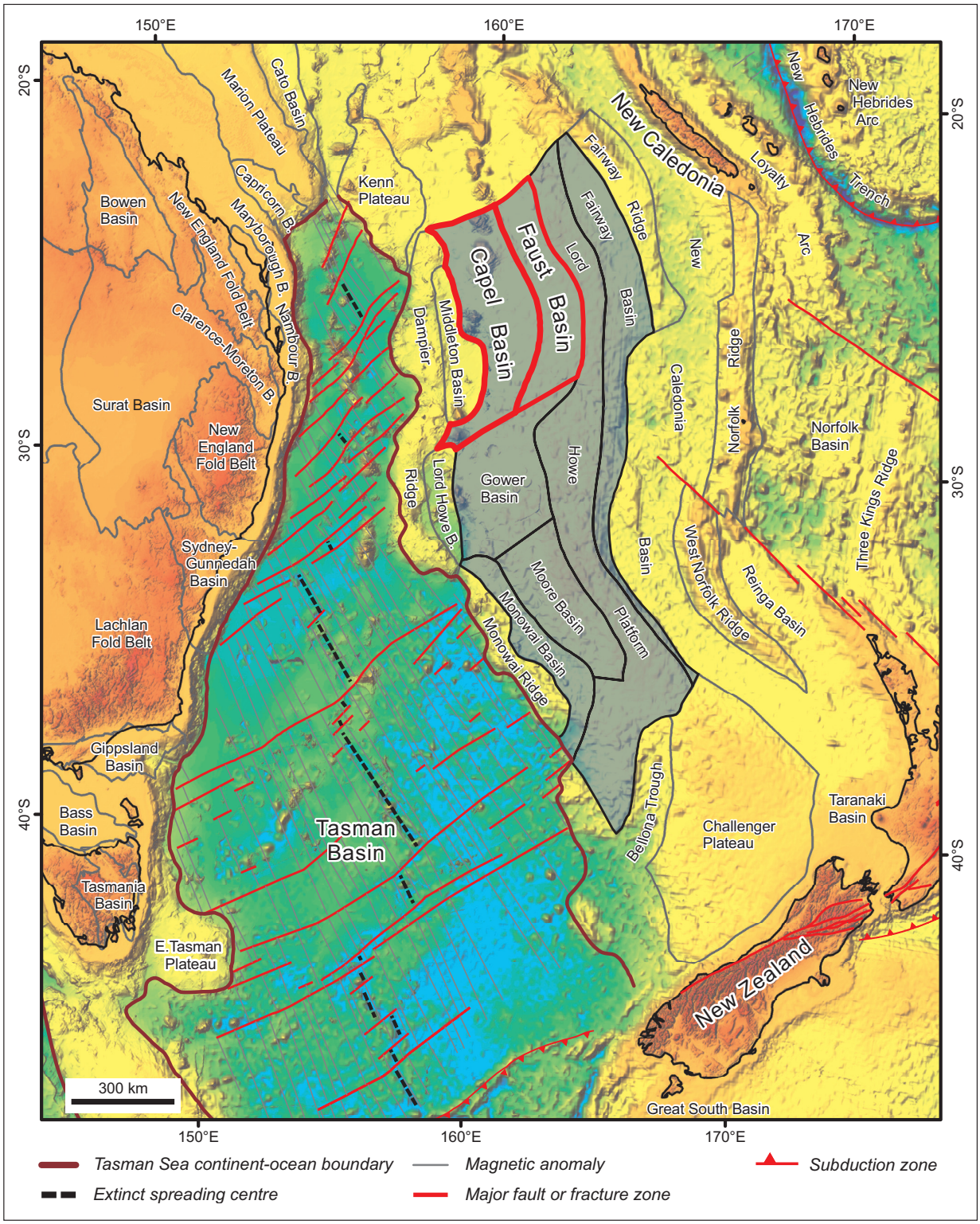

Figure 4.16.: *Map of the northern Tasman Sea showing the Capel and Faust Basins (red outline) within the Lord Howe Rise (Hashimoto et al., 2008).*

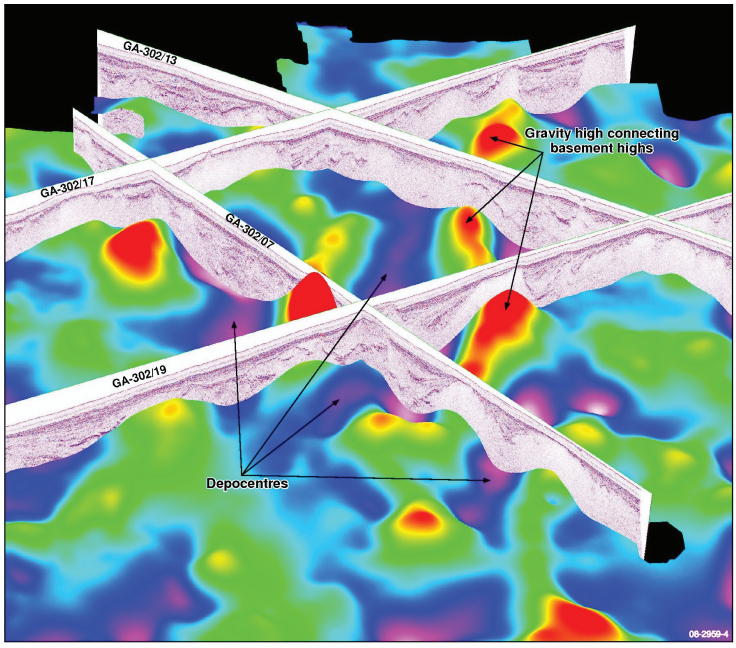

Figure 4.17.: *Four intersecting seismic profiles from survey GA-302 are plotted within the band-pass filtered Bouguer gravity map. This image illustrates the continuity of depocenters, basement highs and faults between the widely spread 2D seismic lines (from Hackney et al., 2009).*

in the north and the Monowai Basin in the south) (Stagg et al., 1999; Willcox et al., 2001). Graben stratigraphy in the Capel Basin appears to include Lower Cretaceous synrift volcanics, Turonian-Maastrichtian synrift clastic megasequences and a Maastrichtian-Recent postrift bathyal phase. Total Jurassic-Recent sediment thickness may be as much as 6-7 km. The southern part of the Capel Basin and the east of the Faust Basin are characterized by a number of smaller graben (Norvick et al., 2008).

Previous surveying of the area included sparse regional seismic lines, a single drill-hole from the Deep Sea Drilling Program (DSDP), and gravity data derived from satellite altimetry. The seismic data provided evidence of depocenters that correlate with lows in the residual Bouguer gravity data (Figure 4.17). In 2006 and 2007 new data was collected within the Australian Government's Offshore Energy Security Program during survey GA-302 (e.g. McKay, 2011). 5,920 km of high-quality 2D seismic reflection lines with line spacing of 20-50 km were acquired to further delineate depocenter geometry and sediment thickness variations (Hackney et al., 2009). The survey was planned on the basis of the gravity map. Data from 50 sonobuoys was recorded in 2006 (Petkovic, 2007). During survey TAN0713 in 2007, 24,000 km^2 of multibeam bathymetry and 11,000 line-km of shipborne gravity and magnetic data were collected in the central part of the two basins (Hashimoto et al., 2008). DSDP 208 is still the only well control in the Capel and Faust Basins area. This drill-hole terminated at 594 m below sea bed within post-rift sediments of Late Maastrichtian age. Petroleum exploration wells are not available in the area.

GA modeled the area by integrating interpretations of 2D seismic reflection, sonobuoy refraction and potential field data. From the seismic reflection data a complex pattern of depocenters could be identified which is separated by basement highs. Estimated sediment thicknesses are based

on velocity data from sonobuoys and stacking velocities, supported by 2.5D gravity modeling (Petkovic, 2007).
From seismic profiles alone it is difficult to correlate sediment packages between depocenters across the survey area but potential field data prove useful as an aid to interpreting the continuation of structures between 2D seismic lines. This is illustrated in Figure 4.17. 2.5D modeling however turned out to be inadequate in this region and a 3D model, using GeoModeller from Intrepid Geophysics, was constructed in order to validate and test the interpretation of sedimentary sequence boundaries and depocenter thickness (Petkovic, 2011).

A model from 2009 is used as an example here. It uses a six-layer configuration of water, three sedimentary layers, basement and mantle. Variations of the inferred densities from refraction data and stacking velocities were tested by GA and in this model version the layers were assigned with 2.00, 2.15, 2.34, 2.45, 2.70 and 3.10 t/m^3, respectively. Gravity values are Bouguer corrected, therefore water is assigned a sediment-like density value. As created by GeoModeller the model is in voxel representation but was also converted into a polyhedron model geometry as used by IGMAS (Schmidt, pers. comm.). Therefore, the model is now available in two different geometric representations which allows for a comparative application of the property inversion tool. 9,514 Bouguer gravity values from shipborne data, with a spacing of 3 km, were provided for this study (Figure 4.18).

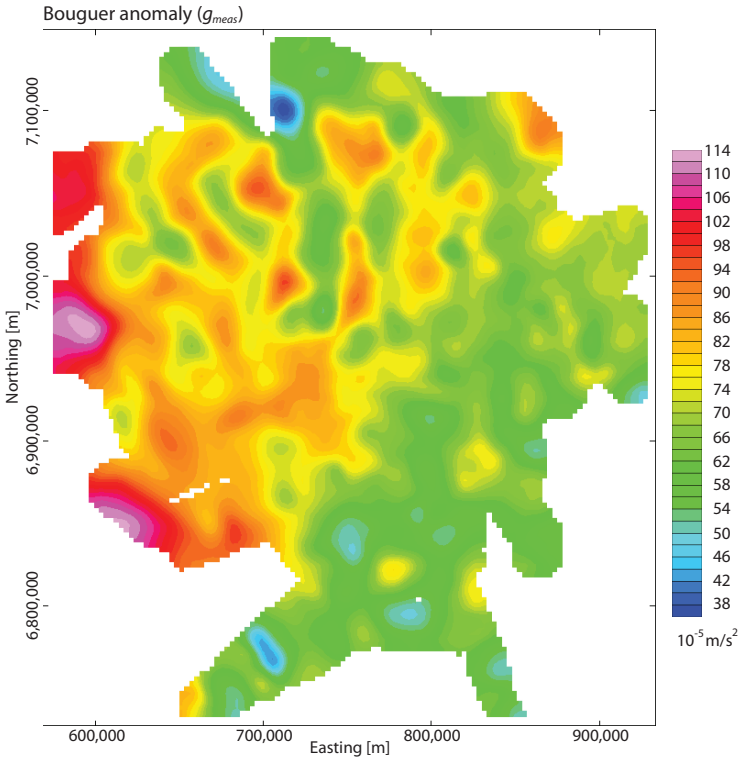

Figure 4.18.: *Bouguer gravity map of the Capel and Faust Basins.*

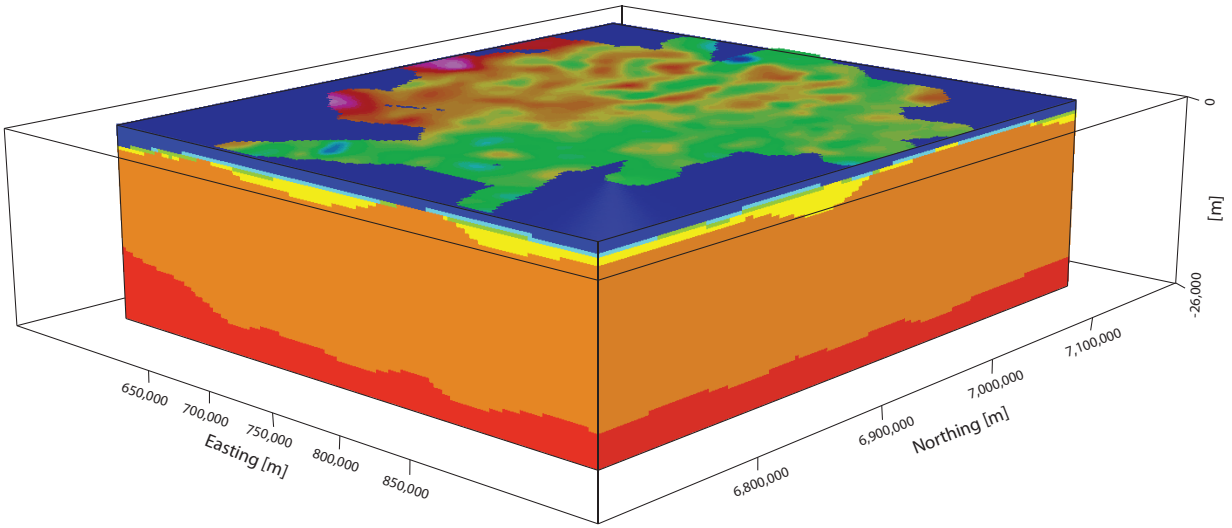

Figure 4.19.: *Original voxel model from the Capel and Faust Basins viewed from the southeast. The Bouguer anomaly is placed on top.*

4.3.1. Voxel-based approach

The provided voxel model is an export from GeoModeller. It spans an area of 360 km × 411 km × 28 km and is built of 920,640 voxels (120 × 137 × 56). A view on the model is given in Figure 4.19. All voxels have the same size of 3000 m × 3000 m × 500 m. This voxel model encompasses only the actual modeling area; the prevention of edge effects was handled by the software via mirroring. The inversion algorithm, however, has no option to deal with this effect. A model with relative densities and a constant background density of zero, similar to the voxel salt model, is not feasible for the layered model of the Capel and Faust Basins, because edge effects remain at the density contrasts where layers end. Therefore, the model needs to be enlarged laterally.

A routine for enlargement was developed which adds voxels to all sides of the model (Figure 4.20). Their vertical cross section and assigned property matches the one of the directly neighboring voxel, i.e. this enlargement works for inhomogeneous voxel models where not all voxels have the same size. Those additional voxels have a much larger size than the ones in the initial model as detailed modeling in the additional area is not desired. The added voxels in this example all have a lateral extent of 250 km in the respective direction. In total, 29,008 voxels were added.

The lithology information contained in the GeoModeller voxel export is used to define the regions of voxels of the same density. The geometry of the basins and the assigned densities were already mentioned in the text above and are used as initial values for the inversion (see also Table 4.7). Because of the enormous size of the Capel and Faust basin model (almost 400 times the size of the diapir model in Section 4.1), the model needed to be modified. The inversion tool implementation has two memory intensive parts. The first refers to the initial triangulation of voxels. All voxels of the model are triangulated in order to be used by the routine for the forward calculation of the gravity effect (Section 3.2.3). This triangulation happens when the voxel file is read in by the program. The forward routine itself only uses the triangles on the surface of the region but they still need to be read in once and saved. The second part refers to the number of regions of voxels with the same property. Depending on the definition of regions, the inversion has more or less

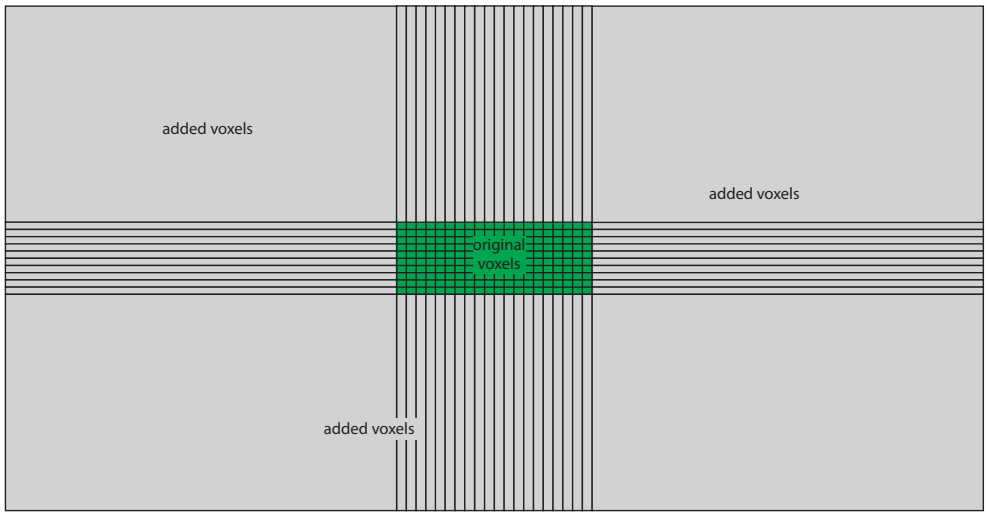

Figure 4.20.: *Sketch of an enlarged voxel model (top view).*

options to estimate physical properties; the finer the region definition, the more freedom for the property inversion (Section 3.1.2). It offers the estimation of individual densities for the voxels and therein allows the layer interfaces to "move". The number of regions affects the anomaly matrix which is used by the inversion routines (e.g. inverted and multiplied). Its size is $N_s \times N_r$, where N_s is the number of stations and N_r is the number of regions. So the finer the region definition becomes the more memory is needed. In order to apply the inversion tool on the model it needs to be reduced or *trimmed*.

Trimming the model

Two routines were implemented to merge voxels in appropriate areas. The first one merges voxels vertically, in case they have the same x-y-extent, lie exactly on top of one another and have the same density. This transforms voxels into rectangular columns. The second routine can be applied to areas within layers where no small-scale changes are necessary or wanted. It replaces all voxels within a defined x-y- and depth-extent by a single (big) voxel. This allows e.g. to reduce the model resolution within layers but at the same time it keeps the given resolution at the interesting layer interfaces.

Figure 4.21 shows a cross section through the Capel and Faust Basins voxel model and the result after merging voxels in the basement layer and vertically merging the remaining voxels. The trimming is applied to the original model which is only afterwards laterally enlarged. Applying the routines in that order is more reasonable and saves computation time. The model is now reduced to about 83,000 voxels. This was planned only as a first attempt but more sophisticated trimming proves to be difficult. Merged voxels need to be rectangular which makes it difficult to effectively merge voxels laterally when layer interfaces vary a lot with depth. Then it would be necessary to define lots of medium sized merge-domains. However, without a GUI or a more comfortable editing option than searching through the ASCII file, this becomes a tremendous task.
The main difficulty in this example is the overall size and dimension of the model. The initial $3\,\text{km} \times 3\,\text{km} \times 500\,\text{m}$ resolution is necessary in the upper part of the model because the distance between two layer interfaces is just 500 m in some areas. To keep the lateral resolution,

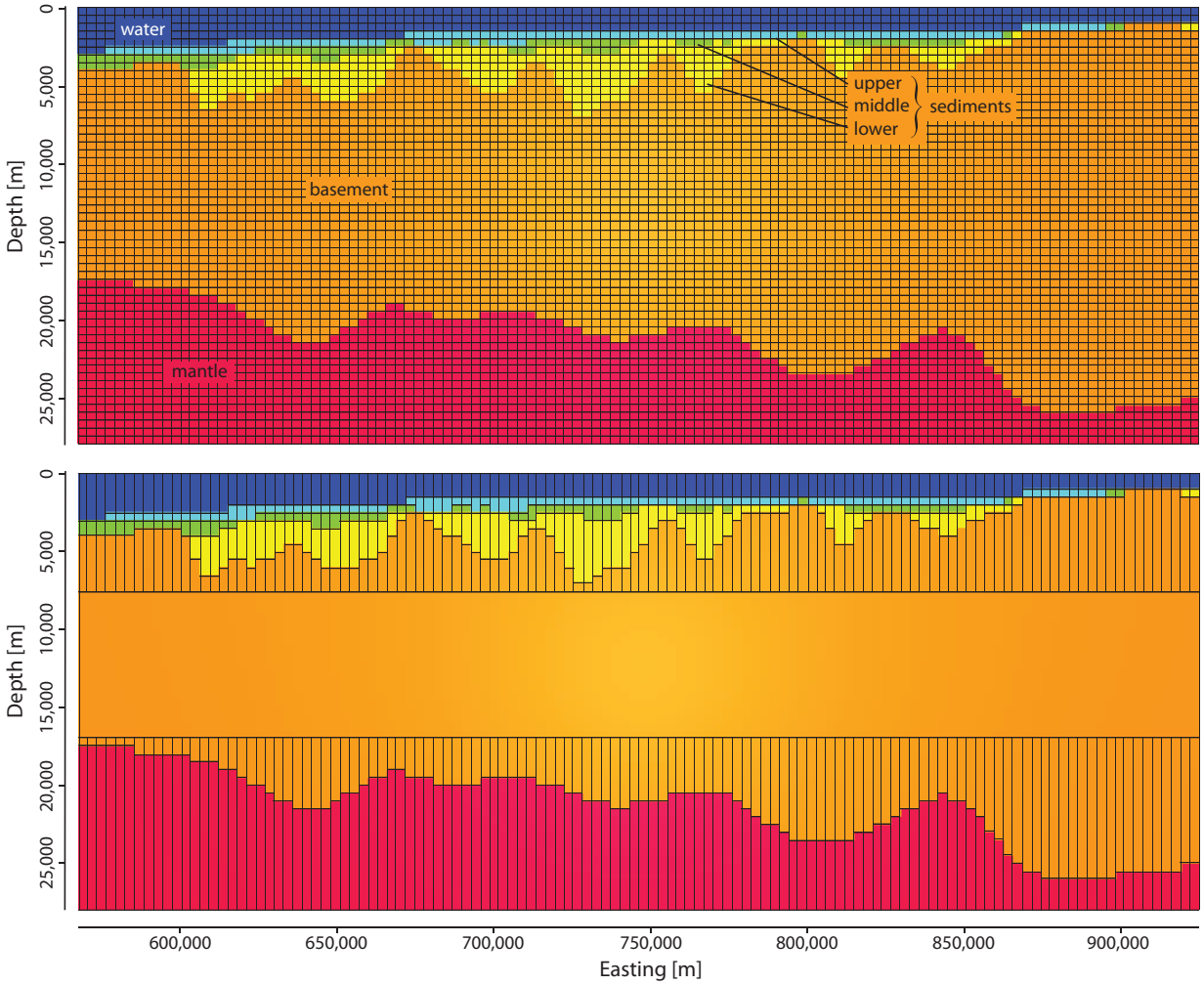

Figure 4.21.: *Voxel model of the Capel and Faust Basins. Top: Cross section through the model at y-offset 7,010,000 m. Bottom: Merged voxels within the basement layer (only one big voxel remains) and vertically merged voxels in water, sediments and mantle.*

$137 \times 120 = 16,440$ voxel are required for only one voxel layer. These are already too many voxels when a fine region definition is wanted (region = voxel; this is what allows for changes in the model). When decreasing the lateral resolution to only 5 km, $82 \times 72 = 5,904$ voxels per voxel layer remain. This is more in the order of magnitude to work with. However, only one voxel layer with fine region definition is not sufficient for a proper inversion application and the number of voxels rapidly increases again when adding more voxel layers.

In the way voxels are now merged, an inversion where regions consist of only one voxel is still not applicable. But this trimmed model now finally allows the application of the tool, although not to its full extent. The initial model has six defined regions and due to the above described difficulties this cannot be changed. The anomaly fit to the measured data is already rather good with a correlation of 96.4 % and a standard deviation of $3.21 \cdot 10^{-5}\,\mathrm{m/s^2}$.

Geology	ρ [t/m^3] Init	Estimated	*pmc* [%]
Water	2.000	(2.000)	8.2
Upper sediments	2.150	2.132	1.6
Middle sediments	2.350	2.354	3.2
Lower sediments	2.450	2.445	7.1
Basement	2.700	2.705	59.1
Mantle	3.100	3.088	20.8
Anomaly correlation [%]	96.4	96.6	
$\sigma_{residual}$ [10^{-5} m/s^2]	3.21	2.99	

Table 4.7.: *Capel and Faust Basins initial densities and result from inversion of the voxel model. Bracketed values were not subject to inversion. The bottom rows list the correlation between measured and calculated anomalies and the standard deviation ($\sigma_{residual}$).*

Inversion

The inversion aims at further improvement of the existing model. The voxel model that can be used is the one reduced to approx. 83,000 voxels and a definition of six regions that correspond to the given lithology in the GeoModeller model. The assigned densities were already mentioned in the text above. They are reduced by a background density of $\rho_{bg} = 2.67\,\mathrm{t/m^3}$ (see Section 3.2.4 for more information about background density) and then used as initial values for the inversion. Except for the water region, the inversion is run with the default variability of $5.0\,\mathrm{t/m^3}$. The water density is not subject to inversion as it was used for the Bouguer correction of the anomaly and should therefore remain unchanged.
About the accuracy of the gravity data, no information was given. Therefore, the error is set to a default of $0.5 \cdot 10^{-5}\,\mathrm{m/s^2}$. Because the voxel inversion does not invert for an anomaly shift, the measured anomaly needs to be adjusted. The shift, calculated as the mean difference between measured anomaly and model response from the initial voxel model, is $g_s = 46.82 \cdot 10^{-5}\,\mathrm{m/s^2}$.

The density result of the inversion, together with the prominence of the lithological regions, is listed in Table 4.7. The values are already adjusted for the background density and are also shown as a density profile in Figure 4.22. Overall, the change compared to the initial densities is relatively small and with it the change in the anomaly. Therefore, calculated and residual anomaly are not shown here.) On the other hand, the initial fit was already quite good. The estimated density changes in the two lower sedimentary layers and the basement are in the order of only $10^{-3}\,\mathrm{t/m^3}$. A slightly stronger density reduction is estimated for the mantle and the strongest change is experienced by the upper sediments. Here, the initial density is reduced by $0.018\,\mathrm{t/m^3}$. But this region has also the smallest prominence (1.6 %) of all model regions. The already good correlation of the anomalies is improved only by 0.2 %, now with a better standard deviation of $2.99 \cdot 10^{-5}\,\mathrm{m/s^2}$.

It would be interesting to see how the algorithm handles a subdivision of the six main geological layers (the regions). A refinement would allow for varying densities within the layers which is especially interesting for the sedimentary layers and the crust. And this would also allow for indirect "movement" of the layer interfaces. However, the voxel-based approach in its current

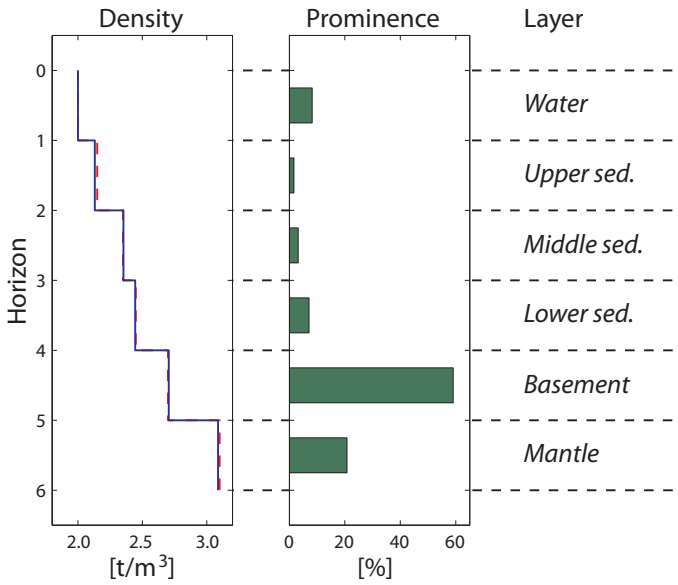

Figure 4.22.: *Capel and Faust Basins inversion results for the voxel model. Initial densities are plotted red, inversion results are plotted blue. Prominence is shown as bar diagram.*

implementation reaches here its limits, due to the necessary but not realizable reduction of the model size and trimming of the model, as described earlier on.

4.3.2. Polyhedra-based approach

The original voxel model from GA was converted and then imported into IGMAS (Schmidt, pers. comm., Figure 4.23). This model is built from 72 vertical sections, three of them are partly shown in the figure, together with the Moho and the top basement horizon. The sections are east-west oriented and have a spacing of 5 km. The six layers of the model are not further divided, therefore only six model bodies are defined. The model is extended laterally beyond the borders of the survey area, by about 265 km, in order to prevent edge effects. The Moho is relatively consistent in the voxel and the polyhedron models but the top basement shows some discrepancies between both models that have slipped in during the model transformation from voxels to polyhedra. Figure 4.24 shows again only the top basement interface and the Moho from the polyhedron model, superimposed with the voxel model. The gravity response calculated from the IGMAS model and a residual anomaly are given in Figure 4.25. The fit of the anomalies is in most areas quite good, the overall correlation is 91.8 % with a standard deviation of $4.7 \cdot 10^{-5}\,\mathrm{m/s^2}$. This is not as good as the fit of the original voxel model anomaly which was at 96.4 %. The greatest misfit occurs at the borders of the model.

For the inversion of the densities two different set-ups are used. The first application uses a shift corrected measured anomaly. The shift value is taken from IGMAS and corresponds to the mean difference between measured anomaly and calculated anomaly from the initial model. In the second application the shift is subject to and estimated by the inversion.

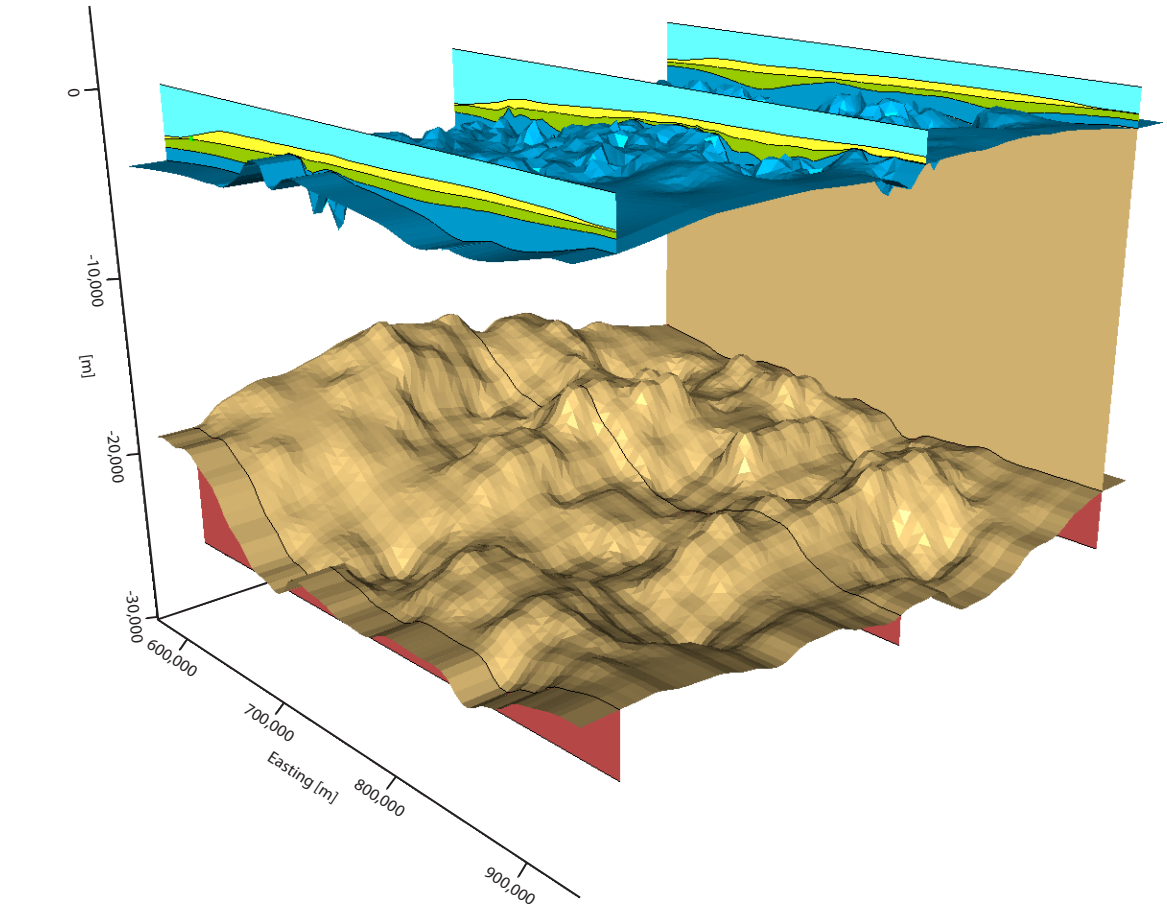

Figure 4.23.: *3D view on the provided polyhedron model of the Capel and Faust Basins (VE: 10). Only the top of basement and Moho interfaces are shown with three clipped vertical sections.*

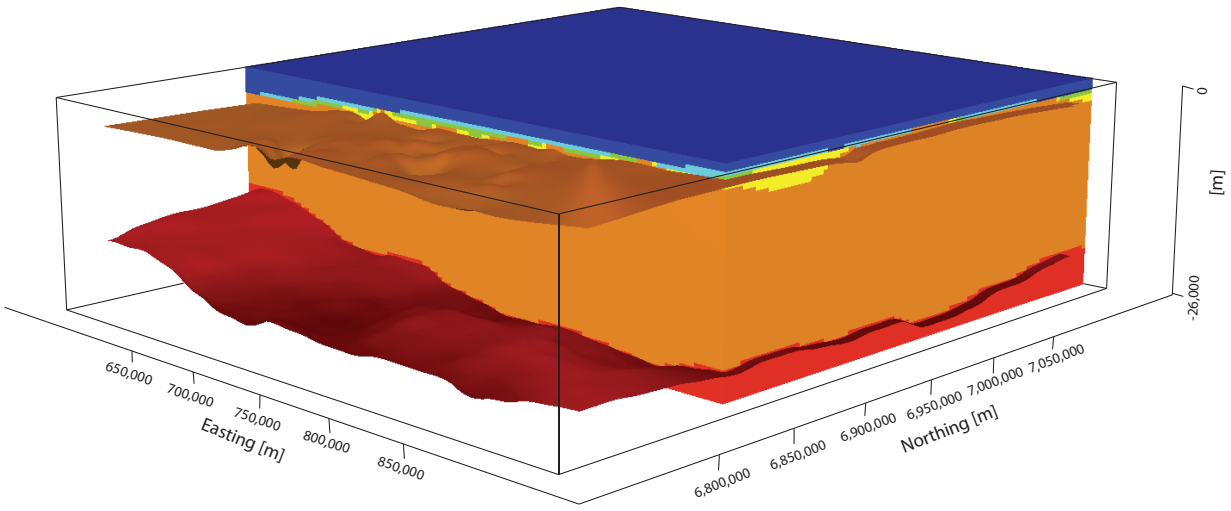

Figure 4.24.: *Capel and Faust Basins - Voxel model and polyhedron interfaces*

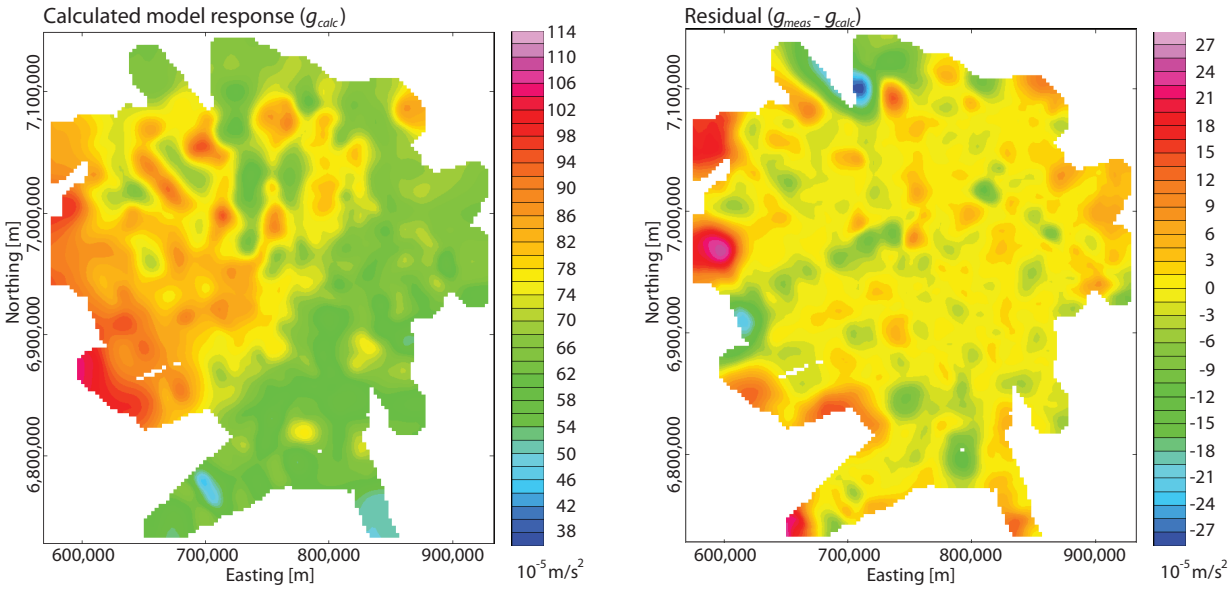

Figure 4.25.: *Bouguer gravity anomalies of the Capel and Faust Basins. Left: Gravity response of the IGMAS model. Right: Residual anomaly after subtracting the modeled from the measured anomaly.*

Inversion application 1 - Constant anomaly shift

The anomaly shift is calculated as $g_s = 46.82 \cdot 10^{-5}\,\mathrm{m/s^2}$. This value is subtracted from the measured anomaly. Same as before, the measurement error is set to the default of $0.5 \cdot 10^{-5}\,\mathrm{m/s^2}$. Also the given densities are used again as initial values for the inversion and the water body density is not inverted for.

The density results are listed in Table 4.8 and plotted in Figure 4.26, together with the prominence of the individual model bodies. The correlation of measured and calculated anomalies, together with the standard deviation, is also given in Table 4.8. Model responses and residual maps are given in Appendix A (Figures A.5-A.7).
The inversion result of *Run1* stays close to the initial density values, showing slight increases for basement and mantle densities, and decreases for sediment densities. However, a particularly strong reduction of the upper sediment density is estimated which is even below the water density from the Bouguer correction. But the densities provide an improved anomaly fit, according to correlation and standard deviation.
The following two inversion runs use constraints on the initial densities. In *Run2* the mantle density is given a high confidence and the value is fixed. Fixing the mantle density in *Run2* slightly reduces the density decrease for the upper sedimentary layer but also increases the density estimates for the remaining model bodies. The anomaly fit improvement is less compared to *Run1*.
In *Run3* the initial density of the upper sedimentary layer is fixed in order to prevent the reoccurring strong density reduction. This causes a stronger drop in density for the second sedimentary layer. Reductions for the following two layers (lower sediments and basement) are minimal, the mantle density is again increased. The anomaly fit is with 91.9 % almost the same as for the initial model, the standard deviation is a bit better.

Geology	ρ [t/m^3] Init	Run1	Run2	Run3	*pmc* [%]
Water	2.000	(2.000)	(2.000)	(2.000)	8.2
Upper sediments	2.150	1.820	1.851	(2.150)	1.6
Middle sediments	2.350	2.345	2.383	2.272	3.2
Lower sediments	2.450	2.437	2.472	2.421	7.1
Basement	2.700	2.703	2.705	2.698	59.1
Mantle	3.100	3.124	(3.100)	3.123	20.8
Anomaly correlation [%]	91.8	92.4	92.2	91.9	
$\sigma_{residual}$ [10^{-5} m/s^2]	4.71	4.45	4.59	4.57	

Table 4.8.: *Capel and Faust Basins initial densities and results from inversion application 1 (applying a shift to the measured anomaly). Bracketed densities were not subject to inversion. The bottom rows show the correlation between measured and calculated anomalies and the standard deviation ($\sigma_{residual}$). Prominence of model bodies (in %) is also given.*

With the different constraints on densities these three runs slightly improve the anomaly fit but the changes are not significant. All inversion results show reduced densities for the sedimentary layers and increased values for basement and mantle. The upper sedimentary layer experiences the strongest changes in density but it is also the least prominent compared to the other model bodies. The basement however is most prominent and its initial density is barely changed by the inversion. A second application will follow, investigating if the inversion for the anomaly shift has influence on the estimates.

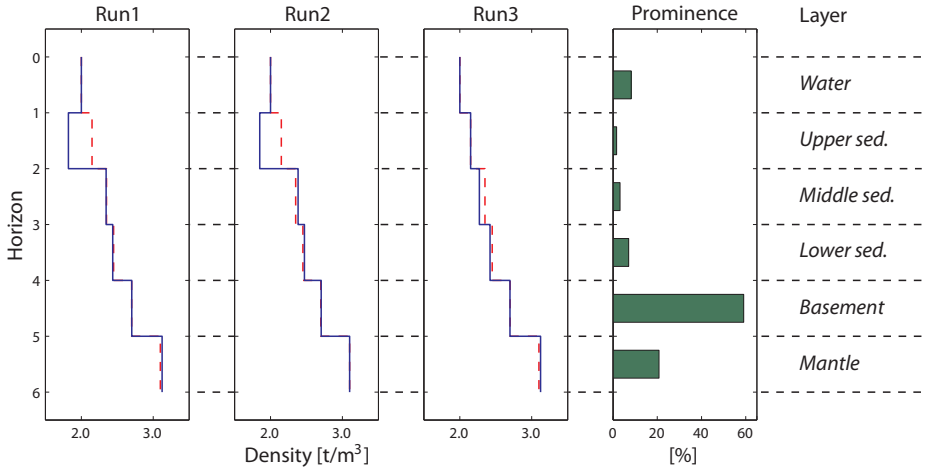

Figure 4.26.: *Capel and Faust Basins inversion results from application 1 plotted as density profiles and prominence of the individual layers (regions). Initial densities are plotted dotted red, inversion results are plotted blue. Prominence is shown as bar diagram.*

Inversion application 2 - Inverting for anomaly shift

The second application uses the same inversion parameters as the previous (measurement error, density variability) but in addition also the anomaly shift is subject to inversion, i.e. the shift

	ρ [t/m^3]				
Geology	Init	Run1	Run2	Run3	*pmc* [%]
Water	2.000	(2.000)	(2.000)	(2.000)	4.9
Upper sediments	2.150	1.803	1.814	(2.150)	1.0
Middle sediments	2.350	2.282	2.324	2.243	1.9
Lower sediments	2.450	2.383	2.419	2.398	4.2
Basement	2.700	2.643	2.684	2.673	35.1
Mantle	3.100	3.047	(3.100)	3.090	12.4
Shift density	0.000	0.101	0.062	0.068	40.6
Shift [10^{-5} m/s^2]	0.0	109.27	66.77	73.31	
Anomaly correlation [%]	91.8	92.4	92.4	91.9	
$\sigma_{residual}$ [10^{-5} m/s^2]	4.71	4.43	4.44	4.57	

Table 4.9.: *Capel and Faust Basins initial densities and results from inversion application 2 (inverting for the shift). Bracketed densities were not subject to inversion.*

density (see Section 3.2.5 for explanation). Again, three runs were performed, using the same constraints on densities as in application 1. The results are given in Table 4.9 and Figure 4.27. In addition to anomaly correlation, standard deviation, and model body prominence, this table also contains the estimated shift densities and the resulting anomaly shift values. Anomaly and residual maps are found in the Appendix again (Figures A.8-A.10).
For all runs the estimated anomaly shift is larger than in application 1 (where it was $46.82 \cdot 10^{-5}$ m/s^2). In *Run1* the estimated anomaly shift is the highest of the three runs. This causes in turn reduced densities for all model bodies. As in application 1, the upper sedimentary layer experiences the strongest density reduction. Fixing the mantle density (*Run2*) in application 1 caused an increase in all remaining model densities in application 1. Here, this increase is transferred to the anomaly shift, estimating a reduction of all model densities instead. The same applies for *Run3* where water and upper sediment densities are fixed.

This second application provided better anomaly fits than the first, where a constant anomaly shift was applied for all runs. The correlation values are better and the standard deviations are smaller. It is therefore advised to include the shift in the inversion rather than applying a shift correction prior to inversion. Especially in cases where the initial model does not produce such a good anomaly fit as in this example. In other software (e.g. Geosoft's Oasis montaj or IGMAS) a new shift is calculated every time the model has been changed. By inverting for the shift this becomes redundant as it is part of the model update.
In this example, the initial model already provides a good anomaly fit, therefore the overall improvement is rather small. Common in all results is the reduced density for the upper sedimentary layer. In Hackney et al. (2009) a density of 1.95 t/m^3 for the post-rift sediments is specified so a reduction for this layer seems to be in agreement with the geology, although maybe not down to 1.8 t/m^3.
In the western part of the model differences between the anomalies are largest. This misfit is slightly reduced by the inversion estimates. An option would be refined modeling in this region and carrying on with the inversion for a more detailed model. The large homogeneous model bodies could be divided vertically to allow for the estimation of lateral density variations. Hack-

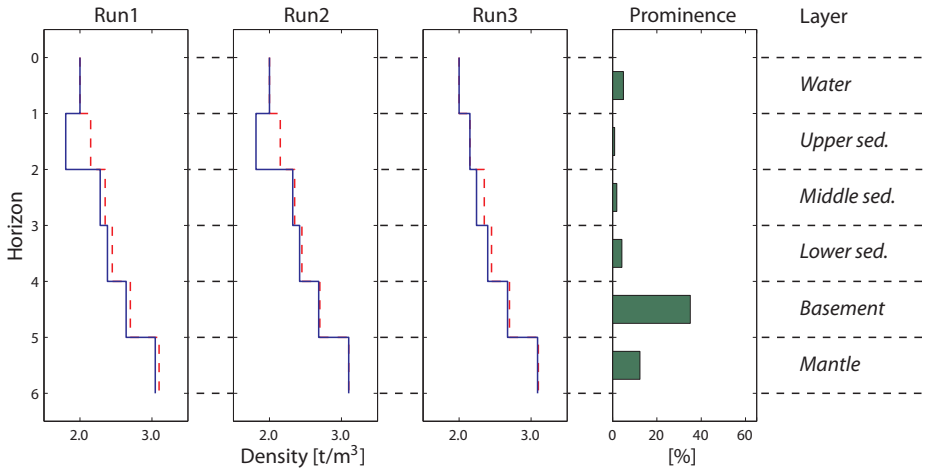

Figure 4.27.: *Capel and Faust Basins inversion results from application 2 (shift inversion). Initial densities are plotted red, inversion results are plotted blue. Notice that the density and prominence of the Bouguer slab, which is with 40.6 % the most prominent body in this model, is not plotted.*

ney et al. (2009) mentioned the presence of high-density magmatic rocks within the sedimentary layers in western part of the area. They could be accounted for by defining new model bodies. As the densities are derived from refraction data and stacking velocities and horizons are based on reflection data interpretation, it might also be a solution to have a cross check with these data. The polyhedron model density inversion alone does not offer much more options here. A few more density constraints could be tested but with the tests so far it seems that also the model geometry would require some changes. Further modeling would be done in the forward modeling approach and this test application leaves the case study here.

4.4. Discussion

In this chapter the extended inversion tool CHAIN has been applied to four different models of varying complexity and built of voxels and/or polyhedral bodies. The applications show that the tool is working properly and that the linear inversion can be used to improve and refine existing models with constrained geometries. In case of voxel models, it is recommended to have a certain prior knowledge of the subsurface structures in order to constrain and guide the estimations. This is necessary because voxel models usually consist of a large number of voxels and without constraints an enormous amount of possible model solutions is possible. Additional information is required to utilize the definition of regions and groups of related regions which allows a structural refinement of the model and also enables the correlation of the estimated properties.
For polyhedron models the tool proves useful especially when structural geometries are transferred from other methods like, e.g. seismics. In that case, the physical properties are often also derived from that method, within a certain range of values, and the inversion helps to adjust and to guide further modeling. Even without initial property values the inversion works remarkably well and fills a structurally gained model with reasonable property values, as seen for the synthetic tests with the NGB case studies. The tool allows a fast first verification of seismically derived models without doing the lengthy forward modeling.

The combination of several data sets is especially useful if measurements are noisy or of poor quality. In this case, the joint inversion provides better estimates than the single inversions. The tests with the Bramsche Anomaly model (Section 4.2.1) showed that when combining data sets of varying quality, the joint result is equally good as, or even better than the single inversion with the best quality data. Meaning that poor data does not profoundly corrupt the result.
The shift between measured and calculated anomaly should either be chosen with great care, e.g. conform with the confidence in the initial model. If it is difficult to decide on a value beforehand, it is useful to integrate the shift in the inversion as it has a noticeable effect on the results. The tests that also inverted for the shift showed a better anomaly fit than those with a fixed shift.
For the evaluation of the inversion results in terms of reliability it is helpful to consider the model body prominences that are related to the potential fields (i.e. the anomaly sensitivity). But this consideration is only appropriate for models with a manageable amount of model bodies/voxels. With larger models it might still be helpful to check the prominence of a few, selected bodies or regions of voxels. Under certain model conditions or when a priori and constraining information is not sufficient, some challenges exist:

Case 1 (with polyhedra-based application): When the model consists only of a few but large model bodies, density inversion might not really provide new insights: Either the model was already quite well defined and only small property changes are estimated (Capel and Faust Basins example, Section 4.3.2) or the defined geometry does not fit and the property estimation leads to unreasonable values (e.g. Bramsche, Section 4.2.1). As no fitting can be gained by density changes it becomes necessary to change model geometry.

Case 2 (with voxel-based application): The application of the inversion tool is problematic, when dealing with large models that consist of a great number of voxels (e.g. Capel and Faust Basins, Section 4.3.1). Because of their configuration they are too cumbersome to handle and edit (e.g. model refinement, region definition). An automated reduction-of-resolution algorithm would help. Such an algorithm could strategically assess the model and merge voxels within layers, leaving a high-resolution-buffer near the layer interfaces. Because of the inadequate editing options, the required definitions of regions and groups of correlated regions, that are the main features of the inversion tool for voxel models, are not applicable. The tool does not allow for a proper application that takes advantage of all the options it actually has to offer. The actual idea of the voxel-based approach cannot be realized. Other options are to move on to more powerful computation facilities (but that would only delay the problem), to improve the implementation itself and make it more efficient and use more advanced matrix computation algorithms.

Case 1 asks for geometry changes which are necessary to fit the potential fields. This is normally addressed by forward modeling or by inverting for the depths of single interfaces, layer thicknesses or volumes of predefined geometries. With a polyhedron geometry this means actual modifications of the geometry and several model bodies at the same time in an automated manner. Case 2 could be tackled by improved implementations and the development of a user interface which would simplify model handling and editing. Also the incorporation of constraints and an advanced, maybe partly automated breakdown of the voxel model into regions and groups would be helpful. In the following, investigations in a tool for automated model geometry modifications are carried out. Geometry changes can be applied exclusively or in addition to model property estimations. The development, application and test of this tool is described in the following chapters.

5. Model geometry optimization

The last case study of the previous chapter showed that, using polyhedra-based model geometries, changing only physical properties of model bodies is sometimes not sufficient to fit modeled to measured data. In addition it might be necessary to also change model body geometries. In the context of inverse modeling this means automated model geometry changes. This task will be approached in the following, starting with a short overview over the basic requirements for solving an optimization problem. Several ideas on model parametrizations suitable for 2D and 3D applications are given. In the course of this thesis, one of these ideas has been implemented and tested in 2D and is therefore discussed in detail. The optimization method used here is a Particle Swarm Optimization (PSO). Implemented is a combination of variations of the most basic PSO that will be explained.

5.1. Optimization

This introductory chapter gives an overview over the basic concept of optimization and some well-established methods in stochastic optimization. The topics of model parametrization and the here implemented optimization method are then following in more detail.

5.1.1. The main components

Optimization problems are usually minimization or maximization problems. Their main components are (1) an **objective function** f, (2) a **set of unknowns** $\boldsymbol{x}$, and (3) a **set of constraints**. The goal of an optimization algorithm is then to *"assign values, from the allowed domain, to the unknowns such that the objective function is optimized and all constraints are satisfied"* (Engelbrecht, 2005). Hence, $f(\boldsymbol{x})$ quantifies the quality of a solution $\boldsymbol{x}$. During the iterative search process for values for the unknowns, the quality of the solution is improved until it reaches an optimum. The search is performed by modifying the values for the unknowns within each iteration step. How this modification is done depends on the applied optimization method.

Objective function f

The objective function represents the quantity that is subject to optimization. The goal in potential field modeling is to build a subsurface model that causes a potential field which is similar to the measured anomaly. The quantity to be optimized in this case is the difference between calculated (y_{calc}) and measured data (y_{meas}), i.e. the misfit $e_i = y_{meas,i} - y_{calc,i}$ with $i = 1 \dots n_d$ data points. The misfit is a distance and measures of distance are expressed as norms. A common norm is the L_n-norm (e.g. Menke, 1989):

$$\|\boldsymbol{e}\|_n = \left(\sum_i |e_i|^n \right)^{1/n}$$

where an increasing order of n denotes an increased weight on larger elements e_i. It therefore determines the treatment of outliers in the data. Very popular is the L_2-norm which is the Euclidean distance between two data points. It has often been used in geophysical applications (Sen and Stoffa, 2013) and is suitable when the misfits are normal distributed. Here, the L_2-norm is also used as objective function, with the modification that the sum is divided by the number of data points. This expression is also known as the root mean square error:

$$f = \left(\frac{1}{n_d} \sum_{i=1}^{n_d} (y_{meas,i} - y_{calc,i})^2 \right)^{1/2}$$

The following implementation of the optimization algorithm is for 2D models. The forward calculation of the gravitational model response (y_{calc}) is using the algorithm from Won and Bevis (1987) which is based on the formulation by Talwani et al. (1959) with modifications suggested by Grant and West (1965). The measured anomaly (y_{meas}) needs to be shift corrected before evaluating the objective function. The issue of the shift (g_s) was already discussed in connection with the linear inversion (Section 3.2.5). Here it is either defined by the user or calculated by the program as the mean difference between measured and calculated anomaly of the initial model. Including the shift in the optimization process is not intended.

Set of unknowns $\boldsymbol{x}$

In general, the set of unknowns describes the system that will be optimized. In the case of potential field modeling the unknowns are the model parameters that define the geometry. These could, for instance, be depths to a certain interface, layer thicknesses or polyhedron shapes. How exactly the model geometry is parametrized will be described in detail in the following chapter. In addition to the model geometry, also the physical properties of the model can be added to the optimization process. This option increases the number of unknowns not insignificantly but, what is more important, it will also increase the diversity of the solution. Physical properties are usually derived from a priori or additional information and have a certain level of confidence. The optimization developed here is configured to perform the optimization of model geometry *and* densities, taking into account the confidence in the individual initial densities. Assuming high confidence, it is also possible to run a geometry-only optimization.

Set of constraints

The definition of constraints is an instrument to control the solution of an optimization. The search space for parameters can e.g. be limited or solutions for sets of unknowns can be excluded. In the present case, the unknowns are only restricted by boundary constraints that define the domain of allowed values. All parameters are scaled and the common constraint for them restricts the search space to $I = [0, 1]$. These restrictions do not constitute a constrained optimization. This is an additional option that will be addressed later in this chapter (Section 5.5).

5.1.2. Major stochastic optimization methods

The non-uniqueness in potential field modeling and the diversity of possible solutions results in an objective function that shows a multiplicity of minima. Many of them are equal with regard to

fitness and the existence of one global minimum is mathematically not necessarily given. This results in a topographically complex objective function and the optimization problem is then called multimodal. These kind of problems ask for stochastic search algorithms that introduce some randomness in the search process. The random component in the parameter update allows the methods to escape a local optimum. Established stochastic optimization methods are, e.g., Simulated Annealing (Metropolis et al., 1953; Kirkpatrick and Vecchi, 1983) and evolutionary methods such as genetic algorithms (Holland, 1992; Goldberg, 1989), evolution strategy (Rechenberg, 1994; Hansen and Ostermeier, 2001) and swarm intelligence optimization (Eberhart and Kennedy, 1995; Karaboga and Basturk, 2007).

Simulated Annealing (SA)

The basic concepts of this search method are based on problems in statistical mechanics. These involve the analysis of the movement of atoms in samples of liquids and solids. Before a physical annealing process occurs, a sample needs to be in liquid phase, where all particles are distributed randomly. Then the sample is slowly cooled down in way that in the end, the particles arrange themselves in the ground state of low energy where crystallization occurs. Transferred to optimization problems this means the simulation of the physical system during cooling and finding the state of minimum energy. The energy state represents the objective function, particles are represented by the model parameters and a state refers to a certain particle configuration, i.e. a model. In the beginning of the process, the entire parameter space is equally searched but local search becomes intensified at higher iterations (progressed cooling). During the slow cooling process, the material is allowed to reach thermal equilibrium at each temperature. The probability of being in a certain state with a specific energy is given by the Boltzmann probability density distribution. After thermal equilibrium has been reached the temperature of the system is further reduced until in the end, the minimum energy state becomes overwhelmingly probable. If the cooling process is too fast, the system might freeze at a local minimum, which makes the requirement of thermal equilibrium the key to this approach. The annealing process causes the material to freeze into an energy state that is at or very close to the global minimum.
The most important, and most difficult, parts of this method are the choice of the starting temperature, as this is responsible for the initial global search, and the definition of a cooling schedule. If the latter is defined badly, the intensification of the local search becomes too strong too early and the system is most likely to freeze in a local minimum. The cooling schedule is a computationally demanding task and a number of SA variations were developed to make the algorithm more efficient (see e.g. Sen and Stoffa, 2013).

Genetic Algorithms (GA)

These algorithms belong to the group of Evolutionary Algorithms (EA) which are stochastic, population-based search algorithms. EAs are based on the analogies with the process of biologic evolution, where a set of model parameters (one possible solution of the optimization problem) is represented as an individual within a population. The EA seek to improve the fitness of the populations from generation to generation.
In GA (Holland, 1992) the main idea is to adopt the genetic process of coding, selection, crossover and mutation. Model parameters are coded using a binary code scheme where each bit corresponds to a gene. Each model in the population is then completely described by its bit string or

chromosome. The genetic information defines, after decoding, forward calculation and evaluation, the fitness of a model. And here, the evolutionary principle of the survival of the fittest is adapted as the algorithm is in favor of those models that produce the best fit. This is the process of selection. Its exact criterion depends on the problem dependent implementation but once selected, individuals are grouped in pairs for reproduction or recombination. This is achieved by crossover of the chromosomes, where the genetic information between the paired models is shared. As a final step, mutation is applied, which is the random alteration of a bit. Mutation can be carried out during crossover. Both crossover and mutation are controlled by user defined probabilities that influence the number of random walks in the search space and therewith convergence of the method. An overview over geophysical applications of GA is found e.g. in Sen and Stoffa (2013) and for reviews on GA see e.g. Goldberg (1989) and Davis and Principe (1991). One fundamental difficulty of the method is the crossover operation which might cause premature convergence as with advanced evolution of the population it is defined by coding that no longer generate new chromosomes. Even with mutation, which allows for diversity, this issue remains as the mutation rate is usually so low that no real improvement is gained in the final generations, even before finding an optimal solution (Sen and Stoffa, 2013).

Evolution Strategy (ES)

Another optimization approach that operates analogue to biologic evolution, but avoids the problem of limited coding sets for crossover, is ES (Rechenberg, 1994). It had also been used for the optimization of potential field models in the past, (e.g. Alvers, 1998; Snopek, 2005). The fundamental principles are natural selection, survival of the fittest, and reproduction but compared to GA, it has no coding and differs in the selection and mutation procedures. The general work flow of an evolutionary algorithm consists of the following steps: Creation of the initial population, selection of parents and then recombination to create offspring. The offspring experiences mutation and after evaluating the fitness, a new parent generation is selected.
One major distinction between different variants of ES lies in the selection procedure. A summary of those procedures is e.g. given in Engelbrecht (2005). One very popular selection procedure is the $(\mu, \lambda), (\mu + \lambda)$-selection, where μ is the number of parents and λ is the number of offspring. In the *comma*-selection, with $\lambda > \mu$, the new generation of parents is selected only from the offspring. In the *plus*-selection the new parent generation is selected from both, offspring and parents. In both cases, the selection is based on the fitness of the individuals. The latter case allows for an individual with good fitness to remain in the evolutionary process without mutation. In other words, a promising location found in the search space is kept and taken into the next iteration.
Mutation is the main component of evolution. This is where the actual development of a species takes place and where the individual adapts to its environment. In terms of evolutionary algorithms this means the development of the individual (model solution) towards an optimal model solution within the search space. The realization of a so-called mutation distribution is added to the individual. The success of the evolutionary search algorithm depends on this distribution and the defined step size. In the basic case, this distribution is a normally distributed random vector. The mutation distribution is controlled by strategy parameters. Hansen and Ostermeier (2001) suggested and tested a self-adaption of the mutation distribution which dynamically adapts strategy parameters during the search process. This covariance matrix adaption evolution strategy (CMA-ES) modifies the mutation distribution and increases the probability that a previously successful mutation step is repeated.
The CMA-ES is an effective local search algorithm which, under certain conditions, also acts as a

global searcher. The latter requires a sufficiently large number of function evaluations. Because the area occupied by the population is comparatively small and the reachable horizon beyond this area is limited by the step size. And only with enough computations the probability is given that the step size adaption allows for further exploration (Hansen and Ostermeier, 2001).

Particle Swarm Optimization (PSO)

The method of PSO (Eberhart and Kennedy, 1995) also copies natural phenomena as it implements the concept of swarm intelligence. It therein adopts the behavior of social animals, e.g. a school of fish or a flock of birds, on their search for a rich feeding ground. These animals live in groups without leaders and they are able to perform complex searches although the individual is rather simple and has no complex knowledge of its environment. When speaking of swarm intelligence the members of a group (or swarm or population) are referred to as individuals or particles, their living environment is the search space. These particles are not to be confused with the particles from SA, where each particle is a model parameter. Here a particle is a vector containing all model parameters of one possible solution. The dimension of the search space is defined by the number of parameters that are optimized. Finding the location of an optimal hunting ground is e.g. a three-dimensional optimization problem. Fundamental for a successful search is the social interaction and exchange of knowledge about the search space each individual has visited. With this exchange individuals are influencing each other. The group has no leader and the knowledge of each individual is equally regarded without any weighting. Another characteristic of PSO is the use of memory. Individuals remember the best position they have obtained so far during the search as well as their previous movement direction.
A number of variations of the basic PSO exist. They are described and examined, e.g., in Van den Bergh (2001), Engelbrecht (2005), Wilken (2009). Their development was motivated by the demand for enhanced convergence of the optimization and improved diversity of the swarm. The optimization implemented here uses a combination of the basic variants, being a charged global best PSO with restart option, as identified to be a very effective tool in multi-parameter and multimodal problems (Wilken and Rabbel, 2012). The numerical description of the PSO and its variations is given a bit later in this chapter. First, the parametrization will be addressed. As will be seen, the implemented parametrization of the optimization problem constitutes a global search problem. Even if the initial model is close to a potential optimal model, the search for the model parameters remains global, which is why the PSO is chosen.

5.2. Parametrization

The here presented method (parametrization and optimization) is designed for vertex-based geometries. In general this means polygons in 2D and triangulated polyhedral bodies or triangulated surfaces in 3D. Model geometry changes are achieved by relocating these vertices. Hence, the parametrization for the optimization problem is fairly simple, on first sight: The positions, i.e. Cartesian coordinates, of vertices. However, the simplest parametrization is not always the best or most applicable, as will be discussed in the following.
Three possible variants of how to find new vertex positions will be described, together with their applicability in an optimization: (1) Direct movement of vertex positions, (2) Spatial distortion and (3) Spatial operator. Unfortunately, all of these parametrizations share one major restriction: The number of model bodies is fixed during geometry optimization, i.e. all model bodies that

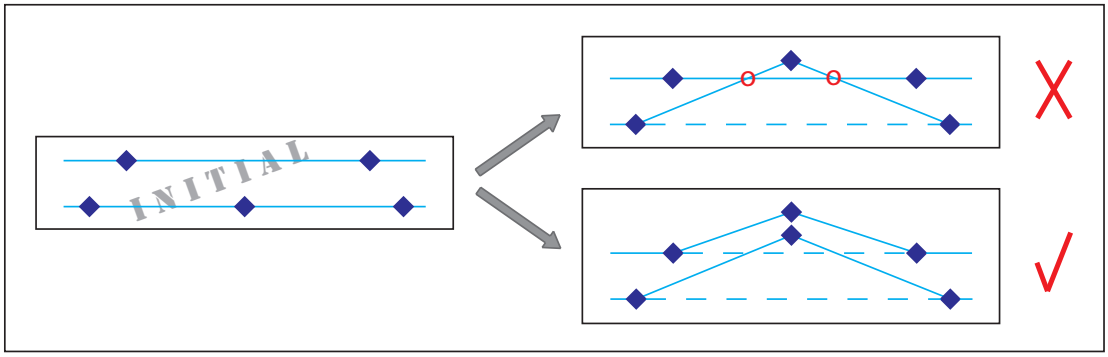

Figure 5.1.: *Changing positions of model vertices can result in crossed polygon lines (top right). This can be prevented if a fine model discretization is used (bottom right).*

might be required must already be present in the initial model. It is not possible to automatically create or insert new model bodies in a given geometry. Likewise it is also not possible to terminate existing model bodies. The latter is not due to the automated process but a general difficulty with polyhedra-based geometries. What comes closest to a model body termination would be to make the polyhedron as small or thin as possible in order to reduce its potential field effect to a negligible value.
When performing automated geometry modifications a major requirement must be satisfied: The topology of the model geometry must be preserved during changes. Changing positions of model vertices can result in crossing polygon lines or punctured planes as schematically illustrated in Figure 5.1. It is essential to avoid these violations. Also relevant is the number of parameters involved in the geometry changes (i.e. in the optimization process) which should be kept in a reasonable range .

5.2.1. Variant 1: Direct movement of vertex positions

In this approach, new vertex positions are found by adding a modification values to the actual coordinates of all vertices. The estimation of this modification value depends on the optimization method that is used. The geometry is changed, the model response calculated and the objective function is evaluated. If the objective function is favorable, the new geometry is adapted and modified again in the next iteration. In this method, a great number of parameters needs to be optimized, i.e. the coordinates of all vertex position which is 3× number of vertices. The essential topology preservation of the model geometry (Figure 5.1) can only be gained by adding constraints. For example, the relocation of vertices could be limited to the boundaries of boxes (used for a 2D case by Alvers, 1998) or ellipsoids that are placed around the vertices (Figure 5.2). Those constraints need to be defined for all vertices which complicates their actual definition. A way to define less many constraints would be, if not all vertices are moved within an iteration. However, such restrictions constitute distinctive reduction of search space. When applying global optimization methods such restrictions are not permitted. These two drawbacks lead to the disqualification of this parametrization.

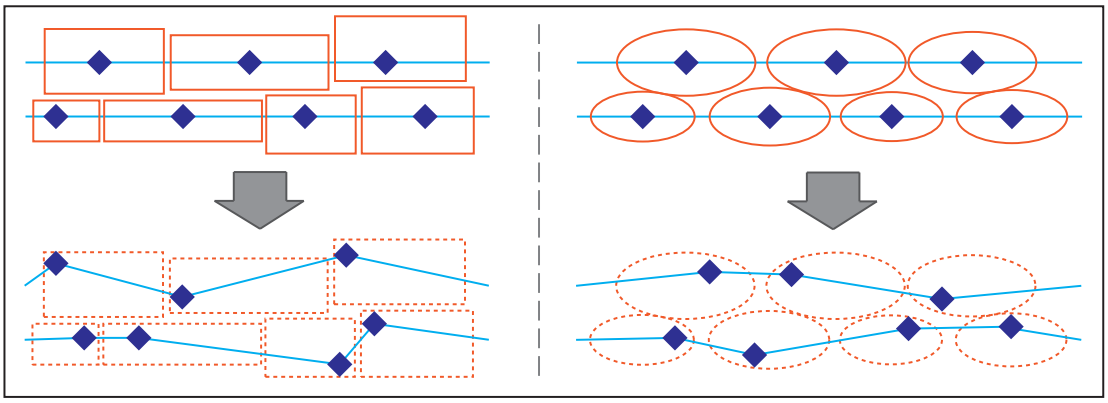

Figure 5.2.: *2D vertex movement restricted by rectangles/boxes (left) or ellipses/ellipsoids (right).*

5.2.2. Variant 2: Spatial distortion

A parametrization suggested by Alvers (1998) follows methods of rectifying images via tie points (e.g. Lillesand and Kiefer, 1994). The model space is overlain by a regular grid and each model vertex has a distinctive position within a grid cell (see Figure 5.3). Then the grid will be distorted by varying the edge lengths of the grid cells, allowing the model geometry to be deformed as well. The new positions of the model vertices are gained by linear interpolation within the grid cells (Figure 5.3b) and c)). If the edge lengths of the grid cells are not allowed to become < 0, the grid cannot cut itself and the topology of the model is preserved. Subject to optimization are no longer the vertex positions but the edge lengths of the grid cells.
But this approach has also a few issues that make it unsuitable as parametrization for the optimization tool but also in general. One point is that the degree of model deformation is controlled by the discretization of the model itself but also by the cell size of the overlying grid. This issue is inconvenient as the degree of possible optimization relies on the initial guess of the interpreter. Alvers (1998) suggested to overlay the model with a finer or coarser grid, depending on the aimed precision. Another option would be to triangulate the polygons/surfaces of polyhedra and to optimize the triangle edge lengths instead of using an additional grid. This variant would also save the calculation time of the interpolations because the vertices are moved directly. However, changing grid cell or triangle edge lengths causes numerous dependencies in the parameters to be optimized. For example, it is not possible to change edge lengths independently, because changing one edge always influences the lengths of the edges in the direct neighborhood and might even drag the entire grid. For the same reason it is not possible to optimize all edge lengths by the search algorithm, as some are forcibly caused by others. This means that this approach is also not suitable as a parametrization.

5.2.3. Variant 3: Spatial operator

Another approach for model parametrization, which does not run into the above mentioned problems, are spatial operators that are applied to the model. Within each iteration of the optimization, several of these operators are swept through the model on straight lines, dragging vertices along their paths and consequently changing the geometry. In Figure 5.4 three operators of different size travel through a layered model geometry. Each model vertex that crosses the way of the operator is moved in the direction of the operator path. The amount of movement is given by

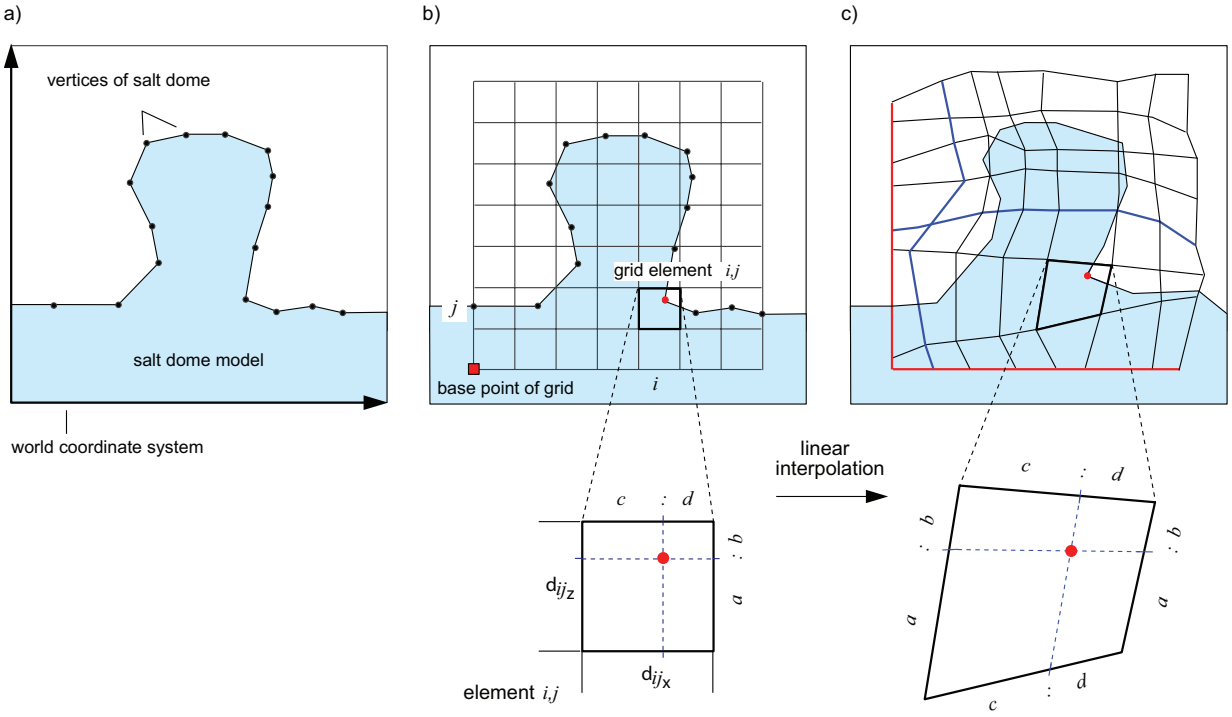

Figure 5.3.: *The model (a) is overlain by a regular gird (b). Each vertex is assigned to a distinctive grid element i, j. (c) Mutation of the grid spacing d_{ij_x} and d_{ij_z} causes a distortion of the grid. Vertices of the model can be interpolated linearly according to the new dimensions of the respective grid element (modified after Alvers, 1998).*

the operator definition. Depending on where within the operator the vertex is located its amount of movement is defined by a bell-shaped distribution. Figure 5.5 illustrates the concept. The distribution chosen here is a Gaussian distribution. Vertices close to the center of the operator experience the largest movement which decreases towards the border of the operator. This allows modifications in a way that the topology is preserved, because whenever a warped polygon line under the influence of the operator approaches another polygon line, the vertices of this line are also influenced and moved by the operator. Also this approach transfers the optimization of the vertex positions to the optimization of the operator parameters. The reduction of parameters is fundamental. A fine model discretization is necessary for this operator to work properly. Therefore, an adaptive model discretization along the operator paths is reasonable. The operator is called Gaussian Warp Operator, in accordance to the kind of modifications it causes to a model geometry. As this parametrization seems capable of fulfilling the requirements, it is chosen for the inversion toolkit. The operator and its implementation will be described in more detail in the following section.

5.3. Implementation of spatial operator

The Gaussian Warp Operator (GWO) is suitable for 2D and 3D geometry modifications, for vertex-based geometries in general. In 2D the operator is a circle, in 3D it becomes a sphere. However, before developing and implementing the novel algorithm in 3D, it is reasonable to test in two dimensions if the approach is promising at all. Also, the visualization of arbitrarily shaped

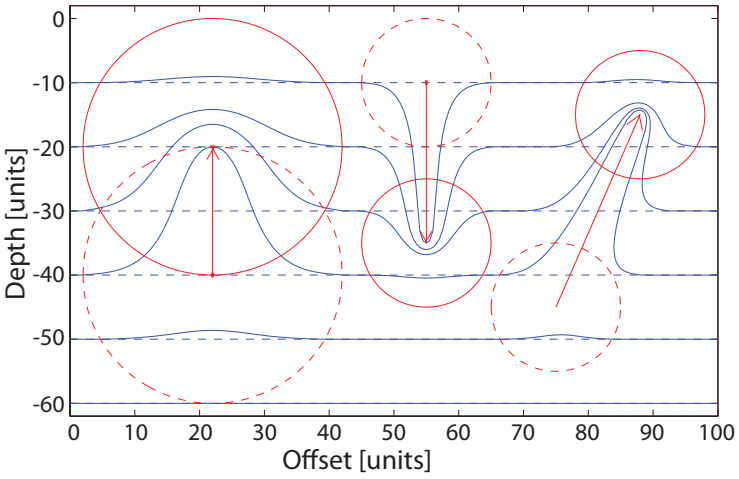

Figure 5.4.: *Principle of the Gaussian Warp Operator. Different operator sizes cause geometry modifications of different wavelengths. Dotted circles show the origin and solid circles the final positions of the operators.*

3D model bodies is complex and a tool for that was not available. And although model geometries are 3D within the modeling software, their modification in the forward approach is usually done on 2D sections, as e.g. in IGMAS+ (described in Chapter 2.2.2). Hence, as a first step towards 3D application, the 2D parametrization can also be applied simultaneously on all model cross sections, resulting in a 3D optimization of the entire model. Therefore, the following descriptions and also the current implementation are in 2D. The aspects for 3D application and necessary modifications to the present implementation are summarized at the end of the chapter.
However, the following 2D implementation could be used together with the IGMAS+ software and perform 3D model modifications. As described earlier, the models in IGMAS+ are defined on 2D vertical sections. 3D model bodies are created by triangulation between the sections. It would not be possible to move vertices out of a 2D section in y-direction (although development is heading that way). At the moment the application of 2D operators on several neighboring sections at the same time and the usage of the 3D model response for the evaluation of the objective function would present a 3D application.

The 2D GWO is a circular operator that is defined by 5 independent *operator parameters*: the **starting point** of the operator defined by coordinates x_s and z_s, the **radius** r of the circular area and the **movement path** described by its length l and directional angle θ.

All parameters of the initial parametrization (0. iteration) are found using random numbers. Some boundary conditions on the operator parameters however are inevitable. They only confine the parameters to their allowed range but they have no influence on the optimization process itself. The starting point of an operator is restricted to lie within the actual modeling area of the model. Furthermore, the operator is not allowed to move out of the modeling area. If a boundary condition is violated the causative parameter(s) will be replaced by random values within the permitted range. The operator itself also needs some adjustments. The so-called *strategy parameters* depend on the nature of the model and the geometry modifications that are desired or expected to reduce the anomaly misfit. Strategy parameters are the maximal path length, the minimal and maximal radius of the operators and the number of operators to be used.

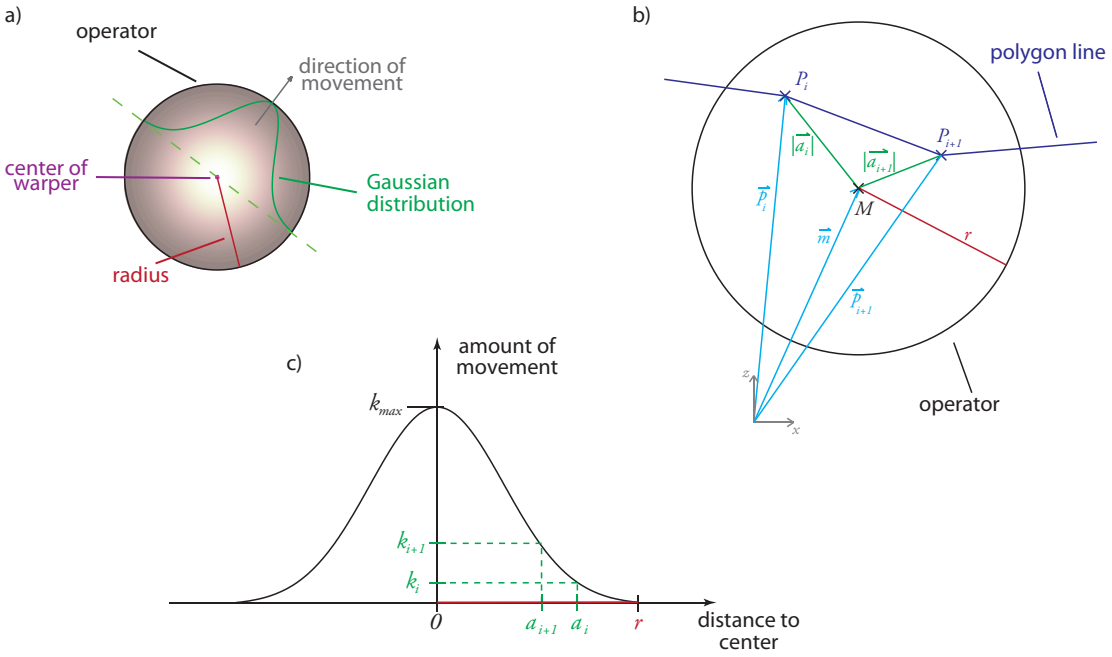

Figure 5.5.: *Schematic illustration of a Gaussian Warp Operator. a) The operator with its main components and terminology. The shading indicates the amount of movement from small (dark color) to large (light color). b) Geometry and parameters used in the text. c) How to calculate the amount of movement (k) for the polygon vertices P_i and P_{i+1} that are distances a_i and a_{i+1} away from the center of the GWO.*

Short path lengths and small radii should be used when fine and local geometric changes are expected. To gain large scale modifications of a model, longer paths and larger radii are recommended. For a demonstration of the functionality of the GWO see Figure 5.6. It shows two examples of deformed geometry where 3 operators were applied. The number of GWOs is model-dependent and for a successful application several preliminary inversion runs are required to find the suitable number of GWO for the current modeling problem.

Vertex movement

A chosen number of operators sweeps through the model geometry step-by-step. The step size s of the operators is related to the model discretization ($s = d_{max}/4$), where d_{max} is the maximal allowed distance between neighboring vertices of a polygon. All vertices that are caught by an operator are moved. Their amount of movement (k) depends on their distance to the center of the GWO and is calculated from a Gaussian distribution which is defined within the operator (Figure 5.5).
The density function of a Gaussian distribution reads

$$k(a) = \frac{1}{\sigma\sqrt{2\pi}} \cdot \exp\left(-\frac{1}{2}\left(\frac{a-\mu}{\sigma}\right)^2\right)$$

where a is the distance from the center point M of the operator to the vertex P of a polygon line: $a = |\boldsymbol{a}| = |\boldsymbol{m} - \boldsymbol{p}|$ and $a \in [0; r]$. The maximum of the distribution, which would be the maximal

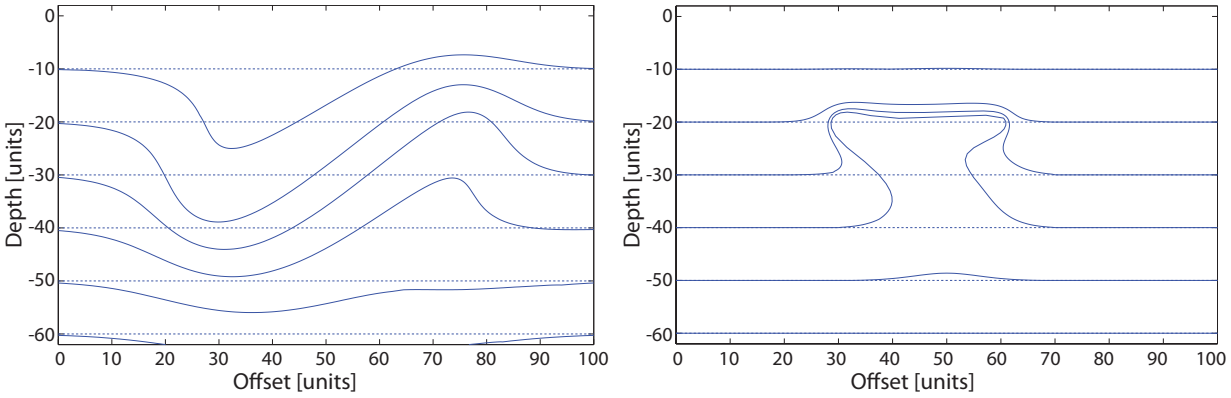

Figure 5.6.: *Two examples of possible geometry modification achieved by 3 operators (dashed line: original geometry, solid line: modified geometry). Left: Long wavelength modifications gained by large operators. Right: Small scale variations performed by smaller operators.*

movement of a vertex captured by the operator, is defined in the middle of the circular operator, therefore $\mu = 0$. Consequently the maximal movement k_{max} an operator can enforce is

$$k_{max}(a = 0) = \frac{1}{\sigma\sqrt{2\pi}}$$

The movement equation for vertices crossing the path of an operator reads

$$k(a) = \frac{1}{\sigma\sqrt{2\pi}} \cdot \exp\left(-\frac{1}{2}\left(\frac{a}{\sigma}\right)^2\right)$$

The amount of movement decreases to zero at the outline of the operator. To achieve this $\sigma = r/3$ is defined. Initial tests showed that the model geometry can get twisted by the operators when all operators take one step at a time but simultaneously. When the operator application is done consecutively, this problem is avoided. The order of application and also the number of operators stays the same during the optimization process.

5.3.1. Adaptive discretization

The principle of the GWO allows smooth geometry changes that do not destroy the topology of a model. But this is only guaranteed if a sufficient discretization of the geometry is provided. Figure 5.7 shows an example of operator application that highlights the reason for sufficient discretization. The geometry is given with two different discretizations and shown after the application of three GWOs. The operators have radii of 60 and 35 length units. With a sparse discretization (25 length units point separation) the deformed model is edgy and, what should be avoided essentially, it now contains crossing polygon lines. However, a finer discretization, of e.g. only 0.5 units, allows for very smooth modifications. Discretizing the complete geometry would be straight forward but would also lead to a large number of vertices. Most of the newly added vertices would then be dispensable because a fine discretization is only required in those parts of the model that are actually subject to modifications. Therefore, the resolution of the model is only refined in the relevant domains, namely along movement paths of operators.
For this, all polygon lines that (1) have a point separation larger than d_{max} and (2) lie within an

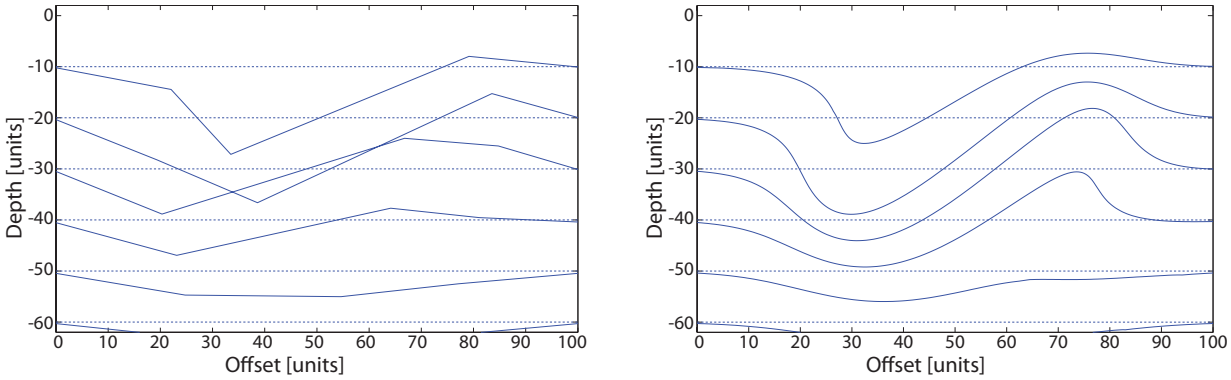

Figure 5.7.: *Two models with same initial geometry (dashed lines) but different discretizations are modified by the same 3 GWOs. The left model has a coarse discretization and the operators cause edgy geometry and also crossing polygon lines. The right model, with a finer discretization, shows a smooth geometry after GWO application.*

operator path will be discretized. The discretization procedure is carried out for every operator and the flowchart in Figure 5.8 highlights the main steps of this procedure. The first step is to estimate the operator path, i.e. the outline of the model area the operator will pass. For reasons of simplicity the path is considered to be rectangular. Figure 5.9 illustrates how the vertices $(S1, S2, E1, E2)$ of the path rectangle are estimated. The operator is initially assumed to be located at the point of origin. Its edge lengths are $a = 2r + l$ and $b = 2r$, where l is the path length and r the operator radius. The vertices are easily derived and in the next steps they are rotated by the direction angle θ and moved so that the operator is located at its proper starting point (x_s, z_s).
Now that the path outline is known, each polygon is checked vertex pair for vertex pair (line for line segment): First the distance d between neighboring polygon vertices (vertex pairs P_i and P_{i+1} with $i = 1 \ldots np$) is compared to the maximal allowed distance (d_{max}). If the discretization is sufficient, the next vertex pair is checked. If $d > d_{max}$, it has to be verified if the line between the two points is crossed by the operator. There are four possibilities of how a polygon line can be crossed by an operator (Figure 5.10). In case of crossing, new vertices will be inserted only on that part of a polygon line which actually lies within the path. Therefore it has to be checked if and which of the two vertices of the polygon line are inside the path.

There is a simple comparison procedure for checking if points are located inside a rectangular polygon which is centered at the point of origin. To apply this comparison, the operator is moved and rotated to the point of origin and with it the vertex in question is moved too. Figure 5.11 shows the work flow and a detailed description of the steps follows.

The center $Mp = (x_{Mp}, z_{Mp})$ of the operator path is given by:

$$x_{Mp} = x_s + \frac{1}{2} l \cdot \cos\theta \qquad z_{Mp} = z_S + \frac{1}{2} l \cdot \sin\theta$$

as shown in Figure 5.11a. Vertex positions are given by $P_i = (x_{P_i}, z_{P_i})$ with i being the vertex index. In the next step (Figure 5.11b) path and vertices are moved so that the center of the path

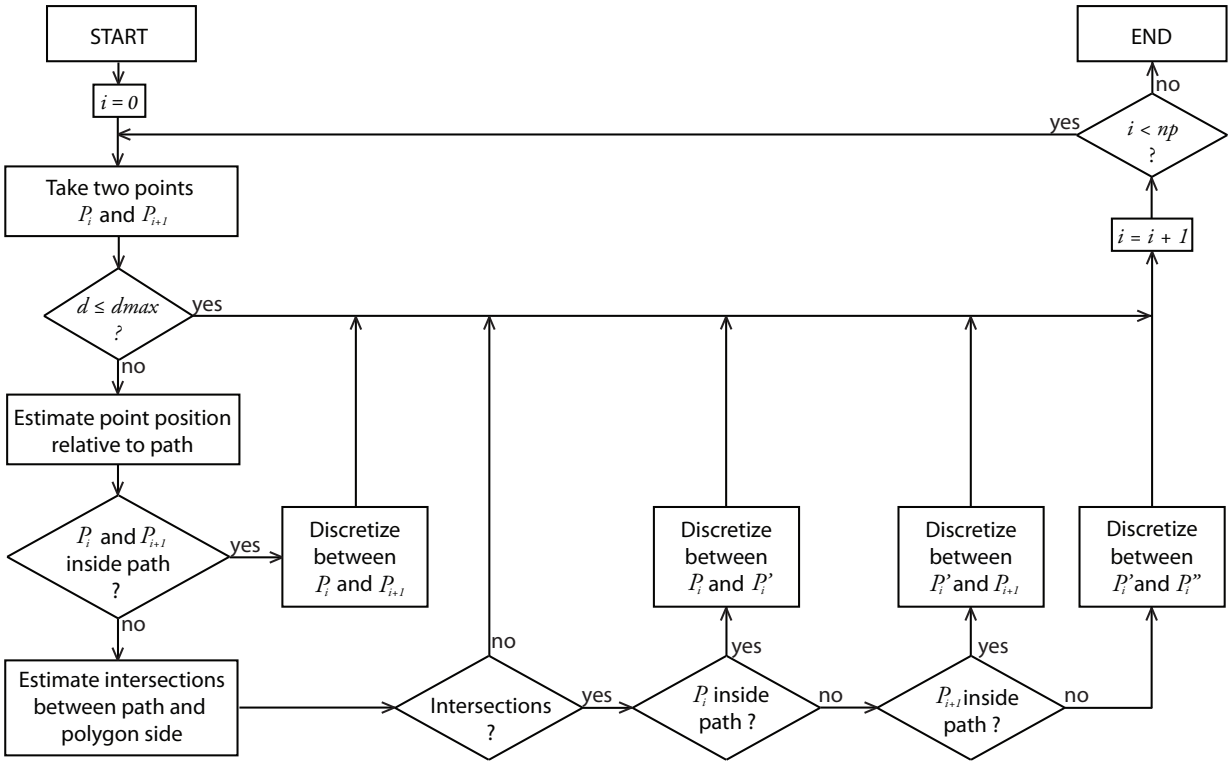

Figure 5.8.: *Flowchart of the discretization procedure for one Gaussian Warp Operator and np vertices of one model polygon. See also text for explanation and Figure 5.10 for illustration of points* P_i.

is at the center of origin. The vertex coordinates now read:

$$x_{P_i'} = x_{P_i} - x_{Mp} \qquad z_{P_i'} = z_{P_i} - z_{Mp}$$

Path and vertices are rotated inversely by the angle θ which is the direction of the operator movement. After this rotation the rectangular operator path is aligned to the axes of the coordinate system and the vertices still have the same relative position to the path (Figure 5.11c,d). Their coordinates are now:

$$\begin{aligned} x_{P_i^{**}} &= x_{P_i^*}\cos(-\theta) - x_{P_i^*}\sin(-\theta) \\ z_{P_i^{**}} &= z_{P_i^*}\sin(-\theta) + z_{P_i^*}\cos(-\theta) \end{aligned}$$

To verify if a point P_i^{**} lies within the path, two comparisons are made. If the following two conditions hold

$$\begin{aligned} &(1) \quad |x_{P_i^{**}}| \le \tfrac{a}{2} \text{ and} \\ &(2) \quad |z_{P_i^{**}}| \le \tfrac{b}{2} \end{aligned}$$

point P_i^{**}, and also the original point P_i, lie either within or on the outline of the operator path. In the case that both vertices under examination are within the path new vertices will be added in between those two points. In case only one vertex lies within the path the intersection point of the polygon line and the path needs to be estimated (Figure 5.10b,c). New points are only added between the vertex within the path and the intersection point, and the intersection point itself is also added. If none of the two vertices under investigation lies within the path it has to be verified

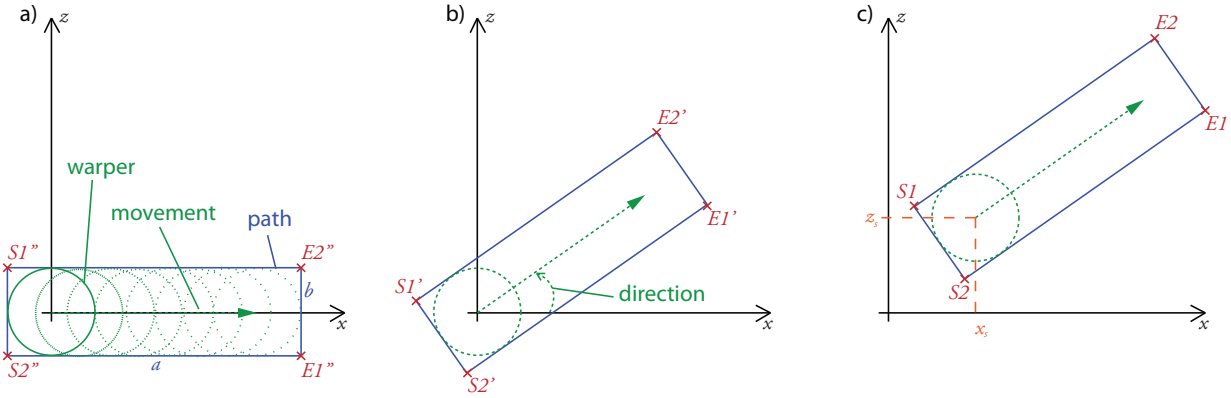

Figure 5.9.: *Estimation of operator path points* $(S1, S2, E1, E2)$ *via vector rotation and displacement. The operator path is a rectangle with edge lengths* a *and* b*. a) The operator is assumed to be located at the point of origin. The path points near the start* $(S1'', S2'')$ *and near the end* $(E1'', E2'')$ *are easily estimated. b) Rotation of the path (and points) by the warper direction given by angle* θ*. c) Displacement of the path to its actual position in the coordinate system. The start point of the operator is at* (x_s, z_s)*.*

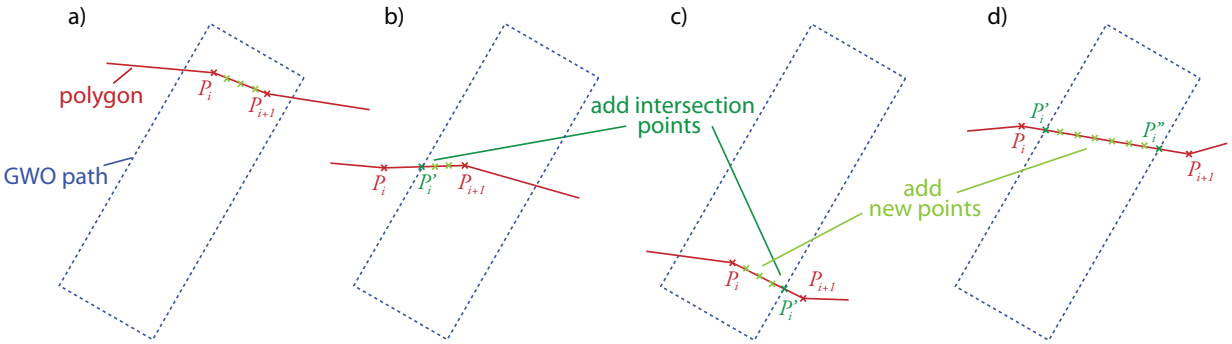

Figure 5.10.: *Four possible ways of how the GWO path might cross the sides of a polygon. a) Both vertices are inside the path. b) and c) Only one point is in the path. d) Both points are outside the path but the polygon side intersects with the path. New points to be inserted are given in light green and new intersection points with the path outline are marked* P_i' *and* P_i''*.*

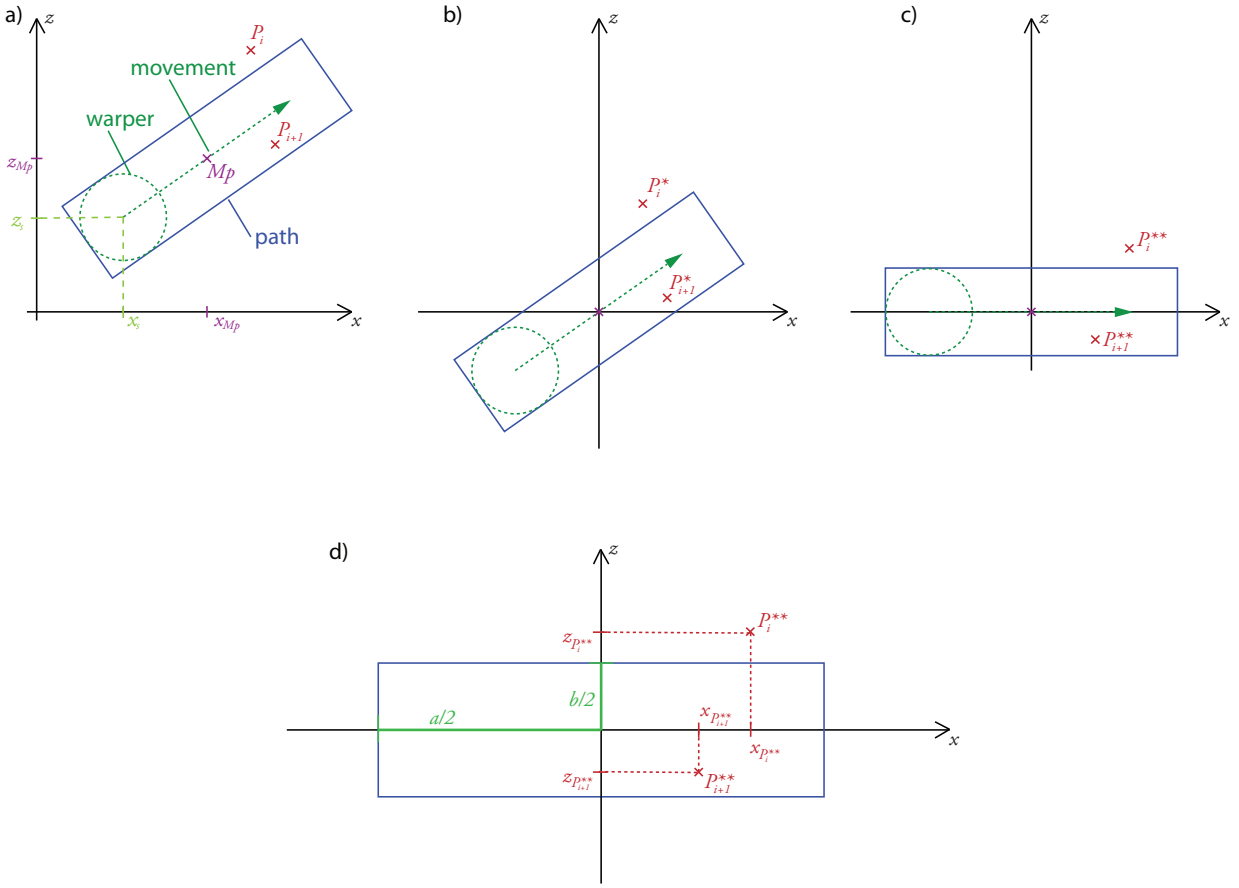

Figure 5.11.: *Verification if polygon vertices (P_i and P_{i+1}) are within the operator path. a) Original setting of vertices and operator path. Mp is the center of the path, $(x_s, z_s$ is the starting point of the GWO. b) Path and points are moved to the center of origin and b) rotated inversely by the angle θ (direction of the operator movement). d) Zoom in on c) for variables needed for the verification. See text for further explanation.*

if there are two intersection points between polygon line and path (Figure 5.10d). If there are no intersections then the polygon line is not affected by the operator at all. If there are intersections then new vertices will be added to the polygon line in between those two intersection points.

The adding of vertices is a non-trivial task, as the order of the vertices in the model polygons is crucial for the forward calculation of the gravity field. All vertices are listed in a clockwise order. In the case that vertices have been inserted in a polygon, the same vertices need to be added to the adjoining polygons. Also keeping track of the correct order, which is inverted to the one in the originally checked polygon.

Aimed for but not implemented yet is a varying discretization (d_{max}) that depends on the operator parameters (r and l). Small operators required a finer discretization than larger operators because of their small wavelength modifications to the geometry. It could also be useful to apply a subsequent coarsening to an optimized model geometry to reduce the number of vertices. The interpreter has almost no influence on how many vertices are added to the geometry during optimization and might want to reduce them again. This could be done e.g. by using a smoothing algorithm. But it needs to be verified how appropriate such an approach really is. After all, the added vertices were required to allow the geometry modifications and the degree of modification can be limited by the interpreter.

In addition to the advantage that model deformations are independent of the initial discretization and vertices are only added to polygons where necessary, the adaptive discretization also saves calculation time. Each time an operator is used on the model, the above described checking procedure needs to be carried out and with every iteration of the optimization process the current discretization is forgotten and the operator applications and discretizations start anew. And although this means a lot of computation steps it is still faster than using a fine and fixed discretization for the entire model because the number of vertices relates directly to the time needed for the forward calculation of the gravity effect. Furthermore, the interpreter is spared the decision on an initial discretization which might then not be sufficient and demands a completely new optimization because the model topology was harmed.

5.4. Particle Swarm Optimization (PSO)

The PSO after (Eberhart and Kennedy, 1995) implements the concept of swarm intelligence. The basic concept has been explained in Chapter 5.1.2 and the description will now go into more detail. As mentioned earlier, a combination of variants of the basic PSO is implemented here. The charged global best PSO with restart option enhances convergence and improves the diversity of the swarm and was presented by Wilken and Rabbel (2012) as a very effective tool in multi-parameter and multimodal problems. The following leads through all these extensions.
For a mathematical description, the nomenclature by Engelbrecht (2005) is used[1]. Let a swarm consist of $i = 1 \dots n$ particles or individuals, where a particle is represented by a vector $\boldsymbol{X}$ that contains a complete set of model parameters that define its location in the search space. When exploring the search space of $j = 1 \dots m$ dimensions the position of each particle $\boldsymbol{X}_i(t)$ at a time

[1] This might in some parts lead to a conflicting notation compared to the earlier chapters.

step t is updated after every iteration:

$$\boldsymbol{X}_i(t+1) = \boldsymbol{X}_i(t) + \boldsymbol{v}_i(t) \tag{5.1}$$

The position update is done by adding a so-called velocity vector $\boldsymbol{v}_i(t)$ to the current position. The exact definition of the velocity equation is addressed in the following sections. The initial positions $\boldsymbol{X}_i(t=0)$ of all particles are chosen randomly, regarding the restrictions listed in the previous section (mainly box constraints).

Global best PSO (gbest PSO)

Particles of a swarm communicate with their neighborhood to gain information and estimate their next position. Defining by what is regarded as neighborhood one can distinguish between two basic variants, the *global best* and the *local best PSO*. The latter defines small neighborhoods for each particle and only particles within the respective neighborhood influence the movement of the individual particle. For a *global best PSO*, which is implemented in this work, the entire swarm is defined as the neighborhood for every particle. The velocity update of a single particle is influenced by all swarm particles. The velocity term in Equation 5.1 is defined after Engelbrecht (2005):

$$v_{ij}(t+1) = \omega v_{ij}(t) + c_1 r_{1j}(t)\left[Y_{Kij}(t) - X_{ij}(t)\right] + c_2 r_{2j}(t)\left[Y_{Gj}(t) - X_{ij}(t)\right] \tag{5.2}$$

where $v_{ij}(t)$ is the velocity and $X_{ij}(t)$ the position of particle i in dimension j at time step t. Y_{Kij} is the individual best position each particle has found so far and Y_{Gj} is the global best position amongst all particles that was reached so far. $r_{1j}(t)$ and $r_{2j}(t)$ are random values in the range of $[0, 1]$ that introduce the stochastic element to the algorithm. ω gives a weight to the particle velocity from the previous iteration and therewith controls the inertia component of the swarm. The weighting constants c_1 and c_2 scale the contribution of cognitive and social components, respectively. They are also referred to as trust parameters as they describe how much trust a particle has in its individual best position and in the global best position (Engelbrecht, 2005). If $c_1 \gg c_2$, then each particle is much more attracted to its own best position than to the global best position, which causes excessive wandering. In the opposite case, if $c_2 \gg c_1$, the particles are stronger attracted to the global best and they move prematurely towards optima. Furthermore, when the parameters are assigned low values, they move along smooth trajectories through the search space and have the possibility to roam and explore far from already known good regions. When the values are high, the swarm moves more abruptly towards (or maybe past) good regions (Engelbrecht, 2005).
The second summand in equation 5.2 is the cognitive component of the swarm. It is understood as the experiential knowledge of a particle and it is proportional to the distance of the particle to its own best position found over all iteration steps. The individual best positions of all particles are estimated within each iteration:

$$\boldsymbol{Y}_{Ki}(t+1) = \begin{cases} \boldsymbol{Y}_{Ki}(t) & \text{if } f(\boldsymbol{X}_i(t+1)) \geq f(\boldsymbol{Y}_{Ki}(t)); \\ \boldsymbol{X}_i(t+1) & \text{if } f(\boldsymbol{X}_i(t+1)) < f(\boldsymbol{Y}_{Ki}(t)). \end{cases}$$

where $\boldsymbol{Y}_{Ki}(t)$ is the vector of individual best positions so far of each swarm particle i and $\boldsymbol{X}_i(t+1)$ is the vector of positions of the swarm particles.
The social component of the velocity equation is found in the third summand of Equation 5.2. This

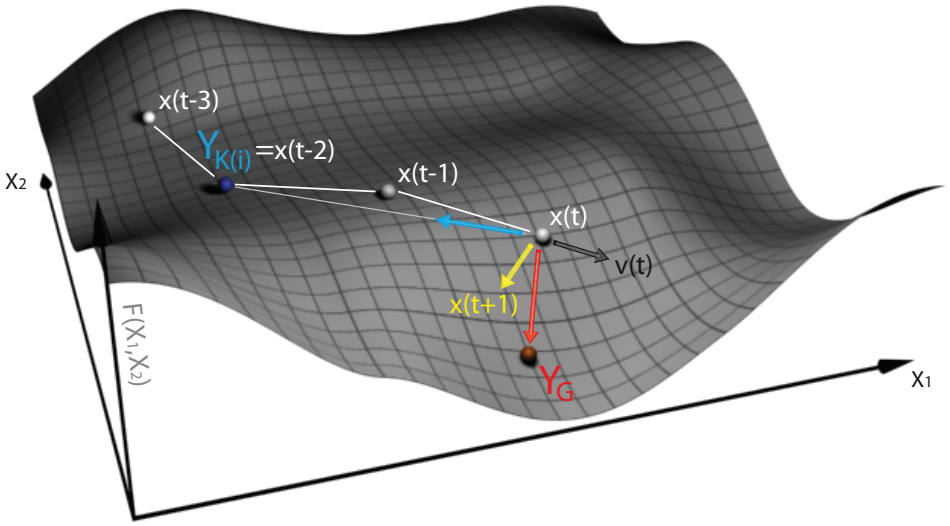

Figure 5.12.: *Illustration of the movement of a particle in a 2D parameter space (Wilken, 2009).*

component refers to the communication within the swarm as it represents the socially exchanged information about the overall best position of all particles found since the first time step. After the individual best positions for all particles are estimated in an iteration step, the global best position of all particles is estimated as follows:

$$\boldsymbol{Y}_G(t) \in \{\boldsymbol{Y}_{K0}(t), \cdots, \boldsymbol{Y}_{Kn}(t)\} \,|\, f(\boldsymbol{Y}_G(t)) = \min\{f(\boldsymbol{Y}_{K0}(t)), \cdots, f(\boldsymbol{Y}_{Kn}(t))\}$$

The movement of a particle in a 2D parameter space is illustrated in Figure 5.12. Shown are the current position of particle $\boldsymbol{X}(t)$, the positions of the particle from the three previous time steps, and the newly estimated position of the particle $\boldsymbol{X}(t+1)$. This new position is found using equation 5.1 and the velocity equation (5.2), taking into account the global best position of the swarm ($\boldsymbol{Y}_G$), the individual best position of the particle ($\boldsymbol{Y}_{K(i)}$), and the velocity and direction from the last iteration ($\boldsymbol{v}(t)$).

Charged global best PSO (gbest cPSO)

A major task with PSO is to establish a good balance between exploration of the search space and exploitation near an optimum. Blackwell and Bentley (2002) introduced the concept of an *atomic* swarm with charged particles that follows the idea of atom models. Half of the swarm particles are identically charged and behave repulsive to each other in accordance to the electrostatic inverse square law. The other half of the swarm particles are neutral. This constellation allows the neutral particles to gather near an optimum (exploitation) while the charged particles keep on searching the parameter space (exploration). See Figure 5.13 for an illustration of the concept. For implementing a charged PSO the velocity equation (Equation 5.2) is changed by adding a particle acceleration ($\boldsymbol{a}_i$) to the standard equation:

$$v_{ij}(t+1) = v_{ij}(t) + c_1 r_{1j}(t)\,[Y_{Kij}(t) - X_{ij}(t)] + c_2 r_{2j}(t)\,[Y_{Gj}(t) - X_{ij}(t)] + a_{ij}(t) \qquad (5.3)$$

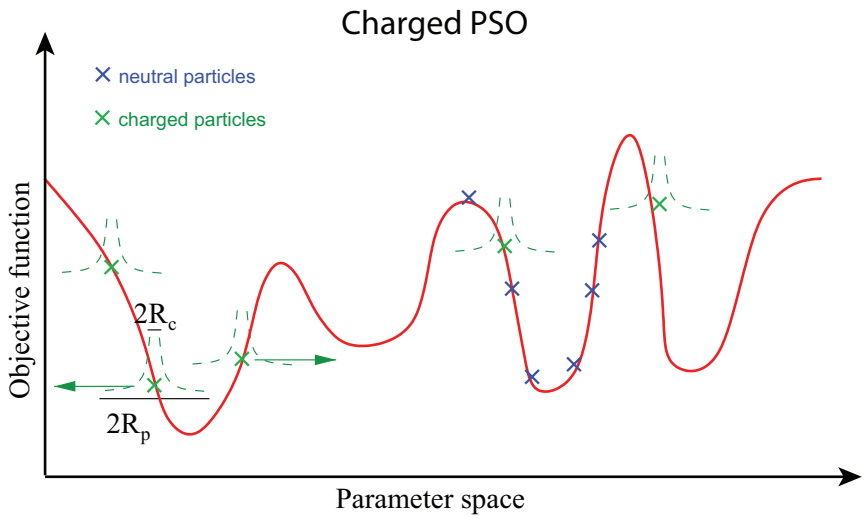

Figure 5.13.: *Illustration of atomic PSO. Green crosses indicate charged particles. They experience a repulsive impulse if they approach each other within the perception limit R_p. Neutral particles (blue crosses) ensure possible convergence. (modified after Wilken, 2009)*

The acceleration term is the sum of all repulsive forces between particles i and l:

$$\boldsymbol{a}_i(t) = \sum_{l=1, i\neq l}^{n_s} \boldsymbol{a}_{il}(t)$$

where $\boldsymbol{a}_{il}$ is defined as

$$\boldsymbol{a}_{il}(t) = \begin{cases} \left(\frac{Q_i Q_l}{||\boldsymbol{X}_i(t) - \boldsymbol{X}_l(t)||^3}\right)(\boldsymbol{X}_i(t) - \boldsymbol{X}_l(t)) & \text{if } R_c \leq ||\boldsymbol{X}_i(t) - \boldsymbol{X}_l(t)|| \leq R_p \\ \left(\frac{Q_i Q_l}{R_c^2 ||\boldsymbol{X}_i(t) - \boldsymbol{X}_l(t)||^3}\right)(\boldsymbol{X}_i(t) - \boldsymbol{X}_l(t)) & \text{if } ||\boldsymbol{X}_i(t) - \boldsymbol{X}_l(t)|| < R_p \\ 0 & \text{if } ||\boldsymbol{X}_i(t) - \boldsymbol{X}_l(t)|| > R_p \end{cases}$$

where Q_i is the charged magnitude of particle i, R_c is referred to as the core radius, R_p is the perception limit of each particle (Engelbrecht, 2005).

Reset global best PSO

The slope of the objective function can be regarded as a criterion for convergence. In case the slope becomes approximately zero the swarm has reached an equilibrium as particles converge to a minimum. This minimum can be global or local. To estimate convergence the following ratio is considered:

$$f' = \frac{f(\boldsymbol{Y}_G(t)) - f(\boldsymbol{Y}_G(t-1))}{f(\boldsymbol{Y}_G(t))}$$

The convergence can be used to initiate a restart of the swarm, e.g. when $f' < \epsilon$ for a certain number of iterations. In that case, the current global best position of the swarm is saved and search begins anew after resetting the global best and all individual best particle positions. This procedure is repeated until the overall stop criterion of the swarm is reached, e.g. a threshold or the maximal number of iterations. After that, not only a single solution for the optimization

problem is provided but an ensemble of solutions, i.e. all saved global best particle positions before the restarts. This is a major advantage in the multimodal application of the PSO in potential field optimization. The decision on ϵ is depending in the problem (and the objective function). The restart criterion should not be too tight as it could prevent the exploitation in the vicinity of an optimum if a restart is initiated too early. Also the overall number of iterations should be large enough in order to allow for several restarts of the swarm.

5.4.1. PSO using the GWO parametrization

The complete optimization process, combined with the just described parametrization, is named POGO[2] and best put together in a flow chart (Figure 5.14). The first thing, before the optimization is actually started, is of course the definition of the initial model and the set-up of the swarm parameters. Then a loop with a maximal number of iterations is started, beginning with the creation of an initial set of particles. They are randomly distributed within the search space. Now an inner loop over all particles is started (the gray box). For each particle, the initial model is deformed according to the respective GWOs and after evaluating the objective function, the individual best position of each particle is estimated. Out of all individual best positions the global best position of the entire swarm is estimated. If the restart criterion is reached, the GWO parameters defining the global best position are added to the ensemble of solutions and a new swarm is initiated. If the objective function does not converge yet, that particles are moved according to the velocity equation (5.2) and the inner loop is executed again. It should be noted that the application of the GWOs is always acting on the initial model. Instead of changing the geometry step by step within every iteration, the GWO parameters are changed bit by bit. This makes the search problem a global one and is the reason why the globally searching PSO was implemented. It also means that every model that results from deformation using the GWOs in the solution ensemble has a different discretization.

Internally, all GWO parameters are scaled to an interval $(0, 1)$. This enables unbiased optimization of all parameters which are coordinates, lengths and angles and whose values differ in several orders of magnitude. This scaling also allows for a straight forward addition of the physical properties to the optimization procedure. As an option, model densities can also be subject to manipulations. The particle vector $\boldsymbol{X}$ is enlarged by the respective number of model body densities and the PSO is applied just as before. The rather small increase of unknowns, that now allows the geometry and densities to vary, opens up a large amount of additional possible model solutions (keeping ambiguity in mind). The applications in Chapter 6 will test this option.

5.5. Implementing constraints

Geological or geophysical information that is available in addition to the potential field data is usually integrated during construction of the initial model. This information can be, e.g. the location of horizons derived from seismic interpretation or depth and density information gained from bore hole data. Depending on the confidence given to this additional information it might be demanded to have some restrictions on the modifications of the initial model, i.e. an identified horizon with high confidence shall not be modified during model optimization. In the following,

[2] *POGO: **P**article swarm **O**ptimization with **G**aussian warp **O**perator*

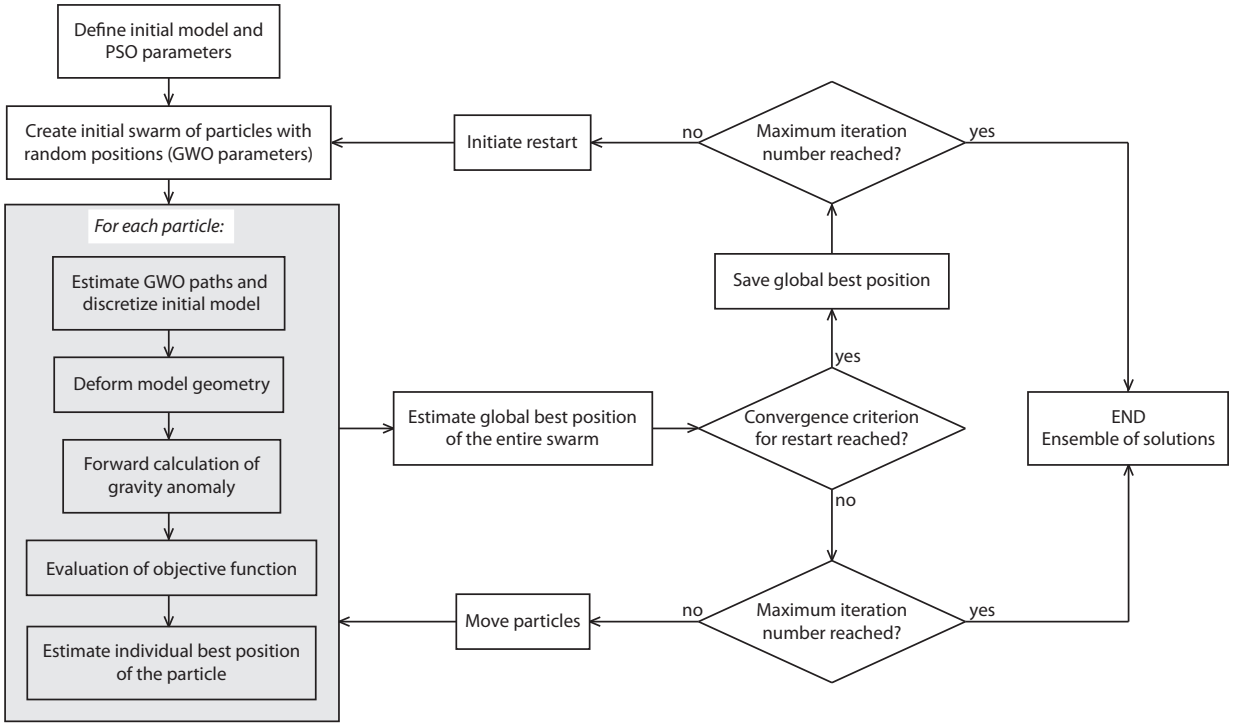

Figure 5.14.: *General flow chart of the particle swarm optimization using the GWO parametrization. The gray box contains the steps that are carried out for each individual particle.*

some options will be described that allow the consideration of additional information to constrain the optimization process.

5.5.1. Property constraints

Two different ways of integrating different kinds of property constraints are implemented in the code and described here. One constrains the solution space to a predefined range of possible values (box constraints) and the other links the estimation of properties for model bodies internally.

Box constraints for initial parameters

Depending on available a priori information, confidence in the densities of the initial model is often diverse. When densities are derived from seismic velocities, most translations provide a valid density range (e.g. the Nafe-Drake curve in Ludwig et al. (1970), Gardner et al. (1984)). Density information from bore holes however is usually given a higher confidence. Therefore, the inversion offers the definition of property constraints. In the parameter file which contains the density information for the model bodies, an additional column is defined containing the allowed variability ($\pm\Delta\rho$) of the initial value (ρ_{init}).

Linking model bodies of the same property

When building up a model it is sometimes necessary to model a structure by using more than one model body, although these bodies have the same physical property. This can have different reasons, e.g. a structure might be punctured by a diapir or layers are disrupted by a fault zone

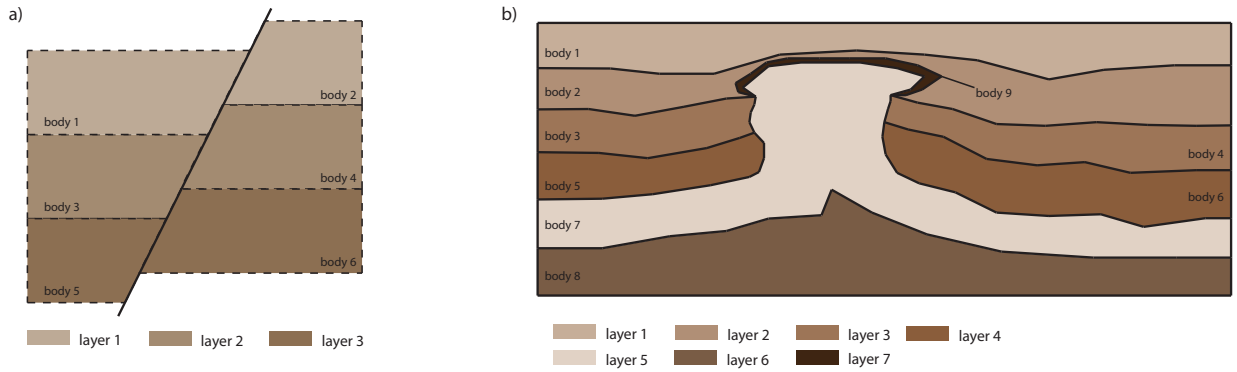

Figure 5.15.: *Examples of model geometries where a geological layer is split into 2 model bodies. a) Splitting the 3 layers into 6 model bodies allows the fault to reach a larger offset during modeling. b) Two layers of the model are clearly pierced by the ascended salt dome. This should be accounted for during inversion - the layer property should remain the same on both sides of the salt.*

(Figure 5.15). But it can also happen during the modeling process when an interpretation proves to be wrong and the model requires substantial changes. For example picture the following case: An initial density model was derived from seismic interpretation. Model bodies are defined in accordance to the seismically imaged horizons. The gravity anomaly shows a high which is not accounted for by the seismic interpretation. A next step could be (if geologically meaningful) the creation of a high density body. In order to create this body it might become necessary to divide one of the existing layers. So when initially there was one model body there are now three and two of them have same physical properties (because they are of the same material). Those two bodies shall still have identical properties after model optimization. To accomplish this model bodies can be referenced by indices and that allow a linking of the properties during optimization.

5.5.2. Geometry constraints

A suggestion to restrict structural changes is given by the definition of *constraining boxes*. The idea is that one or several boxes are defined for model domains where additional information is assigned with high confidence. This offers a way to prioritize e.g. seismic interpretation or bore hole information (Figure 5.16).

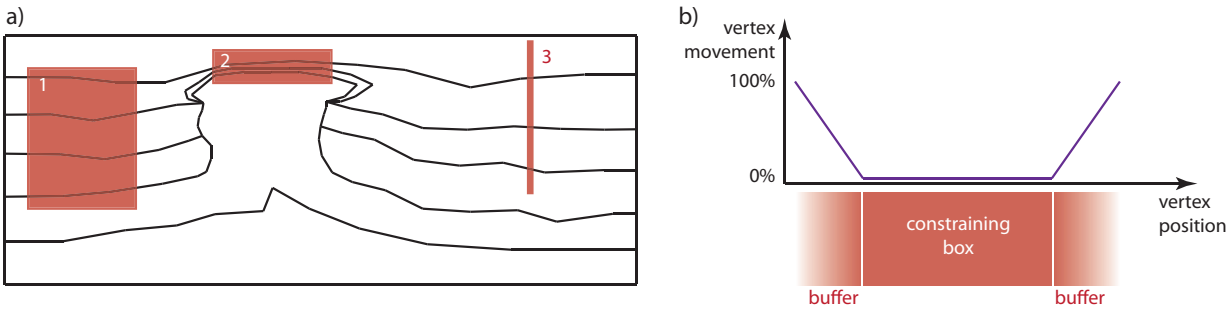

Figure 5.16.: *Functionality of constraining boxes. a) Model geometry with two boxes constraining previous interpretations (1 and 2) or fixing horizons identified in bore holes (3). b) Constraining box with its lateral buffer zones and the allowed movement of vertices affected by the box.*

The definition of constraining boxes would be relatively simple, the user only needs to define two opposing points of the box and the length of a buffer zone. Vertices that are located within a constraining box are fixed and will not be moved by a passing warp operator. The buffer zone is required to avoid peaks at the boundaries of the box. Within this zone the influence of the GWO is reduced linearly with decreasing distance from the box.

5.6. Optimization result assessment

The application of the restart variant of PSO provides an ensemble of possible model solutions. As mentioned previously, a restart is performed when the swarm converges to a point in the parameter space. This point is not necessarily an optimum but particles get attracted to it and in the end the solution is present in the ensemble. The ensemble will most certainly also contain solutions that are not entirely reasonable in a geophysical or geological sense. In other applications of PSO a mean model is estimated from the ensemble of solutions, (e.g. Wilken, 2009; Tronicke et al., 2012). In general, the calculation of a mean model could be done by estimating the mean of the optimized model parameters. In the case of GWO parametrizations, this approach is not applicable because the order of the GWOs in the particle vector $\boldsymbol{x}$ is not necessarily the same for all solutions of an ensemble. As an extreme example, the model in Figure 5.4 can be considered. It is completely irrelevant, in which order the 3 operators are applied to the geometry, the result would always be the same (because in this case, the GWOs do not cross paths). And due to their varying order, it is not possible to estimate a mean 1st, 2nd and 3rd GWO. This also prevents the calculation of a posterior correlation matrix for a statistical assessment of the solutions.
But a mean structural model could be gained from the model geometry itself by computing mean polyhedral bodies. This is a non-trivial task, especially because of the varying geometry discretizations of all model, which has not yet been implemented in the program. Instead, a visual assessment is proposed as a preliminary means. This is easily applicable, at least for the 2D case: By plotting the outlines of several model geometries in one figure, a visual estimation of a mean model is possible. The scatter of the polygon lines can be interpreted as error or confidence in the mean model.
The solutions for the density estimation can be given in density-depth-diagrams. Mean estimates with error bars can be given. In the end a subjective decision on a model must be made by the interpreter.

5.7. Implementation and application in three dimensions

All descriptions in this chapter concern geometry modification and optimization in two dimensions. Of great interest however would be three dimensional applications. Therefore both, the developed model parametrization with the GWOs and the PSO method were designed in a way to also be suitable for three dimensions, where models are built of triangulated polyhedral bodies or triangulated surfaces. The changes and modifications in the implementation are now addressed.

GWO parametrization

The circular spatial operator can easily be extended to a three dimensional spherical operator. Its functionality is the same as the 2D operator, as vertices are dragged in operator direction in case they lie in its movement path. The 2D operator is defined by 5 parameters (Section 5.3), the

third dimension adds two more parameters to its definition: The starting point requires a third coordinate y_s and the angle ϕ is needed as second angle for the movement direction. With these additions, a GWO is defined by 7 parameters: $x_s, y_s, z_s, r, l, \theta, \phi$.
A bit more demanding is the implementation of a 3D adaptive discretization because a sufficient discretization is also required for 3D vertex distributions. The model bodies have triangulated surfaces which means, instead of inserting new points along a polygon line, it is necessary to create smaller triangles. This can be done by dividing triangles along a line from the middle of their longest edge to the opposite corner. Triangles are divided until all edge lengths are smaller or equal to the maximal allowed vertex separation ($< d_{max}$).

PSO

The only change in the PSO implementation is the addition of the new GWO parameters to the particle vector and their consideration in the update of the velocity equation (Equation 5.2). The number of unknowns (i.e. the dimensionality of the search space) increases and changes in the settings for the PSO must be investigated. The new search space dimensions are not only introduced by the 2 new parameters per GWO but, more notably, by the increase of the overall number of GWOs that are needed to cover a third spatial modeling dimension.

Constraints

The definition of property constraints (Section 5.5.1) remains unchanged. This applies to the box constraints as well as to the option to link model bodies of the same property. Using constraining boxes to constrain geometry modifications (Section 5.5.2) requires a further parameter in their set-up. Instead of rectangles the boxes would be proper 3D-boxes, defined by two opposing edge points.

Result assessment

The assessment of optimization results is already challenging in two dimensions. In three dimensions a visual assessment is in most cases not feasible, even when good graphics options and 3D viewer are used. A quantitative assessment is therefore desirable, e.g. mean geometry and parameter with error bounds.

6. Applications with optimization tool

In the previous chapter the development of the optimization tool POGO for model geometry and density was described. In this chapter the application of the optimization will be tested and evaluated using two data sets. The first test case is a synthetic salt structure. This example shows how the method works on a scale of several kilometers and how the operators can deal with expected uplifted structures. The example is used as a demonstration for an application strategy and also the assessment of optimization results will be discussed. The second application will be on the Capel and Faust Basins data and model (Section 4.3). As the method is so far only applicable to 2D models, a section from the original 3D model will be extracted. This model has a lateral extent of several hundred kilometers and a vertical extent of several tens of kilometers which includes the Moho. That allows to investigate whether deep structures are regarded for model optimization or if modifications are predominantly in upper domains of the model.

6.1. Synthetic salt model

Main objectives of this example are the set-up and tuning of the swarm parameters (number of particles, number of iterations, convergence criteria, weighting of the components of the velocity (Equation 5.2), charge for the repulsion of particles) and the operator parameters (number of operators, size and movement path). Furthermore, two different initial models will be used to investigate the influence of the start model on the optimization and the final model ensembles. Optimizations will be run (1) only on the geometry and then (2) also including densities. The latter enhancing ambiguity of the solution. A synthetic salt structure was chosen for this application as salt structures are main targets in potential field interpretation.

Original and initial models

The original salt structure and gravity anomaly are shown in Figure 6.1. The 2D model is a selected cross section from the 3D model that was already used for the exemplary calculation of model body prominences in Chapter 3.3. The model shows a dome structure of Zechstein salt which has risen from a layer between the Permian and Triassic. The salt pierced through the Triassic and Jurassic sedimentary layers. Its top is located in Tertiary sedimentary rocks. For the application here, the Cap rock model body is removed as it is a distinct body that is not present in the initial models and cannot be created during optimization.The densities assigned to the model are also given in Figure 6.1. 50 measurement stations are equally distributed along the surface. The salt diapir causes an anomaly of approximately $12 \cdot 10^{-5}\,\mathrm{m/s^2}$.

The following applications use two different initial models (also Figure 6.1). Both initial models are layered, containing the same number of layers as the expected model. One of them already has a slight uplift of the Zechstein layer that is located at the offset of the anomaly minimum.

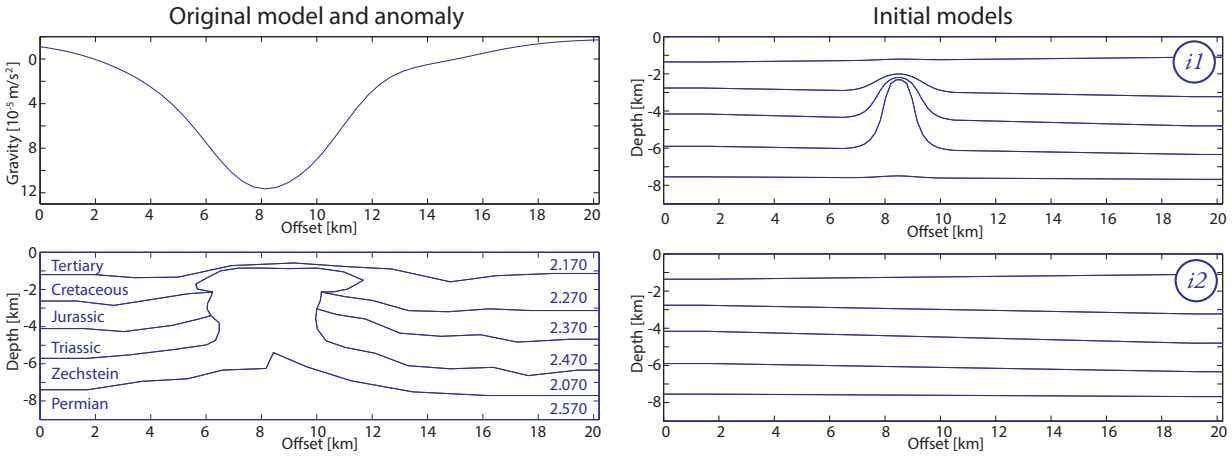

Figure 6.1.: *Synthetic salt diapir and its gravity anomaly (left). The assigned densities are in t/m^3. Two initial models used by POGO (right).*

First applications are done with this initial model. After determining the GWO parameters and the swarm set-up, the strictly layered model is used to see what consequences less information on the initial model has on the solution. Optimizations are run on the geometry alone and in a second approach for geometry and densities.

6.1.1. Parameter set-up

Before applying the POGO tool, some parameters need to be defined. They were mentioned in the descriptions in the previous chapter and concern the model area, the operator and the swarm optimization. The latter two categories also affect each other. The parameters are summarized in Table 6.1

Model parameters	GWO parameters	PSO parameters (general)	PSO parameters (model-dependent)
Active modeling area	Max. path length (l_{max})	Radii (R_c, R_p)	Weights (ω, c_1, c_2)
Constraining boxes	Min/max radius (r_{min}, r_{max})	Charge (Q)	Particles (n_p)
Density box constraints	Number (n_{GWO})	Restart criterion (ϵ)	Iterations (n_{iter})
Linking model bodies			

Table 6.1.: *Summary of the parameters that need to be addressed when running POGO.*

Model parameters

First, the specific area of the model, which should be subject to geometry modifications, needs to be identified. The 2D models used here are usually laterally extended to avoid edge effects. The *active modeling area* was originally only used to limit the optimization to the part of the actual model. Of course, it can also be used to restrict an optimization to specific parts of a model, e.g. only the continental part of a transition zone, only the crustal part of a model or only the Moho interface. The rectangular area is simply defined by four values that frame the specific modeling

area. The application and movement of the GWO is limited to this area and only a single area can be assigned to a model. To avoid geometry changes within an active modeling area, constraining boxes are recommended.
The optimization of densities is not restricted to the active modeling area. If densities are allowed to be modified and in which interval around the initial values these modifications take place, is regulated by box constraints.

In order to deal with edge effects, the model extends laterally for 500 km in both directions. The actual modeling area for the optimization however is restricted to the 20.2 km offset profile that is shown in Figure 6.1. The modeling area covers the entire depth extent of 9 km but leaves out the upper 500 m in order to prevent any layers to reach the surface. The use of constraining boxes and the linking of model bodies is not applied here and the density box constraints are listed in the descriptions of the optimization runs further down.

Decision on GWO parameters

Each model is different in its dimensions and geometry and the application of optimization is used for different purposes, e.g. fitting of a long wavelength or short wavelength effect, providing final adjustments to a well-developed model or giving primary indications for an emerging model.
The *strategy parameters* of the GWO were described in Section 5.3. They control the operator size and its maximal movement. Those are the parameters that control the general behavior of the operators, e.g. if these cause long or short wavelength changes. Depending on the modeling problem at hand and the expected geometry changes these parameters, and also the number of operators, need to be adjusted. To get a feeling for the operator size and path length, it is helpful to apply some different operators on the provided initial model. From these deformations also the rough number of necessary GWOs can be gauged. Too few operators will not be able to perform all the required deformations to reach the desired anomaly fit. On the other hand, too many GWOs can lead to redundant deformations, where the modification of one operator is reversed by another and where computation time is unnecessarily increased.

In this example the operators are supposed to deform the initial model in a way that the salt structure becomes evident. The expected structure has a diameter of about 4 km, with 1 km thick bulges at the top. The required uplift to gain the height of the salt structure is about 8 km. The operator radii determine the wavelengths of modification. In order to find a usable range (r_{min}, r_{max}), operators with three different radii are applied to the layered initial model (Figure 6.2). All have the same path which starts in 8 km depth and then moves 5 km upwards. It seems that the wavelength of deformations caused by the largest GWO is too long for the current purpose. The other two radii cause reasonable deformations and therefore, the operator radii are constricted to lie with the interval $r_{min} = 1,000\,\text{m}$ and $r_{max} = 3,000\,\text{m}$ for the optimization. The decision on the maximal operator path lengths l_{max} is somewhat linked to the number of operators and also to the kind of subsurface model to be expected. The PSO could either use few operators that are allowed to move long distances or, on the other hand, use more operators that are only allowed to move shorter distances. After considering Figure 6.2, the following tests will use parametrizations with 5, 7 and 10 GWOs and the path length is restricted to $l_{max} = 5,000\,\text{m}$. After the first set-up of the GWO parameters, they might need some runs and eventually some further adjustments when properly applied to the entire model.

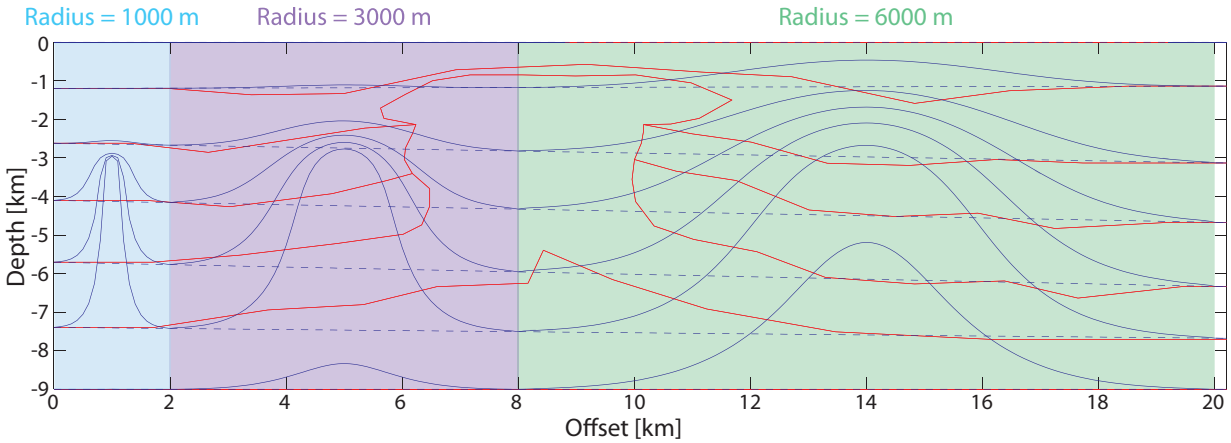

Figure 6.2.: *Deformation caused by GWOs of different sizes, with respect to expected salt diapir. Three different radii (color-shaded) are tested on a layered initial model (blue). The expected salt diapir is underlain (red).*

General PSO parameters

These parameters only needs to be addressed once to set up the swarm for potential field application and the developed GWO parametrization. The implemented PSO is the atomic charged variant where half of the swarm particles have an additional acceleration term in the velocity equation (Equation 5.3). The parameters that determine the acceleration are charge Q, core radius R_c and perception area R_p. The values for these parameters are taken from Blackwell and Bentley (2002). The core radius is set to $R_c = 1$. The perception area is defined as $R_p = \sqrt{3}x_{max}$, where x_{max} is the maximal possible value of a model parameter. As all model parameters are scaled to the range $[0, 1]$, the perception area in this case is $R_p = \sqrt{3}$. The charge of the particles is set to $Q = 16$.
Furthermore, the criterion that initiates a restart of the swarm (Section 5.4) must be defined. If the improvement of the objective function over a given number of iterations is smaller than a certain threshold (ϵ), a restart is initiated. For this application an $\epsilon = 1.0e^{-4}$ is chosen. If convergence improvement is continuously below this value for a number of 20 iterations, the restart criterion is reached.

Model-dependent PSO parameters

These parameters are related to the number of unknowns that is given by the number of GWOs to be applied, which in turn is related to the complexity of the individual model. One important set of parameters are the weighting parameters ω, c_1 and c_2 for the components of the velocity equation, first introduced in Equation 5.2. ω weights the inertia of the swarm and c_1 and c_2 are the weights for the cognitive and the social component, respectively. They regulate the swarm behavior itself and have influence on the diversity of the swarm. Especially c_1 and c_2 influence the exploration and convergence of the swarm (rf. Section 5.4). Depending on their definition, the swarm is regarding the positions of all its particles more equally or it is moving more eagerly towards the best position of an individual.

Weight	Run1	Run2	Run3	Run4	Run5	Run6
ω	0.5	0.5	0.5	0.5	0.5	0.5
c_1	0.9	2.0	1.5	2.0	2.0	1.5
c_2	0.5	0.5	0.5	1.5	0.9	0.9

Table 6.2.: *Listing of the weighting parameters specified for different optimization runs to investigate the influence of inertia (ω), cognitive component (c_1) and social component (c_2).*

It is recommended to define a test problem of the same dimensionality and multi-modality as the actual optimization problem to find a useful combination of these constants (e.g. Wilken, 2009). This is a bit tricky with the POGO because the dimensionality depends on the number of operators which in turn changes for the here planned different optimization runs. Adding one operator means adding 5 dimensions to the search space. As this example constitutes a test application, the initial set-up of the swarm uses the values identified by Wilken (2009). Those constants were estimated for a 18-dimensional problem. Here, tests are made with three different numbers of GWOs (5, 7 and 10) which means 25, 35 and 50 unknowns. Therefore, some crude variations of the initial values are also tested. Overall six runs per number of GWOs are made. The constellation of the respective weighting parameters is given in Table 6.2. All give the same low weight to the inertia ω which means high adaptability. With $c_1 >> c_2$ the PSO is set to a global search which is required because of the high dimensionality and multi-modality.

The number of particles that are required for the PSO is related to dimensionality of the problem. The more unknowns, the more dimensions the search space has and the more particles are needed. Also, the swarm optimization requires an abortion criterion (not to be confused with the restart criterion). This can be a certain minimal misfit that must be reached or a maximum number of iterations. This implementation uses a maximal number of iterations which is influenced by the number of particles. More particles usually require more iterations to reach convergence. Convergence also depends on some of the just mentioned parameters as they also influence each other. For example, more particles search longer before a restart is initiated. With a smaller core radius, the diversity of the swarm is reduced and allows earlier convergence. A high weight on the cognitive component causes a fast convergence towards the one good solution of a single particle. Considering the numbers of unknowns of the following applications, a few runs were used to test suitable numbers of particles. In the end, a swarm consisting of 400 particles is chosen. The number of iterations is limited to 1000 per run which allows for a sufficient number of restarts to get a representable ensemble of solutions.

6.1.2. Optimization

First geometry-only optimizations are run to test the constellations of swarm parameters and GWOs as described above, considering the solution ensembles and convergence. This is done with initial model *i1*. The most promising combination of swarm and GWO parameters is then kept for further applications of POGO. These include the usage of initial model *i2*, in order to address the influence of the starting model, and also geometry optimizations combined with density optimization.

Geometry-only optimization (initial model 1)

For the geometry optimization with initial model *i1* overall 18 runs are made: 6 weighting parameter constellations per number of GWOs, as described above and listed in Table 6.2. The runs are referred to as *RunX_ oY_ iZ*, where X corresponds to the constellation of weighting parameters as defined in Table 6.2 ($X \in \{1, 2, 3, 4, 5, 6\}$), Y refers to the number of GWOs ($Y \in \{5, 7, 10\}$) and Z identifies the initial model that is used ($Z \in \{1, 2\}$). Each of these runs estimates an ensemble of solutions. Not all results are graphically shown here but to get an overview, all results are summarized in Table 6.3 in terms of anomaly misfit (RMS) and standard deviation for each solution ensemble. The misfit shows that the fitting of the anomaly improves with an increasing number of GWOs, although the standard deviation does not improve to the same extent (apart of a few exceptions). When comparing the results of the different runs row-wise, related to the same number of GWOs, then *Run5* was the most successful for 7 and for 10 GWOs. But the anomaly misfit really only gives an overview and tells if optimization was possible. A good misfit does not necessarily mean a good (or reasonable) geometry fit. The solutions must also be considered under the geometric viewpoint which is done here for the two mentioned results. They are displayed in Figure 6.3 and the following discussion is reduced to these two.

	Anomaly misfit and standard deviation [10^{-5} m/s^2]					
n_{GWO}	Run1	Run2	Run3	Run4	Run5	Run6
5	1.094 ± 0.283	0.740 ± 0.236	0.906 ± 0.347	0.475 ± 0.296	0.610 ± 0.284	0.720 ± 0.279
7	0.967 ± 0.214	0.492 ± 0.297	0.562 ± 0.200	0.578 ± 0.295	0.377 ± 0.249	0.528 ± 0.247
10	0.670 ± 0.182	0.290 ± 0.127	0.567 ± 0.246	0.576 ± 0.409	0.173 ± 0.065	0.363 ± 0.233

Table 6.3.: *Test of PSO weighting parameters with varying number of GWOs. Mean and standard deviation are calculated from the gravity anomalies of each ensemble of solutions.*

Figure 6.3 (top) shows the two complete solution ensembles, superposed in one plot each (geometries and anomalies, respectively). Below them is one manually selected solution from the better half of the respective ensemble (according to misfit) which constitutes one of the geophysically most reasonable models. The single model plots also contain the paths of the operators as a means of visualization how the geometry deformations are achieved. The convergence behavior of the runs is plotted in the bottom panels. At the moment, the only quantitative assessment of model solutions is that given in Table 6.3. Further assessment of the geometries is not yet implemented in the program (rf. to Section 5.6). However, the superposed plot of an ensemble conveys a good visual identification of a mean model geometry. This geometry is indicated at places of strongest overlap. The scatter of overlapping geometries can be interpreted as a measure for the reliability of or confidence in the mean model.
In both runs the overlapping geometries indicate the expected diapir structure. The uplift, that was already indicated in the initial model, is continued and in both runs the upper dimensions of the diapir are replicated. *Run5_ o10_ i1* created a broader diapir that comes closer to the expected geometry than the results from *Run5_ o7_ i1*. The amount of scattering within both ensembles is quite similar with the exceptions that *Run5_ o7_ i1* has more uncertainty within the diapir (the crossing polygon lines from different solutions in the upper half of the diapir) and *Run5_ o10_ i1* has more uncertainty in the layering to the sides of the diapir. This tells us that the 7 GWOs are not entirely capable of reproducing the expected structure and the 10 GWOs start to modify areas of the model that already match the expected geometry but help to increase the anomaly

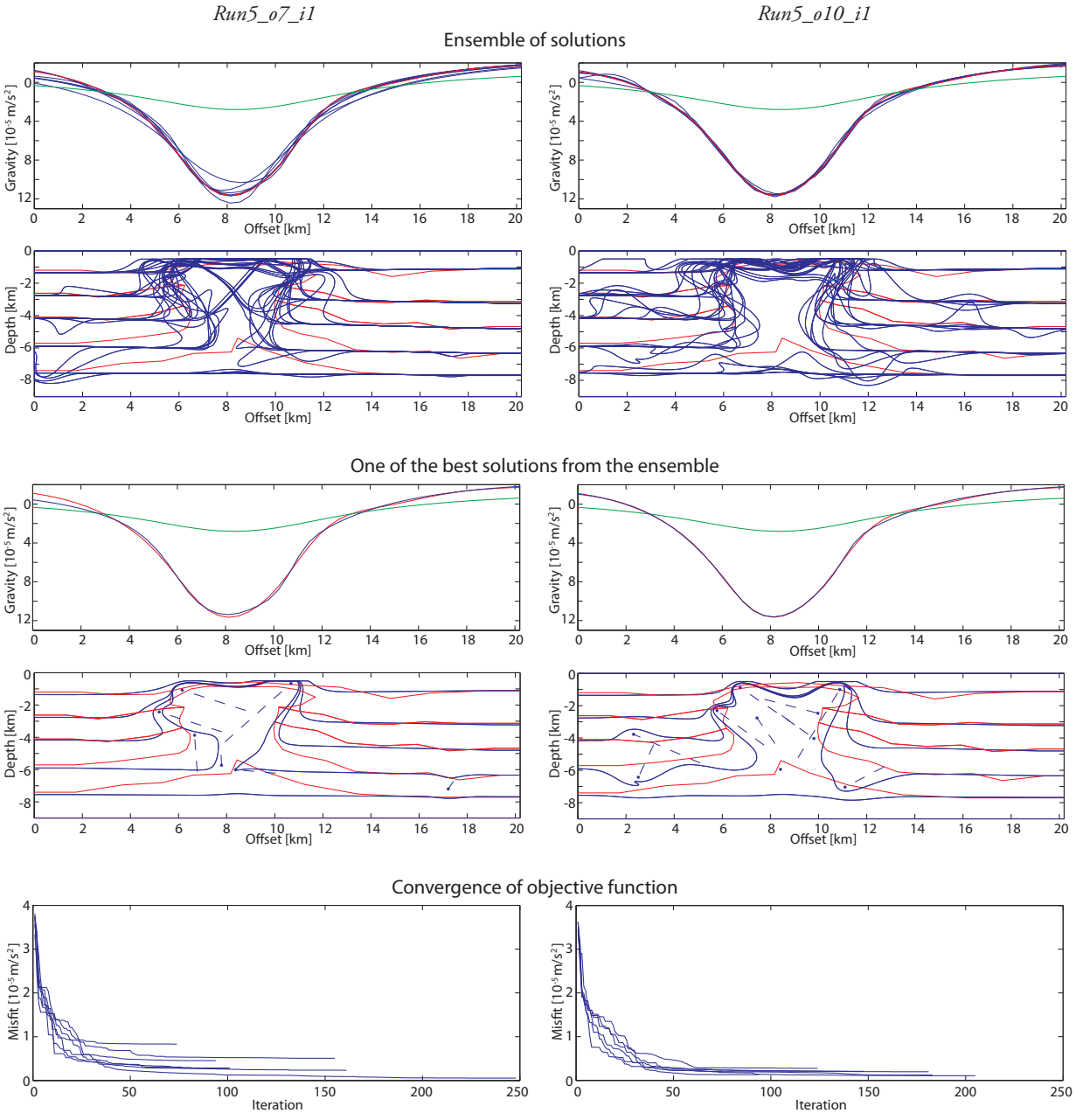

Figure 6.3.: *PSO results for salt diapir from* Run5 *using initial model* i1. *Red: Expected model and anomaly. Green: Initial anomaly. Blue: Results. The dashed blue lines draw the GWO paths, the path end is marked by the asterisk.*

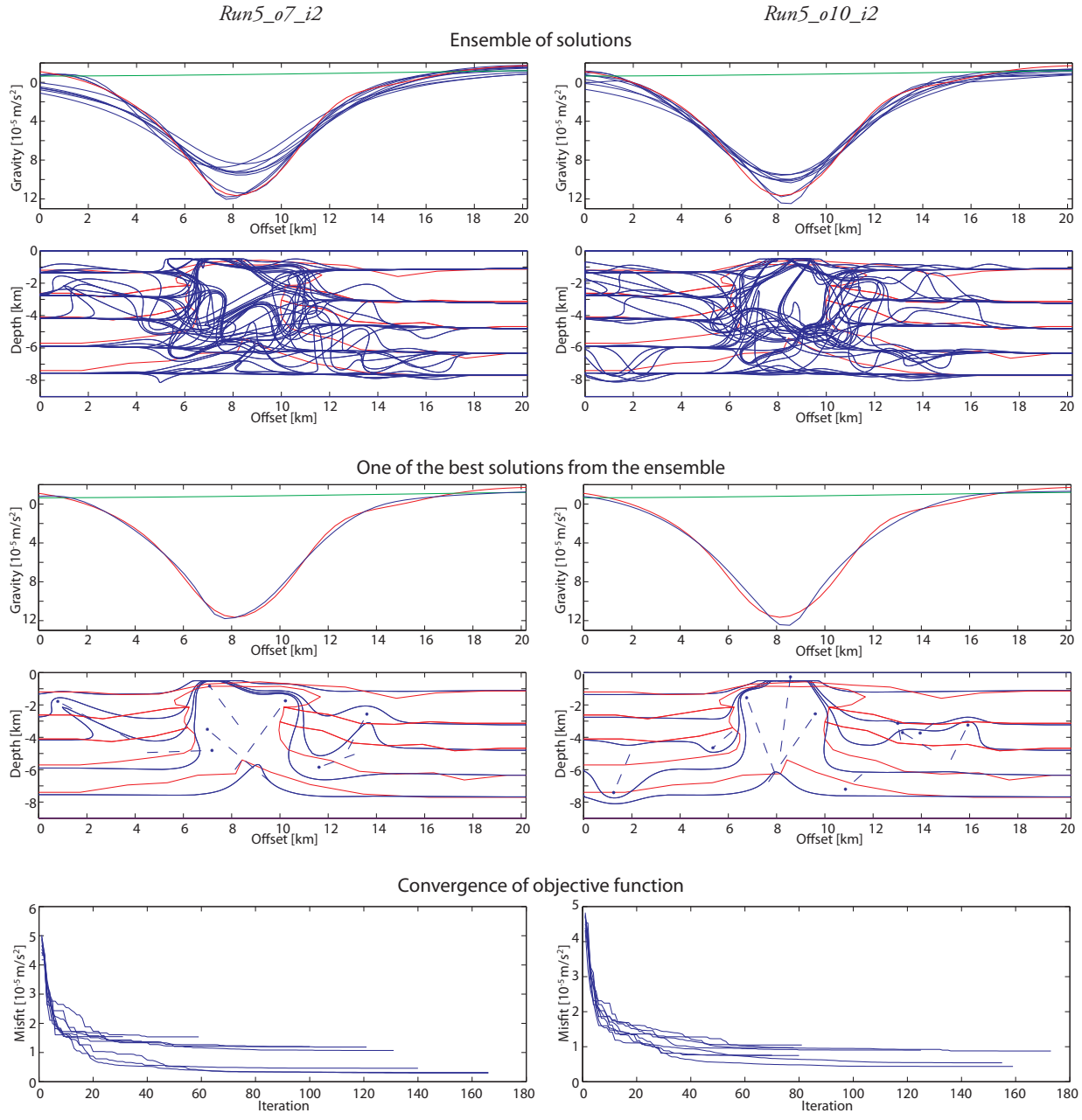

Figure 6.4.: *PSO results for salt diapir from Run5 using initial model* i2*. Red: Expected model and anomaly. Green: Initial anomaly. Blue: Results. The dashed blue lines draw the GWO paths, the path end is marked by the asterisk.*

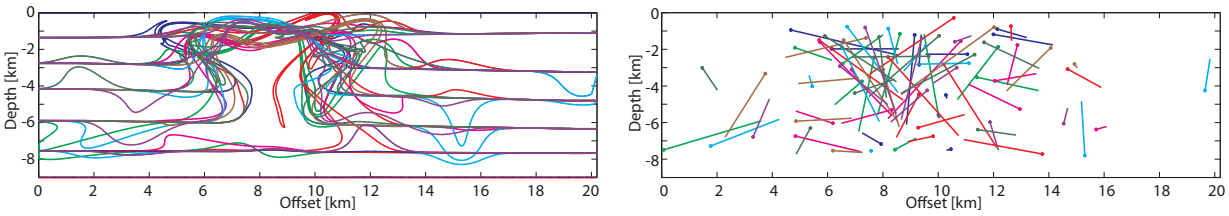

Figure 6.5.: *Plot of the operator paths of all global best constellations within a solution ensemble. Each solution is plotted in a different color. The number of operators per particle was 10, the number of restarts was 8, i.e. 80 operator paths are plotted.*

fit. Both runs did not accomplish the uplift of the Zechstein-Permian horizon directly beneath the anomaly low (except for one single solution). This uplift would have caused the long wavelength fit that was gained in *Run5_o10_i1* by modifying the geometry to the sides of the diapir.
The convergence behavior of the two runs is also similar. *Run5_o7_i1* performed 7 restarts after convergence was reached and *Run5_o10_i1* performed 6. The improvement of the misfit for both runs happens at the same rate and after approximately 50-75 iterations further improvements in misfit are only small, until finally the convergence criterion initiates the restarts. The run with 10 operators converged more often to a similar low misfit value. This behavior is also reflected in the superposed anomaly plot in the top of Figure 6.3, causing the low mean misfit with the extremely small standard deviation (Table 6.3). From a mathematical point of view, the optimization with 10 GWOs is better (in terms of misfit), from a geophysical point of view, it is slightly exaggerated in terms of reasonability. The latter can be controlled by constraints and also by the manual solution selection by the interpreter.

Geometry-only optimization (initial model 2)

When using initial model *i2*, the superposed solution ensembles give no clear indication on the kind of deformation that is expected (Figure 6.4). Two runs were made (*Run5_o7_i2* and *Run5_o10_i2*) that use the same PSO and GWO parameters as the two preferred solutions discussed above with initial model *i1*. The ensembles of solutions are very heterogeneous, with a much bigger scattering than with initial model *i1* and the expected diapir structure is barely recognized. The number of solutions that create a Zechstein diapir and those which explain the anomaly by depression of the upper lower density layers is about the same. Also the PSO converges earlier, initiating 9 and 8 restarts, respectively. The anomaly misfit is with $(0.999 \pm 0.508) \cdot 10^{-5}\,\mathrm{m/s^2}$ for *Run5_o7_i2* and $(0.784 \pm 0.211) \cdot 10^{-5}\,\mathrm{m/s^2}$ for *Run5_o10_i2* considerably higher than for the previous two solutions. However, both runs have in their ensemble at least one solution that matches anomaly and expected model geometry quite well. The both solutions displayed in Figure 6.4 are the ones with overall best misfit. Similar to the previous two runs, both solutions have the unwanted deformations to the sides of the diapir but they also both show an uplift of the Zechstein-Permian horizon. This occurred only for one single solution with initial model *i1* (Figure 6.3, *Run5_o7_i1*).

Variety of global best solutions

An exemplary visualization of the distribution and variety of optimization solutions is given in Figure 6.5. It shows an ensemble of 8 model solutions and also the GWOs that produced these solutions. Geometries and corresponding operators (10 GWOs per geometry) are color-coded to help

identify their belonging. Although the central parts of the deformed geometries show similarities, they are not found in the GWOs. They are well distributed, even moving in opposing directions. An operator constellation does not tend to be found twice, which means that an optimum in the search space in not found twice. In the middle of the modeling area, an accumulation of operators is found. This is expected as this is the region of major modifications (the uplift of the diapir).

Geometry and density optimization

Optimizing both, geometry and densities, increases ambiguity significantly. Therefore, only 7 GWOs are used which keeps the dimension of the search space to 41 (35 GWO parameters and 6 density values). The weighting parameter constellation from previous *Run5*, which was a successful combination in the geometry-only optimizations, is also used here. All other swarm parameters remain the same as before, i.e. 400 particles and 1000 iterations. The optimization set-up is already in favor of the expected model: Initial model *i1* is used which already contains a slightly uplifted structure. Three runs are made with varying constraints on the densities. The first two runs use the original densities as initial values but they are allowed to be modified within box constraints. POGO uses randomly distributed values (within their box constraints) as initial parameters for the unknowns of the optimization. This means initial geometry and densities are not regarded for the estimation of any individual or global best position. Initial values are altered from the first iteration on. This way, the application will show how close the estimates are still to the original/-expected density values. *Run5_o7_i1_d1* allows only very small changes of $\Delta\rho_1 = \pm 0.1\,\mathrm{t/m^3}$. The second test (*Run5_o7_i1_d2*) has a bit more freedom with allowed changes in a range of $\Delta\rho_2 = \pm 0.2\,\mathrm{t/m^3}$. The third application (*Run5_o7_i1_d3*) sets all initial densities equally to $\rho_{init} = 2.3\,\mathrm{t/m^3}$ and allows optimization within $\Delta\rho_3 = \pm 0.3\,\mathrm{t/m^3}$ which is sufficient to reach the expected densities.

The optimization results are shown in Figure 6.6. Next to the superposed anomalies and model geometries, the density results are plotted as density diagrams. These diagrams also contain a mean density model with standard deviation. The density results for the first two runs are additionally listed in the appendix (Tables B.4 and B.5). More interesting, because more heterogeneous, are the density results from the third run. They are listed here in the text in Table 6.4.
In the first two applications, the densities remain relatively close to their initial values (which are also the expected values), although the box constraints actually do allow for larger changes. The sediment densities tend to be increased, whereas the salt density is mainly reduced. This increases

	Densities [t/m^3]									
Geology	Init	Sol_1	Sol_2	Sol_3	Sol_4	Sol_5	Mean	Std	Orig	Diff
Tertiary	2.300	1.924	2.313	2.436	2.689	2.615	2.395	0.302	2.170	-0.225
Cretaceous	2.300	2.210	2.241	2.332	2.330	2.287	2.280	0.054	2.270	-0.010
Jurassic	2.300	2.686	2.691	2.527	2.374	2.612	2.578	0.132	2.370	-0.208
Triassic	2.300	2.546	2.617	2.376	2.466	2.421	2.485	0.097	2.470	-0.015
Zechstein	2.300	1.895	1.880	1.895	1.837	1.903	1.882	0.027	2.070	0.188
Permian	2.300	2.661	2.172	2.378	2.313	2.169	2.339	0.202	2.570	0.232

Table 6.4.: *Ensemble of optimized densities from the third run that used uniform initial densities. The table includes mean densities, standard deviations and differences from expected values.*

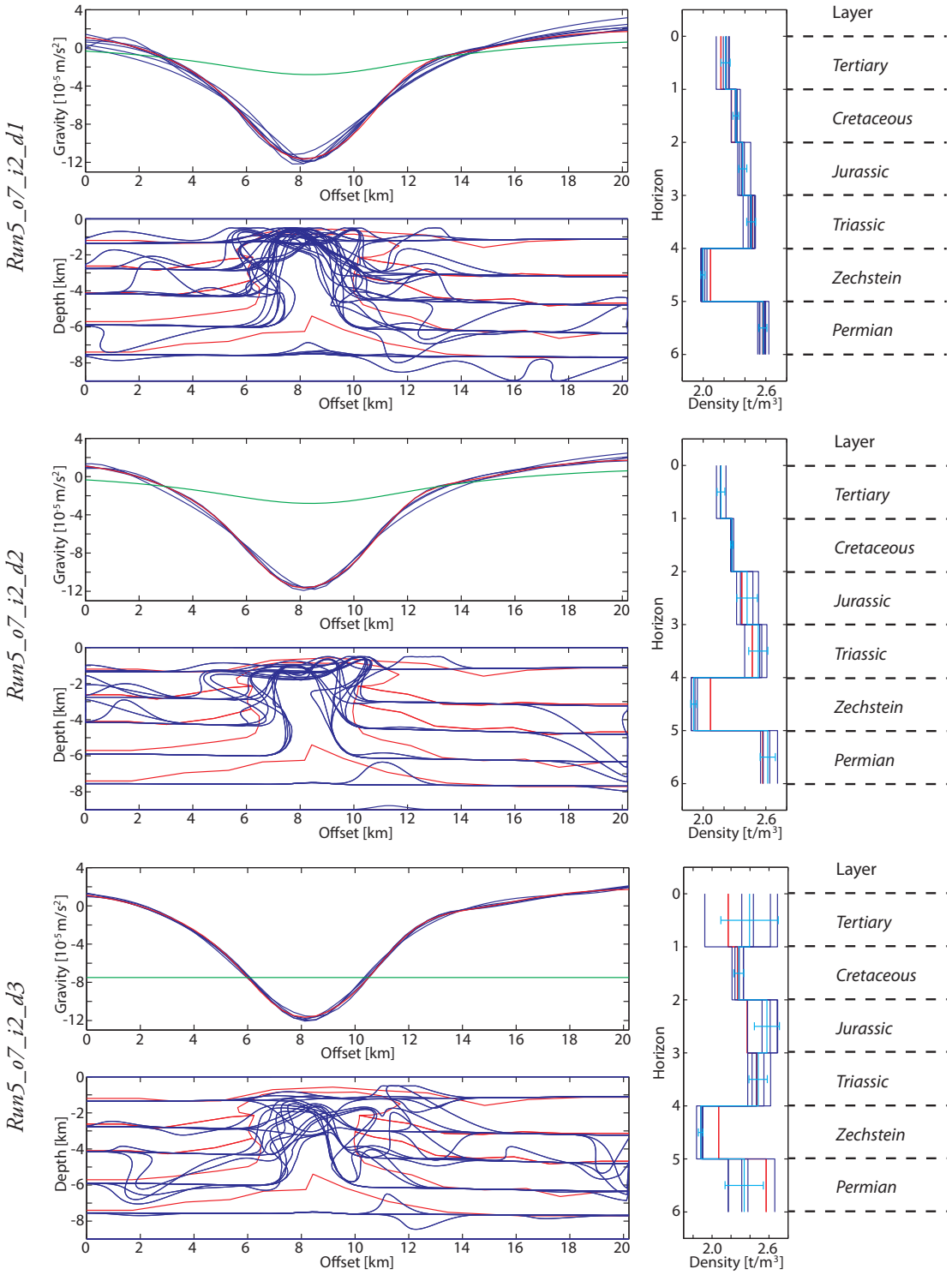

Figure 6.6.: *Ensembles of solutions for salt diapir after optimization of geometry and density. Three runs were made with varying initial densities and density constraints (see text). Red: Expected model and anomaly. Green: Initial anomaly. Blue: Results. Cyan: Mean densities and standard deviations.*

the density contrast between the diapir and the sediments, even more so for *Run5_ o7_ i1_ d2*. The geometry optimization still finds the right GWO constellations and produces the uplift. However, and this is assumed due to the increased density contrast, the diapir becomes smaller, compared to the geometry-only optimization. The number of restarts are fewer for *Run5_ o7_ i1_ d2*, meaning that the PSO required longer to converge towards an optimum. This is caused by the more "flexible" solution due to the less hard density constraints.
Starting the optimization with a homogeneous density model (*Run5_ o7_ i1_ d3*) proves to be more difficult for POGO. The replication of the expected geometry is not as good as in the previous two runs. An uplift is recognizable in the solution ensemble but also a lot of deformations are applied to the sides of the expected diapir. The deformations to the sides - together with the estimated densities - indicate that the GWO parametrization is sensitive to the shift between measured and calculated anomaly. Those deformations most likely occurred in order to fit the "wings" of the anomaly in that region. Interesting are the mean and standard deviations of the estimated densities. Except for the Zechstein body, small standard deviations always correlate with a good fit of the mean density to the expected value. This is not self-evident, as seen with the Zechstein body, which has the smallest standard deviation but a rather poor density fit.

6.2. Capel and Faust Basins

The model of the Capel and Faust Basins, off the east coast of Australia, was already addressed in Section 4.3, where the linear property inversion was applied. One of the conclusions from that previous modeling was that changes in the model geometry might be necessary to further improve the anomaly fit. Therefore, it is now used for application of the geometry optimization tool. The linear inversion continuously estimated a density reduction for the upper sedimentary layer throughout all applications and runs (Sections 4.3.1 and 4.3.2). For this reason, the following applications will be excluding and including a density optimization. Compared to the previous salt dome model, the Capel and Faust Basins setting offers an example of a large modeling area with a vertical extent that includes the Moho.

As the optimization operates only in 2D, a vertical section of the 3D model is extracted and used for the application (Figure 6.7). The 2D model section is built of 6 polygons that are defined by 720 vertices. Measurements were also extracted along this profile, they are given at 116 stations with a spacing of 3 km. The 3D model response is calculated based on the formulas from Götze and Lahmeyer (1988) and the anomaly fit has a correlation of 91.8% with a standard deviation of $4.7 \cdot 10^{-5}\,\mathrm{m/s^2}$. Along the extracted 2D section, the correlation is 90.9% with a standard deviation of $6.7 \cdot 10^{-5}\,\mathrm{m/s^2}$. The optimization tool uses the 2D calculation based on the formulas from Won and Bevis (1987) and the reduction from 3D to 2D modeling has a prominent effect on the anomaly along the profile. In Figure 6.8 the extracted anomaly values calculated in 3D are plotted together with the 2D calculated values. Due to the differences in the calculated anomaly, a new anomaly shift needs to be estimated. Calculating it as the mean difference between measured and calculated anomaly, it is estimated as $g_s = 43.12 \cdot 10^{-5}\,\mathrm{m/s^2}$. The anomaly correlation for the 2D (initial) model is only 86.4% with a standard deviation of $6.6 \cdot 10^{-5}\,\mathrm{m/s^2}$.

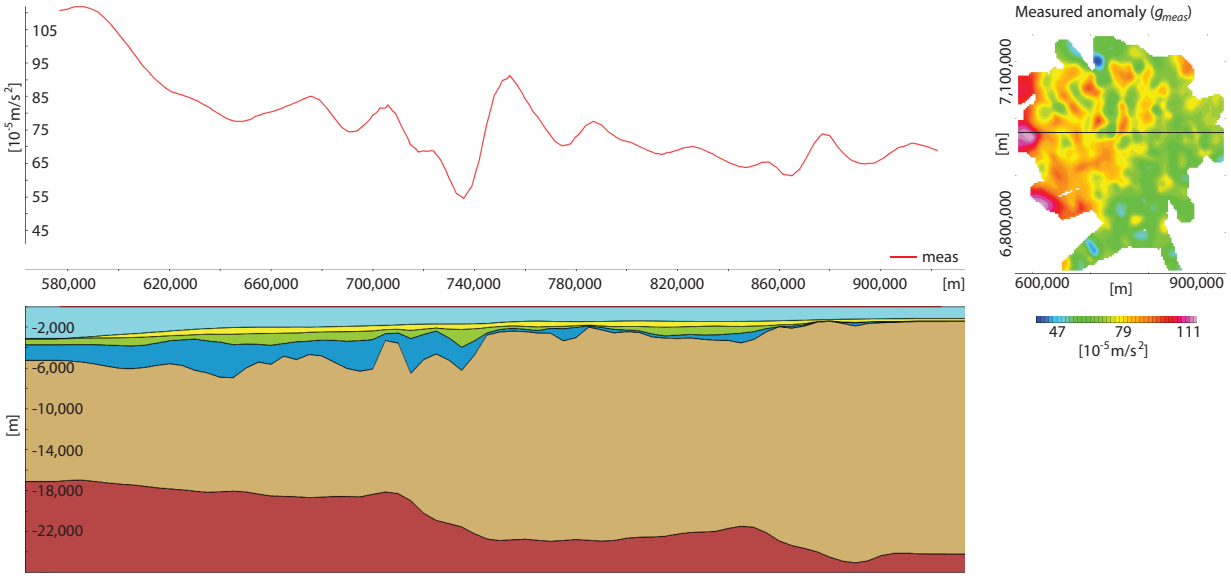

Figure 6.7.: *Extracted cross section from the Capel and Faust Basins IGMAS model (vertically exaggerated by factor 4) with measured gravity anomaly. The location of the section is at $y = 6,980,000\,m$ and indicated by the black line in the gravity map on the right.*

6.2.1. Optimization

This example has a larger lateral and vertical extent than the previous salt diapir. Therefore, the GWO settings for the optimization need to be adjusted. Preceding tests with few particles and few iterations gave adequate indications on operator sizes and movement path lengths as well as on the required number of operators. The basement depocenters have diameters of 10 - 20 km and to gain reasonable geometry modifications operators require radii between 5 - 50 km. Path lengths are limited to up to 4 km, preventing the horizons to be moved too far from their initial positions. Initial tests were made with 10, 15 and 20 operators at which 20 operators proved to be most promising. In the following, a swarm of 300 particles is used and the PSO is run with 2000 iterations. The weighting parameters of the swarm are set to $\omega = 0.5$, $c_1 = 2.0$ and $c_2 = 0.9$ which corresponds to the setting from *Run5* in the previous example.

In total four different optimization set-ups are tested, two optimizations only on the geometry and two that also include densities. Each of these two settings is used on two different depth extents of the active modeling area. The focus of the Capel and Faust Basins interpretation lies on the top basement with its depocenters. Therefore, one optimization set-up has a restricted active modeling area that only comprises the upper part of the model (down to 12 km), excluding the Moho. However, part of the misfit between measured and initial anomaly looks more like a long wavelength signal which would then ask for modifications of the Moho. Also, iterative inverse approaches often tend to mainly explain density anomalies in the upper parts of a model due to the inverse square relation, which is why these algorithms usually contain depth weighting (e.g. Li and Oldenburg, 1998; Fregoso and Gallardo, 2009). It is interesting to test if POGO behaves in a similar way or if the Moho is included in modifications. The two set-ups that include densities in the optimizations use box constraints of $\pm 0.5\,t/m^3$ on the initial densities, except for the water density which is not subject to changes (see Section 4.3).

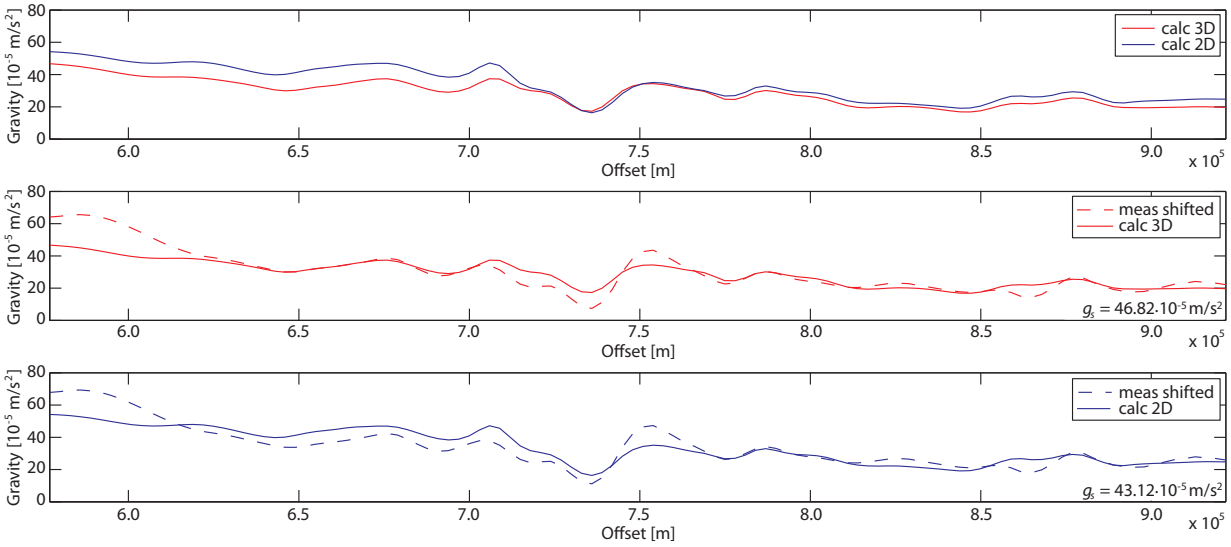

Figure 6.8.: *Gravity anomaly along the cross section extracted from the 3D model, showing the difference between 3D and 2D modeling. Top: The two calculated anomalies using 3D and 2D algorithms. Middle: Measured and calculated anomaly from the 3D model. Bottom: Measured and calculated anomaly from the 2D model. g_s is the respective shift value removed from the measured anomaly.*

Geometry-only optimization

The two ensembles of solutions for shallow and deep active modeling area are given in Figure 6.9. Displayed are the initial model geometry and the solution ensembles, as well as their corresponding gravity anomalies and the measured anomaly. Additionally, all anomaly fits for the solutions of the ensembles are given in Appendix A, Table B.6.

In the first run with the shallow modeling area, the PSO initiated 9 restarts and all solutions provide a clearly improved anomaly fit compared to the initial model (Figure 6.9 a)). All models in the ensemble show the same trend in how to optimally explain the gravity anomaly. They all experienced an uplift of the horizons to the west and at the center of the profile, to compensate for the mass deficit that is present in the initial model. In a similar manner, the mass excess (profile-km 610 to 740) is compensated by a lowering of the horizons.

When geometry modifications are allowed over the entire depth extent of the model, as in the second run, also the Moho geometry is changed (Figure 6.9 b)). The trend of uplifting and lowering of the horizons is the same as in the previous run. However, the amount of movement is smaller because part of the change in the calculated anomaly is gained from the Moho adjustments. The anomaly fit is in general better for all solutions of the ensemble. In this second run, fewer restarts were initiated, although the initial convergence (first 200 iterations) of the objective function is similar to the previous run (Figure 6.11). However, for the deep modeling area, the PSO continues to achieve further improvements of the model that are still big enough to prevent the restart of the swarm.

Plotting the ensembles of model solutions conveys again a visual identification of mean models with deviations. The distribution of the models also allows a clear identification of areas, where

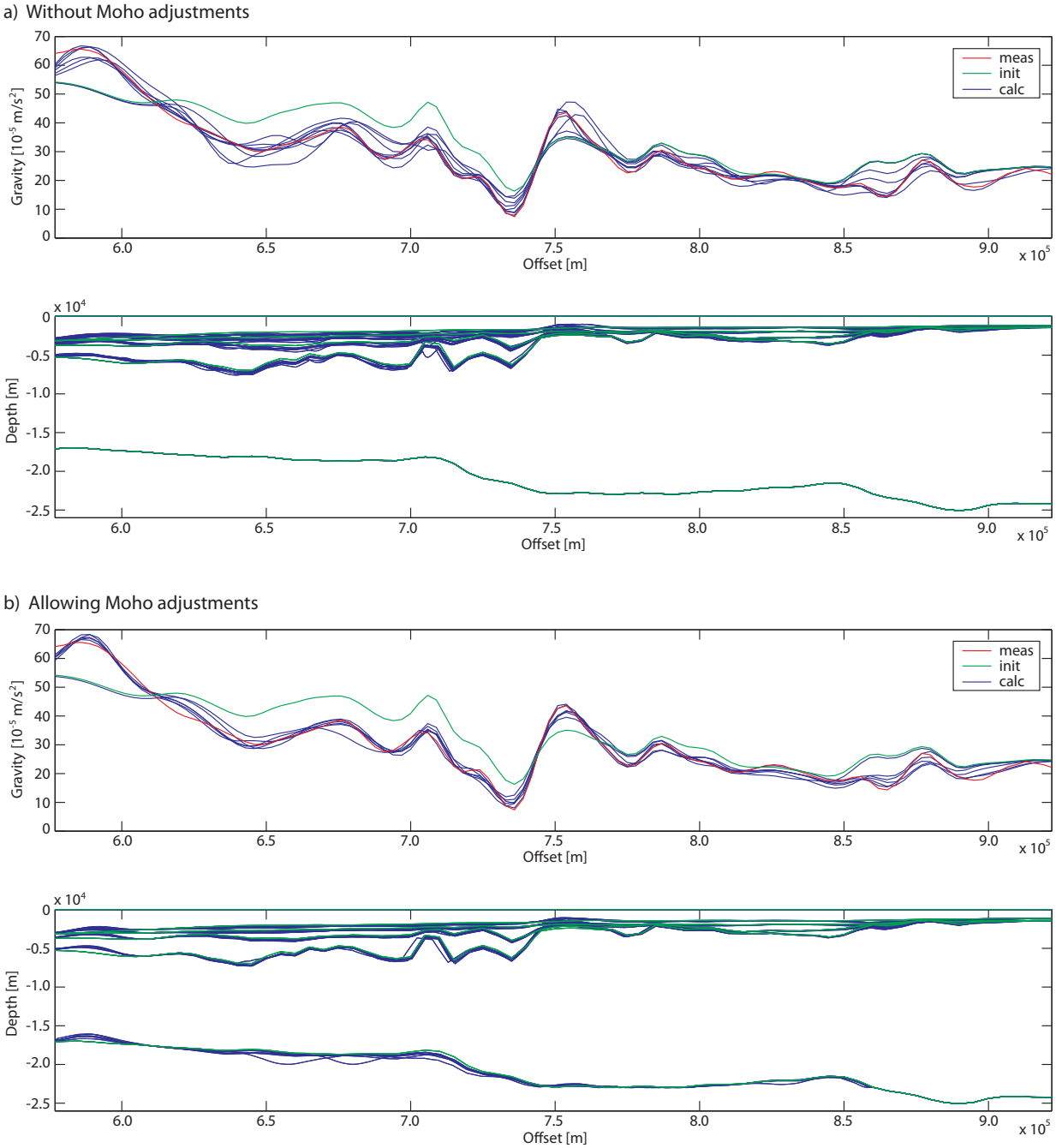

Figure 6.9.: *Two ensembles of model solutions for the Capel and Faust Basins resulting from geometry-only optimizations. a) Shallow modeling area that does not involve the Moho. b) Deep modeling area that also allows Moho modifications. Red: Measured gravity anomaly (shifted). Green: Initial model and anomaly. Blue: Estimated model solutions and anomalies.*

the model needs to be adjusted and how a better anomaly fit can be gained. Although a mean optimized model solution cannot be extracted yet, this interpretation can be used as a measure of confidence in the initial model.
Regarding the anomaly correlations and standard deviations it seems that including the Moho in the optimization process is beneficial. And when considering the convergence behavior of both runs, this is supported. When allowing changes only in the upper part of the model, POGO more often runs into local minima. When including the deeper part of the model in the optimization, the misfit curve is more smooth and constantly reaches a better optimum.

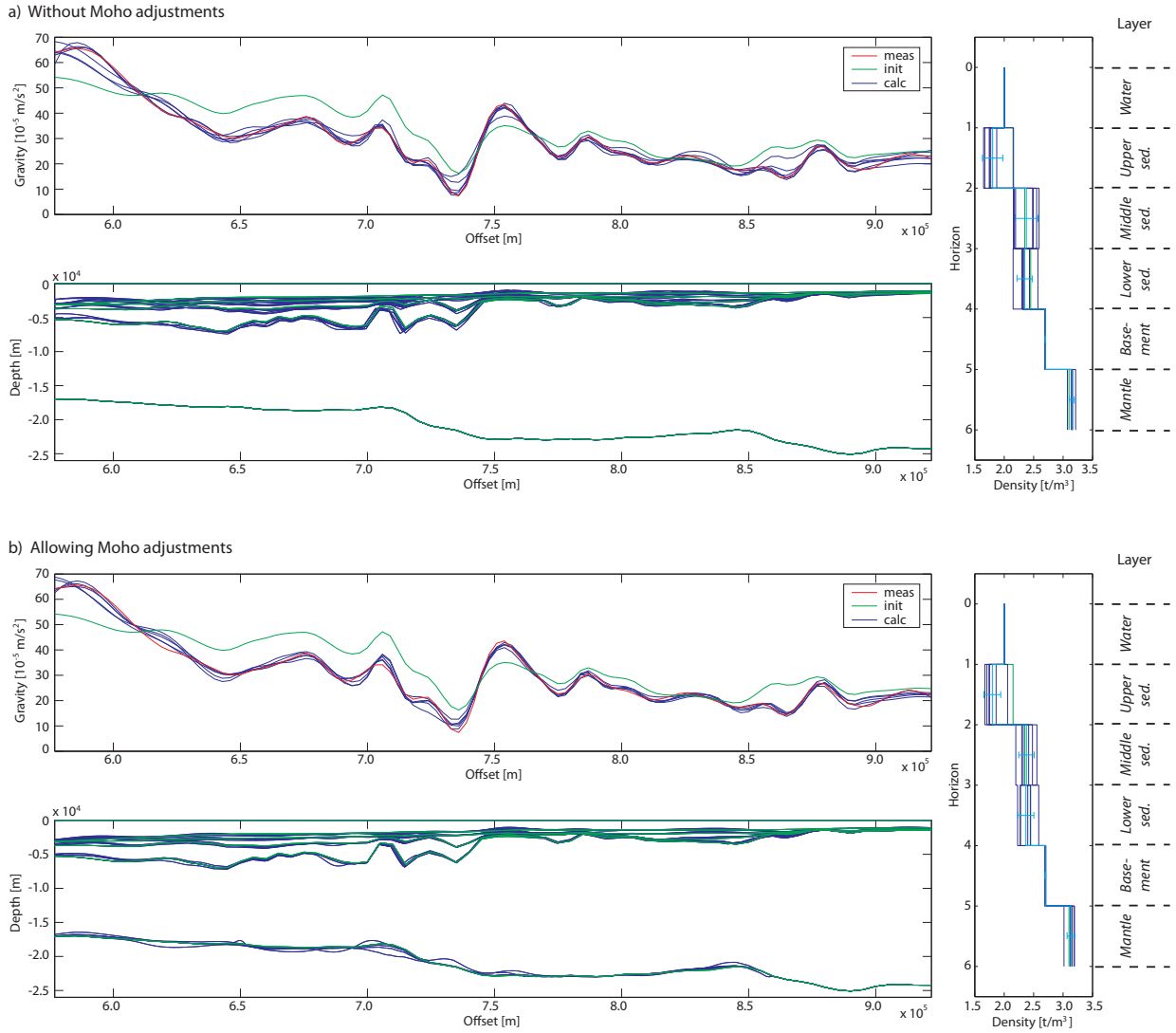

Figure 6.10.: *Two ensembles of model solutions for the Capel and Faust Basins resulting from geometry and density optimizations. a) Shallow modeling area that does not involve the Moho. b) Deep modeling area that also allows Moho modifications. Red: Measured gravity anomaly (shifted). Green: Initial model geometry, densities and anomaly. Blue: Estimated model solutions, densities and anomalies. Cyan: Mean densities and standard deviations.*

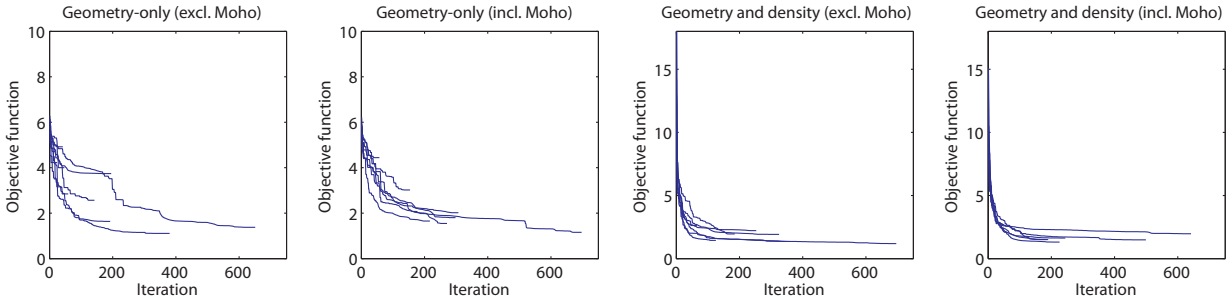

Figure 6.11.: *Convergence of objective function for Capel and Faust Basins.*

Geometry and density optimization

The next two runs add densities to the optimization process. The active modeling areas are the same as before. The optimized geometries and anomalies are plotted in Figure 6.10, together with density profiles. The density plots also contain mean density models with standard deviations calculated from the ensembles and all results are listed in the appendix (Tables B.8 and B.9).
The geometry changes follow the same trend as seen in the geometry-only optimizations but they are not as strong. The remaining part of anomaly fitting is achieved by the density changes. With $\pm 0.5\,\mathrm{t/m^3}$ the constraints in the initial densities were relatively wide. Therefore, variations from the initial values are quite strong for some of the model bodies and in some cases even a negative gradient for the sedimentary layers is produced. The mean densities for basement and mantle show the smallest variations, they also go along with very small standard deviations.
Due to the manipulations of the density during initialization of the swarm, the first values of the objective function are much higher than in the previous two examples (Figure 6.11). But the main improvement of the misfit is already gained after approximately 50 iterations and the PSO is reset earlier.

6.3. Discussion

The two examples in this chapter gave a good demonstration on how geometry modifications can be achieved by applying a PSO with a GWO parametrization, an approach that has potential. Even without a thorough use of constraining data (only box constraints for densities were defined and the extent of the active modeling area was varied), it was possible to reproduce the expected geometry (salt diapir) or modify the depths of structural horizons in a reasonable manner (basins). POGO is able to perform geometry changes of a small scale as seen in the first example of the salt diapir. The optimized GWO parameters were able to cause the expected uplift. But is was also seen that an uplift or diapir is a difficult geometry to attain. Several solutions in the ensembles that do optimize the anomaly fit, show a very different geometry than expected because a depression in the upper (lower density) layers causes a very similar signal as a (low density) diapir. The option of choosing from a solution ensemble is one or even the greatest benefit of global search methods, especially for potential field problems. A good measure to help with the model selection from the ensemble is the value of the objective function. A third of the solutions with the poorest evaluated objective functions most often provide model geometries that are not reasonable in a geophysical or geological sense. For a visual assessment it is therefore likely enough to only regard the best 2/3 of the solutions. This is also the reason why the optimization tool should be used

within a forward modeling environment that allows for a manual selection of a solution.

The first example mainly tested some of the swarm parameters and helped to get a feeling of how they influence the solution. It would now be interesting to carry out a proper assessment of the weighting constants in the velocity equation. The tests showed that the ensembles usually contain a variety of solutions which militates for the diversity of the results. On the other hand, the mean of the solution ensemble indicates a favorable structure that has geophysical reasonability. The influence of the number of particles on the solutions, and especially on the mean solution, would also be interesting to assess.
In the second example, POGO demonstrated a successful performance on a long wavelength application. The tests showed that modifications are applied throughout the entire depth extent of the model, without the need of any depth weighting. It also emphasized the consequences of the active modeling area. Its definition is a helpful means to exclude certain areas from the geometry optimization but this should only be done if the geometry is very well constrained by supplementary data. In comparison with other structural inversions, POGO offers the advantage that several horizons are modified in one go. This allows one horizon to experience larger changes because the neighboring horizons are also modified and do not block the changes.

The visual assessment of the solution ensemble already provides good insight into the optimization result but is only a preliminarily means. The scatter of the superposed polygon lines indicates the error of or confidence in the solution. For practical applications of the tool, the extraction of a mean model will be implemented.
When applying POGO to geometry and densities of a model, the optimization gets more complicated and the results are less clear. This is not surprising because the ambiguity of solutions is increased when densities are not fixed. To assess the solutions it is helpful to estimate a mean density model from the solution ensemble and regard its standard deviations but more investigations are required here. Although the density optimization is dealing with a few problems and requires some regulating parameters, the structural optimization still goes in the right direction and the expected structures are found, which is a very positive outcome. One problem that occurred in both examples is the development of negative density gradients in the sedimentary layers of the models. The compaction with depth should be regarded by the optimization tool, at least as an selectable option.

The two examples showed how the GWO parametrization works and that POGO can be successfully applied to potential field problems. It would be interesting to test and compare PSO to other optimizations, using the same parametrization. For example, a comparison of PSO and CMA-ES was carried out for a seismic optimization problem in Wilken (2009) with the result that a hybrid of both methods works better than the single methods. The hybrid uses PSO for the global search and then applies a local search with the CMA-ES close to a potential minimum. Comparisons like this and therein the evaluation of the method is considered future work.
Some improvements of the parametrization can be gained by smoothing the optimized models in order to remove peaks and spikes. Some of these can also be avoided when operator movement is decelerated while approaching constraining boxes and the borders of the active modeling area. Together with the extraction of a mean model it would be a good idea to eventually remove some vertices in regions where the refined model geometry is no longer required.

And some ideas on performance enhancement developed during the tests. The examples showed the different structural modifications gained by differently sized operators. In order to make use of the anomaly spectrum, it would be interesting to see if it brings advantages when first large and then small operators are applied consecutively. This would mean to first fit the long wavelength content of the anomaly and then continue with the short wavelength signals. This could also be used with the joint optimization of different data sets that have varying sensitivities (e.g. gradients, Chapter 2.1.3).
It is always helpful to include additional information through the definition of constraints in the modeling process. Instead of constraining boxes or in addition to them it would be beneficial to flag individual horizons and/or bodies that are not to be changed during optimization. This can be realized by adding the tool to a suitable user interface.

7. Conclusions and Outlook

The originally planned development of one inversion tool resulted in two tools in the end. The first one, CHAIN, is dealing with voxel and polyhedron models and uses a linear inversion technique to estimate physical properties. The second tool, POGO, can be applied to model geometries of 2D polygonal bodies and uses optimized spatial operators for geometry deformations. The developed parametrization is designed for vertex-based geometries in general, also 3D. It allows for tremendous reduction of unknowns (i.e. dimensionality of the optimization problem) and can also be used with other optimization methods than the here presented PSO.
The tools are applicable to different model representations and allow property estimations as well as structural modifications. Their calculation time, which lies within a few hours but is strongly dependent on model complexity and parametrization, is competitive with methods for other disciplines. Also considering that no parallel computing is yet involved. All this together offers the possibility for them to be combined with other geophysical modeling and interpretation tools.
Both tools are stand-alone programs which permits their further, individual development. They are still very flexible and can be adjusted in order to function with existing software. This will require most probably some format conversions. However, the handling of the tools, and therein the handling of the models themselves, suffers to a certain degree from the missing GUI, as has been seen and discussed in the two application chapters. While the work on the geometry modifications and optimization techniques was started, the implementation of the CHAIN tool (for polyhedrons) within IGMAS+ was carried out.
The planned, and already partly realized, combination with forward modeling helps to deal with the non-uniqueness in potential field modeling. The polyhedron-based property estimation in particular offers quick assessment of structurally derived models. It helps to gain improvements or points out model bodies that require further attention. By interacting with forward modeling, an evolving model can be led into a desired, geologically and geophysically reasonable direction. The estimation of an ensemble of various solutions for structurally optimized models, and the option to compare and choose, is also a great help in this aspect. The tools still leave a great amount of influence with the interpreter, may it be via the initial model geometry, the definition of regions and correlations or the size and amount of spatial operators, and they are purposely designed to be assistant and not autonomous.

3D implementation and method extension

The extension of the geometry optimization tool to a 3D implementation was beyond the scope of this thesis. Until now the tool is stand-alone without GUI or direct connection to one of the existing modeling software. However, the code can be adjusted in order to, e.g. work with the IGMAS+ modeling environment. This realization of a 3D application could use the 2D parametrization and would therefore be straight forward: At the moment, IGMAS+ uses 2D sections to construct a 3D geometry. On these vertical sections the model bodies are given as polygons. The GWOs could be applied simultaneously on several of these sections. After moving the vertices, the model

triangulation is renewed and the anomaly of the 3D model is calculated. This anomaly is then used for the evaluation of the objective function.
Application of the spatial operators to 3D polyhedron geometry requires some significant changes in the implementation, where the most demanding part is the extension of the on-the-fly discretization that the GWOs use when moving through a geometry. Assuming that a 3D model body surface is rendered by triangles, the previously 2D line discretization becomes a triangle discretization. How this could be done and what further changes or extensions of the program code are required was already discussed in Section 5.7.

The geometry optimization was applied to gravity data sets. A next step is now to extend the implementation to gravity gradient and magnetic data applications. Parametrization and optimization can be used just as before, what needs to be added are the respective forward routines. For a joint inversion of gravity and gravity gradient data (because they have the same potential caused by the same sources) it should be sufficient to modify the objective function in order for it to regard all involved data. This also allows for weighting of individual data sets during optimization. Weighting could e.g. be defined with regard to the data quality or with regard to the sensitivity of the data. It is to be expected that a joint inversion leads to improved optimization results. In case of a combination of gravimetric and magnetic data sets, it should be investigated if a multi-objective PSO is required (Engelbrecht, 2005). This implementation regards several different objective functions that might be conflicting. Aim of the joint optimization is a structural model that describes the involved data sets to best possible degree.

Integrated interpretation and combination with other methods

One of the motivations for developing these inversion tools was their usage in multi-method or integrated interpretation approaches. The combination and joint inversion with other potential field methods was already addressed in this work (linear property estimations with CHAIN) or in the outlook (geometry optimizations with POGO). But the multi-methodology should be expanded to further methods. Both presented tools and examples show the usefulness of potential field inversion and should be implemented in a multi-method workflow. Seismic data is usually utilized to guide or constrain potential field modeling and it is the first method to be regarded. In exploration geophysics the coupling is often done in the migration process for the development of the velocity-depth-model. More often these data is now also combined with the interpretation of magnetotellurics (MT) and controlled-source electromagnetics (CSEM). A possible workflow for an integrated approach, that does not necessarily involve joint inversion, is suggested by Lahmeyer et al. (2010) (Figure 7.1). This scenario uses different model representations in an alternating process and takes advantage of inversion methods and interactive forward modeling.

The combination of the methods in a joint inversion approach can be addressed by parameter or structural coupling. One approach could be the joint inversion of gravity and surface waves. The seismic method is sensitive to layered structures and suffers from signal loss in the vicinity of scatterers. Those scatterers are usually bodies or sources with a distinctive property contrast. The gravity method is sensitive to this kind of structures. Density can be used as a coupling parameter as it is directly given in the seismic shear wave velocity. This joint inversion approach would be applicable to imaging problems where a combination of layered subsurface and scatterers is expected. Those targets are present in a range of different scales, e.g. cavities and scatterers in

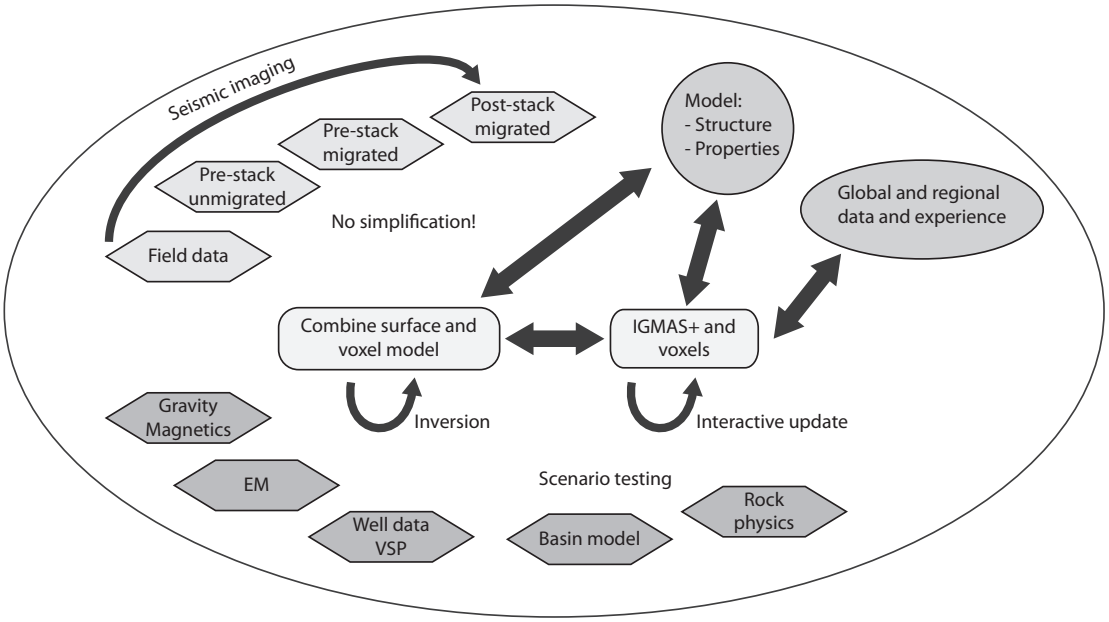

Figure 7.1.: *Possible workflow for interdisciplinary modeling and interpretation (modified after Lahmeyer et al., 2010).*

engineering and archaeological geophysics (small scale), filled trenches (intermediate scale), and salt structures in exploration geophysics (large scale).

8. References

M. R. Alvers. *Zur Anwendung von Optimierungsstrategien auf Potentialfeldmodelle.* PhD thesis, FU Berlin, 1998.

G. Bachmann and S. Grosse. Struktur und Entwicklung des Norddeutschen Beckens - geologische und geophysikalische Interpretation einer verbesserten Bouguer-Schwerekarte. *Niedersächsische Akademie der Geowissenschaften*, 2:24–47, 1989.

R. Baldschuhn, F. Binot, S. Fleig, and F. Kockel, editors. *Geotektonischer Atlas von NW-Deutschland und dem deutschen Nordsee-Sektor—Strukturen, Strukturentwicklung, Paläogeographie.*, volume 153. Geol. Jahrbuch (A), 2001.

G. Barnes, J. Lumley, P. Houghton, and R. Gleave. Noise in FTG Data and its Comparison With Conventional Gravity Surveys, April 11-14 2010.

T. Beilecke, R. Meissner, and W. Rabbel. Abschlußbericht 1997 - 98 DEKORP, Deutsches Kontinentales Reflexionsseismisches Programm. Technical report, Christian-Albrechts Universität Kiel, Institut für Geophysik, 1998.

B. K. Bhattacharyya. Magnetic anomalies due to prism-shaped bodies with arbitrary polarization. *Geophysics*, 29:517–531, 1964.

F. Bilgili, H.-J. Götze, R. Pašteka, S. Schmidt, and R. Hackney. Intrusion versus inversion - a 3D density model of the southern rim of the Northwest German Basin. *International Journal of Earth Sciences (Geologische Rundschau)*, 98(3):571–583, 2009.

T. M. Blackwell and P. J. Bentley. Dynamic search with charged swarms. In *Proceedings of the Genetic and Evolutionary Computation Conference*, GECCO '02, pages 19–26, San Francisco, CA, USA, 2002. Morgan Kaufmann Publishers Inc. ISBN 1-55860-878-8. URL `http://dl.acm.org/citation.cfm?id=646205.682961`.

R. J. Blakely. *Potential Theory in Gravity and Magnetic Applications.* Cambridge University Press, 1996.

M. H. P. Bott. Two methods applicable to computers for evaluating magnetic anomalies due to finite three dimensional bodies. *Geophysical Prospecting*, 11:292–299, 1963.

J. Bouman, S. Fiorot, M. Fuchs, T. Gruber, E. J. O. Schrama, C. Tscherning, M. Veicherts, and P. N. A. M. Visser. GOCE gravitational gradients along the orbit. *Journal of Geodesy*, 85(11), 2011. ISSN 0949-7714. doi: 10.1007/s00190-011-0464-0.

S. P. Boyd. Linear dynamical systems. Technical report, Stanford University, 1996. lecture-notes 13 Estimation.

S. P. Boyd and D. Noll. Mmse estimation for 3D magnetic and gravitational anomaly surveys. Technical report, Statoil, January 1999.

S. P. Boyd and D. Noll. SOMGAN-Software for Interpretation of Magnetic and Gravitational Potential Field Data. Technical report, Statoil, 2000.

H.-J. Brink. The Bramsche-massif anomalies - again an open question? *Erdöl Erdgas Kohle*, 118: 18–22, 2002.

H.-J. Brink. Die Entstehung des Norddeutschen Beckens – ein Metamorphose-Modell. In *Deutsche Geophysikalische Gesellschaft, Mitteilungen*, volume 4, pages 2–18. J. Stoll im Auftrag der Deutschen Geophysikalischen Gesellschaft e.V., 2003.

H.-J. Brink. Die Intrusion von Bramsche - ein Irrtum im invertierten Niedersächsischen Becken? *Zeitschrift der Deutschen Gesellschaft für Geowissenschaften*, 164(1):33–48(16), March 2013. doi: http://dx.doi.org/10.1127/1860-1804/2013/0011.

B. Brockamp. Kurzbereicht über die im Gebiet um Osnabrück durchgeführten seismischen Arbeiten des Instituts für Reine und Angewandte Geophysik der Universität Münster. *Veröffentlichung der Deutschen Geodätischen Komission*, Heft 153(Reihe B):1–12, 1967.

W. C. Campbell. *Introduction to geomagnetic fields.* Cambridge Universit Press, 1997.

T. E. Davis and J. C. Principe. A simulated annealing-like convergence theory for the simple genetic algorithm. In R. K. Belew and L. B. Booker, editors, *Proceedings of the Forth International Conference on Genetic Algorithms*, pages 174–181, 1991.

DEKORPBasinResearchGroup. Deep crustal structure of the Northeast German basin: New DEKORP-BASIN'96 deep-profiling results. *Geology*, 1(27):55–58, 1999.

D. DiFrancesco, T. Meyer, A. Christensen, and D. FitzGerald. Gravity gradiometry - today and tomorrow. In *11th SAGA Biennial Technical Meeting and Exhibition Swaziland, 16-18 September*, pages 80–83, 2009.

M. Dransfield. Advances in airborne gravity gradiometry at Fugro Airborne Surveys. EGM 2010 International Workshop Adding new value to Electromagnetic, Gravity and Magnetic Methods for Exploration Capri, Italy, April 11-14 2010.

J. Ebbing, J. Bouman, M. Fuchs, V. Lieb, R. Haagmans, J. A. C. Meekes, and R. A. Fattah. Advancements in satellite gravity gradient data for crustal studies. *The Leading Edge*, 32(8): 900–906, 2013. doi: 10.1190/tle32080900.1.

R. C. Eberhart and J. Kennedy. A New Optimizer using Particle Swarm Theory. In *Proceedings Sixth Symposium on Micro Machine and Human Science*, pages 39–43, 1995.

A. P. Engelbrecht. *Fundamentals of Computational Swarm Intelligence.* Wiley, 2005.

ESA. Gravity field and steady-state ocean circulation mission. Reports for mission selection; the four candidate earth explorer core missions. ESA SP-1233(1), 1999.

E. Fregoso and L. A. Gallardo. Cross-gradients joint 3D inversion with applications to gravity and magnetic data. *Geophysics*, 74(4):L31–L42, 2009.

C. Gaina, D. R. Müller, J. Y. Royer, J. Stock, J. Hardebeck, and P. Symonds. The tectonic history of the Tasman Sea: a puzzle with 13 pieces. *Journal of Geophysical Research*, 103(B6): 12413–12433, 1998.

G. H. F. Gardner, L. W. Gardner, and A. R. Gregory. Formation velocity and density - The diagnostic basics for stratigraphic traps. *Geophysics*, 39:770–780, 1984.

M. Giebeler-Degro. *Zur Tiefenerkundung des Niedersächsischen Tektogens durch dreidimensionale Simulationsrechnungen.* PhD thesis, TU Clausthal, 1986.

D. Goldberg. *Genetic Algorithms in Search, Optimization and Machine Learning.* Addison Wesley, Reading, Massachusetts, USA, 1989.

F. S. Grant and G. F. West. *Interpretation theory in applied geophysics.* McGraw-Hill Book Co., 1965.

H.-J. Götze. *Ein numerisches Verfahren zur Berechnung der gravimetrischen und magnetischen Feldgrößen fr dreidimensionale Modellkörper.* PhD thesis, Technische Universität Clausthal, 1976.

H.-J. Götze. Über den Einsatz interaktiver Computergraphik im Rahmen 3-dimensionaler Interpretationstechniken in Gravimetrie und Magnetic. Habilitationsschrift. Technische Universität Clausthal, 1984.

H.-J. Götze and B. Lahmeyer. Application of three-dimensional interactive modeling in gravity and magnetics. *Geophysics*, 53(8):1096–1108, 1988.

C. Haase. Inversion of gravity, gravity gradient, and magnetic data with application to subsalt imaging. Diploma thesis, University of Kiel, 2008.

R. Hackney, P. Petkovic, T. Hashimoto, K. Higgins, G. Logan, G. Bernardel, J. Colwell, N. Rollet, and M. Morse. Geophysical studies of Australia's remote eastern deep-water frontier: Results from the Capel and Faust basins. In *ASEG Extended Abstracts*, 2009.

N. Hansen and A. Ostermeier. Completely Derandomized Self-Adaptation in Evolution Strategies. *Evolutionary Computation*, 9(2):159–195, 2001.

T. Hashimoto, N. Rollet, K. Higgins, G. Bernardel, and R. Hackney. Capel and Faust basins: Preliminary assessment of an offshore deepwater frontier region. In *PESA Eastern Australasian Basins Symposium III*, 2008.

T. Hashimoto, K. Higgins, R. Hackney, V. Stagpoole, C. Uruski, N. Rollet, G. Bernardel, G. Logan, and R. Sutherland. Capel and Faust basins: integrated geoscientific assessment of Australia's remote offshore eastern frontier. In *The Australian Petroleum Production and Exploration Association Conference 2009. The APPEA Journal*, volume 49, Extended Abstracts, 2009.

N. Hoffmann, H. Jödicke, B. Fluche, A. Jording, and W. Müller. Modellvorstellung zur Verbreitung potentieller präwestfalischer Erdgas-muttergesteine in Norddeutschland - Ergebnisse neuer magnetotellurischer Messungen. *Zeitschrift für angewandte Geologie*, 44(3):140–158, 1998.

N. Hoffmann, H. Jödicke, and L. Horejschi. Regional distrubution of the lower Carboniferous culm and Carboniferous limestone facies in the North German Basin—derived from magnetotelluric soundings. *Zeitung dt. Ges. Geowiss.*, 156:323–339, 2005.

J. Holland. *Adaption in Natural and Artificial Systems: An Introductory Analysis with Applications to Biology, Control and Artificial Intelligence.* MIT Press/Bradford Books, Cambridge, Massachusetts, USA, 2, first edition 1973 edition, 1992.

R. Inselmann. Dichte-Messungen in der Bundesrepublik Deutschland. *Erdöl-Erdgas*, 101(3):76–78, 1985.

W. Jacoby and P. L. Smilde. *Gravity Interpretation.* Springer-Verlag Berlin Heidelberg, 2009.

D. Karaboga and B. Basturk. A powerful and efficient algorithm for numerical function optimization: artifcial bee colony (ABC) algorithm. *Journal of Global Optimization*, 39:459–471, 2007.

A. Kaufmann, D. Cohen, and R. Yagel. Volume graphics. *Computer*, 26(7):51–64, 1993. ISSN 0018-9162. doi: 10.1109/MC.1993.274942.

G. S. Kimbell, R. W. Gatliff, J. D. Ritchie, A. S. D. Walker, and J. P. Williamson. Regional three-dimensional gravity modelling of the NE Atlantic margin. *Basin Research*, 16:259–278, 2004. doi: 10.1111/j.1365-2117.2004.00232.x.

S. Kirkpatrick and M. Vecchi. Optimization by simulated annealing. *Science*, 220, 1983.

A. Kolmogorov. *Grundbegriffe der Wahrscheinlichkeitsrechnung.* Berlin: Julius Springer, 1933.

J. Kuder. *3D Schwerefeldmodellierung zur Erfassung des tiefen Untergrundes im Nordost-Deutschen Becken.* PhD thesis, FU Berlin, 2002.

B. Lahmeyer, H.-J. Götze, S. Schmidt, M. R. Alvers, C. Plonka, and C. Fichler. Interactive 3D gravity modelling in IGMAS+ and the integration in the depth imaging workflow. In *72nd EAGE Conference & Exhibition incorporating SPE EUROPEC*, 2010.

Y. Li and W. Oldenburg. 3-D inversion of magnetic data. *Geophysics*, 61(2):394–408, 1996.

Y. Li and W. Oldenburg. 3-D inversion of gravity data. *Geophysics*, 63(1):109–119, 1998.

T. M. Lillesand and R. W. Kiefer. *Remote Sensing and Image Interpretation.* John Wiley & Sons, Inc., New York, 3 edition, 1994.

W. J. Ludwig, J. E. Nafe, and C. L. Drake. *The Sea*, chapter Seismic refraction, pages 53–84. Wiley-Interscience New York, 1970.

W. J. McKay. Energy Security Program Achievements - Towards Future Energy Discovery. GA Publication–Report 71823, Geoscience Australia, 20 June 2011.

R. Meissner and R. K. Bortfeld, editors. *DEKORP-Atlas.* 1990. ISBN 0387525122.

J. M. Mendel. *Lessons in Estimation Theory for Signal Processing, Communications, and Control.* Prentice Hall Signal Processing Series. Prentice Hall PTR, 1995.

W. Menke. *Geophysical Data Analysis: Discrete Inverse Theory*, volume 45 of *International Geophysics Series*. Academic Press Inc., revised edition edition, 1989. ISBN 0124909213.

N. Metropolis, A. Rosenbluth, M. Rosenbluth, T. A., and E. Teller. Equation of State Calculations by Fast Computing Machines. *Journal of Chemical Physics*, 21:1087–1092, 1953.

H. Militzer and F. Weber, editors. *Angewandte Geophysik, Bd. 1: Gravimetrie und Magnetik*, volume 51. Springer Verlag Wien, 1984.

M. N. Nabighian, M. E. Ander, V. J. S. Grauch, R. O. Hansen, T. R. LaFehr, Y. Li, W. C. Pearson, J. W. Peirce, J. D. Phillips, and M. E. Ruder. Historical development of the gravity method in exploration. *Geophysics*, 70(5):63ND–89ND, NOVEMBER-DECEMBER 2005a. doi: 10.1190/1.2133785.

M. N. Nabighian, V. J. S. Grauch, R. O. Hansen, T. R. LaFehr, Y. Li, W. C. Pearson, J. W. Peirce, J. D. Phillips, and M. E. Ruder. Historical development of the gravity method in exploration. *Geophysics*, 70(5):33ND–61ND, NOVEMBER-DECEMBER 2005b. doi: 10.1190/1.2133784.

D. Nagy. The gravitational attraction of a right rectangular prism. *Geophysics*, 31(2):362–371, 1966. doi: 10.1190/1.1439779.

L. L. Nettleton. Gravity and magnetic calculations. *Geophysics*, 7:293–310, 1942.

M. S. Norvick, M. A. Smith, and M. R. Power. The plate tectonic evolution of eastern Australasia guided by the stratigraphy of the Gippsland Basin. In K. Hill and T. Bernecker, editors, *Eastern Australasian Basins Symposium: a refocussed energy perspective for the future*, page 15–24. PESA Special Publication, 2001.

M. S. Norvick, R. P. Langford, N. Rollet, T. Hashimoto, K. L. Earl, and M. P. Morse. New insights into the evolution of the Lord Howe Rise (Capel and Faust basins), offshore eastern Australia, from terrane and geophysical data analysis. In J. Blevin, B. Bradshaw, and C. Uruski, editors, *Eastern Australasian Basins Symposium III: Energy security for the 21st century*, page 291–310. Petroleum Exploration Society of Australia Special Publication, 2008.

P. Petkovic. Preliminary results from marine seismic survey GA302 over Capel and Faust Basins. In *ASEG Extended Abstracts*, volume 1, pages 1–4, 2007. doi: 10.1071/ASEG2007ab202.

P. Petkovic. 3D Gravity Models of the Capel and Faust Basins, Lord Howe Rise. GA Publication–Record 70618, Geoscience Australia, 6 June 2011.

S. Petmecky, L. Meier, H. Reiser, and R. Littke. High thermal maturity in the Lower Saxony Basin: intrusion or deep burial? *Tectonophysics*, 304(4):317–344, 1999. doi: 10.1016/S0040-1951(99)00030-X.

I. Rechenberg. *Evolutionsstrategie '94*. Frommann-Holzboog, Stuttgart, 1994.

B. Sæther. *Improved Estimation of Subsurface Magnetic Properties using Minimum Mean-Square Error Methods*. PhD thesis, NTNU Trondheim, 1997.

M. Scheck. *Dreidimensionale Strukturmodellierung des Nordostdeutschen Beckens unter Einbeziehung von Krustenmodellen*. Scientific technical report str97/10, Freie Universität Berlin, GeoForschungsZentrum, Potsdam„ 1997.

S. Schmidt, C. Plonka, H.-J. Götze, and B. Lahmeyer. Hybrid modelling of gravity, gravity gradients and magnetic fields. *Geophysical Prospecting*, 59:1046–1051, 2011. doi: 10.1111/j.1365-2478.2011.00999.x.

M. Sdrolias, D. Müller, and C. Gaina. Plate tectonic evolution of eastern australian marginal ocean basins. In K. Hill and T. Bernecker, editors, *Eastern Australasian Basins Symposium: a refocussed energy perspective for the future.*, page 227–237. PESA Special Publication, 2001.

M. K. Sen and P. L. Stoffa. *Global Optimization Methods in Geophysical Inversion.* Cambridge University Press, New York, 2 edition, 2013. ISBN 978-1-107-01190-8.

G. G. Shor, H. K. Kirk, and H. W. Menard. Crustal Structure of the Melanesian Area. *Journal of Geophysical Research*, 76(11):2562–2586, 1971.

D. C. Skeels. Ambiguity in Gravity Interpretation. *Geophysics*, 12(1):43–56, 1947. doi: 10.1190/1.1437295.

K. Snopek. *Inversion of gravity data with application to density modeling of the Hellenic subduction zone.* PhD thesis, Ruhr Universität Bochum, 2005.

H. M. J. Stagg, I. Borissova, M. Alcock, and A. M. G. Moore. Tectonic provinces of the Lord Howe Rise; Law of the Sea study has implications for frontier hydrocarbons. *AGSO Research Newsletter*, 31:31–32, 1999.

M. Talwani and M. Ewing. Rapid computation of gravitational attraction of three-dimensional bodies of arbitrary shape. *Geophysics*, 25:203–225, 1960.

M. Talwani and J. R. Heirtzler. Computation of magnetic anomalies caused by two-dimensional structures of arbitrary shape. *Stanford University Publications of the Geological Sciences, Computers in the Mineral Industries*, 1964.

M. Talwani, J. L. Worzel, and M. Landisman. Rapid gravity computations for two-dimensional bodies with application to the Mendocino submarine fracture zone. *J. Geophys. Res.*, 64(1): 49–59, 1959.

A. Tarantola. *Inverse Problem Theory and Model Parameter Estimation.* SIAM Publications, Philadelphia, 2nd edition, 2005.

J. Tronicke, H. Paasche, and U. Böniger. Crosshole traveltime tomography using particle swarm optimization: A near-surface field example. *Geophysics*, 77(1):R19–R32, 2012. doi: 10.1190/geo2010-0411.1.

V. Vacquier, N. C. Steenland, R. G. Henderson, and C. St-Hilaire. Interpretation of areomagnetic maps. Geological Society of America, Memoir 47, 1951.

F. Van den Bergh. *An Analysis of Particle Swarm Optimizers.* PhD thesis, University of Pretoria, 2001.

D. Wilken. *Zur Anwendung von Schwarmintelligenz-Optimierung auf die Dispersionsanpassung von Scholtewellen.* PhD thesis, University Kiel, 2009.

D. Wilken and W. Rabbel. On the application of Particle Swarm Optimization strategies on Scholte-wave inversion. *Geophysical Journal International*, 190:580–594, 2012. doi: 10.1111/j.1365-246X.2012.05500.x.

J. B. Willcox, J. Sayers, H. M. J. Stagg, and S. Van De Beuque. Geological framework of the Lord Howe Rise and adjacent oceanic basins. In K. C. Hill and T. Bernecker, editors, *Eastern Australasian Basins Symposium: a refocussed energy perspective for the future*, pages 211–225. PESA Special Publication, 2001.

I. J. Won and M. Bevis. Computing the gravitational and magnetic anomalies due to a polygon: Algorithms and Fortran subroutines. *Geophysics*, 52(2):232–238, 1987.

H. Zhu and P. A. Symonds. Seismic interpretation, gravity modelling and petroleum potential of the southern Lord Howe Rise region. In *New Zealand Petroleum Conference Proceedings*, pages 223–230, 1994.

P. Ziegler. Geological Atlas of Western and Central Europe. *Geol. Soc. Publ. House Bath, 2 edition. Shell International Petroleum*, 1990.

A. Supplementary maps

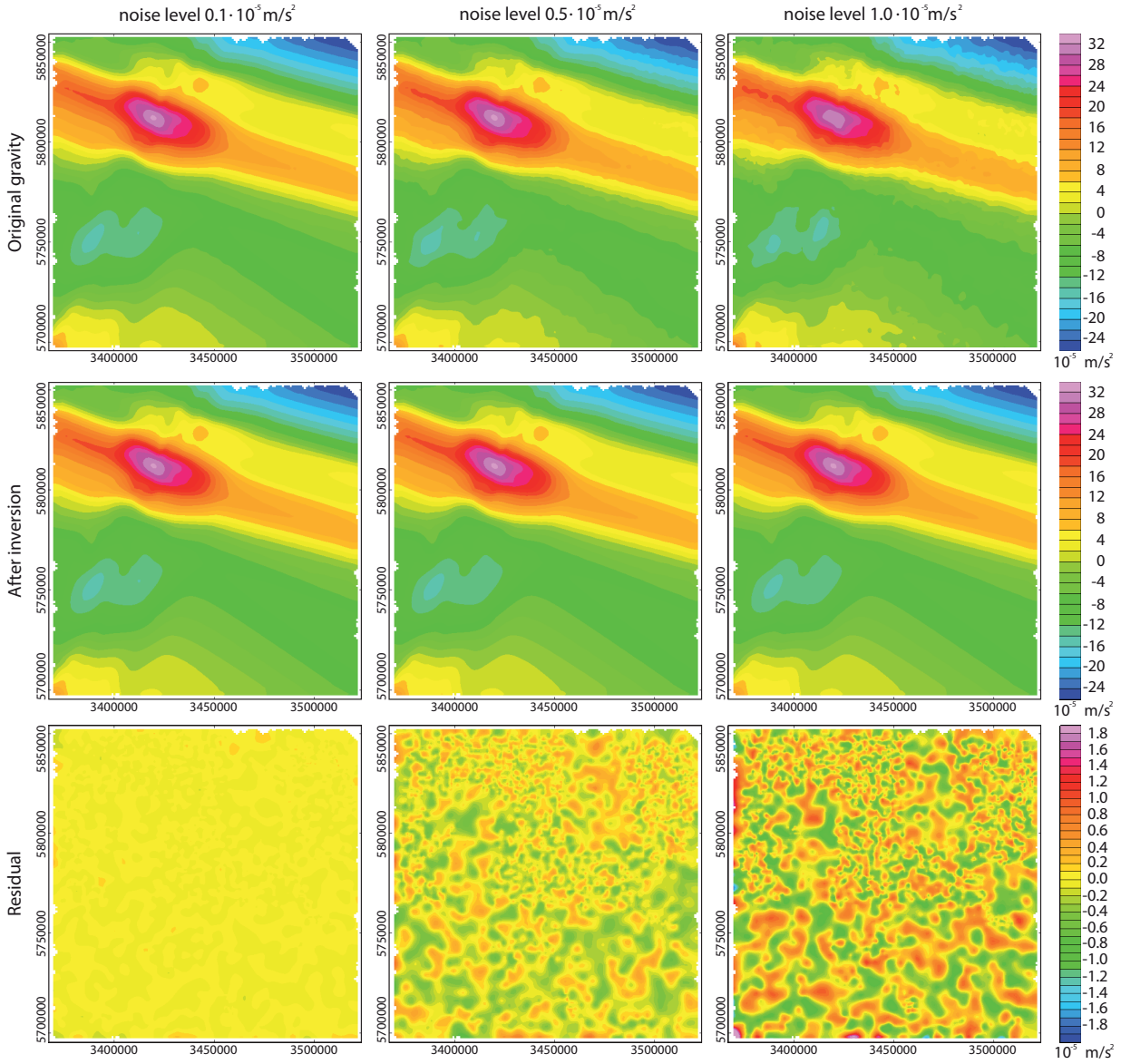

Figure A.1.: *Bramsche Anomaly gravity maps from application 1, with single inversions for three different noise levels. Shown are original anomaly (top), inversion result (middle) and the residual (bottom).*

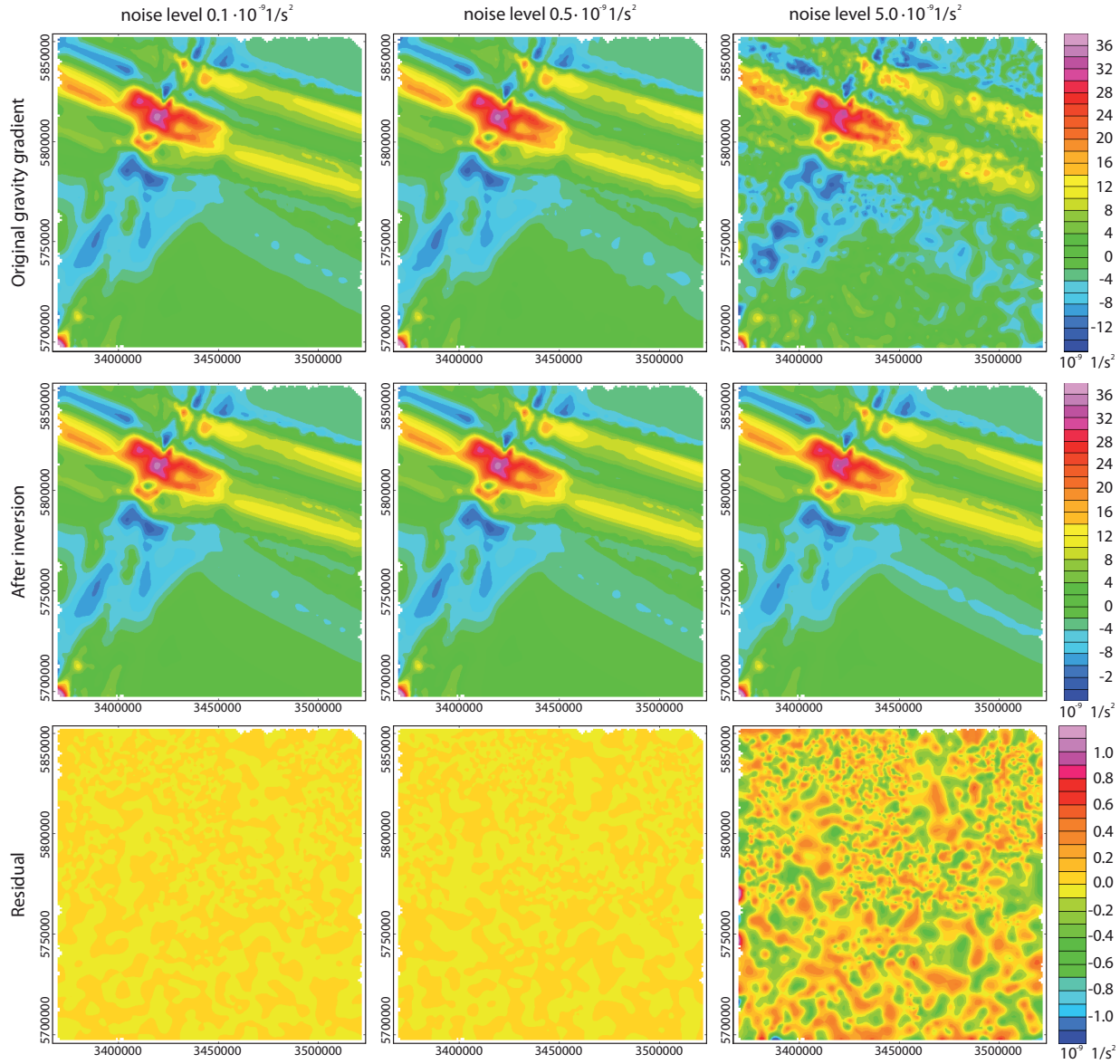

Figure A.2.: *Bramsche Anomaly gravity gradient maps from application 1, with single inversions for three different noise levels. Shown are original anomaly (top), inversion result (middle) and the residual (bottom).*

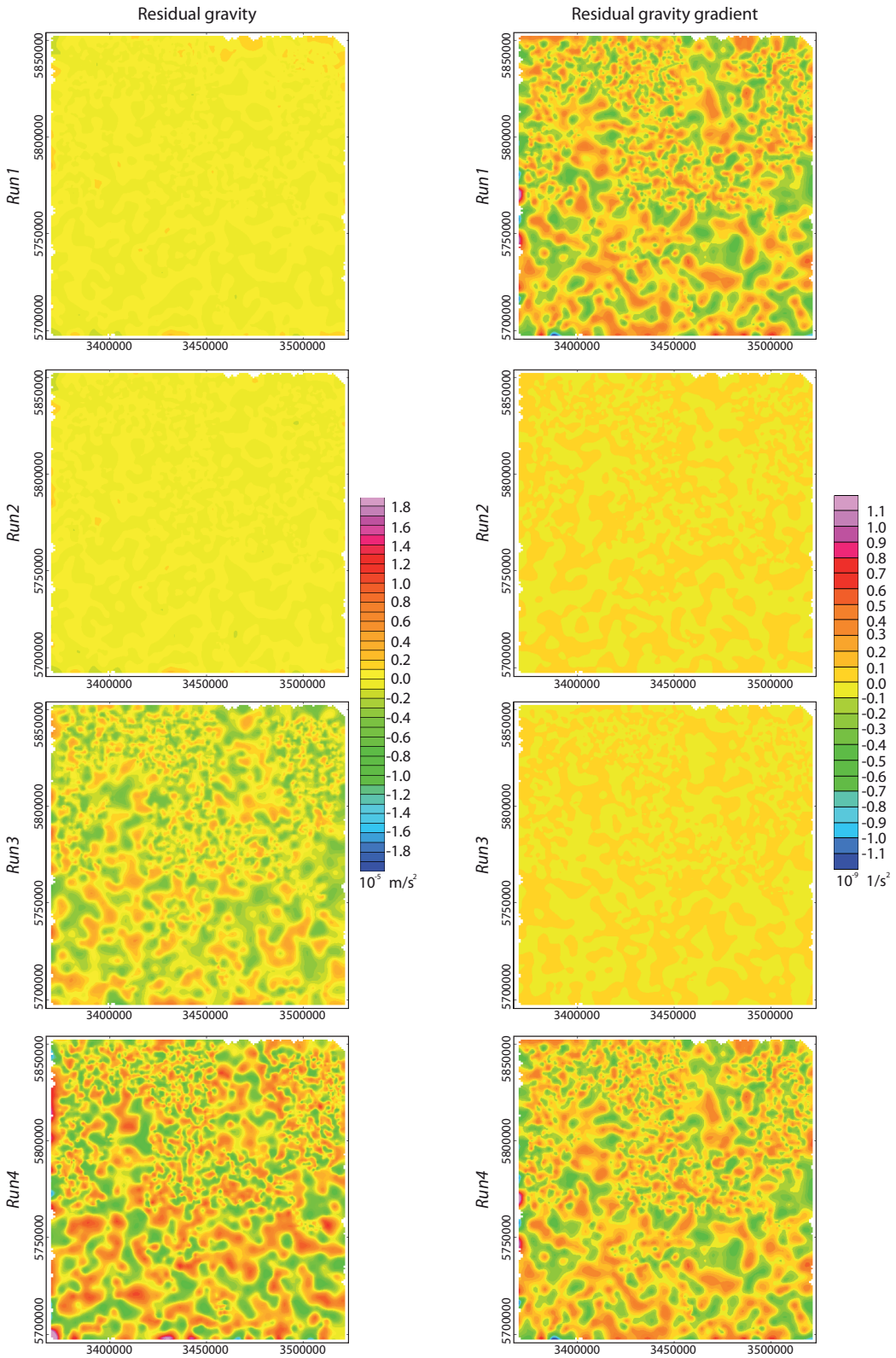

Figure A.3.: *Bramsche Anomaly residual gravity and gravity gradient maps from application 1, Runs1-4.*

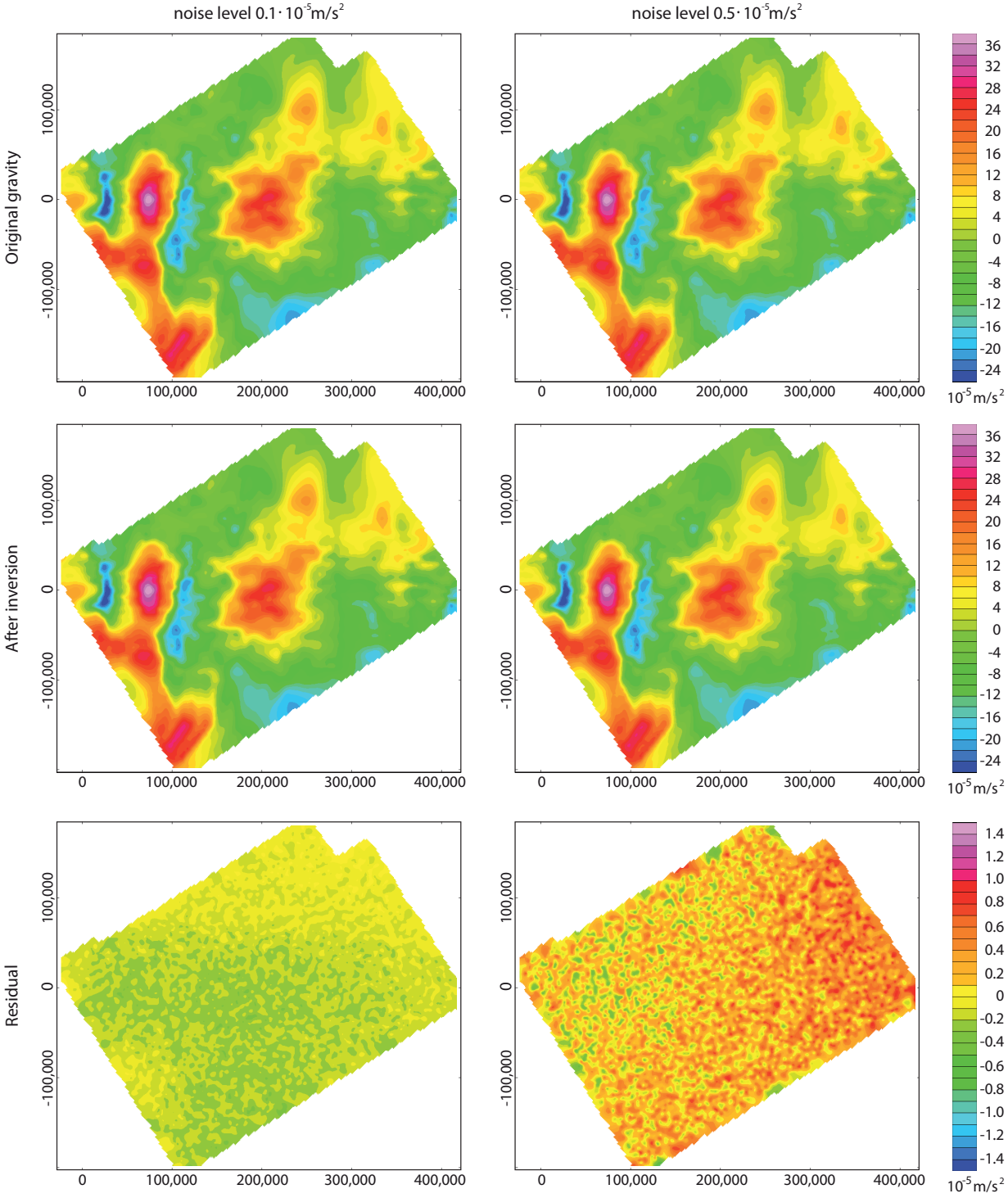

Figure A.4.: *Pritzwalk Anomaly gravity maps. Calculated response anomalies from the Kuder (2002) model with added, normal distributed noise. Left:* g_{n1} *with noise between* $\pm 0.1 \cdot 10^{-5} m/s^2$. *Right:* g_{n2} *with noise between* $\pm 0.5 \cdot 10^{-5} m/s^2$.

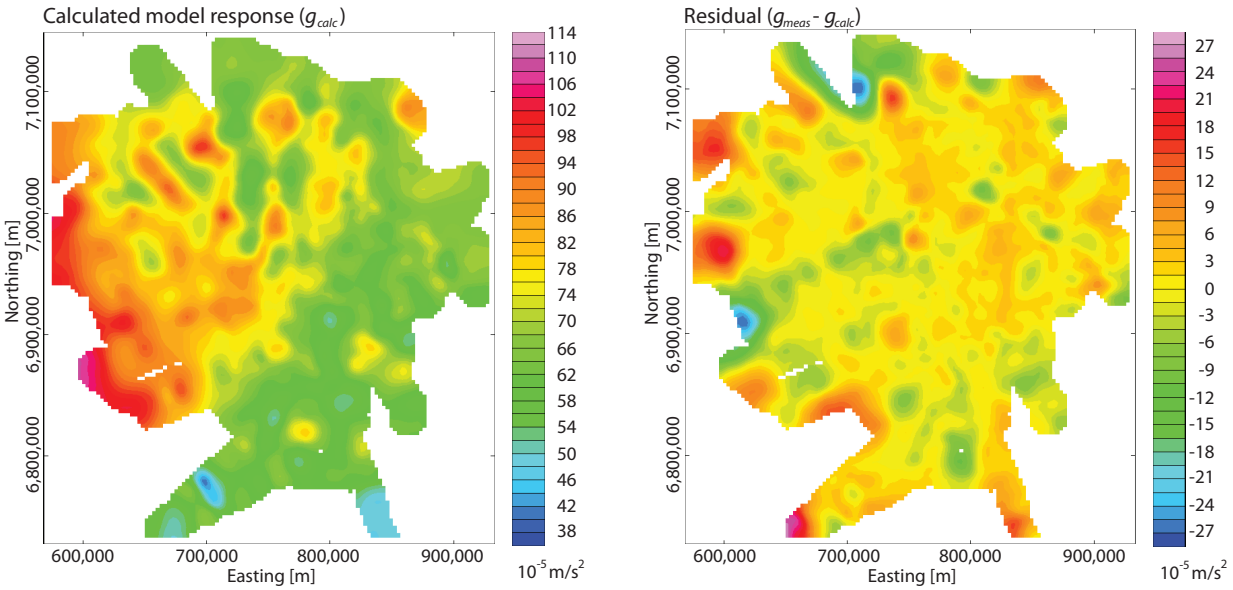

Figure A.5.: *Capel and Faust Basins gravity anomaly and residual map after inversion application 1, Run 1.*

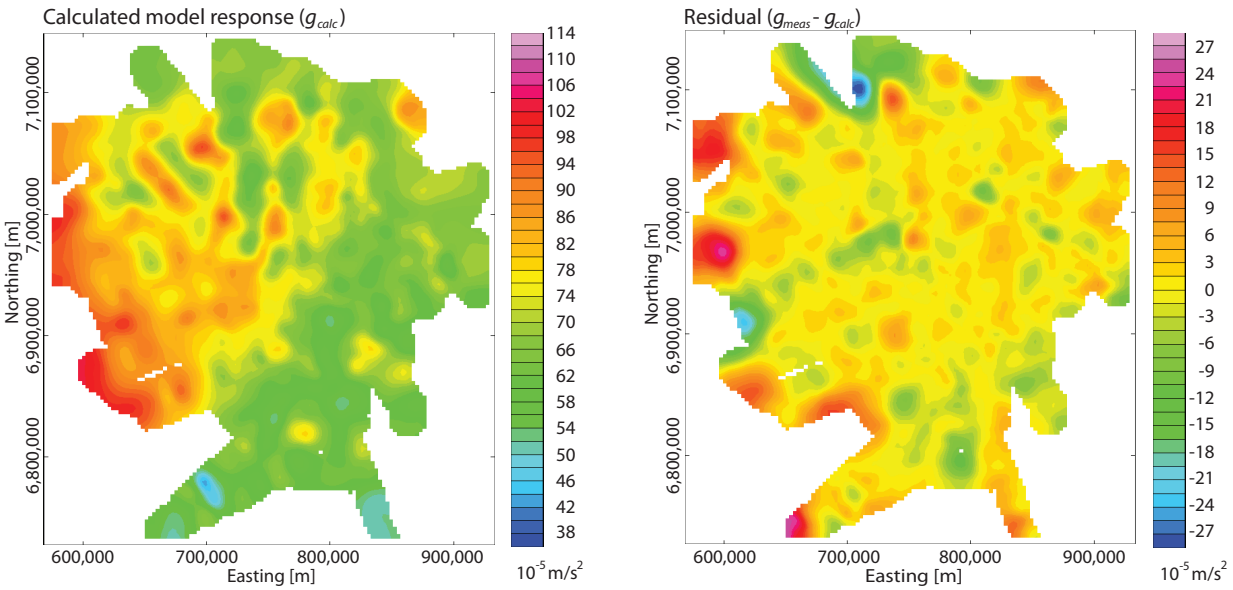

Figure A.6.: *Capel and Faust Basins gravity anomaly and residual map after inversion application 1, Run 2.*

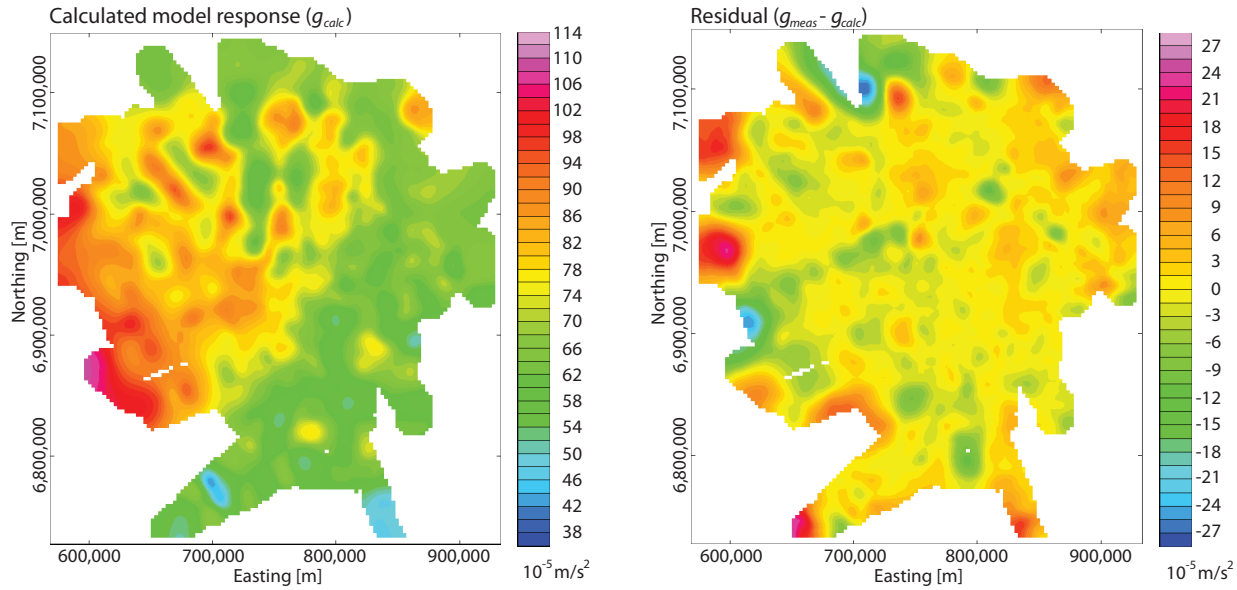

Figure A.7.: *Capel and Faust Basins gravity anomaly and residual map after inversion application 1, Run 3.*

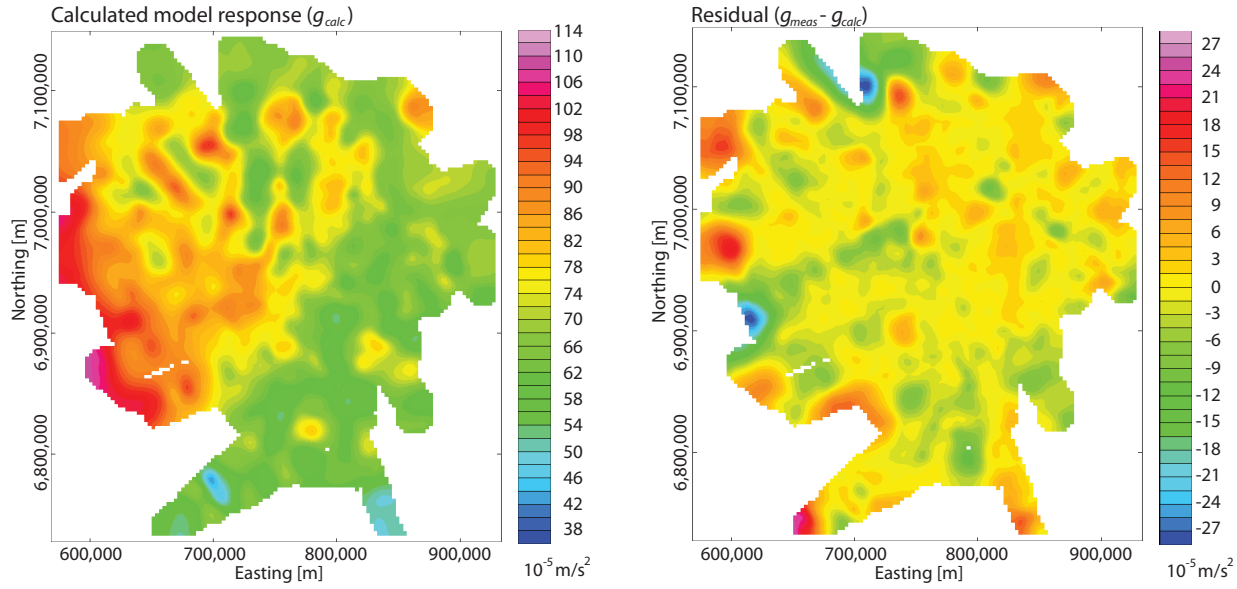

Figure A.8.: *Capel and Faust Basins gravity anomaly and residual map after inversion application 2, Run 1.*

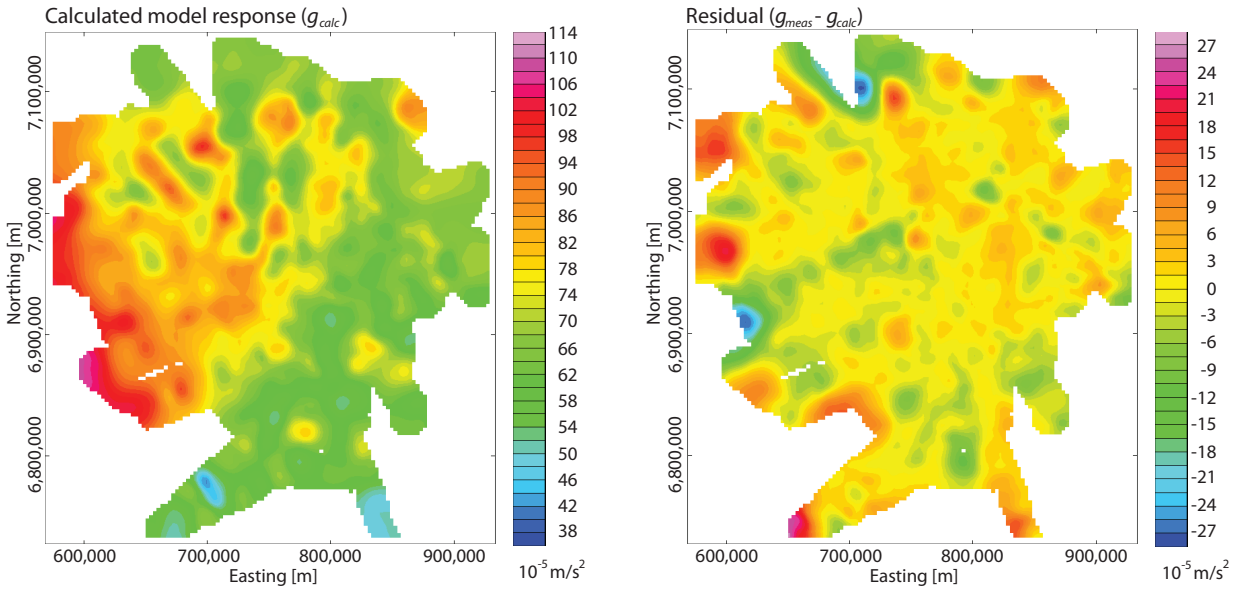

Figure A.9.: *Capel and Faust Basins gravity anomaly and residual map after inversion application 2, Run 2.*

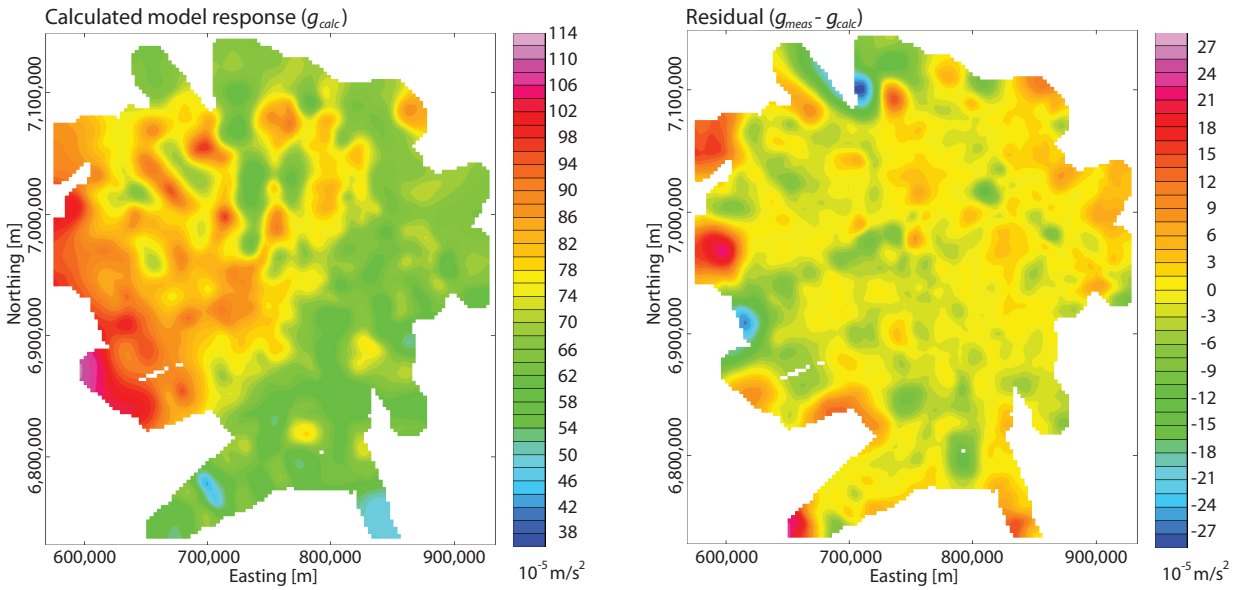

Figure A.10.: *Capel and Faust Basins gravity anomaly and residual map after inversion application 2, Run 3.*

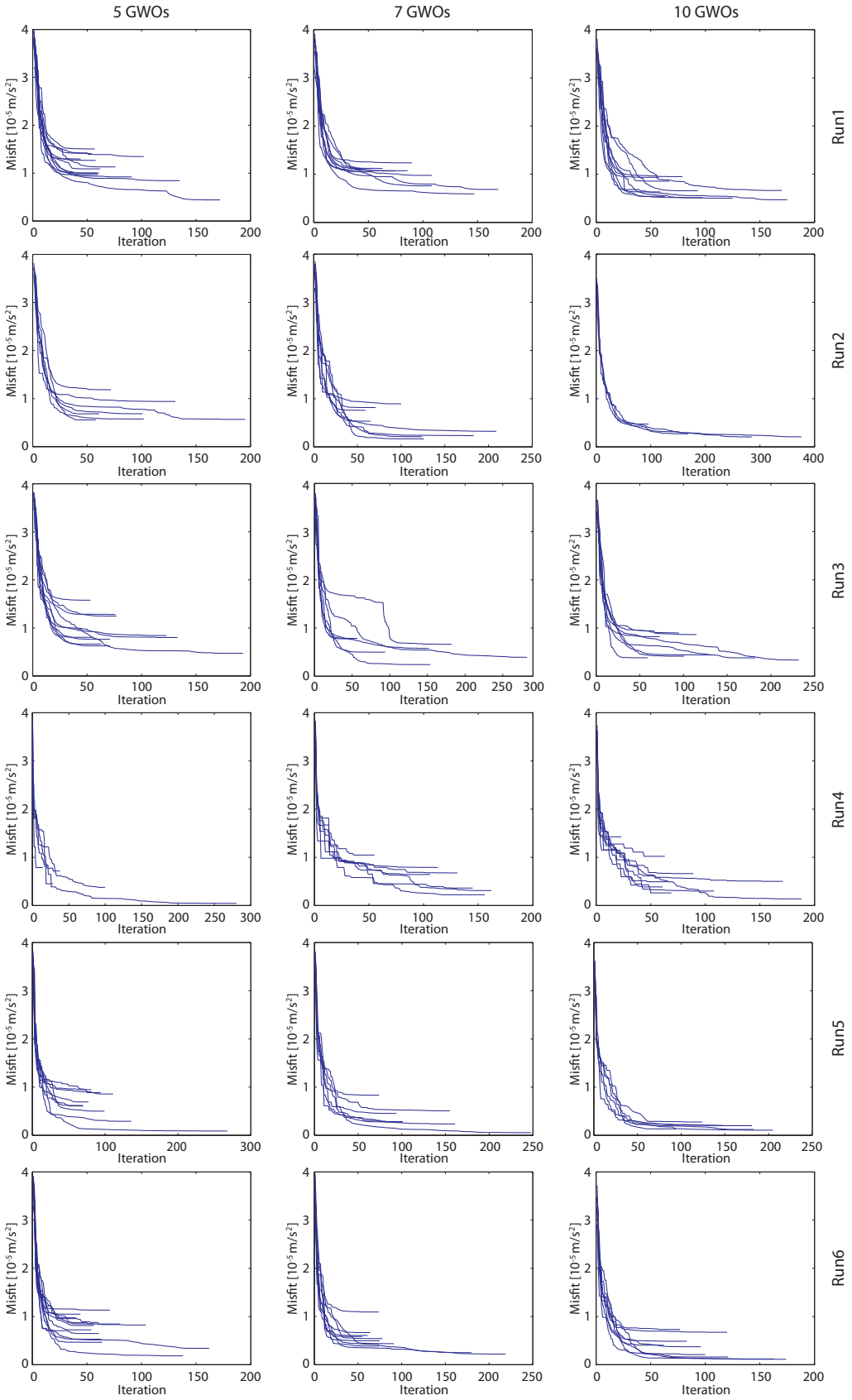
5 GWOs
7 GWOs
10 GWOs
Run1
Run2
Run3
Run4
Run5
Run6
Misfit [10⁻⁵ m/s²]
Iteration

B. Supplementary tables

Index	Geology	pmc_{gz} [%]			$pmc_{gzz,h}$ [%]		
		max	*mean*	*rms*	*max*	*mean*	*rms*
1	Tertiary	13.2	13.0	13.1	15.7	23.7	19.9
2	Cretaceous	15.5	15.8	15.7	18.2	18.4	17.3
3	Jurassic	14.2	15.5	15.4	10.7	11.2	10.9
4	Triassic	16.9	18.5	18.4	6.5	11.0	9.1
5	Zechstein	24.6	21.3	21.4	36.3	23.0	30.3
6	Permian	13.9	15.5	15.4	3.6	8.0	6.3
7	Cap rock	1.7	0.4	0.6	9.0	4.7	6.2

Table B.1.: *Prominences of the model bodies of the synthetic salt dome related to the gravity anomaly (pmc_{gz}), the gravity gradient anomaly (pmc_{gzz}) and magnetic anomaly (pmc_h).*

Index	Density	Geology	Index	Density	Geology
1	2.188	Tertiär	13	2.650	Kambrium_2
2	2.100	Tertiär_2	14	2.500	Kambrium_3
3	2.350	Kreide	15	2.650	Kambrium_4
4	2.350	Kreide_2	16	2.650	Kambrium_5
5	2.350	Kreide_3	17	2.800	Präkambrium
6	2.450	Jura	18	2.800	Präkambrium_2
7	2.450	Jura_2	19	2.800	Präkambrium_3
8	2.450	Jura_3	20	2.650	Intrusion
9	2.500	Rotliegend_bis_Jura	21	2.650	Intrusion_2
10	2.500	Rotliegend_bis_Jura_2	22	2.650	Intrusion_3
11	2.500	Rotliegend_bis_Jura_3	23	2.950	Intrusion_kamb
12	2.650	Kambrium	24	2.900	Intrusion_pra

Table B.2.: *Bramsche model details.*

Index	Density	Geology	Index	Density	Geology
1	2.72	Upper_Crust4v	42	2.0	Upper_Crust5c
2	2.67	Upper_Crust3v	43	2.65	Vulkanite
3	2.8	Upper_Crust6av	44	2.59	Parchim_Fmt.
4	2.65	VulkaniteM	45	2.59	Mirow_Fmt.
5	2.75	Upper_Crust2cv	46	2.56	Elbe-Folge
6	2.8	Upper_Crust1bv	47	2.15	Zechstein
7	3.3	Mantlev	48	2.53	Buntsandstein
8	3.1	Lower_Crust2v	49	2.5	Muschelkalk
9	2.77	Upper_Crust5bv	50	2.56	Keuper
10	2.72	Upper_CrustHDB1av	51	2.45	Jurassic
11	3.1	Lower_Crust3v	52	2.3	Lower_Cretaceous
12	3.1	Lower_Crust1v	53	2.13	Upper_Cretaceous
13	2.8	Upper_Crust6bv	54	2.3	Lower_Cretaceous3
14	2.69	Upper_Crust2bv	55	2.13	Upper_Cretaceous3
15	2.634	Upper_Crust2av	56	2.1	Quat_Tert3
16	2.8	Upper_Crust1av	57	2.83	Upper_CrustHDB2
17	2.77	Upper_Crust5av	58	2.72	Upper_CrustHDB1b
18	2.77	Upper_Crust5cv	59	2.72	Upper_Crust4h
19	2.88	Upper_CrustHDB2v	60	2.753	Upper_Crust3h
20	2.72	Upper_CrustHDB1bv	61	2.8	Upper_Crust6ah
21	2.72	Upper_Crust4	62	2.75	Upper_Crust2ch
22	2.637	Upper_Crust3	63	2.8	Upper_Crust1bh
23	2.8	Upper_Crust6a	64	3.3	Mantleh
24	2.759	Upper_Crust2c	65	3.1	Lower_Crust2h
25	2.774	Upper_Crust1b	66	2.77	Upper_Crust5bh
26	3.3	Mantle	67	2.72	Upper_CrustHDB1ah
27	3.1	Lower_Crust2	68	3.1	Lower_Crust3h
28	2.77	Upper_Crust5b	69	3.1	Lower_Crust1h
29	2.72	Upper_CrustHDB1a	70	2.8	Upper_Crust6bh
30	3.1	Lower_Crust3	71	2.75	Upper_Crust2bh
31	3.1	Lower_Crust1	72	2.75	Upper_Crust2ah
32	2.772	Upper_Crust6b	73	2.8	Upper_Crust1ah
33	2.73	Upper_Crust2b	74	2.77	Upper_Crust5ah
34	2.7	Upper_Crust2a	75	2.77	Upper_Crust5ch
35	2.781	Upper_Crust1a	76	2.88	Upper_CrustHDB2h
36	2.5	Upper_Crust5a	77	2.72	Upper_CrustHDB1bh
37	2.1	Quat_Tert1	78	2.1	Quat_Tert
38	2.13	Upper_Cretaceous1	79	2.446	Upper_Crustx
39	2.3	Lower_Cretaceous1	80	2.88	IntrusionTop
40	2.622	VulkaniteL	81	3.0	IntrusionDown
41	2.65	VulkaniteR	82	2.67	Reference

Table B.3.: *Pritzwalk model details.*

Geology	Densities [t/m^3] Init	Sol_1	Sol_2	Sol_3	Sol_4	Sol_5	Sol_6	Sol_7	Mean	Std
Tertiary	2.170	2.125	2.221	2.248	2.243	2.192	2.248	2.220	2.214	0.044
Cretaceous	2.270	2.315	2.326	2.313	2.356	2.268	2.306	2.313	2.314	0.026
Jurassic	2.370	2.455	2.368	2.349	2.331	2.394	2.377	2.375	2.378	0.040
Triassic	2.470	2.382	2.501	2.450	2.469	2.490	2.431	2.493	2.459	0.042
Zechstein	2.070	1.988	1.982	2.036	1.981	1.996	2.015	1.976	1.997	0.022
Permian	2.570	2.629	2.538	2.543	2.522	2.592	2.582	2.598	2.572	0.038

Table B.4.: *Density estimates for salt diapir gained by POGO together with geometry modifications. The densities were allowed to vary within a range of* $\pm 100\,t/m^3$ *around the initial values.*

Geology	Densities [t/m^3] Init	Sol_1	Sol_2	Sol_3	Sol_4	Mean	Std
Tertiary	2.170	2.165	2.171	2.219	2.127	2.170	0.038
Cretaceous	2.270	2.262	2.270	2.292	2.275	2.275	0.013
Jurassic	2.370	2.530	2.476	2.357	2.320	2.421	0.099
Triassic	2.470	2.397	2.561	2.610	2.542	2.528	0.092
Zechstein	2.070	1.944	1.885	1.887	1.921	1.909	0.029
Permian	2.570	2.637	2.549	2.575	2.712	2.618	0.073

Table B.5.: *Density estimates for salt diapir gained by POGO together with geometry modifications. The densities were allowed to vary within a range of* $\pm 200\,t/m^3$ *around the initial values.*

Solution	Shallow model area Correlation [%]	Std. dev. [10^{-5} m/s^2]	Deep model area Correlation [%]	Std. dev. [10^{-5} m/s^2]
1	97.4	3.2	98.9	1.9
2	93.2	4.8	98.4	2.3
3	96.1	4.0	98.8	2.0
4	97.2	3.1	99.0	1.9
5	99.0	1.9	98.8	2.0
6	95.5	4.1		
7	93.4	4.7		
8	98.0	2.6		
9	98.7	2.1		
initial	86.4	6.6	86.4	6.6

Table B.6.: *Geometry fit along the cross section through Capel and Faust basins after geometry optimization. Listed are the correlations and standard deviations for the shallow modeling area (without Moho) and the deep modeling area (including Moho adjustments).*

Solution	Shallow model area		Deep model area	
	Correlation [%]	Std. dev. [10^{-5} m/s^2]	Correlation [%]	Std. dev. [10^{-5} m/s^2]
1	99.0	1.8	97.9	2.7
2	98.4	2.4	99.1	1.8
3	98.0	2.6	97.4	3.0
4	97.7	3.0	98.4	2.4
5	97.5	2.9	99.4	1.4
6	97.6	3.0	97.8	2.7
7	96.1	3.7		
8	97.3	3.0		
9	97.2	3.1		
10	97.2	3.2		
initial	86.4	6.6	86.4	6.6

Table B.7.: *Geometry fit along the cross section through Capel and Faust basins after geometry and density optimization. Listed are the correlations and standard deviations for the shallow modeling area (without Moho) and the deep modeling area (including Moho adjustments).*

Geology	Density [t/m^3]							
	Init	Sol_1	Sol_2	Sol_3	Sol_4	Sol_5	Sol_6	Sol_7
Water	2.000	2.000	2.000	2.000	2.000	2.000	2.000	2.000
Upper sediments	2.150	1.874	1.650	2.159	1.771	1.747	1.756	1.670
Middle sediments	2.350	2.193	2.551	2.156	2.592	2.169	2.492	2.481
Lower sediments	2.450	2.314	2.338	2.572	2.299	2.429	2.322	2.151
Basement	2.700	2.700	2.696	2.699	2.701	2.697	2.700	2.690
Mantle	3.100	3.155	3.160	3.074	3.143	3.154	3.137	3.212

Geology	Init	Mean	Std
Water	2.000	—	—
Upper sediments	2.150	1.804	0.173
Middle sediments	2.350	2.376	0.194
Lower sediments	2.450	2.346	0.129
Basement	2.700	2.698	0.004
Mantle	3.100	3.147	0.041

Table B.8.: *Density results from the Capel and Faust Basins. Within the shallow modeling area geometry and densities were optimized. The 11 estimations from the solution ensemble are numbered. Also listed are the mean density estimates with standard deviations. These numbers belong to the upper density plot in Figure 6.10.*

Geology	Density [t/m^3]						
	Init	Sol_1	Sol_2	Sol_3	Sol_4	Sol_5	Sol_6
Water	2.000	2.000	2.000	2.000	2.000	2.000	2.000
Upper sediments	2.150	2.058	1.672	1.707	1.743	1.863	1.752
Middle sediments	2.350	2.197	2.322	2.415	2.298	2.556	2.480
Lower sediments	2.450	2.227	2.415	2.400	2.444	2.275	2.587
Basement	2.700	2.691	2.274	2.702	2.698	2.696	2.708
Mantle	3.100	3.189	3.192	3.121	3.155	3.126	3.015

Geology	Init	Mean	Std
Water	2.000	—	—
Upper sediments	2.150	1.799	0.142
Middle sediments	2.350	2.378	0.131
Lower sediments	2.450	2.368	0.136
Basement	2.700	2.698	0.006
Mantle	3.100	3.133	0.065

Table B.9.: *Density results from the Capel and Faust Basins. Within the deep modeling area geometry and densities were optimized. The estimations from the solution ensemble are numbered. Also listed are the mean density estimates with standard deviations. These numbers belong to the lower density plot in Figure 6.10.*

List of Figures

2.1. Flowchart of forward and inverse method . . . 10
2.2. Example of voxel model . . . 12
2.3. Example of layer model . . . 13
2.4. Example of polyhedron model . . . 14
2.5. Ambiguity in potential field modeling . . . 15

3.1. Illustration of voxels, regions and groups. . . . 20
3.2. Mass point vs. exact calculation of voxel model response . . . 23
3.3. Salt structure cross section . . . 27
3.4. Example for prominence of model bodies . . . 28
3.5. Prominence of model bodies related to different potential fields . . . 29

4.1. Synthetic salt dome . . . 32
4.2. Anomalies of synthetic salt dome . . . 33
4.3. RMS error of synthetic salt dome inversions . . . 34
4.4. Results of synthetic salt dome inversion . . . 35
4.5. Data with noise . . . 37
4.6. Northwest German Basin within the Central European Basin System . . . 38
4.7. Bramsche gravity anomaly . . . 39
4.8. Cross section through Bramsche model . . . 40
4.9. Bramsche Anomaly - Original calculated anomalies . . . 41
4.10. Bramsche Anomaly - Inversion results from Application 1 . . . 43
4.11. Bramsche Anomaly - Gravity anomalies after inversion and residual maps . . . 44
4.12. Bramsche Anomaly - Inversion from measured data . . . 45
4.13. Pritzwalk Anomaly gravity map . . . 47
4.14. Pritzwalk Anomaly - Model response and residual . . . 48
4.15. Pritzwalk Anomaly - Inversion results . . . 49
4.16. Map of the northern Tasman Sea, Capel and Faust Basins . . . 51
4.17. Correlation of gravity and seismics in Capel and Faust Basins . . . 52
4.18. Capel and Faust Basins - Bouguer gravity map . . . 53
4.19. Capel and Faust Basins - The voxel model . . . 54
4.20. Sketch of enlarged voxel model . . . 55
4.21. Capel and Faust Basins voxel model cross section . . . 56
4.22. Capel and Faust Basins - Density profile (voxel model) . . . 58
4.23. Capel and Faust Basins - 3D model . . . 59
4.24. Capel and Faust Basins - Voxel model and polyhedron interfaces . . . 59
4.25. Capel and Faust Basins - Calculated and residual gravity anomalies . . . 60
4.26. Capel and Faust Basins - Density profiles . . . 61
4.27. Capel and Faust Basins - Density profiles . . . 63

5.1. Vertex movement and destroyed topology . . . 70
5.2. Direct vertex movement with constraints . . . 71
5.3. Spatial distortion using a superimposed grid . . . 72
5.4. Principle of Gaussian Warp Operator . . . 73
5.5. Sketch of Gaussian Warp Operator . . . 74
5.6. Demonstration of geometry modifications by GWO . . . 75
5.7. Gaussian Warp Operator and discretization . . . 76
5.8. Flowchart if warper path crosses polygon sides . . . 77
5.9. Find path points of operator . . . 78
5.10. Warper path crosses polygon sides . . . 78
5.11. Discretization within warper path . . . 79
5.12. Movement of particle through parameter space . . . 82
5.13. Illustration of atomic PSO . . . 83
5.14. Flow chart of POGO . . . 85
5.15. Linking model bodies of same property . . . 86
5.16. Functionality of constraining boxes . . . 86

6.1. Synthetic salt diapir, anomaly and initial models for POGO . . . 90
6.2. Deformation caused by GWOs of different sizes, with respect to expected salt diapir 92
6.3. PSO results for salt diapir from *Run5* using initial model *i1* . . . 95
6.4. PSO results for salt diapir from *Run5* using initial model *i2* . . . 96
6.5. Operator distribution within ensemble . . . 97
6.6. PSO results for salt diapir from geometry and density optimization . . . 99
6.7. Capel and Faust Basins - Extracted cross section and anomaly . . . 101
6.8. Capel and Faust Basins - 3D vs. 2D modeling . . . 102
6.9. Capel Faust Basins - Geometry-only optimization results . . . 103
6.10. Capel Faust Basins - Geometry and density optimization results . . . 104
6.11. Capel and Faust Basins - Convergence of objective function . . . 105

7.1. Possible workflow for interdisciplinary modeling and interpretation . . . 111

A.1. Bramsche Anomaly - Gravity maps for application 1, single gz-inversion . . . 121
A.2. Bramsche Anomaly - Gravity gradient maps for application 1, single gzz-inversion 122
A.3. Bramsche Anomaly - Residual gravity and gravity gradient maps for application 1, *joint*-inversion . . . 123
A.4. Pritzwalk Anomaly - Original gravity anomaly with noise . . . 124
A.5. Capel and Faust Basins - Anomaly map 1.1 . . . 125
A.6. Capel and Faust Basins - Anomaly map 1.2 . . . 125
A.7. Capel and Faust Basins - Anomaly map 1.3 . . . 126
A.8. Capel and Faust Basins - Anomaly map 2.1 . . . 126
A.9. Capel and Faust Basins - Anomaly map 2.2 . . . 127
A.10. Capel and Faust Basins - Anomaly map 2.3 . . . 127

List of Tables

4.1. Physical properties of synthetic salt model and inversion parameters 31
4.2. Inversion mode abbreviations 34
4.3. Bramsche Anomaly - Inversion parameters and estimated density 41
4.4. Bramsche Anomaly - Inversion results, gravity anomaly misfit 42
4.5. Bramsche Anomaly - Inversion results, gravity gradient anomaly misfit 42
4.6. Pritzwalk Anomaly - Inversion set-up and results 50
4.7. Capel and Faust Basins - Voxel inversion results 57
4.8. Capel and Faust Basins - Inversion 1 results 61
4.9. Capel and Faust Basins - Inversion 2 results 62

6.1. Summary of parameters for POGO 90
6.2. Different weighting parameters for the PSO 93
6.3. Test of PSO weighting parameters with varying number of GWOs 94
6.4. PSO density results for salt diapir using uniform initial densities 98

B.1. Prominences of the salt dome model bodies 129
B.2. Bramsche model details 129
B.3. Pritzwalk model details 130
B.4. Density estimates for salt diapir from POGO, Run5_7d1 131
B.5. Density estimates for salt diapir from POGO, Run5_7d2 131
B.6. Capel and Faust basins - Anomaly fit after geometry-only optimization 131
B.7. Capel and Faust basins - Anomaly fit after geometry and density optimization . . . 132
B.8. Capel and Faust Basins - Geometry and density optimization, shallow modeling area, density results 132
B.9. Capel and Faust Basins - Geometry and density optimization, deep modeling area, density results 133

List of Symbols and Abbreviations

Symbols

γ	Universal gravitational constant
M, $\boldsymbol{M}$	Magnetization
$\boldsymbol{m}$	Magnetic dipole moment
χ	Magnetic susceptibility
ρ	Density
$\boldsymbol{F}$	Vector force field
Φ	Scalar potential
$\boldsymbol{g}$	Gravitational attraction
U	Gravitational or *Newtonian* potential
m	Mass
$\boldsymbol{B}$	Magnetic field
$\boldsymbol{H}$	Induced magnetic field
$\boldsymbol{C}$	Covariance matrix
$\boldsymbol{E}$	Expectation value
g_s	Gravity anomaly shift
ρ_s	Anomaly shift producing density
V	Magnetic potential
μ_0	Permeability of free space
σ	Standard deviation
μ	Parents (in Evolution Strategy)
λ	Offspring (in Evolution Strategy)
R_c	Core radius (in cPSO)
R_p	Perception radius (in cPSO)
Q	Charge (in cPSO)
c_1	Weighting constant for cognitive component (gbest PSO)
c_2	Weighting constant for social component (gbest PSO)
ω	Weighting constant for PSO inertia
d_{max}	Maximal allowed vertex separation
l	Path length of Gaussian Warp Operator
(x_s, y_s, z_s)	Coordinates of GWO starting point
(x_e, y_e, z_e)	Coordinates of GWO end point
Θ	Directional angle of GWO path
ϕ	2nd directional angle of GWO path
Mp	Center of GWO path

Abbreviations

AGG	Airborne Gravity Gradiometry
CDF	Caledonian Deformation Front
CEBS	Central European Basin System
CHAIN	Claudia HAase's INversion
CHAMP	CHAllenging Minisatellite Payload
DEKORP	DEutsches KOntinentales Reflexionsseismisches Programm
DSDP	Deep Sea Drilling Program
EA	Evolution Algorithms
ES	Evolution Strategy
FTG	Full Tensor Gravity
GA	Genetic Algorithms
GM-SYS	Gravity and Magnetic modeling SYStem
GOCE	Gravity field and steady-state Ocean Circulation Explorer
GRACE	Gravity Recovery And Climate Experiment
GUI	Graphical User Interface
GWO	Gaussian Warp Operator
IGMAS	Interactive Geophysical Modelling ASsistant
MMSE	Minimum Mean-Square Error
NEGB	NorthEast German Basin
NGB	North German Basin
NWGB	NorthWest German Basin
PSO	Particle Swarm Optimization
POGO	Particle swarm Optimization with Gaussian warp Operator parametrization
RMS	Root Mean Square
SA	Simulated Annealing
TEF	Trans-European Fault zone
UBC-GIF	University of British Columbia - Geophysical Inversion Facility
VE	Vertical Exaggeration

Acknowledgments

I would like to thank all who helped me in succeeding to prepare this work, whether it has been in a professional, technical or personal manner. I am especially thankful to:

Prof. Dr. Hans-Jürgen Götze for providing me with the possibility to carry out this work in the first place and for supervising me during the process, for the opportunities he opened up for me and the continuing support.

Prof. Dr. Jörg Ebbing for acting as co-referee and for the helpful comments and discussions.

The members of the **AG Geophysik and Geoinformation** and the neighboring teams in the Geophysics department at the University of Kiel for the friendly working environment, interesting discussions and the overall great time I had in Kiel.

The new colleagues from the **Sokkelgeofysikk** group at NGU for their warm welcome and the excellent working environment and especially **Dr. Odleiv Olesen** for his support.

The Basin Research Group at **Geoscience Australia** for the opportunity to work with them and for providing me with the Capel and Faust Basins model. Special thanks go to **Dr. Ron Hackney** and family for their cordial welcome and hospitality during my stay in Canberra.

The School of Geography, Environment and Earth Sciences at **Victoria University of Wellington**, New Zealand, for the possibility to work in their department and **Prof. Dr. Tim Stern** for the splendid accommodation.

Dr. Dennis Wilken for the proof-reading and comments, the many discussions on swarming and warping, the time travels -back and forth- and especially the cruisin' time.

Jan-Hendrik Palic for his help whenever any programming or system software deserted me and the many thought sorting and mind clearing discussions and chats.

Dr. Sofie Gradmann for the thorough proof-reading and helpful comments, the discussions and the ongoing encouragement.

Lina Wildenhain for simply being the best sister-in-law and especially for the small things, supportive and motivating.

My dear mother **Karin Haase** and my big brother and sisters, **Ralf Wildenhain**, **Manuela Hensiek** and **Bianca Haase**, for their love, support, the never-ending encouragement and belief in me. I cannot thank you enough, love you. :)

My father **Rolf-Dieter Haase**, who was the first to show me the world at the age of 5, on board that white-and-green container ship. I am sure that started leading me the way I went. I stayed close to the sea ever since and you are always in my heart.

And to all the musicians and artists out there: Thank you so much for the music!

I would like to thank Wintershall Holding AG for financing the project TIMBA - "Towards the Integration of Multidisciplinary geophysical data in a shelf area: the Büsum-North Area as an example" which allowed me to prepare this work.

Erklärung

Diese Arbeit ist, abgesehen von der Beratung durch meinen Betreuer und die Zuhilfenahme der angegebenen Mittel, nach Inhalt und Form meine eigene. Die Arbeit hat weder ganz noch zum Teil bereits an anderer Stelle im Rahmen eines Prüfungsverfahrens vorgelegen, sie wurde bisher weder veröffentlicht noch zur Veröffentlichung eingereicht. Entstanden ist diese Arbeit unter Einhaltung der Regeln wissenschaftlicher Praxis der Deutschen Forschungsgemeinschaft.

(Ort) (Datum) (Claudia Haase)